UNIVERSITY OF MELBOURNE

DOCTORAL THESIS

Physics Beyond the Standard Model

Author:
Jackson D. CLARKE
ORCID ID: 0000-0001-6480-3716

Supervisors:
Prof. Raymond R. VOLKAS
Dr Robert FOOT

A thesis submitted in fulfilment of the requirements for the degree of Doctor of Philosophy

at the

University of Melbourne
Faculty of Science
School of Physics

within the

ARC Centre of Excellence for
Particle Physics at the Terascale

December 14, 2016

Printed on archival quality paper

"The old man stopped and turned. Andy stopped. The deep-brown eyes looked at Andy and the thin corded lips moved. What happened then Andy was never able either to explain or to forget. For the eyes spread out until there was no Chinaman. And then it was one eye – one huge brown eye as big as a church door. Andy looked through the shiny transparent brown door and through it he saw a lonely country-side, flat for miles but ending against a row of fantastic mountains shaped like cows' and dogs' heads and tents and mushrooms. There was low coarse grass on the plain and here and there a little mound. And a small animal like a woodchuck sat on each mound. And the loneliness – the desolate cold aloneness of the landscape made Andy whimper because there wasn't anybody at all in the world and he was left. Andy shut his eyes so he wouldn't have to see it any more and when he opened them, he was in Cannery Row and the old Chinaman was just flap-flapping between Western Biological and the Hediondo Cannery. Andy was the only boy who ever did that and he never did it again."

— John Steinbeck, *Cannery Row* (1945).

Abstract

Physics Beyond the Standard Model

by Jackson D. CLARKE

In this THESIS we present a collection of original bodies of work pertaining to a number of theoretical/phenomenological questions of the Standard Model, as studied from a "bottom-up" perspective.

In CHAPTER 2: HIGGS SECTOR we consider the implications of extending the Standard Model Higgs sector by a very light (100 MeV $< m_s < m_h/2$) real singlet scalar field. We identify the regions of parameter space which experiments at the Large Hadron Collider are uniquely sensitive to. There is a strong focus on low background displaced decay signatures.

In CHAPTER 3: NATURALNESS we show how a Higgs mass sensitivity measure can be rigorously derived from Bayesian probability theory. We use this measure to constrain the masses of various fermionic and scalar gauge multiplets, obtaining naturalness bounds of $\mathcal{O}$(1–100) TeV.

In CHAPTER 4: NEUTRINO MASS we write down the minimal UV completions for all the Standard Model dimension 7 operators which might be responsible for the radiative generation of Majorana neutrino masses. A detailed collider study of a one-loop realisation is performed.

In CHAPTER 5: BARYON ASYMMETRY OF THE UNIVERSE we present a proof that the three-flavour Type I seesaw model cannot provide an explanation for neutrino masses and the baryon asymmetry of the Universe via hierarchical leptogenesis without introducing a Higgs naturalness problem. We then describe a minimal extension (the "ν2HDM") which can avoid this conclusion.

In CHAPTER 6: STRONG CP PROBLEM we describe a very minimal model (the "νDFSZ") which can explain neutrino masses, the baryon asymmetry of the Universe, the strong CP problem, and dark matter, without introducing a naturalness problem for the Higgs. This model serves as an existence proof that weakly coupled high scale physics can naturally explain phenomenological shortcomings of the Standard Model.

Lastly, in CHAPTER 7: DARK MATTER we consider the implications of a class of self-interacting "plasma dark matter" models for direct detection experiments. A number of qualitatively unique signatures (when compared to single component collisionless dark matter) are identified. We emphasise the prediction for a signal which modulates with sidereal day.

Publications

References [1–11] below form a chronological list of journal publications, conference proceedings, and preprints authored or co-authored during this PhD candidature.

[1] J. D. Clarke, R. Foot, and R. R. Volkas. "Phenomenology of a very light scalar (100 MeV $< m_h <$ 10 GeV) mixing with the SM Higgs". *JHEP* 1402 (2014), p. 123. DOI: 10.1007/JHEP02(2014)123. arXiv: 1310.8042 [hep-ph].

[2] Y. Cai et al. "Testing Radiative Neutrino Mass Models at the LHC". *JHEP* 02 (2015), p. 161. DOI: 10.1007/JHEP02(2015)161. arXiv: 1410.0689 [hep-ph].

[3] J. D. Clarke, R. Foot, and R. R. Volkas. "Electroweak naturalness in the three-flavor type I seesaw model and implications for leptogenesis". *Phys. Rev.* D91.7 (2015), p. 073009. DOI: 10.1103/PhysRevD.91.073009. arXiv: 1502.01352 [hep-ph].

[4] J. D. Clarke. "Constraining portals with displaced Higgs decay searches at the LHC". *JHEP* 10 (2015), p. 061. DOI: 10.1007/JHEP10(2015)061. arXiv: 1505.00063 [hep-ph].

[5] J. D. Clarke, R. Foot, and R. R. Volkas. "Natural leptogenesis and neutrino masses with two Higgs doublets". *Phys. Rev.* D92.3 (2015), p. 033006. DOI: 10.1103/PhysRevD.92.033006. arXiv: 1505.05744 [hep-ph].

[6] J. D. Clarke. "How to avoid unnatural hierarchical thermal leptogenesis". *PoS* PLANCK2015 (2015), p. 026. arXiv: 1509.07242 [hep-ph].

[7] J. D. Clarke and R. R. Volkas. "Technically natural nonsupersymmetric model of neutrino masses, baryogenesis, the strong CP problem, and dark matter". *Phys. Rev.* D93.3 (2016), p. 035001. DOI: 10.1103/PhysRevD.93.035001. arXiv: 1509.07243 [hep-ph].

[8] J. D. Clarke and R. Foot. "Plasma dark matter direct detection". *JCAP* 1601.01 (2016), p. 029. DOI: 10.1088/1475-7516/2016/01/029. arXiv: 1512.06471 [astro-ph.GA].

[9] Y. Cai et al. "TeV-scale pseudo-Dirac seesaw mechanisms in an E_6 inspired model". *Phys. Rev.* D94.3 (2016), p. 033003. DOI: 10.1103/PhysRevD.94.033003. arXiv: 1605.02743 [hep-ph].

[10] J. D. Clarke and R. Foot. "Mirror dark matter will be confirmed or excluded by XENON1T" (2016). arXiv: 1606.09063 [hep-ph].

[11] J. D. Clarke and P. Cox. "Naturalness made easy: two-loop naturalness bounds on minimal SM extensions" (2016). arXiv: 1607.07446 [hep-ph].

Declaration of Authorship

I, Jackson D. CLARKE, declare that this THESIS:

- comprises only my own original work except where indicated in the preface;
- was done wholly while in candidature;
- gives due acknowledgement in the text to all other materials consulted;
- and is fewer than 100,000 words in length, exclusive of Tables, Figures, Bibliographies, or Appendices.

Signed:

Date:

Preface

This THESIS comprises eight Chapters based on publications and preprints mostly written in collaboration.

CHAPTER 1 is an original introduction and literature review.

CHAPTER 2 is based on the publications "Phenomenology of a very light scalar (100 MeV $< m_h < 10$ GeV) mixing with the SM Higgs," written in collaboration with Robert Foot and Raymond R. Volkas [1], and "Constraining portals with displaced Higgs decay searches at the LHC," which was single authored [4]. The original motivation for pursuing the phenomenology of very light scalars arose from the previous work of Foot and Volkas in scale invariant models. The calculations, analyses, and technical writing are primarily my own.

CHAPTER 3 is based on the preprint "Naturalness made easy: two-loop naturalness bounds on minimal SM extensions," written in collaboration with Peter Cox [11]. The original concept was my own, and while the bulk of the technical writing is also my own, the ideas presented within are the result of a series of spirited conversations over which we collaboratively developed our understanding. The numerical calculations were performed in collaboration.

CHAPTER 4 is based on the publication "Testing Radiative Neutrino Mass Models at the LHC," written in collaboration with Yi Cai, Michael A. Schmidt, and Raymond R. Volkas [2]. The UV completions of Section 4.1 were determined by collaborators. Subsection 4.2.5, making up the majority of Section 4.2 and of the Chapter, is largely my own work; otherwise the work in that Section was mostly completed by collaborators.

CHAPTER 5 is based on the publications "Electroweak naturalness in the three-flavor type I seesaw model and implications for leptogenesis," and "Natural leptogenesis and neutrino masses with two Higgs doublets," each written in collaboration with Robert Foot and Raymond R. Volkas [3, 5]. The original motivation for these papers stemmed from the observation of Foot and Volkas that nobody had carried out a three-flavour naturalness analysis in the Type I seesaw model. After confirming that, as the one-flavour case suggested, neutrino masses and hierarchical leptogenesis are inconsistent with naturalness in the three-flavour scenario, a collaborative discussion exploring possible solutions resulted in the "ν2HDM" concept. The calculations, analyses, and technical writing are largely my own.

CHAPTER 6 is based on the publication "Technically natural non-supersymmetric model of neutrino masses, baryogenesis, the strong CP problem, and dark matter," written in collaboration with Raymond R. Volkas [7]. The inspiration for this paper arose from a long term desire of Volkas to write down a technically natural solution to the major phenomenological problems of the Standard Model. We realised that the "νDFSZ" model (originally written down by Volkas and collaborators in a 1988 publication) could, in a certain region of parameter space corresponding to a low scale ν2HDM, solve the eponymous problems. The calculations, analyses, and technical writing in this Chapter are largely my own.

CHAPTER 7 is based on the publication "Plasma dark matter direct detection," written in collaboration with Robert Foot [8]. This work was the end result of collaborative discussions concerning a question Foot has considered for several years: how does plasma dark matter interact with captured dark matter within the Earth? The plasma dark matter conditions in Section 7.1, and the details of captured dark matter in Section 7.2.1, were derived by Foot. The analogy of the solar wind interaction with planetary bodies is my own, and the magnetohydrodynamic simulations and subsequent results are my own. Otherwise the technical writing was a collaborative effort.

CHAPTER 8 is an original conclusion based on the conclusions contained within the aforementioned collaborative works.

All work was supported in part by the Australian Research Council.

Acknowledgements

The three-and-a-half-year experience of my PhD candidature was in fact a thoroughly enjoyable one, and for that I have a number of people to thank.

First and foremost, I am deeply grateful to my supervisors. Ray and Robert never failed to provide advice and support (in their many manifestations) in an open and sincere manner. They have taught me more than I am aware of, well beyond particle physics, and have each, in different ways, become mentors. In particular I want to thank Ray for supporting me in my path beyond PhD, along which I hope we have many more rewarding interactions.

The existence of CoEPP during my candidature was a major boon. I am incredibly appreciative for the support CoEPP gave me to attend multiple conferences and summer schools in Europe. It is difficult to imagine a better culture within a group; the people make it what it is, and I thank them for that. In particular, I would like to thank my PhD candidate contemporaries Iason, Mia, Peter, and Rebecca for their important contributions to the enjoyment of this experience.

I would also like to acknowledge the support of the people at Trinity College. Being a tutor in residence for the entirety of my PhD has made things extremely logistically simple. The extra responsibility that comes with the role has only complemented the experience. Being able to share this journey with students and staff alike has been a pleasure.

Lastly, I would like to thank Helen, in supporting me for the long haul. You understand. Thank you. I am incredibly proud and happy to be married to you.

Contents

List of Figures

List of Tables

List of Abbreviations

2HDM	Two Higgs doublet model
ATLAS	A Toroidal LHS ApparatuS
BAU	Baryon asymmetry of the Universe
BBN	Big bang nucleosynthesis
BSM	Beyond the Standard Model
C.L.	Confidence level
CKM	Cabibbo-Kobayashi–Maskawa
CMB	Cosmic microwave background
CMS	Compact Muon Solenoid
CP	Charge-Parity
D7	Dimension 7
DFSZ	Dine–Fischler–Srednicki-Zhitnitsky
DM	Dark matter
EFT	Effective field theory
GM	Gauge multiplet
$H.c.$	Hermitian conjugate
IO	Inverted ordering
LEP	Large Electron-Positron (Collider)
LFV	Lepton flavour violation
LHC	Large Hadron Collider
LS	Lepton-specific
MDM	Mirror dark matter
MHD	Magnetohydrodynamic
NO	Normal ordering
NP	New physics
p_T	Tranverse momentum
PMNS	Pontecorvo-Maki–Nakagawa–Sakata
PQ	Peccei–Quinn
QCD	Quantum chromodynamics
RG	Renormalisation group
RGE	Renormalisation group equation
SM	Standard Model
SR	Signal region

SUSY	Supersymmetry
UV	Ultraviolet
vev	Vacuum expectation value
WIMP	Weakly interacting massive particle

Dedicated to earnest scientific enquiry.

1 Introduction

1.1 Physics beyond the Standard Model

The Standard Model (SM) has proven extremely successful in describing particle physics phenomenology at energy scales $\lesssim$ TeV. Still, a number of theoretical and phenomenological questions remain. In this THESIS we present a collection of original pieces of work pertaining to six major questions; they are summarised presently.

HIGGS SECTOR
What is the nature of electroweak symmetry breaking? Are there scalars beyond the Higgs?

NATURALNESS
Is the Higgs mass "natural"? That is, is it insensitive to the fine details of the high scale physics?

NEUTRINO MASS
What is the mechanism by which neutrinos gain mass?

BARYON ASYMMETRY OF THE UNIVERSE
How did the Universe end up with more baryons than antibaryons?

STRONG CP PROBLEM
Why is the neutron electric dipole moment so small?

DARK MATTER
What is the nature of the non-luminous, gravitationally interacting matter which permeates our Universe?

Each of these questions either demand or non-trivially constrain particle physics beyond the SM (BSM). We now describe them in more detail.

1.1.1 Higgs sector

Symmetry has been, and still remains, an extremely important principle for the theoretical formulation of fundamental interactions in particle physics. It was known since the late 1920s that the electromagnetic force could be described by a theory with $U(1)_Q$ gauge symmetry [12]. However, it was not until the late 1960s that a consistent gauge theory for the weak interactions was constructed. A puzzle from the gauge symmetric perspective was the short-range of the weak force, which implies massive vector boson mediators not invariant under gauge symmetry. An important insight turned out to be that fundamental symmetries of nature may not be manifest at low energy. The Goldstone theorem of 1961 [13, 14] appeared to be an impedement for the formulation of a broken symmetry explanation for the weak interactions: the theorem states that if a continuous symmetry is not realised at low energy, then there exist massless spin-zero "Goldstone bosons" corresponding to the broken generators of the symmetry. No massless spin-zero bosons are known to exist. A few years later, several scientists [15–18] pointed out that the Goldstone theorem need not hold in gauge theories. Instead, when a gauge symmetry is spontaneously broken by the low energy vacuum state of a scalar field, the would-be Goldstone bosons become longitudinal modes of the hitherto massless gauge bosons, imparting them with a mass. This has become known as the Higgs mechanism (or the BEH or BEHGHK mechanism).

What turned out to be the successful theory of electroweak interactions was proposed by Weinberg and Salam in 1967 [19, 20]. It is based on the gauge group $SU(2)_L \times U(1)_Y$ (first written down by Glashow [21]) spontaneously broken to $U(1)_Q$ by the vacuum state of a complex $SU(2)_L$ doublet scalar field: the SM Higgs doublet. In the unitary gauge the Higgs doublet can be written

$$\Phi = \frac{1}{\sqrt{2}} \begin{pmatrix} 0 \\ v + h \end{pmatrix}, \tag{1.1}$$

where $v \equiv \sqrt{2}\langle\Phi\rangle \approx 246$ GeV is the vacuum expectation value (vev) and h is a real scalar field. The gauge boson mass terms arise from the kinetic term $(D_\mu \Phi)^2$:

$$\frac{1}{2}(0\ ,\ v)\left(\frac{1}{2}g\,\tau_i W_\mu^i + \frac{1}{2}g' B_\mu\right)^2 \begin{pmatrix} 0 \\ v \end{pmatrix}, \tag{1.2}$$

where τ_i are the generators of the $SU(2)_L$ symmetry. Diagonalising the resulting mass matrix gives

$$\begin{aligned} m_W^2 &= \frac{1}{4}g^2 v^2, & W_\mu^\pm &= \frac{1}{\sqrt{2}}\left(W_\mu^1 \mp i W_\mu^2\right), \\ m_Z^2 &= \frac{1}{4}\left(g^2 + g'^2\right) v^2, & Z_\mu &= \frac{-g' B_\mu + g W_\mu^3}{\sqrt{g^2 + g'^2}}, \\ m_A^2 &= 0, & A_\mu &= \frac{g B_\mu + g' W_\mu^3}{\sqrt{g^2 + g'^2}}. \end{aligned} \tag{1.3}$$

Three of the Higgs doublet degrees of freedom are "eaten" to give mass to the $W^\pm$ and Z bosons, while a massless gauge boson (the photon), and a massive scalar spin-zero boson h (the SM Higgs boson) remain.[1] Left-handed leptons appear in $SU(2)_L$ doublets, whilst right-handed counterparts are $SU(2)_L$ singlets, consistent with maximal parity violation first observed in beta decay experiments of the 1950s [22, 23]. The Higgs doublet then allows gauge invariant "Yukawa" terms to be written down which result in fermion mass terms in the vacuum. For example, the Yukawa term

$$-y_e\,(\overline{\nu_L}\,,\;\overline{e_L})\,\Phi\;e_R + H.c. \tag{1.4}$$

leads to an electron mass which is proportional to the Yukawa coupling: $m_e = y_e\langle\Phi\rangle$.

The SM Higgs mechanism is extremely predictive; tree-level Higgs couplings to gauge bosons and to fermions (and loop-induced couplings to photons and gluons) are completely specified once gauge couplings and fermion masses are known, whilst the vev is given by the W and Z boson masses. By early 2010, when the Large Hadron Collider (LHC) first began collisions, the mass (and the existence!) of the Higgs was unknown. The Large Electron-Positron (LEP) collider had excluded $m_h < 114$ GeV [24], and experiments at the Tevatron $p\bar{p}$ collider had excluded $145 < m_h/\text{GeV} < 180$ [25]. There are theoretical reasons to expect a light Higgs mass, in particular with $m_h \lesssim$ TeV, e.g. to cure unitarity problems in WW scattering. Thus the LHC experiments were designed to be essentially guaranteed to discover the SM Higgs, something like it, or something very surprising. As it turned out, a scalar boson very much resembling the SM Higgs was discovered. We will comment on this shortly. Beforehand, since collider phenomenology forms a major part of this THESIS (in particular CHAPTERS 2 and 4), we will use this opportunity to briefly describe the detector apparatuses of ATLAS (A Toroidal LHC ApparatuS) and CMS (Compact Muon Solenoid), and the event simulation chain necessary for statistical inference.

The LHC is a pp collider operating at unprecedented centre-of-mass collision energies. Collisions took place at 7 TeV during 2010–11, and 8 TeV during 2012–13, delivering ≈ 5 fb^{-1} and ≈ 21 fb^{-1} of integrated luminosity to the multipurpose ATLAS/CMS detectors during these runs, respectively.[2] The detectors broadly consist of: an inner detector region for the tracking of charged particles and primary pp collision vertexing; calorimeters for high resolution measurement of charged and neutral particle energy; a muon spectrometer for the tracking and energy measurement of muons; and a multi-level trigger system which selects $< 0.001\%$ of all event data for storage and subsequent high-level analysis. A transverse slice of the CMS detector is shown in Figure 1.1.

[1] To be clear, we will try to call the recently discovered boson, which may or may not coincide with that which enters the SM, the Higgs boson (or simply the Higgs), to be differentiated from the SM Higgs boson (or simply the SM Higgs).

[2] Since late 2015, data taking at 13 TeV has begun.

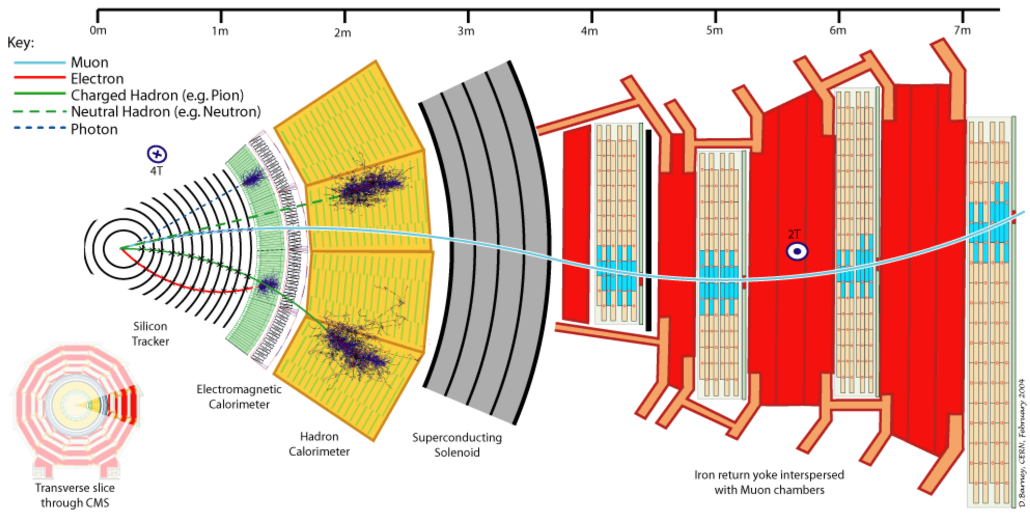

FIGURE 1.1: Transverse slice of the barrel region of the CMS detector.

Monte Carlo event generators are necessary to simulate the expected background and signal processes for statistical inference. It is a non-trivial property of asymptotically free QCD that this event generation can be "factorised" as a low multiplicity underlying perturbative parton process matched to a high multiplicity initial/final state shower of soft, collinear gluons and photons. Below the QCD scale colour radiation then forms hadrons in a non-perturbative process which can be modelled phenomenologically. These "truth-level" event simulations of parton collisions must then be overlayed with beam remnants, radiation from the incoming protons, possible multi-parton interactions, and additional pp collisions from that beam crossing (pile-up) and neighbouring crossings (out-of-time pile-up). The resulting complex event is then passed through a detector simulation to replicate the detector response. This mess of activity can be boiled down to a relatively small number of reconstructed objects for analysis: hadronic jets, photons, electrons, muons, and missing transverse momentum. It is an unenviable task, largely beyond the scope of the typical phenomenologist, to classify the systematic uncertainties involved in each of these steps. Instead, phenomenologists use publicly available parton-level event generators (e.g. MADGRAPH/MADEVENT [26]) and showerers/hadronisers (e.g. PYTHIA [27, 28]), together with rudimentary fast detector simulations (e.g. DELPHES [29]), largely to demonstrate the feasibility of searches for BSM physics. The rest is left to the experimentalists.

The discovery of the Higgs boson by both the ATLAS and CMS Collaborations was announced in July 2012, after ≈ 6 fb^{-1} of integrated luminosity was gathered at 8 TeV collision energy. An excess of events with $> 5\sigma$ combined local significance was observed in the $h \to \gamma\gamma$ and $h \to ZZ^{(*)} \to 4l$ channels at $m_h \approx 126$ GeV [30, 31]. The ATLAS discovery plots are reproduced (for admiration) in Figure 1.2. Henceforth, one of the primary goals of the LHC programme

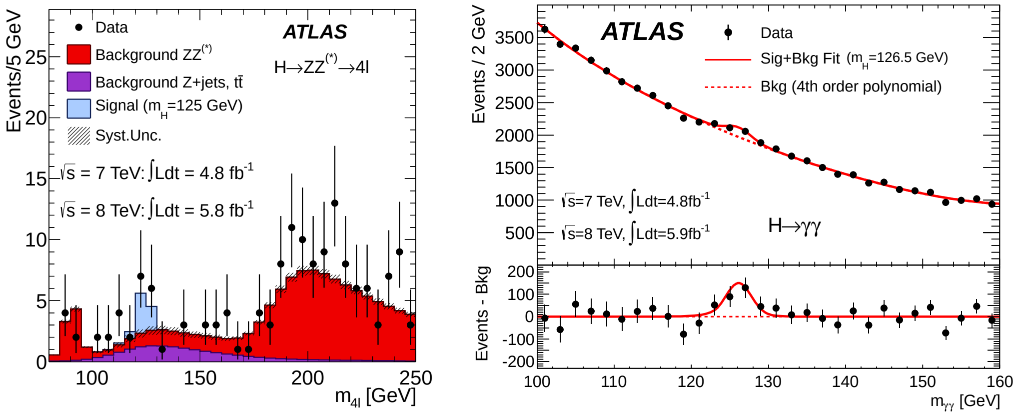

FIGURE 1.2: Higgs boson discovery plots from the ATLAS Collaboration [30].

is to study the properties of the newly discovered state in great detail. So far the state is fully consistent with the SM Higgs [32]. In particular: its mass has been precisely measured as $m_h = 125.09 \pm 0.24$ GeV [33]; decays to $\gamma\gamma$, ZZ, WW, and $\tau\tau$ are discovered, with evidence for $b\bar{b}$ decay; production via gluon fusion and vector boson fusion are discovered, with evidence for Zh+Wh (Vh) and $t\bar{t}h$ production; inferred couplings to the Z and W bosons, and to t, b, and τ fermions are consistent with the SM; and a spin-parity of 0^+ is highly favoured.

Still, plenty of room remains for new physics in the Higgs sector. Exotic decay modes at the $Br(h \to unobserved) \lesssim 20\%$ level are still allowed for an otherwise SM Higgs [34, 35]. As well, by the end of its lifetime, the LHC experiments are expected to measure Higgs couplings to fermions and vector bosons down to the per cent level, and discovery of the self-coupling is plausible. Such measurements will be important in ascertaining whether the Higgs is truly the fundamental scalar predicted by the SM. Of interest for this THESIS is whether the Higgs is the only scalar involved in electroweak symmetry breaking. In particular, we consider Higgs sector extensions by: a real singlet scalar in CHAPTER 2; a second Higgs doublet in CHAPTER 5; and a second Higgs doublet plus a complex singlet in CHAPTER 6. Each of these scalars gains a vev and therefore enters at some level to the details of electroweak symmetry breaking. Furthermore, in CHAPTERS 3 and 4, we consider additional fundamental scalars of various gauge charges which are not involved in electroweak symmetry breaking.

1.1.2 Naturalness

The SM Higgs potential is

$$V_{SM} = \mu^2 \Phi^\dagger \Phi + \lambda (\Phi^\dagger \Phi)^2, \tag{1.5}$$

where Φ is the SM Higgs doublet. Famously, with $\mu^2 < 0$ and $\lambda > 0$, this potential results in the spontaneous breaking of electroweak symmetry [16–

18]. The electroweak scale is set by the Higgs vacuum expectation value (vev) $\langle\Phi\rangle = \sqrt{-\mu^2/\lambda} \simeq 174$ GeV, with the recent discovery of the Higgs boson revealing that $\mu^2 \simeq -(88\text{ GeV})^2$ at low energy [30, 31].

Much of modern high energy physics has been motivated by concern over the "naturalness" of the electroweak scale, in particular in the presence of gravity or other (hypothetical) high scale physics scenarios. In this subsection we will introduce and discuss the concept of Higgs mass naturalness. Actually, a proper discussion requires careful treatment, since the literature on the topic is plagued with oversimplifications, hand-waving, a lack of distinction between physical and unphysical quantities, as well as imprecise and inconsistent definitions. We henceforth adopt the following definitions for use in this THESIS:

- A parameter in a quantum field theory is *unnatural* if it is very sensitive to the input parameters of the theory.
- A small parameter (or a collection of parameters) in a quantum field theory is *technically natural* if the limit whereby it is taken to zero reinstates a symmetry. This requires that quantum corrections to the parameter be proportional to that parameter.
- The happenstance that all dimensionless parameters in a quantum field theory are $\mathcal{O}(1)$ is also often called "natural." We do not ascribe this concept any name, nor do we make use of it in the following.
- A quantum field theory has a *hierarchy problem* if there exists an unexplained hierarchy between mass scales.
- *The hierarchy problem* specifically refers to the unexplained hierarchy between the electroweak scale and the apparent scale of gravity, the Planck scale $\Lambda_{Pl} \sim 10^{19}$ GeV.

With those definitions clearly set out, we will proceed to discuss Higgs mass naturalness in three distinct regimes: in the SM as an effective field theory (EFT); in the SM with gravity; and in the SM with perturbative new physics.

First, a brief excursion is required to explain what in a quantum field theory is of physical relevance. The parameters (and the normalisation of the fields themselves) which enter the Lagrangian of a quantum field theory are so-called *bare* quantities. When we try to perform calculations with these bare quantities, specifically quantum loop calculations, we inevitably run into divergences; simple processes return apparent infinities. Understanding and taming these divergences was an important problem of early quantum field theory. The key insight turned out to be the following: the bare quantities are themselves not measurable. What is measured are instead physical observables, e.g. scattering cross-sections or decay rates, which are manifestly free from infinities. In order to proceed, from a calculational perspective, a *regularisation* procedure must be implemented to capture the divergences arising in the bare quantity calculations. Calculation results can then be made consistent with the finite physical observables by appending divergent *counterterms* to the bare quantities, which cancel with the divergences arising in the calculations. The cancellation between divergences can be interpreted as an unphysical intermediate artifact of the calculation procedure. Indeed, if the calculation results are expressed in terms of only *observable* quantities, the divergences do not appear. Once parameters are regularised (under some scheme) and rewritten in terms of physical observables, they are said to be *renormalised*. An interesting implication of this procedure is that the renormalised parameters become functions of energy scale. The equations which relate the renormalised parameter values at different energy scales are the differential *renormalisation group equations* (RGEs).

Now, the SM parameter μ^2 in Equation (1.5) is an unmeasurable bare quantity which, like all bare quantities appearing in the Lagrangian, should be renormalised in order to understand its physical implications. In a cutoff regularisation scheme, the dominant one-loop quantum correction to μ^2 arises from the top quark,

$$\delta\mu^2 \sim \frac{1}{(4\pi)^2} y_t^2 \Lambda^2, \tag{1.6}$$

where Λ is the cutoff renormalisation scale. This potentially large quantum contribution must be cancelled against a bare μ^2 contribution in order to realise the observed $\mu^2(m_Z) \simeq -m_h^2/2$. It is possible to interpret this as an "unnaturally" large cancellation. However, the viewpoint we will take throughout this THESIS is that this is just the regularisation and renormalisation procedure, i.e. we assign the cancellation of the cutoff contribution no physical significance. Once the μ^2 parameter has been renormalised, the physical effect of the top quark is to (dominantly) contribute to the μ^2 RGE,

$$\frac{d\mu^2}{d\log\mu_R} \simeq \frac{1}{(4\pi)^2} 6 y_t^2 \mu^2, \tag{1.7}$$

where μ_R is the renormalisation scale. Note that the RGE for μ^2 is multiplicative in μ^2.[3] This implies that, since $\mu^2(m_Z) \simeq -(88\,\text{GeV})^2$, $\mu^2(\mu_R)$ remains $\sim -(100\,\text{GeV})^2$ even up to Λ_{Pl}, by which point the SM EFT will be invalidated by gravitational effects. This implies that the SM EFT is natural, since the low scale Higgs mass is not especially sensitive to the high scale input parameter $\mu^2(\Lambda_{Pl}) \sim -(100\,\text{GeV})^2$. Furthermore, the SM EFT appears to be completely valid and consistent up to Λ_{Pl}: the electroweak vacuum remains sufficiently stable, and no dynamical scales are generated.

So where is the problem? In SM with gravity we can distinguish two distinct

[3] In fact, this might have been guessed, since μ^2 is the only explicit scale in the SM.

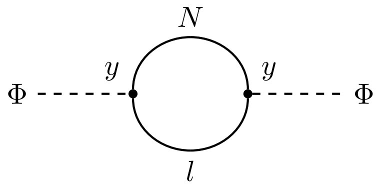

FIGURE 1.3: Loop quantum correction to μ^2 from a right-handed gauge singlet fermion.

concerns. The first is a hierarchy problem: what physics could set the boundary condition $\mu^2(\Lambda_{Pl}) \lll \Lambda_{Pl}^2$? The second is a question of naturalness: is that boundary condition natural? i.e. is it sensitive to changes in the input parameters of the high scale theory? Now, it could be the case that quantum gravitational effects at the Planck scale set the boundary condition, and that this boundary condition is unnatural. However, this cannot be rigorously computed in the absence of a cogent theory of quantum gravity. Thus, we can say that the SM plus gravity suffers a hierarchy problem, but it is not possible to say that it has a definite naturalness problem. This might sound somewhat pedantic, but it is an important distinction, since it is possible to have a hierarchy without having a naturalness problem (as we will demonstrate soon). The issue with gravity is just that we cannot calculate anything to be sure. In a perturbative quantum field theory, we *can* calculate corrections to μ^2 and quantify the resulting naturalness problem which might arise, irrespective of the situation with gravity. Let us explore a simple example.

Consider adding a massive right-handed gauge singlet fermion N to the SM, and coupling it to the Higgs via the term $y\overline{l_L}\tilde{\Phi}N$, where $l_L = (\nu_L, e_L)^T$ and $\tilde{\Phi} = i\tau_2\Phi^*$. The one-loop RGE for μ^2 gains a term

$$\frac{d\mu^2}{d\log\mu_R} \supset -\frac{1}{(4\pi)^2}4y^2 M_N^2 \tag{1.8}$$

from the loop diagram of Figure 1.3. Roughly, one expects a naturalness problem to arise when the quantum corrections are large compared to $\mu^2(m_Z)$, i.e. $d\mu^2/d\log\mu_R \gg \mu^2(m_Z)$; in such a case, $\mu^2(\mu_R)$ will evolve to very large values, and $\mu^2(m_Z)$ will become extremely sensitive to variations around the necessary boundary condition at high scale. Intuitive naturalness criteria are then: bound the RGE contribution itself; or quantify and bound the sensitivity of $\mu^2(m_Z)$ to the high scale input $\mu^2(\Lambda_h)$, where Λ_h is some high scale. That is:

$$\left|\frac{1}{\mu^2(m_Z)}\frac{d\mu^2}{d\log\mu_R}\right| < \Delta_{max}; \qquad \text{or} \qquad \left|\frac{\partial\log\mu^2(m_Z)}{\partial\log\mu^2(\Lambda_h)}\right| < \Delta_{max}. \tag{1.9}$$

Such criteria should not be taken too seriously (and nature may just be fine-tuned after all), but they can certainly serve as guiding principles which capture our subjective sense of physical naturalness (of mass parameters).[4] Most importantly they are calculable in any perturbative model. Taking $\Delta_{max} = 10$, $\Lambda_h = \Lambda_{Pl}$, and ignoring the RG evolution of new parameters or additional contributions to the μ^2 RGE, the criteria of Equation (1.9) result in the bounds $yM_N \lesssim 1700$ GeV or $yM_N \lesssim 320$ GeV, respectively. Notice that M_N can be large as long as y is sufficiently small. Indeed, this is because the limit $y \to 0$ decouples N from the SM, which returns the sensible result: there is no Higgs naturalness problem from a particle which does not couple to the Higgs field. One might get uncomfortable about a small coupling in the theory. However the limit $y \to 0$ is technically natural; the decoupling limit reinstates an enhanced Poincaré symmetry [36, 37] under which independent spacetime transformations can be performed on two decoupled actions.

The example we just considered is in fact a rather interesting one. As we will discuss in more detail in Sections 1.1.3 and 1.1.4, it turns out that such heavy fermionic singlets are capable of generating neutrino masses and the observed baryon asymmetry of the Universe. The neutrino mass is given by $m_\nu = y^2 \langle \Phi \rangle^2 / M_N$, with $m_\nu \sim 0.05$ eV. This additional constraint implies a naturalness bound of $M_N \lesssim 10^7$ GeV (or $y \lesssim 10^{-4}$).[5]

The point of this example was to emphasise that the existence of a very massive particle does not imply a naturalness problem for the Higgs mass. Instead, the particle should fulfil a sensible naturalness criterion which is necessarily a function of how strongly the particle couples to the Higgs field. For some well-motivated BSM particles, the coupling strength is fixed (or there is at least a lower limit), implying an upper mass limit arising from naturalness. For example, particles with SM gauge charges will always couple to the Higgs field at loop-level. We will examine this case in detail in CHAPTER 3. Another example are grand unified models featuring vector fields of mass $\sim 10^{15}$ GeV which couple to the Higgs with gauge strength. Alone, this leads to a severe naturalness problem. Perhaps the most economic way to cure this problem lies in supersymmetry (SUSY). In a supersymmetric theory, every particle has a supersymmetric partner, and contributions to the RGEs of mass parameters exactly cancel at all loop levels. Of course, SUSY is broken at low scale. The Higgs mass is not protected from corrections below the SUSY breaking scale; this implies that the breaking scale must be (roughly) at the TeV scale. Otherwise, strongly coupled heavy supersymmetric particles (in particular the stops) will, rather ironically,

[4] They may also seem arbitrary, which is a fair assessment. In CHAPTER 3 we will show how similar criteria can be rigorously derived from Bayesian logic.

[5] In the low energy theory, the neutrino masses arise from the dimension 5 operator $\frac{1}{\Lambda}\overline{(l_L)^c}\Phi\Phi^T l_L$ with $\Lambda \sim 10^{15}$ GeV. Matching to the parameters of the high scale theory gives $1/\Lambda \equiv y^2/M_N$. Thus, in this simple example, a dimensional argument implies an apparent very large scale $\sim 10^{15}$ GeV in the theory, which could just be due to the appearance of a technically natural small coupling, and even the existence of a large scale $\sim 10^7$ GeV in the renormalisable theory calculably does not introduce a naturalness problem. The reader can draw their own parallels with the Planck scale and gravity.

induce their own naturalness problem. Alas, experiments have thus far seen no evidence of SUSY up to the TeV scale, threatening this paradigm. SUSY is certainly an interesting possibility, but we will have very little to say about it in this THESIS.

1.1.3 Neutrino mass

In the SM, working in the lepton mass eigenbasis, neutrinos are always produced via the weak interactions as flavour eigenstates $|\nu_\alpha\rangle$ with $\alpha = \{e, \mu, \tau\}$. Consider the possibility that, like the quark sector, these flavour eigenstates are non-trivial unitary superpositions of mass eigenstates $|\nu_i\rangle$,

$$|\nu_\alpha\rangle = \sum_i U^*_{\alpha i}|\nu_i\rangle, \tag{1.10}$$

where U is the Pontecorvo-Maki–Nakagawa–Sakata (PMNS) matrix [38, 39]. The mass eigenstates each evolve (in their own frame) according to the Schrödinger equation, i.e. $|\nu_i(\tau_i)\rangle = e^{-im_i\tau_i}|\nu_i(0)\rangle$ in vacuum. In the lab frame ($m_i\tau_i = Et - |\vec{p}|L$), and in the limit $E \gg m_i$ (or $|\vec{p}| \simeq E - m_i^2/2E$), we can write

$$|\nu_i(t)\rangle \simeq e^{-iE(t-L)}e^{-im_i^2\frac{L}{2E}}|\nu_i(0)\rangle. \tag{1.11}$$

Importantly, we see that each of the mass eigenstate components comprising a propagating flavour eigenstate evolves differently, according to the square of its mass. The probability that a flavour eigenstate $|\nu_\alpha\rangle$ is observed as flavour eigenstate $|\nu_\beta\rangle$ after propagating a distance L is then given by

$$\begin{aligned} |\langle\nu_\beta|\nu_\alpha\rangle|^2 \simeq \delta_{\alpha\beta} &- 4\sum_{i>j} \mathrm{Re}\left[U_{\beta i}\, U^*_{\alpha i}\, U^*_{\beta j}\, U_{\alpha j}\right] \sin^2\left(\Delta m^2_{ij}\frac{L}{4E}\right) \\ &- 2\sum_{i>j} \mathrm{Im}\left[U_{\beta i}\, U^*_{\alpha i}\, U^*_{\beta j}\, U_{\alpha j}\right] \sin\left(\Delta m^2_{ij}\frac{L}{2E}\right) \end{aligned} \tag{1.12}$$

where $\Delta m^2_{ij} \equiv m_i^2 - m_j^2$. This is the phenomenon of neutrino oscillation in vacuum (see e.g. Ref. [40] for a review). Plainly, neutrino flavour oscillates if and only if (at least one of the) neutrinos have mass. A positive measurement of neutrino oscillation therefore implies neutrino mass, and precision measurements can probe Δm^2_{ij} and certain aspects of the matrix U.

Neutrino oscillation is now experimentally well established. The atmospheric muon-neutrino deficit (with respect to the prediction from cosmic ray induced production), first observed by the water Cherenkov Kamiokande [41–43] and Irvine-Michigan-Brookhaven [44, 45] experiments, was resolved by muon-neutrino oscillation. In 1998 the Super-Kamiokande experiment reported an up-down asymmetry in the ν_e-ν_μ flux ratio, consistent with ν_μ disappearance via

$\nu_\mu \leftrightarrow \nu_\tau$ oscillation [46]. As well, the solar electron-neutrino deficit (with respect to the standard solar model prediction), first observed by the chlorine-based Homestake experiment [47] in 1967, was eventually resolved by electron-neutrino oscillation in matter [48, 49] and in vacuum. An unambiguous explanation involved a number of experiments from the late 1980s through to the early 2000s. The Kamiokande [50, 51] experiment, and the gallium-based GALLEX [52] and SAGE [53] experiments, confirmed the deficit in high energy solar boron electron-neutrinos and lower energy solar beryllium electron-neutrinos, respectively. In 2001, the Sudbury Neutrino Observatory [54, 55] measured the *total* solar boron neutrino flux, consistent with the solar model together with electron-neutrino disappearance via oscillation.

Many subsequent experiments, including nuclear reactor experiments (e.g. KamLAND [56]) and neutrino beam experiments (e.g. K2K [57], MINOS [58]), have further probed the phenomenon of neutrino oscillation, measuring properties of the PMNS matrix and the mass squared differences Δm^2_{ij}. We will not detail the PMNS matrix here, except to say that it is of a qualitatively different form compared to its quark analogue, the Cabibbo-Kobayashi–Maskawa (CKM) matrix [59, 60]. The Δm^2_{ij} are [61],

$$\begin{aligned} \Delta m^2_{21} &\simeq + \left[8.66 \times 10^{-3}\ \mathrm{eV}\right]^2 , \\ \Delta m^2_{3l} &\simeq \pm \left[4.96 \times 10^{-2}\ \mathrm{eV}\right]^2 . \end{aligned} \tag{1.13}$$

There are two mass-ordering possibilities: $\Delta m^2_{3l} = \Delta m^2_{31} > 0$ with $m_1 < m_2 < m_3$, known as normal ordering; and $\Delta m^2_{3l} = \Delta m^2_{32} < 0$ with $m_3 < m_1 < m_2$, known as inverted ordering. The absolute mass scale is still unknown, although there exist a number of constraints: time-of-flight measurements of neutrinos from supernova SN1987a [62–64] constrain $\left(\sum |U^2_{ei}| m^2_i\right)^{1/2} \lesssim 5.8$ eV [65, 66]; kinematic measurements of tritium beta decay constrain $\left(\sum |U^2_{ei}| m^2_i\right)^{1/2} \lesssim 2$ eV [67, 68]; cosmology constrains $\sum m_i < 0.17$ eV [69], depending on various cosmological assumptions; and neutrinoless double beta decay constrains $|\sum_i U^2_{ei} m_i| \lesssim 0.1$ eV [70] if neutrinos are Majorana particles (to be discussed soon). These measurements reveal that the neutrino mass scale is extremely small compared to that of the other fermions (cf. $m_e \simeq 0.511$ MeV). In fact, it is still phenomenologically possible that one of the neutrinos is massless.

The origin of the neutrino masses and mixings remains an outstanding problem of particle physics. Their unusually small mass, together with the qualitatively different form of the PMNS matrix in comparison to the CKM matrix, suggest that the neutrino mass generation mechanism is different to that of the charged fermions. It is possible that the explanation is related to the fact that ν_L is the only SM fermion field from which one can construct a gauge invariant Majorana mass term $\sim \overline{(\nu_L)^c}\nu_L$. This Majorana neutrino possibility is the one considered in this THESIS, specifically in CHAPTERS 4 and 5.

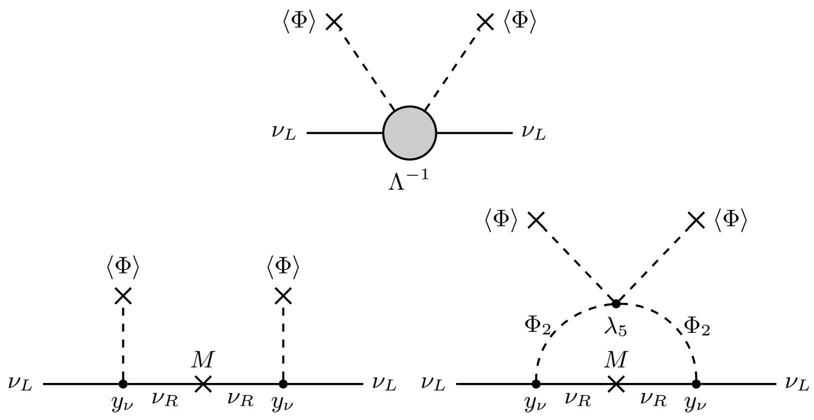

FIGURE 1.4: Neutrino mass from the Weinberg operator (upper), and two UV completions (lower): the Type I seesaw model, and the radiative Ma model.

How might Majorana neutrino masses be generated? A sensible way to approach this question is to begin by constructing gauge invariant operators out of the SM fields which violate lepton number by two units. One may then search for "UV completions" for these operators, i.e. higher scale renormalisable models which generate them as low energy effective operators. We will explore this programme in CHAPTER 4. For now let us consider the simplest such operator, arising at dimension five: the Weinberg operator [71]

$$\frac{1}{\Lambda}\overline{(l_L)^c}\Phi\Phi^T l_L, \tag{1.14}$$

where Φ is the Higgs field. This results in a Majorana neutrino mass $m_\nu = \langle\Phi\rangle^2/\Lambda$ upon electroweak symmetry breaking, as shown in Figure 1.4. An interesting possibility is that $\Lambda \ggg \langle\Phi\rangle$ would explain the smallness of the neutrino masses. One would like to identify Λ with some parameters in a higher scale renormalisable model. Let us now consider two well known possibilities, of particular interest for this THESIS.

Perhaps the most elegant neutrino mass mechanism involves adding to the SM three heavy right-handed neutrinos: the Type I seesaw model [72–74].[6] Gauge invariance allows two additional renormalisable terms in the Yukawa Lagrangian,

$$-\Delta\mathcal{L}_Y = (y_\nu)_{ij}\overline{l_L^i}\tilde{\Phi}\nu_R^j + \frac{1}{2}M_i\overline{(\nu_R^i)^c}\nu_R^i + H.c., \tag{1.15}$$

[6]The Type I seesaw model is one of only three possible single-field tree-level UV completions of the Weinberg operator; the other two are the Type II [75] and Type III [76] seesaw models, though they were each discovered independently, quite apart from this reasoning.

where M_i are the right-handed neutrino masses. Equation (1.15) can be rewritten

$$-\Delta\mathcal{L}_Y = \frac{1}{2}\left(\overline{\nu_L}\,,\,\overline{(\nu_R)^c}\right)\begin{pmatrix} 0 & y_\nu\langle\Phi\rangle \\ y_\nu^T\langle\Phi\rangle & \mathcal{D}_M\end{pmatrix}\begin{pmatrix}(\nu_L)^c \\ \nu_R\end{pmatrix} + H.c., \tag{1.16}$$

where $\mathcal{D}_M = \mathrm{diag}(M_1, M_2, M_3)$. If the eigenvalues of $y_\nu\langle\Phi\rangle$ are much smaller than the M_i, the neutrinos are essentially Majorana with masses given by the eigenvalues of the neutrino mass matrix

$$m_\nu = \langle\Phi\rangle^2 y_\nu \mathcal{D}_M^{-1} y_\nu^T\,, \tag{1.17}$$

suppressed by the presumably large right-handed neutrino mass scale; the associated Feynman diagram is shown in Figure 1.4. Indeed, for $y_\nu \sim 1$ and $m_\nu \sim 0.1$ eV, one expects $M_i \sim 10^{15}$ GeV.[7] Unfortunately, the minimal Type I seesaw model is eminently untestable.

Another possibility is that neutrinos gain a "radiative" mass at loop-level (e.g. Refs. [77–81]). In CHAPTER 5 we will encounter the one-loop Ma model [82], a radiative UV completion of the Weinberg operator. The Ma model requires right-handed neutrinos and a second Higgs doublet Φ_2 which does not gain a vev. The Lagrangian must contain

$$\begin{aligned} -\Delta\mathcal{L}_Y &= (y_\nu)_{ij}\overline{l_L^i}\tilde{\Phi}_2\nu_R^j + \frac{1}{2}M_i\overline{(\nu_R^i)^c}\nu_R^i + h.c., \\ V_{\mathrm{2HDM}} &\supset \frac{\lambda_5}{2}\left[\left(\Phi^\dagger\Phi_2\right)^2 + \left(\Phi_2^\dagger\Phi\right)^2\right]. \end{aligned} \tag{1.18}$$

The neutrino mass is generated radiatively via the diagram shown in Figure 1.4. The masses m_R and m_I of the real $\sqrt{2}\,\mathrm{Re}(\Phi_2)$ and imaginary $\sqrt{2}\,\mathrm{Im}(\Phi_2)$ components of the second doublet are split according to $m_R^2 - m_I^2 = 2\lambda_5\langle\Phi\rangle^2$. If we take this splitting to be small compared to $m_0^2 \equiv (m_R^2 + m_I^2)/2$, then the neutrino mass matrix is given by

$$(m_\nu)_{ij} = \frac{\lambda_5\langle\Phi\rangle^2}{8\pi^2}\sum_k \frac{(y_\nu)_{ik}M_k(y_\nu^T)_{kj}}{M_k^2 - m_0^2}\left[\frac{M_k^2}{M_k^2 - m_0^2}\log\frac{M_k^2}{m_0^2} - 1\right]. \tag{1.19}$$

One observes some similarities with Equation (1.17), particularly in the limit $M_k \gg m_0$. However, in addition to suppression by a potentially large mass scale, the neutrino mass is also suppressed by a loop factor, and an unknown coupling λ_5 (which in fact may be taken to be small in a technically natural way). Thus the smallness of the neutrino masses may be explained by a combination of factors. An interesting additional property of the Ma model is that it provides a dark matter candidate, with the symmetry preventing Φ_2 from gaining a vev

[7] It is of some interest that this scale is of the same order as the grand unification scale, escpecially since a right-handed neutrino together with one generation of SM fermion fields fill a complete representation of the SO(10) gauge group, within which the SM gauge group may be embedded.

implying a stable particle. For that reason it is also known as the "scotogenic" model, meaning "dark-generated."

1.1.4 Baryon asymmetry of the Universe

The non-observation of any astrophysical signature of matter–antimatter annihilations in diffuse (or otherwise) microwave, x-ray, or γ-ray photons, implies that the observable Universe is made up almost entirely of matter and not antimatter [83]. This is known as the baryon asymmetry of the Universe (BAU).

The baryon density is often expressed in terms of the baryon-to-photon number ratio $\eta = n_b/n_\gamma$. This quantity is measured in two different ways. First, η is an unknown input which enters the prediction of big bang nucleosynthesis (BBN) for the primordial abundances of helium-4, helium-3, deuterium, and lithium-7; measurements of these abundances are in good agreement with BBN and $\eta = (5.6 \pm 0.9) \times 10^{-10}$ [84, 85]. Second, η enters in the prediction for the relative heights of peaks in the cosmic microwave background (CMB) power spectrum due to baryon acoustic oscillations; measurements indicate $\eta = (6.19 \pm 0.14) \times 10^{-10}$ [86]. These phenomena occur at very different temperatures ($0.1 \lesssim T/\text{MeV} \lesssim 10$ and $T \sim 0.3$ eV, respectively) and can be considered as essentially independent determinations of η. Thus their agreement is a remarkable success of standard big bang cosmology. The value $\eta \sim 10^{-10}$ should be compared with the expected baryon–antibaryon abundance if the Universe were exactly baryon–antibaryon symmetric; in that case, baryon–antibaryon annihilations freeze out at $T \approx 20$ MeV with $\eta \sim 10^{-19}$ [87]. The implication is that a baryon–antibaryon asymmetry must have been present well above this temperature. It is usually assumed that this asymmetry was somehow generated dynamically from an initially baryon symmetric[8] state: this idea is known as *baryogenesis*.

The necessary conditions for successful baryogenesis are the Sakharov conditions [88]. They comprise: (1) baryon number violation, so that the initial state can evolve from $B = 0$; (2) C and CP violation, so that interactions involving particles and antiparticles differ; and (3) departure from thermal equilibrium, since otherwise (assuming CPT invariance) we have $d\langle B\rangle/dt = 0$. In fact, the SM and standard cosmology fulfil the Sakharov conditions. The latter two conditions are trivially met: CP violation appears in the CKM matrix, and the expansion of the Universe (and electroweak symmetry breaking) provides the necessary departure from equilibrium. For the first condition, despite the fact that baryon number is a very well conserved quantity in the SM at low energy, non-perturbative SM "sphaleron" transitions at high temperatures violate baryon number [89, 90]. The theoretical details of the mechanism are somewhat involved, and not important for our purposes (see e.g. Ref. [91] for a summary).

[8]In standard inflationary scenarios this condition is set at the time of reheating, irrespective of any asymmetry before inflation.

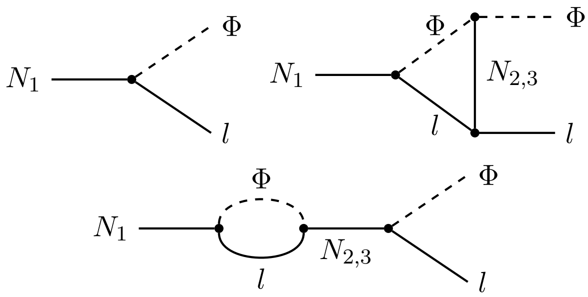

FIGURE 1.5: Feynman diagrams for decay of the lightest right-handed neutrino.

The important point is that the induced $\Delta B = \Delta L = 3$ transitions,

$$\text{vacuum} \longleftrightarrow \sum_{i=1,2,3} Q_{Li} Q_{Li} Q_{Li} l_{Li}, \tag{1.20}$$

preserving $B-L$ while violating $B+L$, are efficient at temperatures $T \gg 100\,\text{GeV}$ and (extremely) inefficient below. However, it turns out that these three effects are not strong enough for successful SM baryogenesis; they result in $\eta \sim 10^{-20}$ [92]. Therefore, explaining the BAU via baryogenesis requires BSM physics. In particular, the $B + L$ violation of sphaleron transitions suggests an intriguing possibility: to generate an asymmetry in the lepton sector which is (partly) transferred to the baryon sector via sphalerons. This idea is known as *baryogenesis via leptogenesis* or simply *leptogenesis*. It is the leptogenesis possibility which is considered in this THESIS, namely in CHAPTERS 5 and 6.

The paradigm example of leptogenesis [93] is within the Type I seesaw model described by Equation (1.15). In the standard scenario the lepton asymmetry is produced via the out-of-equilibrium decays of the lightest right-handed neutrino, assumed to be in thermal equilibrium in the early Universe. In the hierarchical limit $M_{N_1} \ll M_{N_2} \ll M_{N_3}$, and ignoring subdominant details introduced by $\Delta L = 1$ scatterings and possible lepton flavour effects, the baryon asymmetry is largely determined by the interplay of decays and inverse decays at $T \sim M_{N_1}$. Leptogenesis is possible if the rates for these processes are sufficiently out-of-equilibrium. This is captured by the decay parameter,

$$K = \frac{\Gamma_D}{H|_{T=M_{N_1}}} \equiv \frac{\tilde{m}_1}{m_*}, \tag{1.21}$$

where $\Gamma_D \equiv \Gamma(N_1 \to l\Phi) + \Gamma(N_1 \to \bar{l}\bar{\Phi})$ is the decay width of N_1, H is the expansion rate of the Universe, $\tilde{m}_1$ is the "effective neutrino mass," and m_* is the "equilibrium neutrino mass,"

$$\Gamma_D = \frac{1}{8\pi}(y_\nu^\dagger y_\nu)_{11} M_{N_1}, \qquad \tilde{m}_1 = \langle\Phi\rangle^2 \frac{(y_\nu^\dagger y_\nu)_{11}}{M_{N_1}},$$
$$H \simeq 1.66\sqrt{g_*}\frac{T^2}{M_{Pl}}, \qquad m_* \simeq 1.1 \times 10^{-3}\ \text{eV}, \tag{1.22}$$

with $g_* \simeq 106.75$ the effective number of degrees of freedom in the SM at a temperature $M_{N_1} \gtrsim T \gg 100$ GeV. The CP asymmetry in the decays which leads to the lepton asymmetry, $\epsilon_1 \equiv \left[\Gamma(N_1 \to l\Phi) - \Gamma(N_1 \to \bar{l}\bar{\Phi})\right]/\Gamma_D$, is captured by $|\mathcal{M}_{tree} + \mathcal{M}_{loops}|^2$ cross-terms once the one-loop amplitudes of Figure 1.5 Feynman diagrams are included:

$$|\epsilon_1| \simeq \frac{3}{16\pi}\frac{M_{N_1}}{\langle\Phi\rangle^2}\frac{\text{Im}\left[(y_\nu^* m_\nu y_\nu)_{11}\right]}{(y_\nu^\dagger y_\nu)_{11}}, \tag{1.23}$$

where m_ν is given by Equation (1.15). It is useful to re-express the y_ν matrix in the Casas-Ibarra [94] form,

$$y_\nu = \frac{1}{\langle\Phi\rangle} U^\dagger \mathcal{D}_m^{\frac{1}{2}} R \mathcal{D}_M^{\frac{1}{2}}, \tag{1.24}$$

where R is a (possibly complex) orthogonal ($RR^T = R^T R = \mathbb{I}$) matrix. Then

$$|\epsilon_1| \simeq \frac{3}{16\pi}\frac{M_{N_1}}{\langle\Phi\rangle^2}\frac{\text{Im}\left[(R^\dagger \mathcal{D}_m^2 R^*)_{11}\right]}{(R^\dagger \mathcal{D}_m R)_{11}} \lesssim \frac{3}{16\pi}\frac{M_{N_1}}{\langle\Phi\rangle^2} m_3, \tag{1.25}$$

where the final inequality follows from orthogonality properties of R, and $m_3 > m_{atm} \simeq 0.05$ eV is the heaviest neutrino mass.

The resulting baryon asymmetry, once the full thermodynamic system is evolved to low temperatures in the presence of sphaleron transitions, is given by

$$\eta \simeq 10^{-2}|\epsilon_1|\kappa_f, \tag{1.26}$$

where $\kappa_f \leq 1$ is an efficiency factor capturing the conversion efficiency of CP asymmetry into baryon asymmetry; for a thermal initial abundance, $\kappa_f \simeq (0.5/K)^{1.1}$ ($\kappa_f \simeq 1$) for $K > 0.5$ ($K < 0.5$) (see Ref. [95] for better approximations). Taking $m_3 \approx 0.05$ eV and $\eta \approx 6 \times 10^{-10}$, Equations (1.25) and (1.26) imply a lower bound on the lightest right-handed neutrino mass for successful leptogenesis: $M_{N_1} \gtrsim 6 \times 10^8$ GeV. This is known as the Davidson-Ibarra bound [96]. Thorough numerical calculations including scattering contributions, thermal effects, and relaxing the initial thermal abundance, result in three bounds depending on initial conditions [97]:

$$M_{N_1} \gtrsim \begin{cases} 2 \times 10^9 \text{ GeV} & \text{for zero initial } N_1 \text{ abundance,} \\ 5 \times 10^8 \text{ GeV} & \text{for thermal initial } N_1 \text{ abundance,} \\ 2 \times 10^7 \text{ GeV} & \text{for dominant initial } N_1 \text{ abundance.} \end{cases} \tag{1.27}$$

Naturally, since the conception of this idea, alternative leptogenesis scenarios within the Type I seesaw model have been explored. For example, one can imagine scenarios whereby the CP asymmetry is instead dominantly produced in decays of N_2 or N_3. Lepton flavour effects in the thermal bath, which become important when $T \lesssim 10^9$ GeV, are usually invoked to enable this to occur. The general picture (and the leptogenesis scale) is not much changed in such incarnations. Another alternative realisation is resonant leptogenesis [98], which occurs when the right-handed neutrinos are approximately degenerate in mass; in this case the CP asymmetry produced in the decays can be greatly enhanced and leptogenesis can take place at the TeV scale. In this THESIS we will consider only the hierarchical leptogenesis scenario.

1.1.5 Strong CP problem

The QCD Lagrangian,

$$\mathcal{L}_{QCD} = -\frac{1}{4} G^{\mu\nu} G_{\mu\nu} - \sum_i \overline{q_i} \left(-i\gamma_\mu D^\mu + m_i \right) q_i, \tag{1.28}$$

where $G^{\mu\nu}$ is the gluon field strength tensor, has an axial symmetry

$$q_i \to e^{i\gamma_5 \alpha_i} \tag{1.29}$$

in the massless limit $m_i \to 0$. This suggests that, for the u, d quarks with $m_{u,d} \ll \Lambda_{QCD}$, there should exist a corresponding approximately conserved axial current J_5^μ. However, this current is anomolous: a loop of quarks coupling to gluons induces a non-zero divergence, $\partial_\mu J_5^\mu \propto \frac{\alpha_s}{8\pi} G^{\mu\nu} \tilde{G}_{\mu\nu}$, where $\tilde{G}_{\mu\nu} \equiv \frac{1}{2} \epsilon_{\mu\nu\alpha\beta} G^{\alpha\beta}$ is the dual gluon field strength tensor. This is dubbed the chiral anomaly [99–101]. It turns out that $G^{\mu\nu} \tilde{G}_{\mu\nu}$ can be rewritten as a total divergence proportional to the gluon field A^α [102]. Then the action, $\int d^4x \partial_\mu J_5^\mu$, when rewritten as a surface integral at spatial infinity, vanishes under the naive boundary condition $A^\alpha = 0$, suggesting that no physical effect arises from the anomaly. It was 't Hooft who showed that, in fact, for non-abelian gauge groups, many topologically inequivalent degenerate vacua exist such that any pure gauge transformation of $A^\alpha = 0$ is an equally suitable boundary condition at spatial infinity [89].[9] The surface integral is non-vanishing for a subset of these vacua.

[9] This important paper by 't Hooft was cited previously for the introduction of non-perturbative electroweak sphaleron solutions.

The net effect is that gauge invariance and renormalisability insist that a physical CP-violating term

$$\bar{\theta}\frac{\alpha_s}{8\pi}G^{\mu\nu}\tilde{G}_{\mu\nu} \tag{1.30}$$

appear in the QCD Lagrangian. Chiral transformations of the form Equation (1.29) transform $\bar{\theta} \to \bar{\theta} - 2\alpha_i$. Explicitly separating the effect of chiral transformations involved in diagonalising the quark mass matrix M_q gives $\bar{\theta} = \theta_0 + \text{Arg}\left[\det(M_q)\right]$. A priori, $\bar{\theta}$ is expected to be $\mathcal{O}(1)$. However, no CP violation arising from the QCD sector has ever been observed, and bounds on the neutron electric dipole moment constrain $\bar{\theta} \lesssim 10^{-10}$ [103]. The strong CP problem is: why is $\bar{\theta} \approx 0$?

A possible resolution to the strong CP problem is that a chiral symmetry exists so that $\bar{\theta}$ can be rotated away. This would be the case if there existed a massless quark; however, this is not realised in the SM. Instead, as proposed by Peccei and Quinn in 1977, a global chiral $U(1)_{PQ}$ symmetry could exist in the fundamental Lagrangian [104]. This symmetry is necessarily broken at low scale, which implies a (pseudo-)goldstone boson a: the "axion." If the sum of the u_R and d_R charges under $U(1)_{PQ}$ is non-zero, then a interacts with the chiral anomaly and an extra term appears in the Lagrangian:

$$\bar{\theta}\frac{\alpha_s}{8\pi}G^{\mu\nu}\tilde{G}_{\mu\nu} + \xi\frac{a}{f_a}\frac{\alpha_s}{8\pi}G^{\mu\nu}\tilde{G}_{\mu\nu}, \tag{1.31}$$

where f_a is the $U(1)_{PQ}$ symmetry breaking scale and $\xi \neq 0$. The chiral anomaly also induces a non-trival potential for a, and it turns out that the minimum of this potential occurs at $\langle a\rangle = -\frac{f_a}{\xi}\bar{\theta}$. Therefore, remarkably, a acquires a vev which exactly cancels the $\bar{\theta}$ term, solving the strong CP problem dynamically.

A $U(1)_{PQ}$ symmetry is not realised in the SM. Thus the PQ solution to the strong CP problem requires BSM physics. The minimal way to appropriately augment the SM is to add a second Higgs doublet coupling to the down-type quarks [104, 105],

$$-\mathcal{L}_Y = y_u\overline{Q_L}\Phi u_R + y_d\overline{Q_L}\tilde{\Phi}_2 d_R + \ldots . \tag{1.32}$$

This model, with $f_a \sim v$, was quickly excluded by laboratory experiments. Indeed, these experiments together with stellar energy loss constrains $f_a \gtrsim 4\times 10^8$ GeV [106]. Thus the $U(1)_{PQ}$ breaking scale must be very high, implying an extremely weakly coupled "invisible axion," named as such since the axion inherits tiny v/f_a suppressed couplings nucleons, photons, and electrons.

In CHAPTER 6 we will construct a variant of the Dine–Fischler–Srednicki-Zhitnitsky (DFSZ) invisible axion model [107, 108]. The DFSZ model adds a complex scalar singlet to the minimal two-Higgs-doublet solution, which gains a $U(1)_{PQ}$ breaking vev of $\gtrsim 10^9$ GeV. As it turns out, invisible axions can also provide a solution to the dark matter problem, to be discussed presently.

1.1.6 Dark matter

There is overwhelming observational evidence, arising at disparate scales and at various epochs, for a non-luminous, gravitationally interacting "dark matter" (DM) permeating our Universe. Still, the fundamental nature of DM remains an open question.

Large scale observations, i.e. at scales greater than that of a typical galaxy, are well explained by collisionless "cold DM" (CDM), i.e. DM which is non-relativistic at the time when the cosmic horizon contained of order one galactic mass. First, the power spectrum of temperature anisotropies in the cosmic microwave background [109, 110] reveals acoustic oscillations consistent with a significant additional component of purely gravitationally interacting matter. Second, N-body CDM simulations [111, 112] are in good agreement with the observed statistical properties of large scale structure [113–116]. Putting these evidences together under the assumption of the ΛCDM cosmological model, the energy density budget of the Universe today can be determined: $\Omega_b \simeq 0.05$, $\Omega_{\rm DM} \simeq 0.27$, and $\Omega_\Lambda \simeq 0.69$, distributed between baryonic matter, DM, and dark energy, respectively. Third, weak gravitational lensing measurements, in particular of galaxy cluster collisions [117], directly indicate a significant gravitational component distinct from the baryonic gas.

At smaller scales the collisionless CDM paradigm has some shortcomings. Galaxy rotation curves reveal star velocities which scale as $v^2(r) \sim constant$ at large radius (as opposed to the r^{-1} relationship expected from the visible matter) [118, 119]. Measurements are consistent with an approximately uniformly distibuted extended halo of DM with a *cored* central profile forming the dominant mass component of these galaxies. This is at odds with the pure CDM prediction for a *cusped* profile [120]. There are also discrepancies between the observed distribution of Milky Way satellite galaxies and that predicted by CDM simulations: the so-called "missing satellite" and "too big to fail" problems [121, 122]. Still, it could be that baryonic effects alone, once properly taken into account, are able to solve these problems (see e.g. Ref. [123]).

The possibility remains that DM interacts only gravitationally. Indeed, cluster collisions and extended galaxy halos appear largely consistent with a dissipationless and collisionless DM [124, 125]. On the other hand, dissipational and/or self-interacting DM can help to explain small scale discrepancies. Dissipational DM can explain correlations between the shape of rotation curves and the baryonic properties of galaxies [126]. Self-interacting DM (particularly with light mediators) can provide a simple resolution to the core-cusp problem. It has also been suggested that the Abell 520 [127, 128] and Abel 3827 [129] cluster collisions show some evidence for a non-vanishing DM self-interaction. None of these hints are definitive; it is plainly difficult to draw strong conclusions from necessarily simplified numerical simulations together with a finite catalogue of astrophysical observations. Thus collisionless, dissipationless, cold DM remains the benchmark for DM.

Perhaps the most studied DM candidate is the weakly interacting massive particle (WIMP), hypothesised to have fallen out of equilibrium with the thermal bath in the early Universe. This "freeze out"occurred when the WIMP annihilation rate fell below the expansion rate of the Universe. Under this paradigm, the energy density stored in DM mass density is given approximately by

$$\frac{\Omega_{\mathrm{DM}}}{0.2} \sim \frac{10^{-8}\,\mathrm{GeV}^{-2}}{\sigma}, \tag{1.33}$$

if the freezeout temperature is taken to be $T_f \sim m_{\mathrm{DM}}/20$. Much has been made of the "WIMP miracle" that this cross-section happens to coincide with weak scale parameters:

$$\frac{\sigma}{10^{-8}\,\mathrm{GeV}^{-2}} \sim \left(\frac{g^2}{0.1}\right)^2 \left(\frac{\mathrm{TeV}}{m_{\mathrm{DM}}}\right)^2. \tag{1.34}$$

If DM interacts via the weak force in such a way then there is a realistic hope that it might be detected in terrestrial experiments. Another well-motivated DM candidate is the axion, whose existence is implied by the PQ solution to the strong CP problem discussed in Section 1.1.5. The typical axion associated with DM is extremely light ($\sim \mu$eV). Instead of a mass density, the observed Ω_{DM} is explained by energy stored in the coherent oscillations of the classical non-relativistic axion field. This field has not yet decayed due to its tiny couplings to standard matter. We will discuss the axionic DM scenario in more detail in CHAPTER 6.

These single-component, collisionless DM scenarios are certainly well-motivated. However, there is no a priori reason that DM could not consist of a more complex, multi-component sector, and/or with appreciable self-interactions. In fact, a multi-component self-interacting sector is the generic prediction of asymmetric DM scenarios [130] in which the DM abundance is set by a small particle–antiparticle asymmetry while the symmetric component is efficiently annihilated away. In this scenario it is rather natural to consider the DM as contained within a hidden sector with its own gauge interactions. The hidden sector DM might then interact with standard matter through "portals" arising from gauge kinetic mixing or scalar quartic mixing terms in the Lagrangian [131–133]. We will study these portal possibilities in CHAPTERS 2 and 7.

The identification of DM is clearly of primary importance to our fundamental understanding of the Universe. Fortunately, its nature can be probed in terrestrial experiments. There are three generic possibilities: production via SM+SM $\rightarrow$ DM+DM, e.g. at the LHC; observation of DM+DM $\rightarrow$ SM+SM annihilation in galaxies; and direct detection via DM+SM $\rightarrow$ DM+SM scattering. In CHAPTER 7 we will be interested in the latter, therefore let us spend the remainder of this subsection introducing the fundamentals of direct detection.

In order to make predictions (or inferences) for direct detection experiments, we require a model of the DM distribution within our galaxy, and in particular in the vicinity of the Earth. In the "standard halo model," the velocity distribution of the (single-component) DM in the halo frame is everywhere locally described by an isotropic Maxwell-Boltzmann distribution with an escape velocity cutoff:

$$f_{\mathrm{DM}}(\mathbf{v}) \propto \exp\left(-\frac{|\mathbf{v}|^2}{v_0^2}\right) \times \Theta(v_{esc} - |\mathbf{v}|), \tag{1.35}$$

where $v_0 = (2T/m)^{1/2} = v_{rot}$, and Θ is the step function, as motivated by the virial theorem and N-body simulations. The velocity parameters, usually taken as $v_{rot} \approx 220$ km/s and $v_{esc} \approx 550$ km/s, along with a local DM density of $\rho_{\mathrm{DM}} \approx 0.3$ GeV/cm^3, completes this description of the DM distribution in the halo frame [134]. Due to the movement of the solar system through the halo, and the movement of the Earth around the Sun, in the Earth frame this distribution is boosted by a time-varying bulk velocity

$$|\mathbf{v}_{wind}| \approx \left[232 + 15\cos\left(2\pi\frac{(t - t_0^{yr})}{T_{yr}}\right)\right] \text{ km/s}, \tag{1.36}$$

where $t_0^{yr} \approx 153$ days (June 2^{nd}); this is termed the "DM wind." We note that the standard halo model description is obviously a simplification and may not provide an adequate description even under the CDM paradigm. For example, recent CDM simulations including baryonic matter suggest significant departures from this model in Milky-Way-like simulated galaxies at solar radius [135–137]. Furthermore, as we will emphasise in CHAPTER 7, in multi-component scenarios the standard halo model is in general not at all applicable. This should be kept in mind when interpreting null results from direct detection experiments, which are often presented as exclusion regions in parameter space *assuming* the standard halo model.

From the local description of the DM distribution (Equations (1.35) and (1.36) in the standard halo model), and the differential scattering rate $d\sigma/dE_R$ of a given DM candidate with the target material, one can make predictions for the total scattering rate in direct detection experiments. If any possible spatial dependence and the rotational velocity of the Earth are ignored,

$$\frac{dR}{dE_R}(E_R, t) = N_T \frac{\rho_{\mathrm{DM}}}{m_{\mathrm{DM}}} \int_{|\mathbf{v}|>v_{min}} \frac{d\sigma}{dE_R}(E_R, |\mathbf{v}|)\, f_{\mathrm{DM}}(\mathbf{v}, t)\, |\mathbf{v}|\, d^3v\,, \tag{1.37}$$

where $v_{min}(E_R)$ is the minimum DM velocity for a recoil energy E_R.

Currently, there is a huge experimental effort aimed at directly detecting DM via keV recoil scatterings off a target material (see e.g. Ref. [138] for a review).

We will be interested in experiments which detect scatterings via the scintillation photons resulting from the de-excitation of an excited target nucleus, or via the direct ionisation of the target atoms themselves. These experiments include those with liquid xenon (e.g. XENON100 [139], XMASS [140], LUX [141]) and scintillator crystal (e.g. DAMA/LIBRA [142]) target materials. Two major direct detection methods are currently sensitive. First, a pure sensitivity search above background for a signal with a differential event rate matching that expected of DM. The liquid xenon experiments have set particularly stringent bounds on spin-independent DM-nucleon scattering for $m_{\rm DM} \gtrsim 1$ GeV using this method. Second, the annual modulation signal due to the velocity modulation in Equation (1.36) can in principle be used to discriminate signal and background. The DAMA and DAMA/LIBRA experiments have long claimed significant observation of DM scattering via this signature [143, 144]. The claimed signal could come from nuclear or electron scattering, since the experiment cannot discriminate between the two, although an interpretation in terms of nuclear scattering is disfavoured by results from the xenon experiments. Even so, the signal could in principle arise from some unknown seasonally modulating terrestrial effect, such is the ambiguity in the annual modulation signature. Recently, the XENON100 and XMASS xenon experiments have also searched for the annual modulation signature, with some hints of a positive signal [145, 146]. In CHAPTER 7 we describe an interesting class of models which might be able to accommodate the DAMA signal via electron recoils, and which makes the distinctive prediction for an additional sidereally modulating signal.

1.2 THESIS Outline

In Section 1.1 we introduced six major unanswered theoretical/phenomenological questions of the SM. Each of these questions non-trivially constrain and/or demand BSM particle physics. For example, measurements of the newly discovered Higgs boson require that electroweak symmetry breaking is largely SM-like, and naturalness requires that no (trivial) heavy physics which strongly couples to the Higgs boson should exist. Solutions to the phenomenological problems of neutrino masses, the BAU, the strong CP problem, and dark matter seem to *demand* new fields (with particular properties) in addition to the SM content. In this THESIS we present a collection of original bodies of work which follow the "bottom-up" philosophy in studying these six questions: we explore the phenomenological implications of minimal extensions to the already existing SM framework, constrained to explain the aforementioned problems and/or to satisfy theoretical/experimental bounds.

In CHAPTER 2: HIGGS SECTOR we study the simplest extension of the SM scalar sector by a real singlet scalar field. We examine the existing constraints when the additional mass eigenstate is very light, 100 MeV $< m_s < m_h/2$, and identify regions of parameter space which experiments at the LHC are uniquely sensitive to. In particular the opportunity to search for low background displaced decay signatures is explored.

In CHAPTER 3: NATURALNESS we will attempt a balanced discussion of the Higgs mass naturalness problem that might be introduced when perturbative new physics is added to the SM. As in Section 1.1.2 we distinguish this potential problem from any hierarchy problem, or the potential naturalness problem induced by gravity. We derive a Higgs mass sensitivity measure from Bayesian probability theory and use it to constrain the masses of various fermionic and scalar gauge multiplets.

In CHAPTER 4: NEUTRINO MASS we outline a systematic search strategy for TeV scale radiative Majorana neutrino mass mechanisms at the LHC. A detailed collider study of a one-loop realisation is performed.

In CHAPTER 5: BARYON ASYMMETRY OF THE UNIVERSE we reconsider the three-flavour Type I seesaw model for neutrino masses and the generation of the BAU via hierarchical leptogenesis. We present a proof that the minimal scenario cannot provide a natural explanation, and list the simplest ways to avoid this conclusion which already exist in the literature. We then describe a new solution which can be accommodated with the addition of a second Higgs doublet.

In CHAPTER 6: STRONG CP PROBLEM we describe a very minimal model which solves the strong CP problem and explains neutrino masses, the BAU, and dark matter, without introducing a naturalness problem. This model serves as an existence proof that weakly coupled high scale physics can naturally explain phenomenological shortcomings of the SM, and rounds out a model building programme which began in CHAPTER 5.

Lastly, in CHAPTER 7: DARK MATTER we consider a scenario in which the DM exists mostly in the form of a plasma in spiral galaxies like the Milky Way, and describe the unique phenomenological implications for direct detection. The unique prediction for a signal which modulates with sidereal day is emphasised.

We conclude in CHAPTER 8.

2 Higgs Sector

This Chapter is based on the publications "Phenomenology of a very light scalar (100 MeV $< m_h <$ 10 GeV) mixing with the SM Higgs," written in collaboration with Robert Foot and Raymond R. Volkas [1], and "Constraining portals with displaced Higgs decay searches at the LHC," which was single authored [4].

Measurements following up on the newly discovered [30, 31] Higgs boson, h, at $m_h \approx 125$ GeV, have revealed a CP-even scalar particle fully consistent with a SM Higgs [33, 147]. This appears to confirm the basic picture of electroweak symmetry breaking. That is, $SU(2) \times U(1)$ gauge symmetry is spontaneously broken by the non-trivial vacuum of an elementary scalar field. This raises an obvious question: is the Higgs the only scalar?

In this Chapter we investigate the phenomenological implications of extending the SM by a very light real singlet scalar s, with mass 100 MeV $< m_s < m_h/2$ GeV, which mixes with the SM Higgs. We point out apparently unresolved uncertainties in the branching ratios and lifetime of s in a crucial region of parameter space for LHC phenomenology. Bounds from LEP, meson decays, and fixed target experiments are reviewed. We then examine prospects at the LHC, grouped by production mechanism:

- *Production at parton-level* via those mechanisms made familiar by the SM Higgs, i.e. gluon fusion, vector boson fusion, Vs and $t\bar{t}s$. We demonstrate that searches for subdominant Vs production have the best sensitivity at the LHC for $m_s \gtrsim m_B$ and that future bounds in this region could conceivably compete with those of LEP.

- *Production via meson decay*, which is the dominant production mechanism at the LHC for $m_s \lesssim m_B$. We calculate the differential p_T spectrum of s scalars originating from B mesons and predict up to thousands of moderate (triggerable) p_T displaced dimuons at ATLAS/CMS and at LHCb.

- *Production via Higgs decay $h \to ss$*. We examine the region of parameter space where s is long-lived ($c\tau_s \gtrsim 1$ mm). Here, the LHC experiments are particularly sensitive via searches for the low background signature of back-to-back pairs of displaced narrow hadronic jets and/or lepton jets. We demonstrate that it is possible to reinterpret existing searches using a

Monte Carlo method utilising efficiency tables. We emphasise the importance for LHC collaborations to include a complete set of multidimensional efficiency tables in future displaced work.

2.1 A very light real singlet scalar

2.1.1 Motivation

In general, if the SM is extended by a real singlet scalar S, then the SM Higgs doublet state $\phi_0' \equiv \phi - \langle\phi\rangle$ and $S' \equiv S - \langle S\rangle$ will mix to form mass eigenstates h and s,

$$\begin{pmatrix} h \\ s \end{pmatrix} = \begin{pmatrix} \cos\rho & -\sin\rho \\ \sin\rho & \cos\rho \end{pmatrix} \begin{pmatrix} \phi_0' \\ S' \end{pmatrix}, \tag{2.1}$$

where ρ is a mixing angle and h is to be identified with the observed SM-like Higgs state. Such a setup is of phenomenological interest as a benchmark simply because it is the minimal extension to the SM scalar sector. We will study the diverse phenomenological implications of a very light s, with a mass in the region $100\ \text{MeV} < m_s < m_h/2$.

In addition to the minimality consideration, a very light s is motivated by various BSM scenarios. For example: (1) Realistic perturbative Coleman-Weinberg [148] models with classical scale invariance broken radiatively and spontaneously generally feature at least one additional (real) singlet scalar [e.g. 149–157]. If scale invariance is broken at the electroweak scale, by the vev $\langle S\rangle$, then a GeV scale s (the pseudo-Goldstone boson of spontaneously broken scale invariance) is predicted [158, 159]. (2) The Bezrukov & Gorbunov [160, 161] class of inflationary models feature a light scalar. (3) More generally, some hidden sector (which may or may not contain dark matter) might exist which couples to the singlet scalar. In this case a "Higgs portal" quartic interaction term then facilitates interactions involving the two sectors. Depending on the mass of the hidden states, invisible decays of s and/or h could be allowed, and this could serve as a probe of the hidden sector.

To make some explicit connection to the theory space, we will consider two benchmark scenarios throughout our discussion.

- The Foot & Kobakhidze [159] benchmark, motivated by a scale invariant model in which the cosmological constant (a finite and calculable parameter in these models [162]) is set to be small, consistent with observations. This in turn implies that the effective couplings Hss and $Hsss$ are very small and the mass of s and the angle ρ are correlated:

$$\sin\rho \sim 4\times 10^{-2}\left(\frac{m_s}{\text{GeV}}\right) . \tag{2.2}$$

- The Bezrukov & Gorbunov [160, 161] benchmark, motivated by cosmological inflation. In this set of models, constraints from primordial density perturbations imply the relation

$$1 \times 10^{-4} \left(\frac{\text{GeV}}{m_s} \right) \lesssim \sin\rho \lesssim 1 \times 10^{-3} \left(\frac{\text{GeV}}{m_s} \right) \quad . \tag{2.3}$$

Plainly, this defines a band in the $(m_s, \sin\rho)$ parameter space.

2.1.2 Model

Extending the SM by an extra real singlet scalar field S, the SM potential can be written generally as

$$V = +\mu^2\phi^\dagger\phi + \lambda\phi^\dagger\phi\phi^\dagger\phi + \zeta\phi^\dagger\phi S^2 + \xi\phi^\dagger\phi S + \mu_s^2 S^2 + \lambda_s S^4 + \alpha S + \beta S^3 \ , \tag{2.4}$$

where ϕ is the Higgs field. The limits $\alpha, \beta, \xi \to 0$ and $\zeta, \xi \to 0$ are technically natural. Once ϕ develops a non-zero vev, the cubic term $\xi\phi^\dagger\phi S$ induces mixing as in Equation (2.1). If $\mu_s^2 > 0$, then to first order in α, β, ξ, and ζ, the mixing ρ and the effective hss coupling κ are given by

$$\tan\rho = \frac{\xi v}{|m_h^2 - m_s^2|}, \qquad \kappa = \zeta v, \tag{2.5}$$

where $v \approx 246$ GeV. Terms odd in S can be forbidden by demanding some symmetry, for example $\mathbb{Z}_2$ ($S \to -S$), or classical scale invariance. Then $s = S$ is stable and a dark matter candidate [163] unless $\mu_s^2 < 0$ and an effective cubic term is generated by S acquiring a non-zero vev $\langle S \rangle = v_s$. In this case, at tree-level and to leading order in ζ,

$$\tan\rho = \frac{\zeta v v_s}{|m_h^2 - 2m_s^2|} = \zeta v \frac{m_s}{\sqrt{\lambda_s}|m_h^2 - 2m_s^2|}, \qquad \kappa = \zeta v \frac{m_h^2 + 4m_s^2}{m_h^2 - 2m_s^2}. \tag{2.6}$$

This is the simplest "Higgs portal" model [132, 133].

The decay width of the Higgs to light scalars is

$$\Gamma(h \to ss) = \frac{\kappa^2}{32\pi m_h} \sqrt{1 - \frac{4m_s^2}{m_h^2}}. \tag{2.7}$$

In the simplest Higgs portal model this width is a function of m_s, ρ, and λ_s; the perturbativity requirement $\lambda_s < 4\pi$ implies $\rho^2 \gtrsim 2 \times 10^{-9} \left(\frac{m_s}{\text{GeV}}\right)^2 \frac{Br(h \to ss)}{0.1}$. However, no such connection exists in the general case of Equation (2.5), and the mass m_s and mixing ρ can be considered completely independently of $Br(h \to ss)$.

Our approach in this Chapter is to explore generally the $(m_s, \sin\rho)$ parameter space. The very light scalar s decays only to SM particles with a vertex factor

$\sin\rho$ compared to the SM Higgs. The production cross section (in all channels we consider) is proportional to $\sin^2\rho$, the branching fractions are independent of $\sin^2\rho$, and the lifetime is inversely proportional to $\sin^2\rho$,

$$c\tau_s = \frac{c\tau_{SM}}{\sin^2\rho}, \tag{2.8}$$

where $c\tau_{SM}$ is the mean decay length of a scalar of mass m_s with exactly SM Higgs couplings, i.e. s when $\sin^2\rho = 1$. Evidently s becomes long-lived as $\sin^2\rho \to 0$. We also note that, in extended models where s decays also into invisible exotic states, one may repeat our analysis in the following way: the production cross section is unaffected, the branching fraction to SM final states is altered by a generally mass-dependent quantity $\mathcal{B}_{SM} \equiv Br(h \to X_{SM}) \leq 1$, and the lifetime becomes shorter by a factor $\mathcal{B}_{SM}$. The branching to invisible states must be taken into account for the invisible searches considered. We take $\mathcal{B}_{SM} = 1$ and comment on the $\mathcal{B}_{SM} < 1$ case when appropriate.

2.2 Bounds

2.2.1 Branchings and lifetime

Before discussing bounds we must determine the branching fractions and lifetime for s as a function of m_s. For $\sin^2\rho = 1$, s is a hypothetical SM Higgs boson of mass m_s. We may therefore appeal to the literature on the SM Higgs before it was ruled out below $2m_b$ [164].

The decay width to leptons is given by

$$\Gamma(s \to l^+l^-) = \sin^2\rho \times \frac{m_l^2 m_s}{8\pi v^2}\beta_l^3, \tag{2.9}$$

where $\beta_l = \left(1 - 4m_l^2/m_s^2\right)^{\frac{1}{2}}$, and $v \approx 246$ GeV. For $m_s < 2m_\mu \approx 210$ MeV, s decays almost entirely to e^+e^-. Above $2m_\mu$ the decay to $\mu^+\mu^-$ takes over until the $2m_\pi \approx 280$ MeV threshold, where the ratio $R_{\pi\mu} = \Gamma(s \to \pi\pi)/\Gamma(s \to \mu\mu)$ was historically the subject of much debate [164–171]. In Figure 2.1 we reproduce a selection of results to illustrate the large uncertainty in this mass range attributable to resonant $\pi\pi$ enhancements. We note that Ref. [171] is the most recent paper, that we are aware of, that is dedicated to the subject. Above the $2m_K \approx 1$ GeV threshold the decay to KK must be taken into account, and has been by a selection of these authors [169–171]. Above the $2m_\eta \approx 1.1$ GeV threshold we know of no reliable prediction. Somewhere above 2 GeV, where the energy involved in the decay is much larger than the typical quark binding energy, the perturbative spectator approach may be utilised (we call the strange quark q_s here to avoid

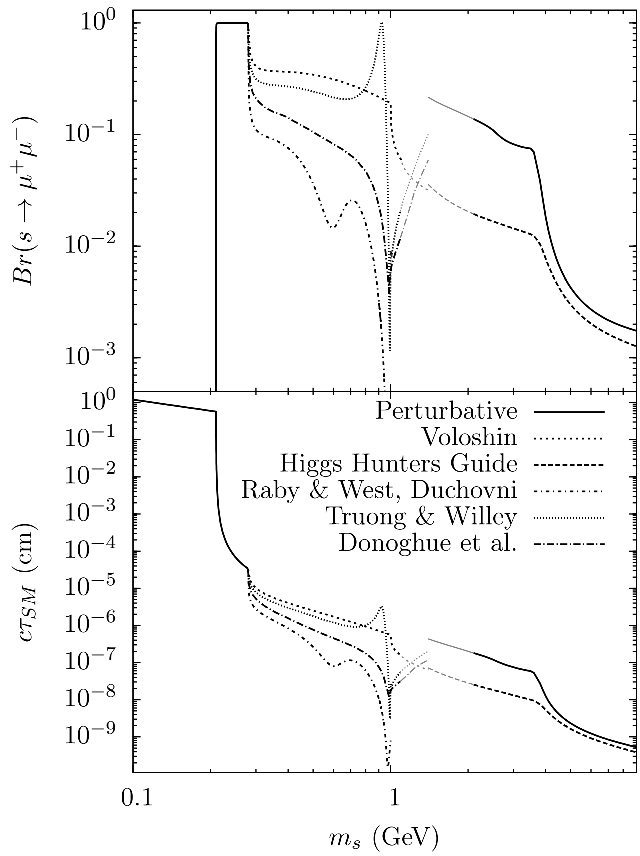

FIGURE 2.1: Branching fraction for a light scalar s decaying into muons and its mean decay length for $\sin^2\rho = 1$ (see Equation (2.8)) as predicted by a number of models (see text) [164, 165, 168, 170, 171]. The Duchovni et al. prediction is an application of the Raby & West result [167].

confusion with s) [164]:

$$\Gamma_{\mu\mu} : \Gamma_{q_s\bar{q}_s} : \Gamma_{c\bar{c}} : \Gamma_{\tau\tau} : \Gamma_{gg} \approx m_\mu^2\beta_\mu^3 : 3m_{q_s}^2\beta_K^3 : 3m_c^2\beta_D^3$$
$$: m_\tau^2\beta_\tau^3 : \frac{\alpha_s(m_s)^2 m_s^2}{9\pi^2}\left|\sum_q I\left(\frac{m_q^2}{m_s^2}\right)\right|^2, \quad (2.10)$$

where

$$I(z) = 3\left[2z + 2z(1-4z)\left(\sin^{-1}\frac{1}{\sqrt{4z}}\right)^2\right]. \quad (2.11)$$

In Figure 2.1 we plot this result alongside that given in the classic text "The Higgs Hunter's Guide" [164].[1]

[1]Ref. [164] set $m_u = m_d = 40$ MeV, $m_{q_s} = 450$ MeV, and $\alpha_s = 0.15\pi$ in order to match the result of Ref. [165] at $m_s \approx 1.5$ GeV; this is no longer well-motivated. We use $m_{q_s} = 100$ MeV and run α_s according to Figure 17 of Ref. [172]

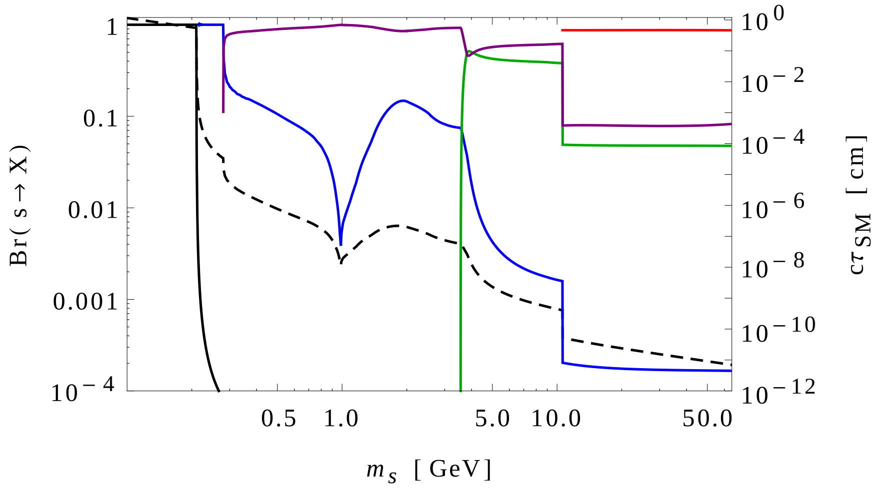

FIGURE 2.2: Branching fractions (solid, left axis) and mean decay length (dashed, right axis) for the very light scalar s, adopting the most recent calculation [171] for $R_{\pi\mu}$ below 1.4 GeV and smoothly interpolating to the spectator result above 2 GeV. Here $X = (ee$, $\mu\mu$, light hadrons, $\tau\tau$, $bb)$ in solid (black, blue, purple, green, red).

For definiteness we henceforth adopt the most recent calculation [171] below 1.4 GeV and smoothly interpolate to the spectator result above 2 GeV, with the result shown graphically in Figure 2.2. We acknowledge the apparently unresolved large uncertainties between $2m_\pi < m_s \lesssim 4$ GeV. It would be interesting to know whether a more sophisticated approach is now possible which would provide new insight. A new result would be useful since, in this region, the mean decay length plays an important role in LHC phenomenology.

We will now determine the experimentally excluded regions in $(m_s, \sin\rho)$ parameter space arising from collider, B factory, and beam dump experiments. The results are summarised in Figure 2.4, presented at the end of this subsection. The reader should keep in mind that this Figure assumes the aforementioned branching fractions and lifetimes in the uncertain region $2m_\pi < m_s \lesssim 4$ GeV; exclusion regions which are independent of these assumptions can be found in Ref. [1].

2.2.2 LEP

Constraints from the LEP collider experiment arise from the Bjorken process $e^+e^- \to Z \to Z^* s$.

Below $m_s = 2m_\mu$, the unboosted mean decay length of s is ~ 1 cm / $\sin^2\rho$. With a typical momentum of ~ 8 GeV [173] at this mass scale, s escapes the LEP detector and the appropriate bound to apply is that for an invisibly decaying scalar. The 95% C.L. bound is $\sin\rho \lesssim 5 \times 10^{-2}$ [174, 175]. The limits given in Refs. [174–177] would also apply to scalars with $\mathcal{B}_{SM} < 1$ for $m_s > 2m_\mu$.

Somewhere not far above $m_s = 2m_\mu$, prompt searches become relevant.[2] The best constraints are from the LEP1 searches of ALEPH and L3 [174, 175]. The 95% C.L. bounds are reproduce in Figure 2.4 as green dashed and green solid lines, respectively. For $m_s \gtrsim 30$ GeV, the combined LEP analysis sets the best limit [24]. These bounds are the best available for $m_s > (m_B - m_K) \approx 4.8$ GeV, and are enough to exclude the Foot & Kobakhidze benchmark for $m_s \gtrsim m_B$.

We would like to add a short note on these results. L3 considered only hadronic s decays in the $sZ^* \to s\nu\nu, se^+e^-, s\mu^+\mu^-$ channels for $m_s > 4$ GeV. ALEPH used $sZ^* \to s\nu\nu$, with $s \to$ *hadronic* or $s \to$ *two/four charged prongs* in the region $2m_\mu < m_s < 2m_b$. Figure 5.5 in the Ref. [178] shows that, for $m_s > 5$ GeV, the efficiency of the charged prong search falls and the hadronic search dominates. Therefore, in this region, the LEP limits are unique in that the limit is set by the hadronic decay of s. This is attributable to the comparatively low hadronic background at an e^+e^- collider and the fact that the hadrons appear as a monojet due to the boost of s when $m_s \lesssim 15$ GeV. The LEP limits for $m_s < 2m_b$ could have been significantly improved beyond LEP1. The L3 search analysed 114 pb^{-1} of data, while the full LEP dataset is ~ 3000 pb^{-1}. As well, with $\sqrt{s} > (m_Z + m_s)$, production of a real Zs pair becomes significant and background falls away [179]. Instead, analyses focused on the search for the SM Higgs above the $b\bar{b}$ threshold [24]. We can only surmise that, without motivation, this area of parameter space was overlooked.

2.2.3 Meson decays

The effective $\bar{q}_s ds$ ($\bar{b}q_s s$) vertex contributing to kaon (B meson) decay is obtained by integrating out the top-W loop from the diagram shown in Figure 2.3. This effective vertex leads to the decays $K \to \pi s \to \pi\mu^+\mu^-$ and $B \to Ks \to K\mu^+\mu^-$, with branchings [180, 181]

$$Br(K^+ \to \pi^+ s) \approx \sin^2\rho \times 0.002\,\frac{2|\vec{p}_s|}{m_K}, \tag{2.12}$$

$$Br(B^+ \to K^+ s) \approx \sin^2\rho \times 0.5\,\frac{2|\vec{p}_s|}{m_B}\mathcal{F}_K^2(m_s), \tag{2.13}$$

where $|\vec{p}_s|$ is given by two-body kinematics and the form factor $\mathcal{F}_K^2(m_s) = \left(1 - m_s^2/38\,\text{GeV}^2\right)^{-1}$ [182].

In applying experimental constraints from these decays one must properly take into account the lifetime of s; either s decays "promptly enough" so that the muons are reconstructed with the associated meson, or it does not and the experiment sees missing momentum. In the following, we take into account lifetime by requiring s to decay within a certain (experiment-dependent) distance of the meson decay. For simplicity, and because we only expect a small correction, we

[2] We do not labour on exactly when this occurs, since we find that meson decays set the best limits for $m_s < (m_B - m_K)$.

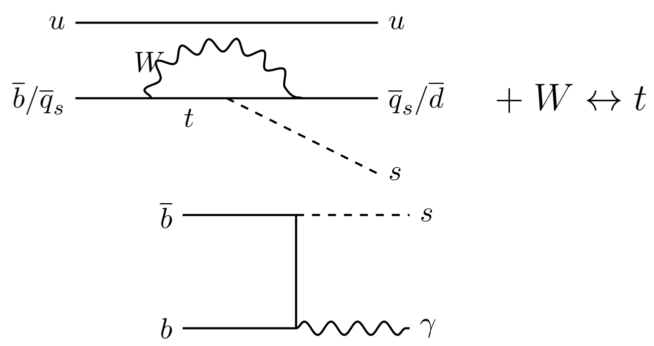

FIGURE 2.3: Kaon, B meson, and radiative Υ decays involving s.

do not impose any angular constraints. We stress that, where lifetime has an effect, these can only be considered as rough estimates. As discussed in Section 2.2, there is large uncertainty in the lifetime of s above the $\pi\pi$ threshold. We find that the dependence of the following bounds on s lifetime above this threshold is small, and negligible for $m_s > 400$ MeV with the existing experimental reach.

Kaon decays

The NA48/2 collaboration has measured $Br(K^{\pm} \to \pi^{\pm}\mu^{+}\mu^{-}) = (9.62 \pm 0.25) \times 10^{-8}$ [183], in good agreement with the theoretical predictions $(8.7 \pm 2.8) \times 10^{-8}$ and $(12 \pm 3) \times 10^{-8}$ [184, 185]. To derive limits on $\sin^2\rho$ we assume that a $\pi\mu\mu$ vertex is reconstructed if the $s \to \mu^{+}\mu^{-}$ decay occurs within the longitudinal vertex resolution, $\sigma_z \approx 100$ cm [186], of the kaon decay, and not reconstructed otherwise. A conservative limit on additive new physics is obtained by taking the difference between the low end of SM theoretical predictions, $Br(K^{\pm} \to \pi^{\pm}\mu^{+}\mu^{-})_{theory} \gtrsim 6 \times 10^{-8}$, and the experimental measurement:

$$Br(K \to \pi s) \times Br(s \to \mu^{+}\mu^{-}) \times \left(1 - \exp\left[\frac{-\sigma_z}{\gamma\beta c\tau}\right]\right) \lesssim 4 \times 10^{-8}, \tag{2.14}$$

where the bracketed term is the probability that a particle with lifetime τ, speed βc and boost γ decays within a distance σ_z, with $\gamma\beta \approx 120$ inherited from the kaon with momentum 60 GeV. Note that both $Br(K \to \pi s)$ and $c\tau$ depend on $\sin\rho$, so that this inequality may be used to constrain $\sin\rho$. The obtained constraint is given by the solid orange curve in Figure 2.4.

The E949 collaboration has published a 90% C.L. upper limit on the two-body decay $Br(K^{\pm} \to \pi^{\pm}X) \times Br(X \to \mathit{invisible})$ that is better than 10^{-9} between 170 MeV and 240 MeV [187]. The limit was derived assuming the decay of X was detected and vetoed with 100% efficiency if X decayed within the outer radius of the barrel veto, $l_{BV} \approx 145$ cm [188]. We therefore impose the following:

$$Br(K \to \pi s) \times \int_0^{\pi} \frac{\sin\theta d\theta}{2} \exp\left[\frac{-l_{BV}}{\sin\theta}\frac{1}{\gamma\beta c\tau}\right] < \text{E949 limit}, \tag{2.15}$$

where $\gamma\beta \sim 1$ is determined using two-body kinematics assuming a stationary kaon. This bound applies where s escapes the detector (it also applies to invisibly decaying scalars if $\mathcal{B}_{SM} < 1$), resulting in the exclusion region depicted by the orange dashed line in Figure 2.4. Notice that, for $m_s > 2m_\mu$, this constraint results in a non-trivial excluded region in $(m_s, \sin\rho)$ parameter space. This is because the invisible yield falls with decreasing $\sin\rho$, thereby making the total cross section smaller, or with increasing $\sin\rho$, thereby making the decay more prompt.

B meson decays

The LHCb collaboration has measured $Br(B^+ \to K^+\mu^+\mu^-) = (4.36 \pm 0.15 \pm 0.18) \times 10^{-7}$ [189], the most accurate measurement to date and in good agreement with the theoretical prediction of $(3.5 \pm 1.2) \times 10^{-7}$ [190]. However, here we will use the results from B-factories [191–194], since the nature of an e^+e^- collider makes it easier to predict the boost factor, and it is convenient to use the same experiment to constrain both the prompt and long-lived case:

$$\begin{aligned} Br(B^+ \to K^+\mu^+\mu^-) &= \begin{cases} (5.3^{+0.8}_{-0.7} \pm 0.3) \times 10^{-7} & \text{(Belle)} \\ (4.1^{+1.6}_{-1.5} \pm 0.2) \times 10^{-7} & \text{(BaBar)} \end{cases}, \\ &\approx (5.0 \pm 0.8) \times 10^{-7} \text{ (combined)} \end{aligned} \tag{2.16}$$

$$Br(B^+ \to K^+\nu\bar{\nu}) < \begin{cases} 1.4 \times 10^{-5} & \text{(Belle)} \\ 1.3 \times 10^{-5} & \text{(BaBar)} \end{cases}, \tag{2.17}$$

where the combined visible decay bound is obtained by first adding statistical and systematic uncertainties for each measurement in quadrature and then combining the measurements in the usual way assuming they are independent unbiased estimators of $Br(B^+ \to K^+\mu^+\mu^-)$. A conservative limit on additive new physics is obtained by taking the difference between the low end of SM theoretical predictions, $Br(B^+ \to K^+\mu^+\mu^-)_{theory} \gtrsim 2.3 \times 10^{-7}$, and the experimental measurement:

$$\begin{aligned} &Br(B \to Ks) \times Br(s \to \mu^+\mu^-) \\ &\quad \times \int_0^\pi \frac{\sin\theta d\theta}{2} \left(1 - \exp\left[\frac{-l_{xy}}{\sin\theta}\frac{1}{\gamma\beta c\tau}\right]\right) \lesssim 3 \times 10^{-7}, \end{aligned} \tag{2.18}$$

$$\begin{aligned} &Br(B \to Ks) \\ &\quad \times \int_0^\pi \frac{\sin\theta d\theta}{2} \exp\left[\frac{-l_{xy}}{\sin\theta}\frac{1}{\gamma\beta c\tau}\right] < 1.4 \times 10^{-5}, \end{aligned} \tag{2.19}$$

where we follow Ref. [181] in taking $l_{xy} \approx 25$ cm as the maximum reconstructed transverse decay distance from the beampipe, and $\gamma\beta \approx m_B/(2m_s)$ is dominated by the energy inherited from the B decay in the region $m_s < 400$ MeV. The resulting bounds are shown in red in Figure 2.4. We do not set limits in the invariant mass regions surrounding J/ψ and ψ' since the experiments vetoed such muons to remove $B \to J/\psi X, \psi' X \to \mu^+\mu^- X$ background.

The visible B meson decay bound is stronger than the kaon bound since $K \to \pi s$ is CKM-suppressed compared to $B \to K s$. In the invisible case this suppression is overcome by the $\mathcal{O}(10^{-4})$ stronger bound resulting from a dedicated two-body kaon decay search. These bounds are enough to exclude the Foot & Kobakhidze benchmark for 100 MeV $< m_s < (m_B - m_K) \approx 4.8$ GeV. Indeed, for this benchmark to be viable, it must be that $m_s \ll 100$ MeV.

Visible decay bounds could be stronger if dedicated searches in the dimuon invariant mass spectrum were performed. Such a search was carried out in the $B^0 \to K^{*0} X, (K^{*0} \to K^+\pi^-, X \to \mu^+\mu^-)$ channel at Belle in the region 212 MeV$< m_X < 300$ MeV [195]. No excess was found and an upper limit on the branching ratio of $\mathcal{O}(10^{-8})$ was set. Using this upper limit and the expression for $Br(B \to K^* s)$ in Ref. [181] we derive a limit similarly to Equation (2.18). This limit is given by the maroon line in Figure 2.4.

In our Ref. [1], we noted that both the B-factories and LHCb could conceivably improve on these B decay bounds by exploiting s lifetime for background rejection when $\sin\rho \lesssim 10^{-3}$. The mean decay length for s in the region above the $\pi\pi$ threshold ranges between 10^{-9} cm $/\sin^2\rho$ and 10^{-5} cm $/\sin^2\rho$ (see Figure 2.2). These mean decay lengths are to be compared with those for B mesons, $c\tau_B \approx 5 \times 10^{-2}$ cm, for which LHCb for example is designed to measure a displaced vertex. The lifetime of s must be treated carefully at LHCb due to the large boost factors expected. We encouraged, as did Refs. [161, 181, 196] for the B-factories and Ref. [197] for LHCb, dedicated displaced searches. We also estimated the reach of these kind of searches at the LHC, to be presented in Section 2.4. Encouragingly, after our Ref. [1] was published, both BaBar and LHCb performed such dedicated searches for the displaced decays of very light scalars produced in B decays [198, 199]. The regions of parameter space excluded by these searches are shown in Figure 2.4: the BaBar limit (grey) is reinterpreted from Figure 3 of Ref. [198] (1 cm $\leq c\tau_s \leq$ 100 cm) assuming $Br(B \to s X_s) \approx 5.6 \sin^2\rho \left(1 - m_s^2/m_B^2\right)^2$ [166]; and the LHCb limit (magenta) is reinterpreted from Figure 4 of Ref. [199] assuming the branching expression found in Ref. [181]. It is clear from the improvement in the bound that exploiting the displaced phenomenology in this region of parameter space is indeed a very powerful technique.

Upsilon decays

Limits also arise from the radiative $\Upsilon(nS) \to \gamma s$ decay shown in Figure 2.3. The BaBar collaboration has searched in this channel for light bosons decaying to $\mu^+\mu^-$, $\tau^+\tau^-$, hadrons, or escaping invisibly [200–203]. We reproduce the limits from dimuon and ditau decays [200, 201] in Figure 2.4 in solid purple and dashed purple, respectively, assuming the QCD correction factor $\mathcal{F}_{QCD}$ discussed therein is equal to unity. Ref. [204] discusses limits in light of CLEO data; for masses $m_s < 2m_\tau$, scalar decays to pions and kaons can be more constraining than decays to muons (see Figure 14 therein), though one must keep in mind the significant uncertainties in branching fractions. In any case, B meson decays are easily more constraining for $m_s \lesssim (m_B - m_K) \approx 4.8$ GeV. For $m_s \gtrsim 4.8$ GeV, ditau limits give the best meson decay bound on $\sin\rho$ since $Br(s \to \tau^+\tau^-)$ is about $m_\tau^2/m_\mu^2 \approx 290$ times larger than $Br(s \to \mu^+\mu^-)$. Even so, these bounds do not yet challenge the LEP limit of $\sin\rho \lesssim 10^{-1}$.

2.2.4 Fixed Target

Our scalar s can be produced either directly (through gluon fusion) or indirectly (via meson decays) in fixed target experiments. The dominant process depends on the centre of mass energy $\sqrt{s}$ and m_s. Meson decays dominate in the experiment we will consider below.

Two important regions of parameter space may be identified for indirect production: below the kaon threshold, $m_s < (m_K - m_\pi) \approx 360$ MeV, where kaon decays dominate, and below the B meson threshold, 360 MeV $\lesssim m_s \lesssim m_B$, where B meson decays dominate. We note that there is a small region where η decays can be important, but D meson decays are sufficiently CKM-suppressed to ignore. Some discussion and analysis may be found in Ref. [160].

As an example, following Ref. [160], we look at the bounds set by the CHARM Collaboration [205]. In this experiment, a 400 GeV proton beam was dumped into a thick copper target ($\sqrt{s} \approx \sqrt{2E_p m_p} \approx 27.4$ GeV) and the decay of a long-lived axion to photons, electrons, or muons was searched for in a 35 m long decay region placed 480 m from the target. Zero decays were observed.

The total number of scalars intersecting the solid angle covered by the detector, N_s, is related to the number of decays in the decay region, N_{dec}, by

$$\begin{aligned} N_{dec} \approx N_s \times &\left[Br(s \to e^+e^-) + Br(s \to \mu^+\mu^-)\right] \\ &\times \left[-\exp\left(\frac{-L_2}{\gamma\beta c\tau}\right) + \exp\left(\frac{-L_1}{\gamma\beta c\tau}\right)\right], \end{aligned} \tag{2.20}$$

where $\gamma\beta m_s \sim 10$ GeV, $L_1 = L_2 - 35 \text{ m} = 480$ m, and $N_s \approx 2.9 \times 10^{17} \times \sigma_s/\sigma_{\pi_0}$ is normalised to the neutral pion yield [205]. We adopt $\sigma_{\pi_0} \approx \sigma_{pp}M_{pp}/3$, where M_{pp} is the average hadron multiplicity and σ_{pp} is the proton-proton cross section [160]. The s production cross section is dominated by kaon decays:

$$\sigma_s \approx \sigma_{pp}M_{pp} \left[\begin{array}{c} \chi_s \times \frac{1}{2}Br(K^+ \to \pi^+ s) \\ +\chi_s \times \frac{1}{4}Br(K_L \to \pi^0 s) \\ +\chi_b \times Br(B \to s + X) \end{array}\right], \tag{2.21}$$

where $\chi_s = 1/7$, $\chi_b = 3 \times 10^{-8}$, $Br(K_L \to \pi^0 s) = Br(K^+ \to \pi^+ s) \times \Gamma(K^+)/\Gamma(K_L)$, and [166]

$$Br(B \to s + X) \approx \sin^2 \rho \times 0.26 \left(\frac{m_t}{m_W}\right)^4 \left(1 - \frac{m_s^2}{m_B^2}\right)^2 . \tag{2.22}$$

Since the CHARM experiment observed zero decays, we may constrain N_{dec} at 90% C.L. to be less than 2.3 (the solution of $0.1 = \lambda^k e^{-\lambda}/k!|_{k=0}$). Our result is shown in Figure 2.4 by the blue curve, with the enclosed region being excluded. Observe that scalar masses 100 MeV $< m_s <$ 280 MeV are ruled out for the Bezrukov & Gorbunov model by this analysis; the $K \to \pi + invisible$ and CHARM bounds also extend this exclusion substantially below 100 MeV, although it is not shown in Figure 2.4.

The reach of the CHARM experiment is testament to the enormous production cross section of mesons in hadron collisions, as well as the exploitation of the long s lifetime to remove all background. These two points, as we will see, are important for LHC phenomenology when $m_s \lesssim m_B$.

Other beam dump experiments exist which may complement the CHARM bound due to, in particular, differing beam energy and detector position (for a partial list see Refs. [206–210]). These include fixed target neutrino experiments, which have recently been considered as possibilities to probe GeV scale portals (see e.g. Refs. [211–214]). It is beyond the scope of this study to analyse these experiments in detail. However, we note that it does not appear that any of these experiments has probed the area above the eta meson threshold for s, because of insufficient direct or indirect production at given $\sqrt{s}$ (see Figure 30 of Ref. [215] for B meson production rates) and/or the distance to the detector being too great. Ideally, high luminosity (and acceptance) fixed target experiments with energy $\sqrt{s} \gtrsim 20$ GeV and a detector placed at a distance $\mathcal{O}$(1–10 m) would be needed to probe parameter space below the B decay bound for $m_s \gtrsim 360$ MeV. Just such an experiment — the SHIP experiment — is proposed for implementation at the CERN Super Proton Synchroton [216], with the physics case made in Ref. [217].

2.3 Production at parton-level

For $m_s \gtrsim m_B$, s is dominantly produced in the ways made familiar by the SM Higgs: gluon fusion, vector boson fusion, Vs, and $t\bar{t}s$. Table 2.1 shows the production cross sections for an example scalar of mass 5 GeV and $\sin^2 \rho = 1$. Cross sections were obtained using the HIGGSEFFECTIVE model in MADGRAPH/MADEVENT5 V1.5.9 [26] equipped with CTEQ6L1 parton distribution

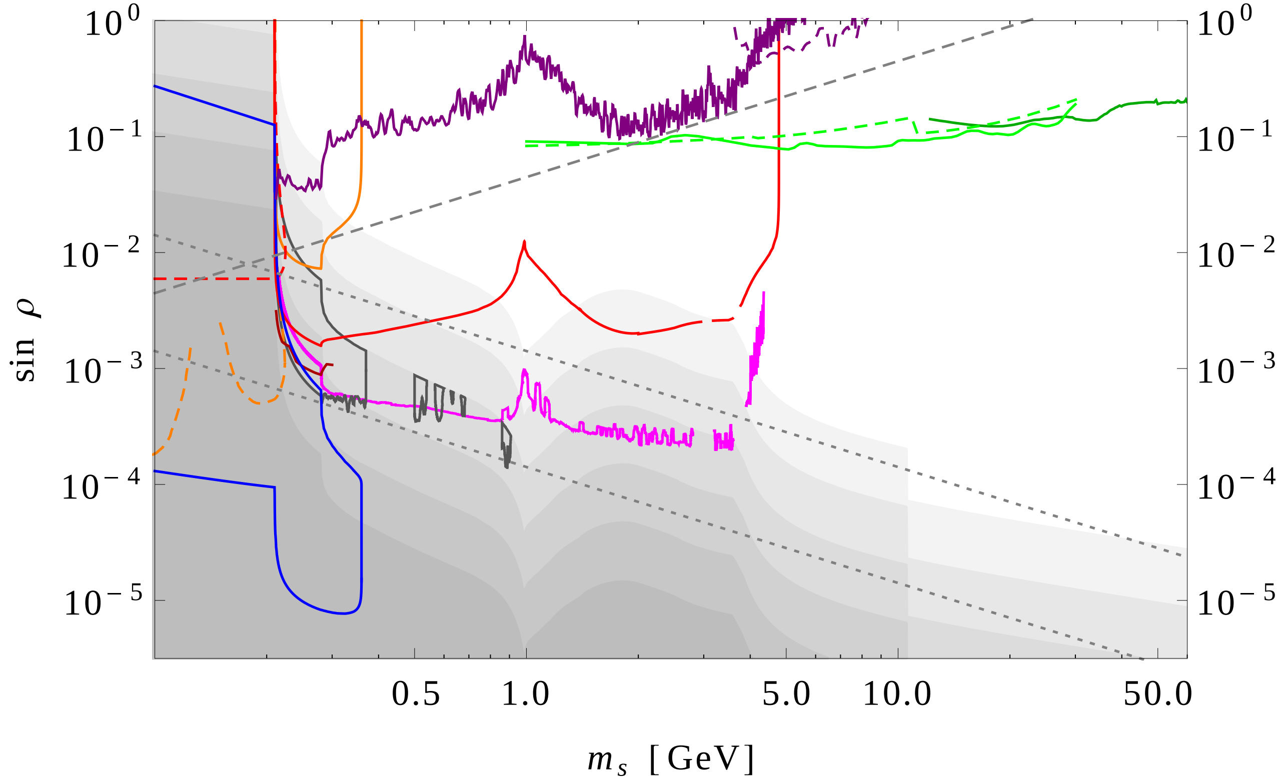

FIGURE 2.4: Exclusion regions in $(m_s, \sin\rho)$ parameter space from: LEP experiments (greens), $K \to \pi\mu^+\mu^-$ (orange solid), $K \to \pi + invisible$ (orange dashed), $B \to K\mu^+\mu^-$ (red solid), $B \to K + invisible$ (red dashed), $B \to K^{*0}\mu^+\mu^-$ dedicated search (maroon), $\Upsilon \to \gamma s \to \gamma\mu^+\mu^-$ (purple), $\Upsilon \to \gamma s \to \gamma\tau^+\tau^-$ (purple dashed), and the CHARM beam dump experiment (blue enclosed is excluded). Also shown are the benchmark models of Foot & Kobakhidze (upper grey dashed) and Bezrukov & Gorbunov (enclosed within lower grey dotted). The incremental shadings mark areas of non-negligible lifetime $(0.1\text{ mm}, 1\text{ mm}, \ldots, 10\text{ m})$.

Parton-level process	$\sigma(pp \to s+X)$ (pb) $\sqrt{s}=7$ TeV	$\sqrt{s}=13$ TeV	α_{ideal} $\sqrt{s}=7$ TeV
$gg \to s$	~ 770	~ 1300	$\sim 5\times10^{-4}$
Ws	170	360	1.7×10^{-3}
Zs	70	150	2.3×10^{-3}
$t\bar{t}s$	5.5	27	2.4×10^{-2}
$qq's$	0.87	1.9	1.3×10^{-1}

TABLE 2.1: Cross sections contributing to s production at the LHC for $m_s = 5$ GeV and $\sin^2\rho = 1$. Also shown is the acceptance factor α_{ideal} for a CMS dimuon search (see text).

functions [218], except in the case of gluon fusion where we used [164]

$$\frac{d\sigma}{dy}(pp\to h) = \frac{\pi^2}{8m_h^3}\Gamma(h\to gg)\times g_p\left(\frac{m_h e^y}{\sqrt{s}}, m_h^2\right)\times g_p\left(\frac{m_h e^{-y}}{\sqrt{s}}, m_h^2\right), \qquad (2.23)$$

where $g_p(x,Q^2)$ is the gluon distribution function in the proton evaluated at momentum fraction x and scale Q^2, and we integrated over all possible rapidities y using CTEQ5M parton distribution functions [219].[3] Table 2.1 reveals that gluon fusion is dominant, but Vs production is comparable. Such associated production is important from an experimental point of view; trigger limitations and backgrounds affect the gluon fusion channel much more than for Vs or $t\bar{t}s$. In the next two subsections we will demonstrate that the Vs channel is in fact the most sensitive search channel at the LHC for $m_s \gtrsim m_B$.

2.3.1 Inclusive dimuon search

Both ATLAS and CMS have performed a search for a light pseudoscalar, a, produced via gluon fusion and decaying to two muons [220, 221]. The CMS search analysed the mass range between 5.5 and 8.8 GeV and between 11.5 and 14 GeV, avoiding the Υ resonances. They provide a 95% C.L. upper limit on $\sigma(pp\to a)\times Br(a\to\mu^+\mu^-)$. The production cross section of s through the gluon fusion mechanism is given by Equation (2.23). To constrain s we assume that the acceptance in the CMS analysis is the same for our scalar as for the pseudoscalar, and consider only the dominant production of s by gluon fusion. We then apply the $\sigma(pp\to a)\times Br(a\to\mu^+\mu^-)$ limit, evaluating Equation (2.23) by integrating over all possible rapidities using CTEQ5M parton distribution functions [219]. The result is a limit of $\sin^2\rho\times Br(h\to\mu^+\mu^-)\lesssim 5\times10^{-3}$, which is comparable to the limit from $\Upsilon\to\gamma s\to\gamma\mu^+\mu^-$ decays, but far from that of LEP.

The 1.3 fb^{-1} of data analysed by CMS was collected with the opposite-sign dimuon trigger, requiring $p_T^{\mu\mu} > 6$ GeV, and $m_{\mu\mu} > 5.5$ GeV with a prescale factor of 2. These low p_T, low invariant mass dimuons are evidently plentiful at the LHC. Thus, as the luminosity and centre-of-mass energy are increased the

[3] MADGRAPH/MADEVENT5 returns a value for gluon fusion of 670 pb in the $\sqrt{s}=7$ TeV case, but breaks at $\sqrt{s}=13$ TeV.

trigger thresholds and/or the prescale factor must increase. In short, we are background-restricted and trigger-restricted in the region that maximises signal.

So what happens if we demand high dimuon p_T, so as to minimise background and avoid trigger-dependence? CMS have performed a search for light resonances in the dimuon spectrum with 35 pb^{-1} of data collected at $\sqrt{s} = 7$ TeV [222]. At $m_s = 5$ GeV, they set a 95% C.L. limit on $\alpha_{ideal} \times \sigma(pp \to s+X) \times Br(s \to \mu^+\mu^-) < 0.1$ pb, where α_{ideal} is an acceptance factor calculated in your favourite event generator by requiring

$$p_T^{\mu} > 15\,\text{GeV}, \qquad p_T^{\mu\mu} > 80\,\text{GeV}, \qquad |\eta_\mu| < 0.9. \tag{2.24}$$

Using MADGRAPH/MADEVENT5 we found $\alpha_{ideal} \approx 1.1 \times 10^{-3}$ for $m_s = 5$ GeV; it is broken down by channel in Table 2.1. For the gluon fusion channel we simulated $gg \to gs$ at parton-level, the hard gluon being necessary to give s necessary p_T. Interestingly, every channel contributes comparable amounts to the result of $\alpha_{ideal} \times \sigma(pp \to s + X) \approx 1 \times \sin^2\rho$ pb. From this we can constrain $\sin^2\rho \times Br(s \to \mu^+\mu^-) \lesssim 0.1$ for $m_s = 5$ GeV. Assuming that the bound will scale as $\sim 1/\sqrt{N}$, with 100 times more data — comparable in size to the CMS pseudoscalar search — we expect a bound of $\mathcal{O}(10^{-2})$. Therefore we have not gained anything on the pseudoscalar search bound by requiring high dimuon p_T. This is not surprising, since both the background and the dominant gluon fusion production mechanism have muons recoiling only against initial-state radiation, so that acceptance falls quickly with $p_T^{\mu\mu}$; this is reflected by the small value of α_{ideal} for gluon fusion in Table 2.1.

This leads us to consider instead triggering on associated activity so that some background is removed and we may probe lower p_T muons from the s decay. In the next section, we demonstrate that bounds using the Ws channel, triggering on a high p_T lepton from the W decay, are potentially stronger than the bounds obtained from an inclusive dimuon search.

2.3.2 Associated search

There are three associated search possibilities: Ws, Zs, and $t\bar{t}s$. In this section we consider the $Ws \to W\mu^+\mu^-$ channel. Because it is in general difficult (and not just for us) to model the combinatoric background, we appeal to the results of experiment. ATLAS has performed a search in 4.6 fb^{-1} of $\sqrt{s} = 7$ TeV data for J/ψ mesons produced in association with a W boson, where both decay muonically [223]. The search amounts to a measurement of the "bump size" in the dimuon invariant mass spectrum around the J/ψ mass of 3.1 GeV; they search in the region 2.5 GeV $< m_{\mu\mu} <$ 3.5 GeV. If s exists in this region we would expect to see a bump above the combinatoric background. We aim to estimate the reach of a $Ws \to (\mu\nu)(\mu^+\mu^-)$ search using the background distribution therein.

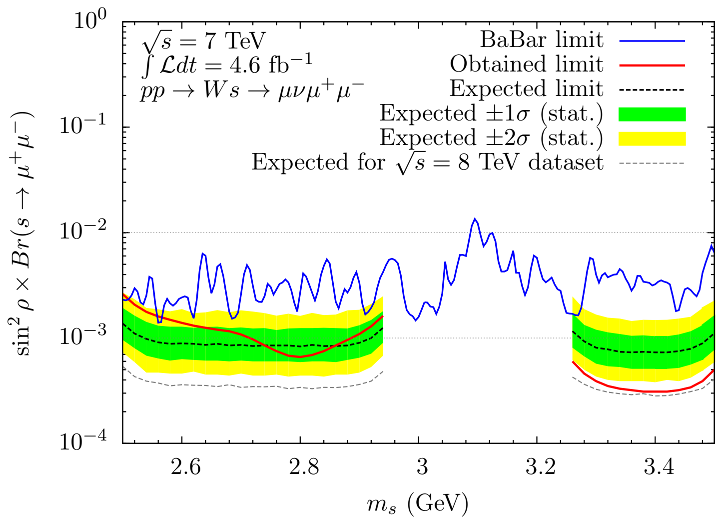

FIGURE 2.5: The obtained and expected 90% C.L. upper limit on $\sin^2\rho \times Br(s \to \mu^+\mu^-)$ from the Ws channel using 4.6 fb^{-1} of $\sqrt{s} = 7$ TeV data from ATLAS. Variance of the expected limit is statistical only. Also shown is an approximation of the expected limit using the 8 TeV dataset (see text) and the limit from $\Upsilon \to \gamma s \to \gamma\mu^+\mu^-$ decays.

We generate Ws ($W \to \mu\nu$, $s \to \mu^+\mu^-$) parton-level events in $\sqrt{s} = 7$ TeV pp collisions for a scalar of mass 2.7 GeV with SM Higgs couplings using the HIGGSEFFECTIVE model in MADGRAPH/MADEVENT5. We performed the following cuts to match those in Ref. [223]:

$$\begin{aligned} |\eta_\mu| &< 2.4, & p_T^{\mu[1]} &> 25\text{ GeV}, \\ \Delta R_{\mu\mu} &> 0.3, & p_T^{\mu[2]} &> 4\text{ GeV}, \\ \not{E}_T &> 20\text{ GeV}, & p_T^{\mu[3]} &> \begin{cases} 3.5\text{ GeV} & \text{if } |\eta_{\mu[3]}| < 1.3 \\ 2.5\text{ GeV} & \text{if } |\eta_{\mu[3]}| > 1.3 \end{cases}, \end{aligned} \tag{2.25}$$

where the muons are ordered by p_T. We subsequently performed the following intermediate state cuts (which made little difference):

$$8.5\text{ GeV} < p_T^s < 30\text{ GeV}, \qquad |\eta_s| < 2.1. \tag{2.26}$$

The results allow us to estimate the number of signal events in 4.6 fb^{-1} of data as $\approx 1 \times 10^4 \times \sin^2\rho \times Br(s \to \mu^+\mu^-)$.

We take the combinatoric background and the number of observed events from Figure 2 of Ref. [223], restricting ourselves to the regions 2.50 GeV $< m_{\mu\mu} <$ 2.94 GeV and 3.28 GeV $< m_{\mu\mu} <$ 3.50 GeV to avoid the J/ψ peak, since the peak is fitted to the data in this region. The signal is modelled as a gaussian with width 50 MeV and mean m_s.

Let μ^b and μ^s be the vectors representing the expected number of background events and the expected number of signal events in k bins. Let y be the data vector. If we normalise μ^s to one event, then $\lambda\mu^s$ represents a signal bump with λ expected total events. The likelihood of the data is

$$L(y|\lambda) = \prod_{j=1}^{k} (\mu_j^b + \lambda\mu_j^s)^{y_j} \exp\left[-(\mu_j^b + \lambda\mu_j^s)\right]. \quad (2.27)$$

Bayes' theorem relates this likelihood to our degree of belief in λ:

$$p(\lambda|y) \propto L(y|\lambda)\pi(\lambda), \quad (2.28)$$

where π is the prior distribution for λ. If we take a flat prior,

$$\pi(\lambda) = \begin{cases} 1 & \lambda \geq 0, \\ 0 & \text{otherwise}, \end{cases} \quad (2.29)$$

then the 90% C.L. upper limit on λ, λ_{UL}, is found by solving

$$0.90 = \frac{\int_0^{\lambda_{UL}} L(y|\lambda)}{\int_0^{\infty} L(y|\lambda)}. \quad (2.30)$$

Given the result for the number of signal events, the 90% C.L. upper limit on $\sin^2\rho \times Br(h \to \mu^+\mu^-)$ is then $\approx 10^{-4}\lambda_{UL}$. We have performed this analysis for a signal centred on each of 36 m_h values spread 20 MeV apart.

The obtained upper limit is given by the red line in Figure 2.5. An expected ($\pm 1\sigma / \pm 2\sigma$ stat.) limit was derived by performing the above analysis on 10^3 pseudodatasets generated assuming the background only hypothesis, ordering them by the obtained λ_{UL}, and taking entry 500 $\binom{841}{159}/\binom{977}{023}$, shown by the dashed line and bands in Figure 2.5. We also show the expected limit for the case with five times the data, which serves as an approximation for the reach of the 8 TeV dataset. One can see that the limit of $\mathcal{O}(10^{-3})$ is better than that set by radiative upsilon decays. A similar limit would be expected for $m_s > m_B$, potentially setting the best LHC limit on $\sin^2\rho \times Br(s \to \mu^+\mu^-)$ in that region. However, it would still be an order of magnitude weaker than the LEP limit on $\sin\rho$.

We note that the expected sensitivity of a Zs search, where both the Z and s decay muonically, is expected to be higher because the extra lepton would help to remove combinatoric background. In the future, a search for the production of prompt J/ψ mesons in association with a Z boson may allow the above analysis to be reperformed. The reach of the 13 TeV run is not clear because we do not know the combinatoric background, but one could speculate that more data and higher sensitivity in the Zs channel may be enough to compete with LEP bounds of $\mathcal{O}(10^{-5})$.

2.4 Production via meson decay

For $m_s \lesssim m_B$, the dominant s production mechanism at the LHC is indirect production via the decay of mesons. The $B\bar{B}$ cross section in 7 TeV (8/13 TeV) pp collisions has been calculated as $\approx 2.5 \times 10^{11}$ fb ($\approx 3/10 \times 10^{11}$ fb) [215]. Then, for example, using Equation (2.22), at $\sin\rho = 10^{-3}$ and $\sqrt{s} = 7/8$ TeV the s production cross section is $\sim 10^6$ fb, to be compared with ~ 1 fb through gluon fusion. This is also an area of parameter space where s lifetime becomes non-negligible. In the following subsection we determine the differential p_T spectrum for scalars originating from B mesons at ATLAS/CMS and LHCb. We then show that up to thousands of moderate (triggerable) p_T displaced decays could have already been produced at the LHC by very light scalars which are not yet excluded.[4]

2.4.1 Production via B decays

We developed an in-house simulation to calculate the differential cross section $d\sigma_s/dp_T$ for scalars from B decays, given $d\sigma_B/dp_T$ and $d\sigma_B/dy_B$ for B mesons in $\sqrt{s} = 7$ TeV pp collisions at ATLAS/CMS and at LHCb. It works in the following way: within loops over p_T^B and y_B, there is a loop simulating N_{dec} isotropic B decays to s, which are then boosted from the B frame to the lab frame given p_T^B and y_B, rejected to a rejection bin in a histogram if they fall outside the angular acceptance, or else p_T^s is measured and we add $f(p_T^B)f(y_B)/N_{dec}$ to the appropriate p_T^s bin in a histogram, where $f(p_T^B)$ and $f(y_B)$ define the discrete probability distributions for the transverse momentum and rapidity of the B mesons. The histogram (which should now have unit area) is then normalised to $Br(B \to s + X) \times \int \frac{d\sigma_B}{dp_T^B} dp_T^B$. We infer $f(p_T^B)$ from the fixed-order-next-to-leading-logarithm (FONLL) predictions in Refs. [224–226]; this amounts to creating a probability density function by normalising $d\sigma_B/dp_T^B$ to unity over a chosen p_T range and then discretising to allow for numerical integration. The $d\sigma_B/dp_T^B$ distributions used are reproduced in Figure 2.6. We interpolate $f(y_B)$ for ATLAS/CMS from the FONLL prediction in Figure 6 of Ref. [225], and for LHCb from the experimental measurements in Figure 4 of Ref. [226]. We make the approximations that $f(y_B)$ is independent of p_T^B, $|\vec{p}_s|$ in the B frame is equal to that from $B \to Ks$ decay, and the decay of the B meson is prompt.

Our results for a selection of m_s are shown in Figure 2.6. Note that we have only considered B^+ decays; results for B^- would be identical, and for B^0 or $\overline{B}^0$ would be very similar, so that the total s cross section from B meson decay gains a factor ≈ 4. For larger m_s the p_T tail falls more slowly because s is produced at lower velocity in the B frame and therefore tends to follow the direction of

[4] We note that for $m_s < m_K$ we also expect production via kaon decays. We ignore this area since, in our benchmark model, it has been explored by CHARM (see Section 2.2.4). Below the CHARM limit the lifetime becomes long enough so that the majority of moderate p_T scalars would escape the detector. The situation may be different in models with $\mathcal{B}_{SM} < 1$, since the lifetime becomes shorter, though one must take into account non-negligible kaon lifetime.

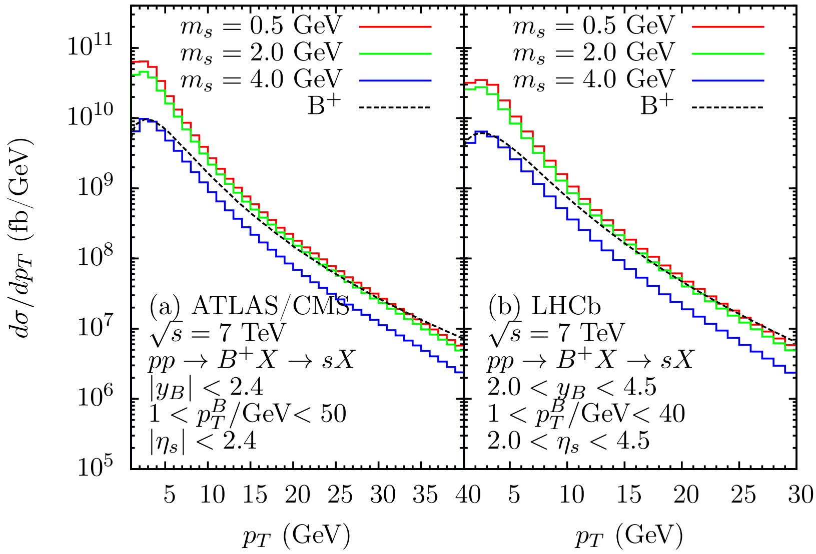

FIGURE 2.6: The differential cross section of s produced in B^+ decays in $\sqrt{s} = 7$ TeV pp collisions for $\sin\rho = 1$ and $m_s = 0.5, 2.0, 4.0$ GeV descending. The mother B^+ mesons are constrained in transverse momentum and rapidity as indicated.

the B meson; the overall cross section also falls due to kinematic suppression in $Br(B \to s + X)$.

With the information that is available to us, we are limited to using B mesons within a certain p_T range and within rapidities that would be accepted at ATLAS/CMS or at LHCb. These limitations are written in the inset of Figure 2.6. Consequently, values of $d\sigma/dp_T$ in the LHCb case for $p_T \lesssim m_B$ are an underestimate, since smaller rapidity B mesons will contribute. Otherwise we believe our results are a very good approximation. They could be improved by looping over the entire range of allowed B momentum and rapidity if the complete $d^2\sigma_B/dp_T^B dy_B$ distribution were available.

The point to be gleaned from the distributions in Figure 2.6 is that, in unexplored parameter space with $\sin\rho \lesssim 10^{-3}$ (recall that production will scale with $\sin^2\rho$), there are still a large number of moderate (triggerable) p_T scalars being produced via B decays at ATLAS/CMS and at LHCb. While inclusive searches for such light s scalars are limited by huge backgrounds (see e.g. Ref. [222] for $\mu^+\mu^-$ background), we contend that searches for low background displaced decays might be a viable way forward, especially seeing that B-factory bounds are already pushing the boundary of non-negligible s lifetime. For m_s between 360 MeV and 5 GeV, $c\tau$ ranges between 10^{-9} cm / $\sin^2\rho$ and 10^{-5} cm / $\sin^2\rho$, to be compared with $\approx 5 \times 10^{-2}$ cm for B mesons (which produce measurably displaced vertices at the LHC). Therefore, we expect a substantial region of parameter space with $\sin\rho \lesssim 10^{-3}$ for which this production mechanism will result in a large number of displaced decays. It is this possibility that we pursue presently.

2.4.2 Displaced decays

At the time that our Ref. [1] was published, the only existing search for long-lived exotic light particles at the LHC was an ATLAS search for approximately back-to-back collimated dimuons appearing outside the inner detector but within the muon spectrometer, i.e. with transverse distance from the beamline 1 m $\lesssim L_{xy} \lesssim$ 7 m [227]. In that search the prompt muon background was heavily suppressed (there is almost zero background) by requiring a lack of tracks in the inner detector within a cone surrounding the direction of the muon jet; no events are observed in 1.9 fb^{-1} of $\sqrt{s}$ = 7 TeV pp collision data. There was no existing displaced exotica search by LHCb. The LHCb detector is *designed* to be able to efficiently identify displaced decays of B mesons, thus LHCb should be particularly sensitive to decays of s within their vertex locater (which extends 1 m beyond the interaction point and has excellent reconstruction capabilities), especially if its origin can be traced to a $B^{\pm}$ decay vertex. In this subsection we will estimate the expected number of moderate (triggerable) p_T displaced dimuons arising via $pp \to B + X \to s + X \to (\mu^+\mu^-)_{displaced} + X$ and occurring within the ATLAS/CMS or LHCb detector volume. We assume s production only via B meson decays, with the independent possibility of $h \to ss$ production treated in Section 2.5.

Making the approximation $p \approx E$ ($\beta \approx 1$), the probability that a particle of mass m will decay within absolute (transverse) distance $L_1 < L < L_2$ ($L_1 < L_{xy} < L_2$) is given by

$$\mathcal{P}_{dec}(p_{(T)}) \approx -\exp\left(\frac{-mL_2}{p_{(T)} \times c\tau}\right) + \exp\left(\frac{-mL_1}{p_{(T)} \times c\tau}\right), \tag{2.31}$$

where the bracketing indicates the absolute (transverse) case. Note here that $c\tau$ is inversely proportional to $\sin^2\rho$ as in Equation (2.8). For ATLAS/CMS we require the decay of s to occur within transverse distance 1 m $< L_{xy} <$ 7 m, with $|\eta_s| < 1.3$, and $p_T^s > 8$ GeV. For LHCb we require the decay of s within 1 mm $< L <$ 10 cm, with $2.0 < \eta_s < 4.5$, and $p_T^s > 4$ GeV. The cross section of displaced s decays can be obtained from results like those in Figure 2.6 by integrating over the differential distributions. For example, for ATLAS/CMS we perform the numerical integral

$$\sigma_s^{displaced} \approx \sin^2\rho \times \int_{8\,\text{GeV}} \mathcal{P}_{dec}(p_T)\frac{d\sigma_h}{dp_T}dp_T, \tag{2.32}$$

and multiply by $4 \times Br(B \to s + X) \times Br(s \to \mu^+\mu^-)$ to account for production via B^0, $\overline{B}^0$, B^+, and B^- decays. For LHCb we perform a similar integral but with $p_T \to p$, and multiplying by $2 \times Br(B^+ \to K^+ s) \times Br(s \to \mu^+\mu^-)$ to account for production only via $B^{\pm}$.

In Figure 2.7 we show contours of the number of expected displaced dimuon

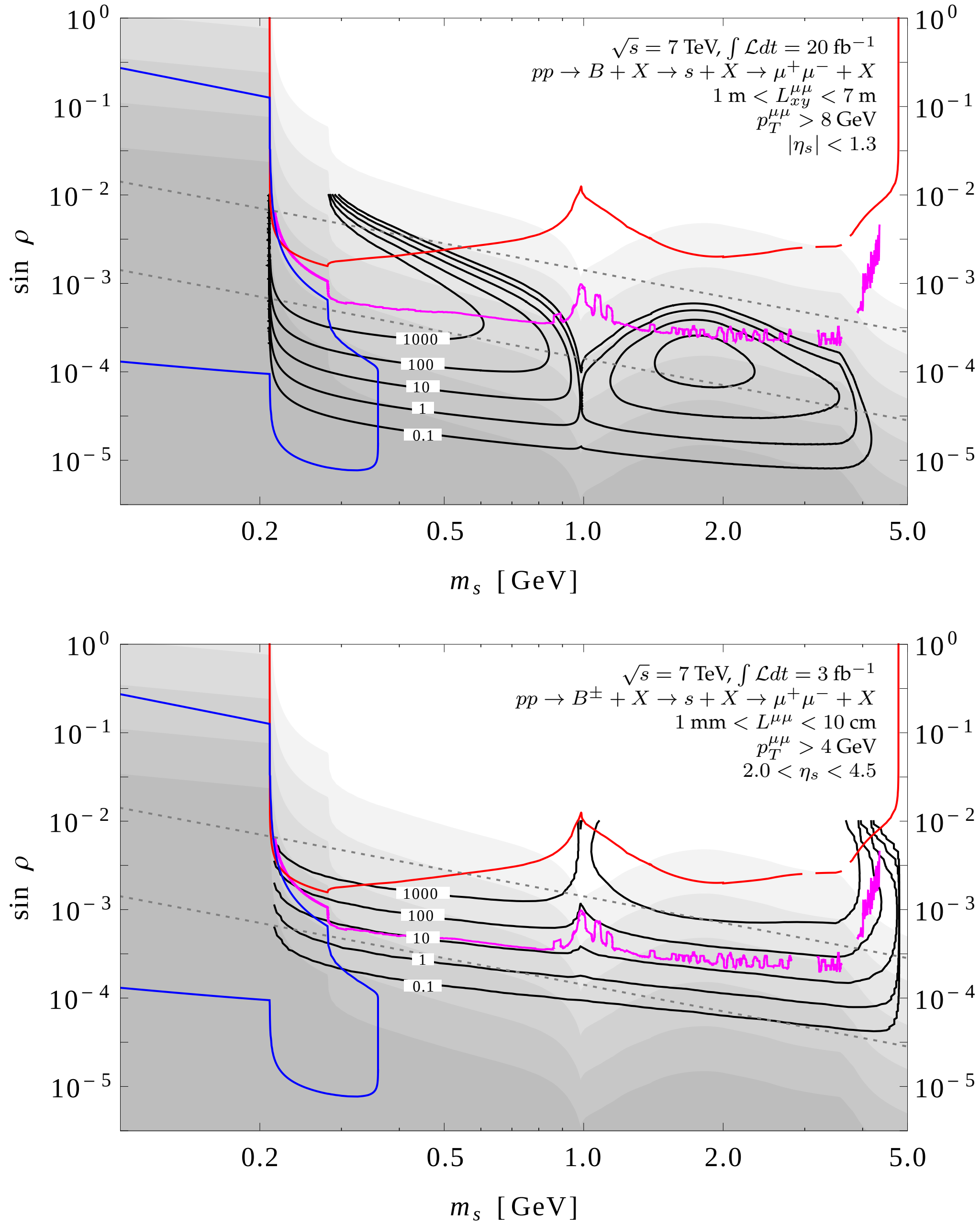

FIGURE 2.7: Contours $(0.1, 1, 10, 100, 1000)$ representing the expected number of moderate p_T displaced dimuons produced via $pp \to B \to s + X \to (\mu^+\mu^-)_{displaced} + X$ and occurring within the detector volumes of (top) ATLAS and (bottom) LHCb. Kinematic requirements and integrated luminosities are as indicated. Efficiency factors have not been considered. Shown in colour are the excluded regions from B decays and the CHARM experiment (see Section 2.2.3 and Figure 2.4). Also shown is the Bezrukov & Gorbunov benchmark (grey dotted).

events in 20 fb^{-1} (3 fb^{-1}) of $\sqrt{s}$ = 7 TeV pp collision data for ATLAS/CMS (LHCb); this plot serves to indicate the approximate reach of the 8 TeV dataset.[5] Note that as $\sin\rho$ gets smaller, the tuning of the mean decay length to maximise $\mathcal{P}_{dec}$ plays off against the falling cross section to create a window in unexplored parameter space where the number of displaced decays can be significant. The ATLAS/CMS detector is in principle capable of probing longer lifetimes since the lab-frame displacement can be larger, and the boost factors (momenta) are much smaller than for a forward detector. Also notice that the area of parameter space which ATLAS/CMS and LHCb are sensitive to coincides with the Bezrukov & Gorbunov benchmark, meaning that the model might be extensively probed.

Of course, we have only estimated the number of truth-level decays in these detectors. A dedicated study incorporating proper acceptance, trigger efficiency, reconstruction efficiency, and backgrounds is desirable to say more about the reach of the LHC. The greatest unknown for us is the trigger efficiency for these exotic events, particularly at ATLAS/CMS, where muons detected by the muon spectrometer are often required to pass quality criteria by matching to an inner detector track. It may be that dedicated triggers are necessary to capture these displaced events. We also note that at ATLAS/CMS the reconstruction efficiency falls with muon impact parameter, which is generally non-zero for displaced decays. Still, since we typically have $E \gg m_s$, the collimated muons will point back along the s direction to the B decay point so that we don't expect reconstruction efficiency to be significantly impacted. SM backgrounds can only arise from neutral particles with lifetimes in the range $c\tau \sim$ 1–100 cm. Of note are K_S^0 mesons ($c\tau_{K_S^0} \approx$ 2.7 cm) decaying to pions which may fake muons with $m_{\mu\mu} \approx 500$ MeV either through decays-in-flight or punching through the calorimeters; such background appears to be well modelled by Monte-Carlo [228]. Neutral strange baryons Ξ^0 and Λ^0 with masses 1.3 GeV and 1.1 GeV respectively are the only other neutral SM particles with lifetimes in this range; it is not obvious how their decays could fake a $\mu^+\mu^-$ vertex. Therefore, at least for $m_s \gtrsim 500$ MeV, the background is expected to be very low so that even a few events, particularly since they will occur at the same dimuon invariant mass, may be significant.[6] At ATLAS/CMS, the SM background might also be suppressed by requiring s to decay outside the hadronic calorimeter, 3 m $\lesssim L_{xy} \lesssim$ 7 m. In this regime one could also consider complementary signatures of decays to charged objects such as hadrons or $\tau^+\tau^-$ that might be picked up by the muon spectrometer. Whether these kind of events can be triggered on is an interesting and open question for us. Further analysis is beyond the scope of this study.

[5]For the LHCb results we observe that the bound from the subsequently performed search agrees well with our 10 event contour, confirming that our estimate was a good one.

[6]Since publication of our Ref. [1], LHCb has performed a search for displaced dimuons in $B^0 \to K^{*0}(\mu^+\mu^-)$ [199]. Indeed, for sufficiently long lifetime, the backgrounds are essentially nil.

2.5 Production via Higgs decay

As we noted in the Section 1.1.1, one of the primary goals of the LHC programme is to study the properties of h in great detail. So far the state is consistent with a SM Higgs. Still, plenty of room remains for new physics, particularly in its decays; $Br(h \to unobserved) \lesssim 20\%$ is still allowed for an otherwise SM Higgs [34, 35]. The real singlet scalar model predicts the possibility of $h \to ss$ decays. As such, regions of $(m_s, \sin\rho)$ parameter space can be excluded under the assumption of some value for $Br(h \to ss)$.

If s decays "promptly enough," then the most sensitive $h \to ss$ searches leptonic or tauonic final states. Above the ditau threshold $m_s > 2m_\tau$, the existing dedicated searches in $(ll)(l'l')$ $(l = e, \mu)$ and $(\mu\mu)(\tau\tau)$ final states [229, 230] are not yet powerful enough to exclude $(m_s, \sin\rho)$ parameter space for any assumed value of $Br(h \to ss)$, since the $s \to \mu\mu$ branching fraction in this region is just too small. However, for $2m_\mu < m_s \lesssim 2$ GeV, recent searches exploiting the unique signature of collimated dimuons (or muonic lepton jets) have reached the required level of sensitivity to constrain the real singlet scalar model [231, 232]. The strongest limit arises from a CMS search [232], which for promptly decaying s in this mass range bounds $Br(s \to \mu^+\mu^-) \lesssim 0.015\sqrt{\frac{0.2}{Br(h\to ss)}}$, to be compared with $Br(s \to \mu^+\mu^-) \sim \mathcal{O}(1\text{–}10)\%$ in Figure 2.2. This bound holds for $c\tau_s/m_s \lesssim 1$ mm, then falls precipitously by about two orders of magnitude by $c\tau_s/m_s \approx 1$ cm due to the rapid fall in trigger and reconstruction efficiency when decays become displaced. In this regime, which must be considered separately, the displaced decays of s produced via $h \to ss$ leads to the spectacular signature to be studied the remainder of this section: an approximately back-to-back pair of displaced narrow hadronic jets and/or lepton jets [233, 234].

Null searches for displaced hadronic jet and/or lepton jet pairs have already been performed by the LHC collaborations [227, 235–244]. The peculiarity of the signature presents two complementary challenges: how do collaborations present their results in the most model-independent way possible? and how do phenomenologists reinterpret the results in the context of their own models? In this subsection we will describe a simple Monte Carlo method which has implications for both. The short message is the following: if the relevant efficiency tables are published, then phenomenologists need only take Monte Carlo events and fold in these efficiencies to reinterpret searches. No displaced decays need be simulated since decay probabilities are easily calculated. We will describe this method by way of example, reinterpreting two ATLAS searches, and present exclusion regions in $(m_s, \sin\rho)$ parameter space for the real singlet scalar model.

In passing we note that this analysis is relevant to a variety of BSM scenarios in addition to the real singlet scalar extension, including (see our Ref. [4]

for more details): vector portal models with dark photons [131, 245–249]; right-handed neutrinos [250–253]; R-parity violating supersymmetry [254–258]; hidden valley models predicting hidden cascades, hidden hadrons, or hidden jets [233, 234, 259–266]; and "neutral naturalness" models [267–269]. The reason this phenomenology is so generic is because long-lived neutral states decaying to SM particles arise naturally in models with approximate symmetries. There are four mechanisms often encountered in the literature: an approximate enhanced Poincaré symmetry [37], which if exact would completely decouple a hidden sector; an approximate discrete symmetry, which if exact would produce a stable lightest particle; a low-energy accidental symmetry, with decays only proceeding via a heavy off-shell mediator; and small mass-splittings. The first mechanism is associated with the real singlet scalar model. This variety of models serves as a reminder that displaced searches would benefit from a model-independent approach, currently lacking in the existing analyses. Our analysis will provide some insight as to how to acheive this.

2.5.1 Reinterpreting displaced searches

In the following section we describe a Monte Carlo method for recasting displaced searches by way of example. The important point to be made is that phenomenologists cannot reliably simulate the detector response to displaced decays, and are therefore reliant upon efficiency information provided by the collaborations.[7] The recast examples will serve to highlight which efficiency information is of most interest.

Displaced hadronic jets

The ATLAS Collaboration has presented a search for the displaced hadronic decays of pair-produced long-lived neutral particles in 20.3 fb^{-1} of data collected at $\sqrt{s} = 8$ TeV [236, 237]. They considered pair production via the parton process $gg \to \Phi \to \pi_v \pi_v$, where Φ is a scalar particle and π_v is a hidden valley pseudoscalar. The decay of π_v is dominated by $b\bar{b}$ for $m_{\pi_v} \gtrsim 10$ GeV (the $c\bar{c}$ and $\tau\tau$ decays are subdominant, see their Table 1). No excess was observed, and limits were placed on the branching fraction of Φ as a function of m_{π_v} lifetime. Presently we describe a method to reproduce the result.

Validation samples of $gg \to h \to ss \to (b\bar{b})(b\bar{b})$ events in $\sqrt{s} = 8$ TeV pp collisions were generated using PYTHIA 8.180 [27, 28] with the default tune. We took $m_h = 126$ GeV and $m_s = 10, 25, 40$ GeV to match the ATLAS benchmarks.[8]

The cuts used in the ATLAS analysis are listed in the auxiliary Table 6 of Ref. [237]. We recreate them as follows. The pair produced long-lived particles

[7]This point was also made (and a similar recast method was used) in Ref. [270].

[8]The accuracy of the Monte Carlo for an s of mass $m_s = 10$ GeV decaying directly to $b\bar{b}$ is questionable, nevertheless it is possible to force PYTHIA to do the decay, and it appears that this is what was done in the ATLAS analysis.

are required to have[9]

$$E_T(s_1) > 60 \text{ GeV}, \qquad\qquad E_T(s_2) > 40 \text{ GeV}, \tag{2.33}$$

where $E_T \equiv E \sin\theta$ is a proxy for the measured transverse energy of the resulting jet, and the s subscript indicates p_T-ordering. This is a fine approximation except for the (non-hadronic) $s \to \tau\tau$ decays with $\sim 10\%$ branching. We also demand $\Delta R(s_1, s_2) > 0.4$ to ensure well-separated jets; this makes very little impact on the benchmarks considered by ATLAS, but will matter as $m_s \to m_h/2$. None of the relevant remaining cuts, such as on isolation and on electromagnetic fraction, nor the trigger efficiency can be replicated since no public tool exists to simulate the detector response to displaced decays.[10] Therefore the remainder of the analysis necessarily involves the folding in of efficiencies provided by ATLAS.

The CalRatio trigger [273, 274] was used to search for π_v decays at or beyond the edge of the electromagnetic calorimeter. This trigger selects narrow jets with $E_T \gtrsim 35$ GeV, $\log_{10}(E_H/E_{EM}) > 1.2$, and a lack of tracks in the inner detector. The trigger efficiency is given as a function of radial (longitudinal) decay position for decays in the barrel (endcap) region corresponding to the pseudorapidity region $|\eta| < 1.5$ ($1.5 < |\eta| < 2.5$) in Figure 1 of Ref. [236]. Based on these plots we take the trigger+reconstruction efficiency of the trigger jet to be non-zero and constant only between 2.0 to 3.5 m in the barrel and 4.0 to 5.5 m in the endcap, with a respective ratio of $0.20/0.06$. The reconstruction efficiency for the non-trigger jet is not given, but we take it similarly. By construction, the following quantity is then *proportional* to the trigger/reconstruction probability for a given s of lifetime $c\tau$:

$$\hat{\varepsilon}(s, c\tau) = \begin{cases} 0.20 P(s, c\tau) \text{ if in barrel,} \\ 0.06 P(s, c\tau) \text{ if in endcap,} \end{cases} \tag{2.34}$$

where P is the probability that a state x decays between L_{min} and L_{max},

$$P(x, c\tau) = -\exp\left(-\frac{L_{max}}{\gamma\beta c\tau}\right) + \exp\left(-\frac{L_{min}}{\gamma\beta c\tau}\right), \tag{2.35}$$

with γ and β the relativistic parameters for x. The timing of the s decay is required to satisfy $\Delta t < 5$ ns with respect to a $\beta = 1$ particle. This corresponds to requiring an absolute decay distance

$$L_{abs} < \frac{\beta}{1-\beta} 1.5 \text{ m} \equiv L_{abs}^{max}. \tag{2.36}$$

[9]Selections were made using the MADANALYSIS5 v1.1.10beta SAMPLEANALYZER framework [271].

[10]Though some attempts have been made [261, 272].

Thus after the aforementioned selection cuts, each event is weighted by a factor

$$W(c\tau) = \hat{\varepsilon}(s_1, c\tau)\hat{\varepsilon}(s_2, c\tau), \tag{2.37}$$

where we take

$$(L_{min}, L_{max}) = \begin{cases} \left(\min\left(\frac{2.0\,\mathrm{m}}{\sin\theta}, L_{abs}^{max}\right), \min\left(\frac{3.5\,\mathrm{m}}{\sin\theta}, L_{abs}^{max}\right)\right) & \text{if in barrel,} \\ \left(\min\left(\frac{4.2\,\mathrm{m}}{\cos\theta}, L_{abs}^{max}\right), \min\left(\frac{5.2\,\mathrm{m}}{\cos\theta}, L_{abs}^{max}\right)\right) & \text{if in endcap,} \end{cases} \tag{2.38}$$

for each s, where θ is the polar angle from the beam line. After this, the remainder of the cuts used in the ATLAS analysis should be largely independent of $c\tau$. As such, penultimately, we rescale the events (with a common number for all $c\tau$ and m_s) to fit ATLAS results; the factor turns out to be $\approx 6 \times 19.0$ pb $\times 20.3$ fb$^{-1}/N_{sim}$, where N_{sim} is the number of simulated events. We ignore for simplicity the additional m_s-dependent $\lesssim 10\%$ effect related to sub-dominant but non-zero $s \to \tau\tau$ branching.

After these requirements we find good agreement for the $m_s = 10, 25$ GeV samples, but we overpredict for $m_s = 40$ GeV. This is because as m_s approaches E_s (Equation (2.33)), the s decay products spread out and the narrow jet trigger efficiency decreases. To properly take this into account we require information on how the efficiency depends on the $b\bar{b}$ opening angle, or equivalently, in the limit $E_s^2 \gg m_b^2$, the boost. In the absence of such information, and in an attempt to capture the physics involved, we demand the following (admittedly crude) bound on the opening angle of the $b\bar{b}$ pair from the leading s:[11]

$$\Delta R(b, \bar{b}) < 1.5. \tag{2.39}$$

This cut has been tuned so that our results for $m_s = 40$ GeV best agree with those of ATLAS. Note that the spatial separation of the $b\bar{b}$ pair as seen by the hadronic calorimeter is smaller than such a large ΔR would normally suggest, since the pair appears late.

In Figure 2.8a we compare the number of events predicted by our analysis to those of ATLAS assuming 100% Higgs branching. Despite the apparent crudeness of some of our assumptions, we observe good agreement. The 95% CL limit of 20 events (inferred from the ATLAS plots) can be used to obtain a limit on the Higgs exotic branching fraction as a function of $c\tau$. To obtain the exclusion for alternative masses, PYTHIA signal samples $gg \to h \to ss \to (b\bar{b})(b\bar{b})$ of varying m_s were fed through our analysis. In Figure 2.8b we present our results as limits on $Br(h \to ss) \times Br(s \to hadronic)^2$ as a function of m_s and $c\tau$. Given the good match to ATLAS, we are confident that our results for 10 GeV $< m_s <$ 40 GeV are reliable, and for $m_s >$ 40 GeV are at least sensible.

[11] Another option is to reject leading s with boost lower than γ_{cut}, forbidding particles which have the potential to produce opening angles $\approx \arccos\left[1 - 2/\gamma_{cut}^2 + 8m_x^2(\gamma_{cut}^2 - 1)/(m_s^2\gamma_{cut}^4)\right]$, where m_x is the decay product mass.

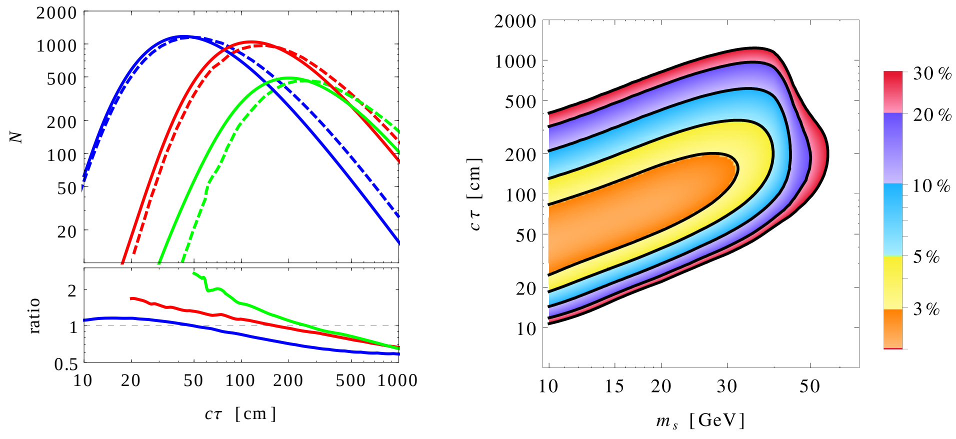

(A) (B)

FIGURE 2.8: (a) Predicted number of events for the displaced hadronic jet analysis assuming 100% Higgs branching. Upper: the results from ATLAS (dashed) and our results (solid) for $m_s = 10, 25, 40$ GeV beginning left-to-right. Lower: the ratio of our results to those of ATLAS. (b) Excluded parameter region for s assuming fixed $Br(h \to ss) \times Br(s \to hadronic)^2$; the contours mark branchings of 30%, 20%, 10%, 5%, 3%.

We were fortunate in this analysis because the topology of interest was essentially already considered by ATLAS for three benchmark values of m_s. This allowed us to demonstrate the not obvious fact that much of the $c\tau$ dependence is taken into account simply by reweighting events with easily calculated decay probabilities (Equation (2.35)). In the region where $\gamma_s \sim 1$ we saw that there was an additional effect that had to be considered, related to the boost-dependence of the trigger/reconstruction efficiency. This could have been anticipated, since any momentum dependence was already integrated out of the efficiency plots provided by ATLAS. For this reason our analysis as it stands cannot be reliably reapplied to another model since the overall efficiency will scale non-trivially with the (correlated) p_T distributions of the two long-lived particles. However it should serve as a conservative estimate for models with more boosted (on average) long-lived pairs. In the next analysis the p_T dependence of the efficiencies is provided and taken into account.

Displaced lepton jets

In Ref. [239], the ATLAS Collaboration presented the search for a SM-like Higgs decaying to a long-lived pair of $\mathcal{O}(100\text{ MeV})$ dark photons in 20.3 fb^{-1} of data collected at $\sqrt{s} = 8$ TeV. The benchmark process considered was

$$gg \to h \to f_{d_1}\overline{f}_{d_1} \to (f_{d_2}\gamma_d)(\overline{f}_{d_2}\gamma_d), \tag{2.40}$$

where the f_{d_i} are hidden fermions and γ_d is the long-lived dark photon, inspired by Falkowski–Ruderman–Volansky–Zupan (FRVZ) models [260, 261]. Each dark photon decays at or beyond the outer edge of the electromagnetic calorimeter to either $\mu\mu$ or $ee/\pi\pi$, resulting in a muon jet (Type 0) or a narrow jet (Type 2) respectively.[12] No excess over the SM expectation was observed and limits were placed on the exotic branching fraction of the Higgs as a function of γ_d lifetime. These limits are clearly model-dependent, and it is not clear how the phenomenologist might translate them. We describe a simple method below.

A validation sample of FRVZ events was generated in PYTHIA 8.180 [27, 28] by changing the properties of in-built particles. We took $(m_h, m_{f_{d_1}}, m_{f_{d_2}}, m_{\gamma_d}) = (125, 5, 2, 0.4)$ GeV and $Br(\gamma_d \to \text{Type } 0) = 0.45$ to match the ATLAS benchmark.

The selection criteria (cuts) for the ATLAS analysis are detailed in Table 1 of Ref. [239]. We recreate the analysis as follows. The dark photons are required to satisfy

$$|\eta(\gamma_d)| < 2.5, \qquad |\Delta\phi(\gamma_{d_1}, \gamma_{d_2})| > 1, \tag{2.41}$$

as a proxy for the jet acceptance. The remainder of the analysis necessarily involves the folding in of efficiencies. After each γ_d decays, the final states are of Type 0-0, 0-2, or 2-2 in the obvious way. After selection, each event is weighted by a factor

$$W(c\tau) = \frac{19.2 \text{ pb} \times 20.3 \text{ fb}^{-1}}{N_{sim}} P_{reco}(\gamma_{d_1}, c\tau) P_{reco}(\gamma_{d_2}, c\tau) \varepsilon_{trig}(\gamma_{d_1}, \gamma_{d_2}), \tag{2.42}$$

where $P_{reco}(\gamma_d, c\tau)$ is the reconstruction probability[13] for a γ_d of lifetime $c\tau$, and $\varepsilon_{trig}(\gamma_{d_1}, \gamma_{d_2})$ is the trigger efficiency given that the event is reconstructed. Equation (2.42) assumes that the reconstruction probability for each of the lepton jets can be considered independently. Both P_{reco} and ε_{trig} depend on the event Type, and will be described presently.

The reconstruction efficiencies for a γ_d with transverse momentum p_T decaying at a length L, $\varepsilon_{reco} \equiv \varepsilon_{reco}(p_T, L)$, are provided in the ATLAS auxiliary Tables 1–4 [239] for Type 0 and Type 2 jets decaying in the barrel and endcap regions, as defined in Table 2.2. We assume $\varepsilon_{reco} = 0$ outside of those L, η, p_T regions, which appears to be stricter (and therefore more conservative) than the barrel/endcap regions used in the full analysis. Since the γ_d are very boosted, we do not require a timing veto. The reconstruction probability for each jet is then

$$P_{reco}(\gamma_d, c\tau) = \sum_{L \text{ bins}} P(\gamma_d, c\tau) \varepsilon_{reco}(p_T^{\gamma_d}, L), \tag{2.43}$$

[12] Note that electrons in the hadronic calorimeter will resemble a narrow hadronic jet.
[13] This term includes additional rejection criteria such as inner detector isolation.

Type 0		Type 2	
Barrel	Endcap	Barrel	Endcap
$14 \leq L_{xy}/\text{cm} \leq 780$ $\lvert\eta\rvert < 0.9$ $10 \leq p_T/\text{GeV} \leq 100$	$50 \leq L_z/\text{cm} \leq 1400$ $1.2 < \lvert\eta\rvert < 2.5$ $10 \leq p_T/\text{GeV} \leq 100$	$150 \leq L_{xy}/\text{cm} \leq 410$ $\lvert\eta\rvert < 1.0$ $20 \leq p_T/\text{GeV} \leq 100$	$350 \leq L_z/\text{cm} \leq 650$ $1.5 < \lvert\eta\rvert < 2.4$ $20 \leq p_T/\text{GeV} \leq 100$

TABLE 2.2: Definitions of barrel and endcap regions for $\varepsilon_{reco}(p_T, L)$ as defined by ATLAS.

where $P(\gamma_d, c\tau)$ is given by Equation (2.35) with

$$(L_{min}, L_{max}) = \begin{cases} \left(\frac{L^{min}_{xy\text{-bin}}}{\sin\theta}, \frac{L^{max}_{xy\text{-bin}}}{\sin\theta}\right) & \text{if in barrel,} \\ \left(\frac{L^{min}_{z\text{-bin}}}{\cos\theta}, \frac{L^{max}_{z\text{-bin}}}{\cos\theta}\right) & \text{if in endcap.} \end{cases} \tag{2.44}$$

For any event involving a Type 2 jet, ATLAS used the previously described CalRatio trigger. ATLAS provides the CalRatio trigger efficiency ε_{cal}, defined as the fraction of jets passing the offline selection which also pass the trigger, separately as a function of p_T and η. Type 0-0 events are collected by the 3mu6_MSonly trigger [227, 239], which requires at least three standalone (not combined with an inner detector track) muons with $p_T > 6$ GeV. The efficiency of this trigger is dominated by the granularity of the muon spectrometer; to reconstruct three muons at least one of the dark photons must produce a pair of muons which have a discernible opening angle. ATLAS provides the efficiency ε_2, defined as the fraction of γ_d passing the offline selection and also producing two distinguishable muons, separately as a function of p_T and η. The efficiency for detecting at least one muon is quoted as $\varepsilon_{\geq 1} = 0.8$ (0.9) in the barrel (endcap) region. For our purposes we converted these efficiencies, making the assumption of independence, into functions of two variables, $\varepsilon_{cal} \equiv \varepsilon_{cal}(p_T, \eta)$ and $\varepsilon_2 \equiv \varepsilon_2(p_T, \eta)$. For each event, the trigger efficiency given event reconstruction is taken as

$$\varepsilon_{trig}(\gamma_{d_1}, \gamma_{d_2}) = \begin{cases} \varepsilon_{\geq 1}(\gamma_{d1})\varepsilon_2(\gamma_{d2}) + \varepsilon_{\geq 1}(\gamma_{d2})\varepsilon_2(\gamma_{d1}) & \\ \quad -\varepsilon_2(\gamma_{d1})\varepsilon_2(\gamma_{d2}) & \text{if Type 0-0,} \\ \varepsilon_{cal}(\gamma_{d_{\text{Type-0}}}) & \text{if Type 0-2,} \\ \varepsilon_{cal}(\gamma_{d_1}) + \varepsilon_{cal}(\gamma_{d_2}) - \varepsilon_{cal}(\gamma_{d_1})\varepsilon_{cal}(\gamma_{d_2}) & \text{if Type 2-2,} \end{cases} \tag{2.45}$$

where, in an obvious notation, $\varepsilon(\gamma_d) \equiv \varepsilon(p_T^{\gamma_d}, \eta^{\gamma_d})$. This is not quite a model-independent trigger efficiency, since ε_{cal} and ε_2 are derived from a lepton-jet gun event sample, in which the γ_d are generated uniformly in (p_T, η), but it serves as a good approximation for our purposes. After weighting by reconstruction probabilities, we find that this trigger efficiency for the FRVZ sample rescales the number of events by an approximately global number, ≈ 0.5 for $c\tau_{\gamma_d} = 0.1$ cm and ≈ 0.3 for $c\tau_{\gamma_d} = 100$ cm.

In Figure 2.9a we compare the number of events predicted by our analysis

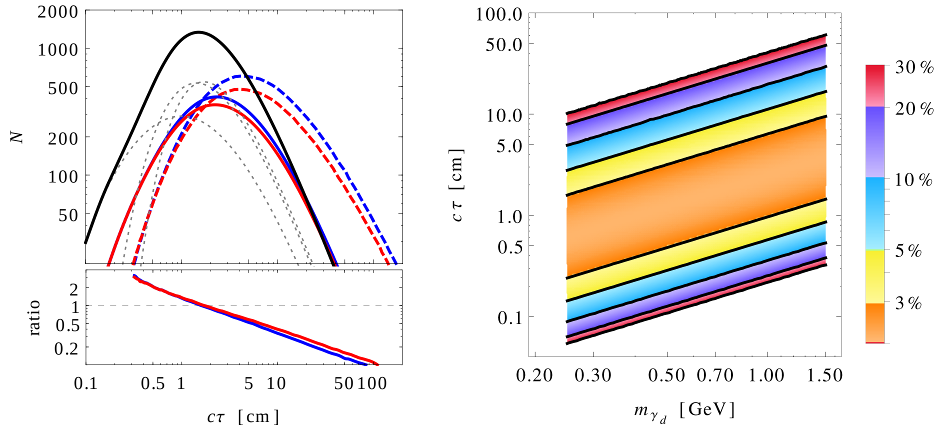

(A) (B)

FIGURE 2.9: (a) Predicted number of events in the lepton jet analysis assuming 100% Higgs branching, $m_{\gamma_d} = 400$ MeV, and $Br(\gamma_d \to \text{Type } 0) = 0.45$. Upper: the FRVZ model results from ATLAS (dashed) and our results (solid) for all event Types (blue/upper) and excluding Type 2-2 events (red/lower). Also shown are the number of events expected for the $h \to \gamma_d\gamma_d$ model in solid black; dotted curves beginning left-to-right show the break down in terms of Type 0-0, 0-2, 2-2 events respectively. Lower: the ratio of our FRVZ model results to those of ATLAS. (b) Excluded parameter region for γ_d assuming fixed $Br(h \to \gamma_d\gamma_d) \times Br(\gamma_d \to \mu\mu)^2$. The contours mark branchings of 30%, 20%, 10%, 5%, 3%.

to those of ATLAS as a function of $c\tau$ assuming 100% Higgs branching. The obtained ≈ 330 events at $c\tau = 4.7$ cm is an underprediction compared to the full simulation results of 600 ± 40, most likely due to the stricter barrel/endcap regions employed. For alternative lifetimes we cannot come up with a physical explanation that could account for the shape discrepancy between our curve and the reweighted result of ATLAS.[14]

Let us now attempt to reinterpret the ATLAS analysis for $h \to \gamma_d\gamma_d$ decays predicted by the vector portal model. A signal sample $gg \to h \to \gamma_d\gamma_d$ for $m_{\gamma_d} = 400$ MeV was generated in PYTHIA and fed through our analysis. Figure 2.9a shows the total number of events predicted as a function of $c\tau$, as well as broken down by event Type. More events are predicted than in the FRVZ model, and they peak at a lower $c\tau$, since on average the γ_d are more boosted. The 95% CL upper limit of ≈ 120 (≈ 30) on the total (total excluding Type 2-2) number of events can be inferred from the ATLAS plots. These numbers can be used along with Figure 2.9a to limit exotic Higgs branching fractions for $m_{\gamma_d} = 400$ MeV.

For alternative masses, since $E \gg m$, the properties of the simulated γ_d will

[14]It is not without careful consideration that we make this statement. Various possibilities were excluded, including effects of: the Monte Carlo generator; a bug in the code; applying each efficiency independently; and the stricter barrel/endcap region used. Instead, what we found was that the results were surprisingly robust to stricter/looser assumptions. Even a trip to La Sapienza Università di Roma to discuss with the ATLAS investigators could not resolve this discrepancy.

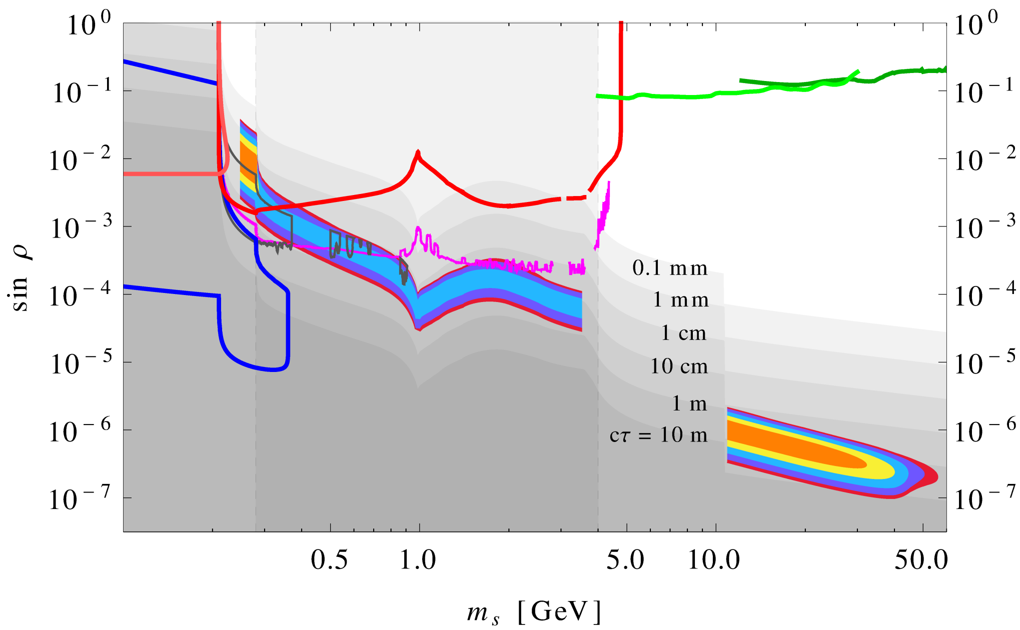

FIGURE 2.10: Exclusion plot for the real singlet scalar (Higgs) portal (see text). Incremental shadings mark areas of non-negligible lifetime. The coloured regions (this analysis) mark the exclusions assuming $Br(h \to ss) = 30\%, 20\%, 10\%, 5\%, 3\%$.

be approximately the same but for the boost $\gamma = E/m_{\gamma_d}$. If the efficiencies do not change significantly surrounding $m_{\gamma_d} = 400$ MeV, which according to ATLAS is at least a good assumption for $0.25 \lesssim m_{\gamma_d}/\text{GeV} \lesssim 1.5$ [239], then according to Equation (2.35) the number of events plotted as a function of $c\tau/m_{\gamma_d}$ remains invariant. Limits for alternative masses can be derived from the $m_{\gamma_d} = 400$ MeV results using this observation. In Figure 2.9b we present an example exclusion plot derived from Figure 2.9a in this way: the limit on $Br(h \to \gamma_d\gamma_d) \times Br(\gamma_d \to \mu\mu)^2$ as a function of m_{γ_d} and $c\tau$. This is also a good approximation for the limit on $Br(h \to ss) \times Br(s \to \mu\mu)^2$.

Exclusion regions

In Figure 2.10 we reinterpret the analyses of Section 3.3 within the real singlet scalar model.[15] The coloured regions mark the exclusion assuming $Br(h \to ss) = 30\%, 20\%, 10\%, 5\%, 3\%$. We remind the reader that within the region $2m_\pi < m_s \lesssim 4$ GeV the branching fractions and lifetimes are known to be uncertain by up to an order of magnitude. See Section 2.2.3 and Figure 2.4 for a description of the reproduced exclusion regions.

[15] An exclusion region also for the vector portal model can be found in our Ref. [4].

2.5.2 Discussion

Searching for the displaced decays of long-lived neutral states is a sensitive way to look for exotic Higgs physics. Already, searches at the LHC have probed branching fractions at the per cent level. The huge variety of BSM scenarios which predict these signatures demands a model-independent approach. However, unlike for prompt events, no public tool exists to simulate the detector response to displaced decays. Hence phenomenologists wanting to reinterpret displaced searches are reliant upon efficiencies provided by the collaborations. In general, the reconstruction efficiency for a long-lived particle will depend on its mass m, transverse momentum p_T, lab-frame decay length L, pseudorapidity η, and its decay mode. Ideally the phenomenologist would know the reconstruction efficiency as a function of all five of these parameters together,[16] and then the simple Monte Carlo method we have described in Section 3.3, requiring no simulation of displaced decays, could be used to determine the reconstruction probability for any event. In the interests of simplicity, the dependence on η is likely to be weak enough to be split into barrel and endcap regions, and then the reconstruction efficiencies could be provided as three-dimensional (m, p_T, L) functions for each final state in the barrel/endcap. In certain limits the dependence on one of these variables might even be removed. For example, in the limit $E \gg m$, the efficiency dependence on m for hadronic jets is expected to be weak. The trigger efficiency, defined as the probability of triggering given reconstruction, could subsequently be taken into account in a similar way.

2.6 Conclusion

In this Chapter we studied the phenomenological implications of extending the SM by a real singlet scalar, s, with mass 100 MeV $< m_s < m_h/2$, which mixes with the SM Higgs. We explored $(m_s, \sin\rho)$ parameter space, where ρ is the mixing angle.

The existing limits, derived in Section 2.2, are summarised in Figure 2.4. Fixed target experiments, B meson decays, and $Z \to Z^*h \to Z^* + hadrons$ searches at LEP1 set the most stringent limits in the regions $m_s < (m_K - m_\pi)$, $2m_\mu < m_s < m_B$, and $m_B < m_s < m_h/2$, respectively. These limits are enough to exclude the scale invariant benchmark model of Foot & Kobakhidze [159] for light scalar masses 100 MeV $< m_s <$ 10 GeV.

We also studied three phenomenologically distinct regions of parameter space at the LHC. For production at parton-level, we demonstrated that the subdominant Vs production channel has the best sensitivity at ATLAS/CMS for $m_s \gtrsim m_B$. The bound on $\sin^2\rho \times Br(s \to \mu^+\mu^-)$ from the Ws channel using

[16] Although it is only possible to provide a two-dimensional efficiency plot on paper, we see no reason why collaborations couldn't provide higher dimensional plots as an online resource.

4.6 fb^{-1} of $\sqrt{s} = 7$ TeV data was found to be stronger than those set by upsilon decays. This bound is still about two orders of magnitude weaker than that of LEP1, though it is conceivable that future LHC bounds could compete, with the main uncertainty being knowledge of the combinatoric background at $\sqrt{s} = 13$ TeV.

For $m_s \lesssim m_B$, s is dominantly produced at the LHC via the decay of B mesons, with a rate $\sim 10^6$ times larger than gluon fusion. In the region $\sin\rho \lesssim 10^{-3}$, s lifetime is non-negligible. We investigated the possibility of searching for displaced dimuons at ATLAS/CMS or at LHCb, showing that, in unexplored parameter space coinciding with the benchmark model of Bezrukov & Gorbunov [160], more than 10^3 potentially background free moderate p_T displaced decays (before efficiency factors) occur within the detector volumes. This motivates a search for displaced dimuons at ATLAS/CMS and/or LHCb.

Lastly, we considered the displaced decay regime of when s is pair-produced via Higgs decays $h \to ss$. We motivated a simple Monte Carlo method to reinterpret displaced searches utilising efficiency tables. Although the ideal set of efficiency tables were not provided for either of the ATLAS displaced searches considered, we were still able to demonstrate the principles of this Monte Carlo method, and we used it to constrain $(m_s, \sin\rho)$ parameter space for $Br(h \to ss)$ at the per cent level. Our hope is that this inspires the following take-home message regarding displaced searches: if the relevant multidimensional efficiency tables are provided, then phenomenologists will be able to reinterpret searches in the context of their own models.

3 Naturalness

This Chapter is based on the preprint "Naturalness made easy: two-loop naturalness bounds on minimal SM extensions," written in collaboration with Peter Cox [11].

The Standard Model (SM) appears to represent a very good effective field theory (EFT) for energies at least $\lesssim$ TeV. Still, it has several well known theoretical and phenomenological shortcomings, e.g. neutrino masses, dark matter, and the baryon asymmetry of the Universe. It is possible to address these shortcomings with minimal extensions of the SM by heavy fermionic and/or scalar gauge multiplets (GMs). However, the Higgs mass parameter $\mu^2(m_Z) \approx -(88\,\text{GeV})^2$, appearing in the SM potential $\mu^2 H^\dagger H + \lambda(H^\dagger H)^2$, is sensitive to such heavy new physics; GMs couple (at the very least) at loop level to the SM Higgs, thereby inducing corrections to the Higgs mass and potentially introducing a naturalness problem.

The subject of naturalness in the modern literature is rife with various (and often conflicting) definitions. Let us therefore, at the outset, state the definition used in this Chapter: *a parameter in a quantum field theory is "natural" if its measured value at low scale is (sufficiently) insensitive to details of the physics at high scale*. Plainly, then, to examine naturalness of the Higgs mass parameter we require: (1) a description of the low scale physics; (2) a description of the high scale physics; (3) a map which relates them; and (4) a measure which quantifies sensitivity of $\mu^2(m_Z)$ to the high scale physics.

In this Chapter we confront the question, *at what mass does a heavy GM introduce a physical Higgs naturalness problem?* Vector-like fermionic and scalar GMs of various charges are studied. We advocate a renormalisation group (RG) approach to naturalness. The description of the low (high) scale physics is provided by the $\overline{\text{MS}}$ Lagrangian parameters of the SM (SM+GM) EFT defined at the scale m_Z (Λ_h), and the map which relates them is the set of RG equations (RGEs). We employ a sensitivity measure which can be interpreted as a Bayesian model comparison. Bayesian approaches to naturalness have previously been considered in the literature [275–287]. We propose a particular model comparison, which captures the "naturalness price" paid for promoting the Higgs mass parameter from a purely phenomenological input parameter at low scale to a high scale input parameter of the model. We show that this sensitivity measure then reduces in a well-motivated limit to a Barbieri–Giudice-like [288, 289] fine-tuning measure.

Quantifying and bounding this sensitivity results in naturalness bounds on the masses of the various GMs.

The Chapter is organised as follows. In Section 3.1 we describe an intuitive and physical concept of naturalness built upon the RGEs, and the sensitivity measure as a Bayesian model comparison. In Section 3.2 we describe how this concept is applied to the SM+GM EFTs. Our main result is a list of naturalness bounds presented in Section 3.3. These results are discussed in Section 3.4, and we conclude in Section 3.5.

3.1 Physical Naturalness

In this section we describe a physical way to understand the Higgs naturalness problem, especially pertinent in the context of bottom-up extensions of the SM. To frame the discussion, let us appeal to an illuminating toy model.

3.1.1 Toy model

Consider a perturbative EFT consisting of the SM plus a heavy particle of mass M (whose mass is obtained independently of electroweak symmetry breaking). The μ^2 RGE valid at a renormalisation scale $\mu_R > M$ takes the form

$$\frac{d}{d\log\mu_R}\mu^2(\mu_R) = C_1(\mu_R)\mu^2(\mu_R) + C_2(\mu_R)M^2(\mu_R)\,, \tag{3.1}$$

where $C_1(\mu_R) \simeq 6y_t(\mu_R)/(4\pi)^2$, with y_t the top quark Yukawa coupling. The quantity $C_2(\mu_R)$ might be comprised of SM and/or beyond-SM couplings. The RGEs allow μ^2 (and other low scale parameters) to be extrapolated to a high scale Λ_h, at most up to the scale at which the EFT is no longer valid. At Λ_h, these renormalised parameters can be interpreted as "input parameters" which might be derived from even higher scale physics. The input parameters are, by construction, connected with the low energy parameters via the RGEs. If the low energy parameters are very sensitive to these input parameters, then this signifies a naturalness problem.

Let us now, under this paradigm, try to understand when a heavy particle introduces a Higgs naturalness problem. One can fully solve Equation (3.1) in the limit where C_1, C_2, and M^2 have no scale dependence. Including a possible threshold correction, $\mu_+^2(M) = \mu_-^2(M) - C_T M^2$, when the SM EFT parameters $(-)$ are matched onto the full EFT parameters $(+)$ at the threshold M, and in the limit $C_1\log(\Lambda_h/m_Z) \ll 1$,

$$\mu^2(m_Z) \simeq\; \mu^2(\Lambda_h) - \Theta(\Lambda_h - M)\left[C_2 M^2 \log\left(\frac{\Lambda_h}{M}\right) - C_T M^2\right], \tag{3.2}$$

where Θ is the step function. It is now easy to see when a naturalness problem arises. If either of $C_2 M^2$ or $C_T M^2$ is $\gg \mu^2(m_Z)$, then the input parameter $\mu^2(\Lambda_h)$

must be finely tuned against a very large contribution in order to realise the observed Higgs mass. A small change in $\mu^2(\Lambda_h)$ ruins this cancellation, and thus the Higgs mass is unnatural, i.e. it is sensitive to details of the high scale physics. Note that the $C_2 M^2$ piece captures a steep $\mu^2(\mu_R)$ RG trajectory, whereby only a very particular input $\mu^2(\Lambda_h)$ will lead to the observed low scale $\mu^2(m_Z)$; a small change in this value leads to significant over- or under-shooting.

In this picture, the Higgs naturalness problem is cast in terms of a potential sensitivity between *measurable* parameters (as opposed to a large cancellation between an unmeasurable bare mass and an unphysical cutoff contribution), connected by fully calculable (in a perturbative theory) RG trajectories and matching conditions.[1]

3.1.2 Sensitivity measure

To actually quantify the sensitivity to high scale physics is somewhat arbitrary and subjective. There are many approaches in the literature. In this Chapter we will adopt a sensitivity measure which can be interpreted as a Bayesian model comparison, and which reduces (in the cases we consider) to an intuitively motivated Barbieri–Giudice-like [288, 289] fine-tuning measure. We provide below a short description; more details can be found in Appendix A.1.

Assuming a flat prior belief in the high scale input parameters $\mathcal{I} = (\mathcal{I}_1, \ldots, \mathcal{I}_n)$, and a perfectly measured set of $m \leq n$ independent observables $\mathcal{O} = (\mathcal{O}_1, \ldots, \mathcal{O}_m)$, the Bayesian evidence B for a model $\mathcal{M}$ is a function of the unconstrained input parameters $\mathcal{I}' = (\mathcal{I}_{m+1}, \ldots, \mathcal{I}_n)$:

$$B(\mathcal{M}; \mathcal{I}') \propto \left. \frac{1}{\sqrt{|JJ^T|}} \right|_{\substack{\mathcal{O}_{ex} \\ \mathcal{I}'}} , \tag{3.3}$$

where J is the $m \times n$ matrix defined by $J_{ij} = \partial \mathcal{O}_i / \partial \mathcal{I}_j$ [283]. Let us take, for model $\mathcal{M}$, $\mathcal{I}_1 = \log \mu^2(\Lambda_h)$ and $\mathcal{O}_1 = \log \mu^2(m_Z)$. The logarithms here ensure that our result is independent with respect to units or parameter rescalings (absolute values are implied for the argument of any $\log$ and dimensionful parameters can be normalised by any unit). Our Higgs mass sensitivity measure arises from a particular Bayesian model comparison: we compare to a model $\mathcal{M}_0$ in which we instead take $\mathcal{I}_1 = \mathcal{O}_1 = \log \mu^2(m_Z)$, i.e. the Higgs mass parameter is considered as an input parameter at scale m_Z. The sensitivity measure can then be written as a function of the unconstrained parameters,

$$\Delta(\mathcal{M}; \mathcal{I}') = \frac{B(\mathcal{M}_0; \mathcal{I}')}{B(\mathcal{M}; \mathcal{I}')} . \tag{3.4}$$

This measure captures the "naturalness price" paid for promoting the Higgs mass parameter to a high scale input parameter of the model as opposed to a

[1] See Refs. [290–299] for similar naturalness philosophies.

purely phenomenological input parameter at low scale. In our context, a large value of Δ essentially tells us that, given a flat prior density in $\log \mu^2(\Lambda_h)$, the observed value $\mu^2(m_Z)$ is unlikely [specifically with respect to a flat probability density in $\log \mu^2(m_Z)$], i.e. $\mu^2(m_Z)$ is sensitive to the realised input parameters. In the special case that the low scale observables, except for possibly $\mu^2(m_Z)$, are approximately insensitive to the unconstrained inputs, $B(\mathcal{M}_0; \mathcal{I}')$ becomes independent of $\mathcal{I}'$ and Equation (3.4) reduces to

$$\Delta(\mathcal{M}; \mathcal{I}') \simeq \sqrt{\left(\frac{\partial \log \mu^2(m_Z)}{\partial \log \mu^2(\Lambda_h)}\right)^2 + \sum_{j \geq m+1} \left(\frac{\partial \log \mu^2(m_Z)}{\partial \mathcal{I}_j}\right)^2}\Bigg|_{\substack{\mathcal{O}_{ex} \\ \mathcal{I}'}} . \tag{3.5}$$

In the absence of unconstrained inputs ($n = m$) the summation disappears and the equality is exact. This is clearly reminiscent of the Barbieri–Giudice fine-tuning measure. A value of $\Delta = 10$ can now be interpreted as the onset of strong Bayesian evidence (for $\mathcal{M}_0$ over $\mathcal{M}$) on the Jeffreys scale [300], or a 10% fine-tuning from the Barbieri–Giudice perspective.

Notice here that we have a sensitivity measure which depends on unconstrained inputs. It might be that we want to "project out" some of these nuisance parameters. In this Chapter we will minimise over them, which picks out a conservative best case naturalness scenario in the model. Our SM+GM models $\mathcal{M}$ are defined by $\overline{\text{MS}}$ inputs at the high scale Λ_h, with the renormalised mass parameter $M^k(\Lambda_h) \subset \mathcal{I}'$ [and $k = 1$ (2) in the fermionic (scalar) case]. We minimise over all unconstrained parameters apart from $M^k(\Lambda_h)$ to obtain a sensitivity measure which depends only on M and Λ_h:

$$\Delta(M, \Lambda_h) = \min_{\mathcal{I}' \setminus \{M^k(\Lambda_h)\}} \left[\Delta(\mathcal{M}; \mathcal{I}')\right] . \tag{3.6}$$

In practice we minimise over Equation (3.5), which is now valid under the looser criterion that the low scale observables, except for possibly $\mu^2(m_Z)$, are approximately insensitive to the unconstrained inputs in the vicinity of the minimum.

This all may sound rather abstract. Let us now check that, in the relevant cases, the sensitivity measure Equation (3.6) captures the sensitivity we expect in our toy model when $C_2 M^2, C_T M^2 \gg \mu^2(m_Z)$.

3.1.3 Fermion-like case

In the minimal fermionic SM+GM there are no new dimensionless parameters; C_2 is fully constrained by experiment so that $\mathcal{O}_i = \{\log \mu^2(m_Z), \log C_1, \log C_2\}$ and $\mathcal{I}_j = \{\log \mu^2(\Lambda_h), \log C_1, \log C_2, \log M\}$. It is easy to show directly from Equation (3.4) that, even allowing for possible $C_{1,2}$ correlation $\partial \log C_1 / \partial \log C_2 \neq$

0,

$$\Delta(M, \Lambda_h) = \sqrt{\left(\frac{\partial \log \mu^2(m_Z)}{\partial \log \mu^2(\Lambda_h)}\right)^2 + \left(\frac{\partial \log \mu^2(m_Z)}{\partial \log M}\right)^2}. \tag{3.7}$$

This is just a Barbieri–Giudice-like fine-tuning measure comparing percentage changes in the low scale Higgs mass parameter to those in the input parameters. In the limit $C_1 \log(\Lambda_h/m_Z) \ll 1$ and taking $\Lambda_h > M$, we see that $\Delta(\Lambda_h)$ is made up of two pieces:

$$\begin{aligned} \left|\frac{\partial \log \mu^2(m_Z)}{\partial \log \mu^2(\Lambda_h)}\right| &= \left|1 + \frac{C_2 M^2}{\mu^2(m_Z)} \log\left(\frac{\Lambda_h}{M}\right) - \frac{C_T M^2}{\mu^2(m_Z)}\right|, \\ k\left|\frac{\partial \log \mu^2(m_Z)}{\partial \log M^k}\right| &= \left|\frac{C_2 M^2}{\mu^2(m_Z)}\left[2\log\left(\frac{\Lambda_h}{M}\right) - 1\right] - 2\frac{C_T M^2}{\mu^2(m_Z)}\right|. \end{aligned} \tag{3.8}$$

The "1" piece is the SM contribution, the $\log(\Lambda_h/M)$ pieces reflect sensitivity to the RG trajectory (with slope $C_2 M^2$), the $C_T M^2$ piece is due to the finite threshold correction, and the log-independent $C_2 M^2$ piece arises because a variation in $\log M$ results in a shift in the matching scale, which reintroduces a small amount of RG evolution. Clearly $\Delta \gg 1$ if $C_2 M^2$ or $C_T M^2$ is $\gg \mu^2(m_Z)$, as expected. This even holds in the limit where the high scale approaches the heavy particle mass, $\Lambda_h \to M^+$.

In the fermionic SM+GM EFT at two-loop order with one-loop matching, we have

$$C_2 \sim \frac{g^4}{(4\pi)^4}, \qquad\qquad C_T = 0, \tag{3.9}$$

where g is a placeholder for a gauge coupling(s). It is interesting to note that in the limit $\Lambda_h \to M^+$, Equation (3.7) just becomes

$$\Delta(M^+) = \sqrt{1 + \left(\frac{C_2(M) M^2}{\mu^2(m_Z)}\right)^2}. \tag{3.10}$$

If we bound this sensitivity measure by Δ_{max}, this is almost equivalent to simply bounding the contribution to the $\mu^2(\mu_R)$ RGE in Equation (3.1) at the scale $\mu_R = M$, i.e. $C_2(M)M^2 \lesssim \Delta_{max}\mu^2(m_Z)$. This is not an uncommon practice as a zeroth-order naturalness bound for M.

There is one case we wish to comment on here: the special case where $C_2(M)$ happens to vanish, somewhat reminiscent of the Veltman condition [301]. In this case there is plainly no naturalness bound on M from the $\Delta(M^+)$ measure we have written above, no matter the size of M. So it appears that there is a fine-tuning which is not captured by our framework in this limit. Is this indeed the case? One can show that extending this toy model to include RG evolution of C_2

is not enough to reintroduce the naturalness bound (we will see this in our numerical analysis). Instead, it turns out that this apparent "Veltman throat" is only a limitation of the order to which we are working. In the fermionic SM+GM EFT with *two*-loop matching, C_T becomes a non-zero function of the gauge couplings. In general $C_T(M) \neq 0$ when $C_2(M) = 0$, and thus a sensitivity proportional to M^2 and powers of gauge couplings is recaptured at this special value of M. In any case, we do not attribute much physical significance to this special case; in the full model, even if $C_2(M) = 0$, RG effects reinstate $C_2(\mu_R) \neq 0$ at $\mu_R > M$, and the sensitivity of $\mu^2(m_Z)$ to M^2 is *rapidly* recaptured in the realistic case with $\Lambda_h > M$.

3.1.4 Scalar-like case

Let us first consider the SM plus scalar GM case with only one portal quartic $\lambda_{H1}(H^\dagger H)(\Phi^\dagger \Phi)$ and one self quartic $\lambda_\Phi(\Phi^\dagger\Phi)(\Phi^\dagger\Phi)$. This occurs whenever the scalar is an $SU(2)$ singlet. At two-loop with one-loop matching, we have

$$C_2 = C_2^{SM} + 2Q_3 \frac{\lambda_{H1}}{(4\pi)^2} + \ldots, \qquad\qquad C_T = Q_3 \frac{\lambda_{H1}}{(4\pi)^2}, \tag{3.11}$$

where $C_2^{SM} \sim g^4/(4\pi)^4$, and (Q_1, Q_2, Q_3) are the $(U(1)_Y, SU(2), SU(3))$ charges of the GM. Assuming for simplicity no RG evolution of these parameters, we have $\mathcal{O}_i = \{\log \mu^2(m_Z), \log C_1, \log C_2^{SM}\}$ and $\mathcal{I}_j = \{\log \mu^2(\Lambda_h), \log C_1, \log C_2^{SM},$ $\log \lambda_{H1}, \log \lambda_\Phi, \log M^2\}$. The sensitivity measure, assuming C_1 and C_2^{SM} are insensitive to changes in λ_{H1} and λ_Φ, is given by

$$\Delta(M, \Lambda_h) = \min_{\lambda_1} \left[\sqrt{ \left. \begin{array}{l} \left(\frac{\partial \log \mu^2(m_Z)}{\partial \log \mu^2(\Lambda_h)}\right)^2 + \left(\frac{\partial \log \mu^2(m_Z)}{\partial \log M^k}\right)^2 \\ + \left(\frac{\partial \log \mu^2(m_Z)}{\partial \log \lambda_1}\right)^2 \end{array} \right|_{\lambda_1} } \right], \tag{3.12}$$

where we have ignored the subdominant $\partial/\partial \log \lambda_\Phi$ term for clarity. Before minimisation, the contribution of the first two terms under the square root are exactly those in Equation (3.8). Note that the $C_2 M^2$ contributions are removed if λ_{H1} takes the fortuitous value $-(4\pi)^2 C_2^{SM}/(2Q_3)$, however the $C_T M^2$ contributions remain. Conversely, $\lambda_{H1} = 0$ removes the threshold correction contributions, leaving non-vanishing $C_2 M^2$ contributions. Thus it seems that, even with the extra freedom granted by λ_{H1}, one cannot remove the naturalness problem. Indeed, the minimisation over λ_{H1} can be performed analytically in this toy model. The result is rather lengthy, and we do not reproduce it here. It is anyway not terribly illuminating, since this toy model is too strong of an oversimplification to reflect the full scalar SM+GM case when $\Lambda_h \gg M$; pure gauge contributions in the $\lambda_{H1}(\mu_R)$ RGE which destabilise any fortuitous cancellation for $C_2(\mu_R) = 0$ must be taken into account. Nevertheless, the toy model result can serve as an argument for the existence of a finite naturalness bound even in the limit $\Lambda_h \to M^+$, where we obtain

$$\Delta(M^+) = \sqrt{\frac{1}{12}\left[10 + 4\frac{C_2^{SM}M^2}{\mu^2(m_Z)} + \left(\frac{C_2^{SM}M^2}{\mu^2(m_Z)}\right)^2\right]}, \tag{3.13}$$

if $C_1 \log(\Lambda_h/m_Z) \ll 1$. Again, clearly $\Delta \gg 1$ when $C_2^{SM}M^2 \gg \mu^2(m_Z)$, as expected. If we bound this sensitivity measure by $\Delta(M^+) < \Delta_{max}$, this is approximately equivalent to $C_2^{SM}(M)M^2/\sqrt{12} \lesssim \Delta_{max}\mu^2(m_Z)$.

The scalar $SU(2)$ doublet or triplet SM+GM EFT case with two portal quartic couplings is more delicate. At two-loop with one-loop matching we have

$$C_2 = C_2^{SM} + 2Q_3Q_2\frac{\lambda_{H1}}{(4\pi)^2} - 24Q_3\frac{\lambda_{H2}^2}{(4\pi)^4} + \dots, \qquad C_T = Q_3Q_2\frac{\lambda_{H1}}{(4\pi)^2}, \tag{3.14}$$

where $\lambda_{H1,2}$ will be defined in Section 3.2.2. There is now enough freedom for a minimisation analogous to Equation (3.12) to select $\lambda_{H1,2}$ such that $C_2 = 0$ and $C_T = 0$ simultaneously, removing the sensitivity of $\mu^2(m_Z)$ to M^2. Still, in the realistic case including RG effects beyond our toy model, $C_2 \neq 0$ and $C_T \neq 0$ will be reinstated at $\mu_R > M$, and $\Delta(\Lambda_h)$ with $\Lambda_h > M$ will sensibly capture the $\mu^2(m_Z)$ sensitivity to M^2. A question remains as to whether $\Delta(M^+)$ acts sensibly in this scenario. Is it possible to choose $\lambda_{H1,2}(M)$ such that $C_2(M) = 0$ and $C_T(M) = 0$ and the relevant terms $\propto M^2$ in Equation (3.8) vanish? Indeed, it is possible. However, once RG effects are included, this is not sufficient to minimise $\Delta(M^+)$. In particular, $dC_T/d\log\mu_R$ will generally be non-zero, leading to an extra term in the $\partial/\partial\log M^2$ sensitivity measure:

$$\lim_{\Lambda_h\to M^+}\left|\frac{\partial\log\mu^2(m_Z)}{\partial\log M^2}\right| = \frac{1}{2}\left|\frac{M^2}{\mu^2(m_Z)}\left(C_2(M) + 2C_T(M) + \left.\frac{dC_T}{d\log\mu_R}\right|_{\mu_R=M}\right)\right|. \tag{3.15}$$

The extra term can be thought of as arising from a shift in the matching scale. If $\lambda_{H1}(M) = 0$ is chosen so that $C_T(M) = 0$ in order to minimise the $\partial/\partial\log\mu^2(\Lambda_h)$ sensitivity, the full sensitivity measure is no longer minimised for $C_2(M) = 0$. Instead, one would like to set $[C_2(M) + dC_T/d\log\mu_R|_{\mu_R=M}] = 0$. However, $dC_T/d\log\mu_R|_{\mu_R=M}$ is itself a function of $\lambda_{H1,2}$ (and gauge couplings), thus it is not guaranteed that this is possible. Indeed, in the cases we explore, it is not; remarkably, $dC_T/d\log\mu_R|_{\mu_R=M} \supset +24Q_3\lambda_{H2}^2/(4\pi)^4$, which cancels the negative contribution in Equation (3.14) and leaves $[C_2(M) + dC_T/d\log\mu_R|_{\mu_R=M}]$ positive for any value of $\lambda_{H2}(M)$ when $\lambda_{H1}(M) = 0$.[2] Our numerical study captures this, and we always recover a sensible value for $\Delta(M^+)$.

[2]The reader might wonder if this is just a convenient happenstance. It is possible. However, we note that extending to three-loop RGEs with two-loop matching, this objection becomes moot. At higher loop matching the threshold correction will generally become a function of both λ_{H1} and λ_{H2}. The $\partial/\partial\log\mu^2(\Lambda_h)$ sensitivity is minimised for $C_T(M) = 0$. However, $\partial/\partial\log\lambda_{H1,2}(\Lambda_h)$ terms also appear in the full sensitivity measure. The simultaneous vanishing of these terms is in

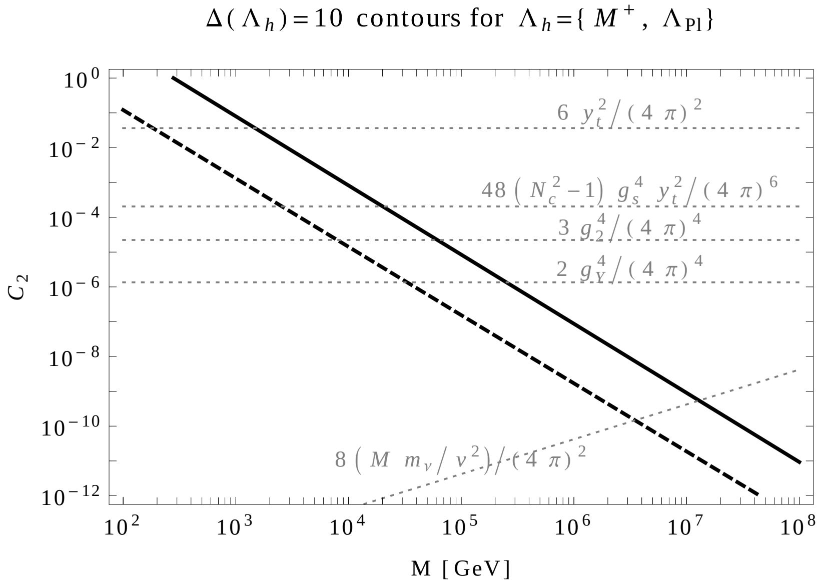

FIGURE 3.1: $\Delta(M, \Lambda_h) = 10$ contours for $\Lambda_h = M^+$ (solid), or $\Lambda_{Pl} \sim 10^{19}$ GeV (dashed). Also shown as gray dotted lines are approximate C_2 contours for some benchmark heavy particles. The results for negative values of C_2 are very similar.

Much of the discussion here has only been of technical interest since we have chosen to project out our unknowns by minimising the sensitivity measure over them. Clearly the possibility of a miraculous cancellation is not the generic case, and such cancellations are anyway quickly violated in the realistic scenario with RG effects and $\Lambda_h > M$. Nevertheless we find it interesting that, in this framework (and even in the limit $\Lambda_h \to M^+$ limit), there is a certain amount of $\mu^2(m_Z)$ sensitivity which cannot be made to go away by a judicious choice of quartic couplings.

3.1.5 Naturalness bounds

Naturalness bounds can be derived simply by bounding the sensitivity measure Equation (3.6). In Figure 3.1 we show the $\Delta(\Lambda_h) = 10$ contours for $\Lambda_h = M^+$, or $\Lambda_{Pl} \sim 10^{19}$ GeV in our fermion-like toy model Equation (3.7). Points in parameter space below these lines can be considered natural, and points above increasingly unnatural.

Figure 3.1 can be used to estimate naturalness bounds on the masses of fermionic particles. Consider for example a heavy fermion with a top-like coupling strength such that $C_2 = 6y_t^2/(4\pi)^2$; taking $y_t^2 = y_t^2(m_Z) \approx 0.96$ and reading across one finds a naturalness bound $M \lesssim$ TeV. For a right-handed neutrino involved in a Type I see-saw, $C_2 = 4y_\nu^2/(4\pi)^2$ with $y_\nu^2 \simeq Mm_\nu/(174\,\text{GeV})^2$; taking

general only guaranteed if $\lambda_{H1}(M) = \lambda_{H2}(M) = 0$. Plainly this restriction is too severe to absorb sensitivity arising elsewhere.

$m_\nu = 0.05$ eV results in a naturalness bound $M \lesssim 10^7$ GeV [3, 302].[3] The reason that this naturalness bound is so large is simply because C_2 is so small. Indeed, in the limit $C_2 \to 0$ there is no naturalness bound on M. In models with gauge singlets, $C_2 \to 0$ can correspond to a technically natural limit [36, 37] associated with decoupling of the particle from the SM fields. It makes sense that there is no Higgs naturalness bound on the mass of such a particle, given that in this limit the heavy particle can no longer "talk" to the Higgs at all.

The focus of this Chapter will be Higgs naturalness within the EFT of the SM plus a heavy GM. For fermionic GMs with $SU(3)$, $SU(2)$, or $U(1)_Y$ charge Q_3, Q_2, or Q_1, the leading pure gauge contributions to C_2 are $-2Q_1^2 g_1^4/(4\pi)^4$, $-\frac{1}{2}Q_2(Q_2^2-1)g_2^4/(4\pi)^4$, and $+48(N_C^2-1)g_3^4 y_t^2/(4\pi)^6$, respectively. Taking $g_1^2 \approx 0.13$, $g_2^2 \approx 0.43$, and $g_3^2 \approx 1.48$, these correspond to rough naturalness bounds of (perhaps surprisingly to some) tens to hundreds of TeV, as sketched in Figure 3.1. The size of the mass bounds is just a reflection of the smallness of $g^4/(4\pi)^4$. The main purpose of this Chapter is to derive these bounds more rigorously; we perform a full two-loop analysis to examine the effects of adding various (vector-like) fermionic and scalar GMs to the SM. The above naturalness bound approximations turn out to be quite good for the fermionic GMs, but they significantly deviate for scalar gauge multiplets, since these always couple directly to the Higgs via a quartic term(s). As already indicated, sensitivity to the RG evolved quartics must be properly taken into account.

3.1.6 Comment on the Planck-weak hierarchy

Before leaving this section, we want to comment on how the Planck-weak hierarchy fits into in this picture. From Equations (3.2) and (3.5), one can see that $\Delta \simeq 1$ in the pure SM limit, i.e. there is no enhanced sensitivity when the Higgs mass is promoted to a high scale input parameter. This should come as no surprise, since the only explicit scale in the SM is μ^2 itself: the value $\mu^2(\Lambda_h)$ is multiplicatively related to the value $\mu^2(m_Z)$ and remains electroweak scale up to high scales.[4] Indeed, the effective Higgs potential remains consistent (albeit metastable) even up to the very highest scale to which the SM can be valid: $\Lambda_{Pl} \sim 10^{19}$ GeV. Now, it could be that gravity introduces large and physical corrections to $\mu^2(\mu_R)$ [or some related parameter(s)] at or below this scale. However, without a complete theory of quantum gravity, we cannot calculate these corrections. This picture therefore claims that the SM with inputs at Λ_{Pl} is natural, in the sense that the low-energy observable $\mu^2(m_Z)$ is not extremely sensitive to the input $\mu^2(\Lambda_{Pl})$. In such a case, one could sensibly ask: why is $\mu^2(\Lambda_{Pl}) \ll \Lambda_{Pl}^2$? We do not address

[3] This is not quite the correct thing to do, since the observable at low scale is m_ν and not C_2 [which was assumed to derive Equation (3.8)]. Rest assured that using the appropriate sensitivity measure derived from Equation (3.4) only marginally changes this picture.

[4] For the SM at two-loop we find $\mu^2(\Lambda_{Pl}) \simeq -(94\text{ GeV})^2$ and $\Delta(\Lambda_{Pl}) \simeq 1$ to one part in 10^6.

this problem. By construction our sensitivity measure remains agnostic to this input value by assuming a flat prior in $\log \mu^2(\Lambda_{Pl})$. Of course, as we have argued, the presence of a heavy gauge multiplet *can introduce a calculable and physical naturalness problem irrespective of the situation with gravity*, and this is the problem that we study. In such models a flat prior belief in $\log \mu^2(\Lambda_h)$ devolves to a low scale posterior belief which favours $\mu^2(m_Z) \gtrsim C_2 M^2$. It could be that gravity behaves in a similar way, but we cannot yet perform the calculation.

3.2 Method

The main purpose of this Chapter is to derive and present naturalness bounds on the masses of GMs within SM+GM EFTs valid up to scale Λ_h. In Section 3.1 we motivated a general procedure for determining these bounds: take the low energy observables at m_Z, evolve them under the RGEs to the scale Λ_h, then evaluate and bound the sensitivity measure Equation (3.4). Presently we detail our method. We use sets of two-loop RGEs generated using a modified version of PYR@TE [303].

The low scale observables are taken as the logarithms of SM $\overline{\text{MS}}$ Lagrangian parameters at scale m_Z: $\exp(\mathcal{O}_i) = \{\mu^2(m_Z),\ \lambda(m_Z),\ g_1(m_Z),\ g_2(m_Z),\ g_3(m_Z),\ y_t(m_Z),\ y_b(m_Z),\ y_\tau(m_Z)\} = \{-(88\,\text{GeV})^2,\ 0.13,\ 0.36,\ 0.66,\ 1.22,\ 0.96,\ 0.017,\ 0.010\}$. For simplicity we ignore the Higgs and the top quark thresholds. The high scale input parameters are taken as the logarithms of the minimal set of SM+GM $\overline{\text{MS}}$ Lagrangian parameters at scale Λ_h (to be explicitly listed in the following subsections); by minimal we mean that terms in the SM+GM Lagrangian which can be set to zero in a technically natural way are not included. The observables are numerically evolved under the two-loop SM RGEs up to the threshold of the GM, $\mu_R = M$, where we perform one-loop matching onto the parameters of the SM+GM EFT. The mass parameter for the GM is also a renormalised $\overline{\text{MS}}$ parameter, which we set equal to M at the scale $\mu_R = M$.[5] New parameters are introduced in the case of a scalar GM; these are left as free parameters which are numerically minimised over when evaluating the sensitivity measure. The two-loop SM+GM RGEs are used to evolve all parameters up to the high scale Λ_h. The approximation to the full sensitivity measure, Equation (3.5), is then evaluated numerically by varying the appropriate input parameters around their values at Λ_h, evolving all parameters back down to the scale m_Z, matching the SM+GM EFT onto the SM EFT at the matching scale μ_R given by $M(\mu_R) = \mu_R$, and measuring the change in the Higgs mass parameter.

[5]The bounds we present are therefore bounds on the parameter M (i.e. the $\overline{\text{MS}}$ mass of the GM at the scale M), not the pole mass.

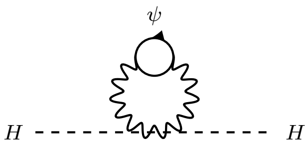

(A) (g_1^4, g_2^4) corrections.

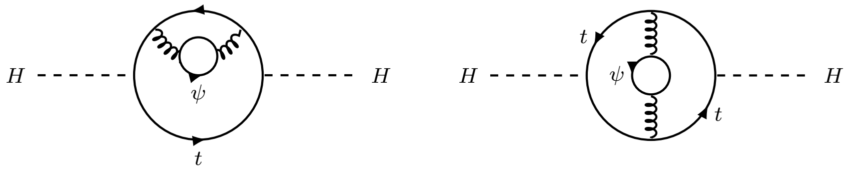

(B) $g_3^4 y_t^2$ corrections.

FIGURE 3.2: Corrections to μ^2 from a heavy vector-like fermion.

3.2.1 Vector-like fermion

The minimal SM+GM Lagrangian for a vector-like fermion is that of the SM plus

$$\Delta\mathcal{L} = \bar{\psi} D^\nu \gamma_\nu \psi - M\bar{\psi}\psi. \tag{3.16}$$

The high scale input parameters of this model are those of the SM plus the renormalised parameter $M(\Lambda_h)$, i.e. $\mathcal{I}_j = \{\mu^2(\Lambda_h),\ \lambda(\Lambda_h),\ g_1(\Lambda_h),\ g_2(\Lambda_h),\ g_3(\Lambda_h),$ $y_t(\Lambda_h), y_b(\Lambda_h), y_\tau(\Lambda_h), M(\Lambda_h)\}$. The one-loop matching conditions are trivial,

$$\mu_+^2(\mu_R) = \mu_-^2(\mu_R)\ , \qquad\qquad \lambda_+(\mu_R) = \lambda_-(\mu_R)\ , \tag{3.17}$$

where the $+$ $(-)$ subscript denotes the SM+GM (SM) EFT parameter.

The $\mu^2(\mu_R)$ RGE takes the form of Equation (3.1) with $C_2(\mu_R)$ a function of SM parameters. Recall that it is primarily the $C_2(\mu_R)$ term which leads to a potential naturalness problem, as argued in Section 3.1.1 for constant C_2. In the vector-like fermionic SM+GM EFT it takes the form

$$C_2 = -2Q_3Q_2Q_1^2\frac{g_1^4}{(4\pi)^4} - \frac{1}{2}Q_3Q_2(Q_2^2-1)\frac{g_2^4}{(4\pi)^4} + 96Q_2(N_c^2-1)c(r_\psi)\frac{g_3^4y_t^2}{(4\pi)^6}, \tag{3.18}$$

where $c(r_\psi) = \frac{1}{2}$ (3) for $Q_3 = 3\,(8)$, and dependence on scale μ_R is implied. Representative diagrams leading to these terms are shown in Figure 3.2. Note that we have added by hand the leading three-loop $SU(3)$ correction, arising from three diagrams [see Figure 3.2b], since otherwise the two-loop RGEs do not capture any $SU(3)$ correction beyond multiplicity factors.[6] This correction turns out to be competitive with the two-loop pure gauge corrections at scales $\mu_R \lesssim 10^5$ GeV due to the relatively large couplings g_3 and y_t below this scale. It is also opposite in sign, thus potentially delaying the growth of $\mu^2(\mu_R)$ (and the

[6]This three-loop correction was calculated with the aid of MATAD [304].

corresponding naturalness problem) if it happens to approximately cancel with the other gauge contributions.

There are no unconstrained high scale dimensionless inputs to minimise over, so the sensitivity measure Equation (3.5) is just

$$\Delta(M, \Lambda_h) = \sqrt{\left(\frac{\partial \log \mu^2(m_Z)}{\partial \log \mu^2(\Lambda_h)}\right)^2 + \left(\frac{\partial \log \mu^2(m_Z)}{\partial \log M(\Lambda_h)}\right)^2}. \tag{3.19}$$

Results are obtained by numerically evaluating $\Delta(M, \Lambda_h)$ at points of interest in (M, Λ_h) space.

3.2.2 Complex scalar

The minimal SM+GM Lagrangian for a complex scalar is that of the SM plus

$$\Delta\mathcal{L} = D^\nu \Phi^\dagger D_\nu \Phi - \left(M^2 \Phi^\dagger \Phi + \sum \lambda_{\Phi i} \Phi^\dagger \Phi \Phi^\dagger \Phi + \sum \lambda_{Hj} H^\dagger H \Phi^\dagger \Phi\right), \tag{3.20}$$

where H is the SM Higgs field, and the sums are over all possible contractions. Explicitly, we take the following convenient contractions for the portal quartics

$$\Delta\mathcal{L} \supset \lambda_{H1} H^\dagger H \,\mathrm{Tr}(\Phi^\dagger \Phi) + \lambda_{H2} \left(2\,\mathrm{Tr}(H^\dagger \Phi \Phi^\dagger H) - H^\dagger H \,\mathrm{Tr}(\Phi^\dagger \Phi)\right), \tag{3.21}$$

where the second term is relevant only for $Q_2 \geq 2$. The high scale input parameters of the model are those of the SM plus the extra self and portal quartics and renormalised mass parameter, i.e. $\mathcal{I}_j = \{\mu^2(\Lambda_h), \lambda(\Lambda_h), g_1(\Lambda_h), g_2(\Lambda_h), g_3(\Lambda_h), y_t(\Lambda_h), y_b(\Lambda_h), y_\tau(\Lambda_h), \lambda_{\Phi 1}(\Lambda_h), \ldots, \lambda_{H1}(\Lambda_h), \ldots, M^2(\Lambda_h)\}$. The one-loop matching conditions are

$$\mu_+^2(\mu_R) = \mu_-^2(\mu_R) - Q_3 Q_2 \frac{\lambda_{H1}(\mu_R)}{(4\pi)^2} M^2(\mu_R) \left[1 - \log\left(\frac{M^2(\mu_R)}{\mu_R^2}\right)\right], \tag{3.22}$$

$$\lambda_+(\mu_R) = \lambda_-(\mu_R) - \frac{Q_3 Q_2}{2} \frac{\lambda_{H1}^2(\mu_R)}{(4\pi)^2} \log\left(\frac{M^2(\mu_R)}{\mu_R^2}\right), \tag{3.23}$$

where the $+$ $(-)$ subscript denotes the SM+GM (SM) EFT parameter and we have neglected terms suppressed by powers of v^2/M^2. We will always work in the limit where Φ does not obtain a vacuum expectation value. This is a well-motivated simplification, since for masses at the naturalness bounds we will obtain (typically $M >$ TeV), experimental agreement with the canonical Higgs mechanism for electroweak symmetry breaking generically constrains any scalar GM to observe this limit, and of course a coloured scalar multiplet must exactly satisfy it. Evidently the μ^2 term receives a threshold correction when matching is performed at the scale $\mu_R = M(\mu_R)$.

The $\mu^2(\mu_R)$ RGE in the SM+GM EFT with a complex scalar takes the form of Equation (3.1) with $C_2(\mu_R)$ a function of both the SM parameters and the extra

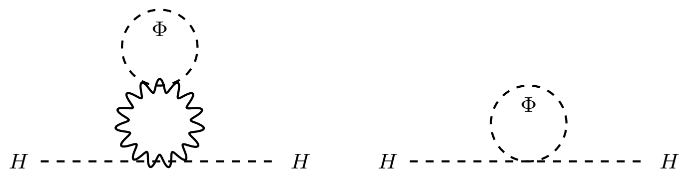

(A) (g_1^4, g_2^4) and λ_{Hi} corrections to μ^2.

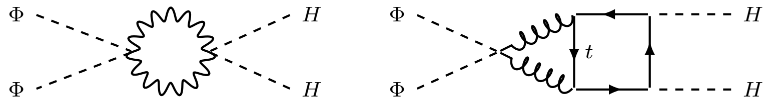

(B) $(g_1^4, g_2^4, g_1^2 g_2^2)$ and $g_3^4 y_t^2$ corrections to λ_{Hi}.

FIGURE 3.3: Corrections to μ^2 from a heavy scalar, and related corrections to λ_{Hi}.

quartics,

$$\begin{aligned} C_2 = &+ 2Q_3Q_2\frac{\lambda_{H1}}{(4\pi)^2} - 4Q_3Q_2\frac{\lambda_{H1}^2}{(4\pi)^4} \\ &+ 5Q_3Q_2Q_1^2\frac{g_1^4}{(4\pi)^4} + \frac{5}{4}Q_3Q_2(Q_2^2-1)\frac{g_2^4}{(4\pi)^4} \\ &+ 16Q_3Q_2Q_1^2\frac{g_1^2\lambda_{H1}}{(4\pi)^4} + 4Q_3Q_2(Q_2^2-1)\frac{g_2^2\lambda_{H1}}{(4\pi)^4} \\ &- 24Q_3\frac{\lambda_{H2}^2}{(4\pi)^4} + 64Q_2\frac{g_3^2\lambda_{H1}}{(4\pi)^4} \ , \end{aligned} \tag{3.24}$$

where the final line λ_{H2}^2 $(g_3^2\lambda_{H1})$ term appears only if $Q_2 = 2, 3$ $(Q_3 = 3)$, and dependence on scale μ_R is implied.[7] Representative diagrams which lead to these terms are shown in Figure 3.3a. Recall that the naturalness problem can be ameliorated in the limit $C_2 \to 0$. Indeed, it could be the case that at some scale the λ_{Hi} conspire to give $C_2(\mu_R) = 0$. However, this will not be stable under RG evolution; the portal quartics receive gauge corrections via the diagrams shown in Figure 3.3b:

$$\frac{d\lambda_{H1}}{d\log\mu_R} \supset 3Q_1^2\frac{g_1^4}{(4\pi)^2} + 3c_2(r_\Phi)\frac{g_2^4}{(4\pi)^2} - 32\frac{y_t^2 g_3^4}{(4\pi)^4} \ , \tag{3.25}$$

$$\frac{d\lambda_{H2}}{d\log\mu_R} \supset 3n_2Q_1\frac{g_1^2 g_2^2}{(4\pi)^2} \ . \tag{3.26}$$

Here, $n_2 = 1\,(2)$ and the quadratic Casimir $c_2(r_\Phi) = 3/4\,(2)$ for $Q_2 = 2\,(3)$; and the term proportional to g_3 applies to the case $Q_3 = 3$. Note that there exist corrections with odd power in Q_1; this means that (unlike the fermion case) RG evolution will depend on the sign of the hypercharge, however we do not observe any noticeable consequences from this effect. Also, in this case, we see

[7] We encountered difficulties with PYR@TE when generating the two-loop scalar octet RGEs. Thus, regrettably, they are left out of this study.

that the two-loop scalar RGEs *do* capture an $SU(3)$ correction $\sim g_3^4 y_t^2$, through a two-loop correction to the portal quartics. Thus we do not add by hand the three-loop $g_3^4 y_t^2$ term to the μ^2 RGE in our scalar SM+GM analysis.

The portal and self quartics are unknown and unconstrained high scale input parameters which must be projected out to obtain a sensitivity measure which is a function of (M, Λ_h). Our measure Equation (3.6) requires them to take on such values which minimise the Bayes factor, i.e. such values which give a conservative "best case scenario" for Higgs mass sensitivity in the given model. In Equation (3.5), we wrote down an approximation to the full sensitivity measure Equation (3.4), which is valid when the low scale dimensionless SM observables are approximately insensitive to the unconstrained inputs in the vicinity of the minimum. In that case we can evaluate the sensitivity measure Equation (3.5),

$$\Delta(M, \Lambda_h) = \min_{\lambda_{Hi}} \left\{ \sqrt{ \begin{array}{l} \left(\frac{\partial \log \mu^2(m_Z)}{\partial \log \mu^2(\Lambda_h)} \right)^2 + \left(\frac{\partial \log \mu^2(m_Z)}{\partial \log M^2(\Lambda_h)} \right)^2 \\ + \sum \left(\frac{\partial \log \mu^2(m_Z)}{\partial \log \lambda_{Hi}(\Lambda_h)} \right)^2 + \sum \left(\frac{\partial \log \mu^2(m_Z)}{\partial \log \lambda_{\Phi j}(\Lambda_h)} \right)^2 \end{array} } \Bigg|_{\substack{\lambda_{\Phi j}(M)=0 \\ \lambda_{Hi}}} \right\}, \tag{3.27}$$

where $\lambda_{\Phi j}(M) = 0$ is minimally consistent with our assumption that Φ attains no vacuum expectation value.[8] We will now make an argument for why we indeed expect this approximation to be valid in the scalar SM+GM.

Intuitively, since $C_2 M^2$ is the primary quantity which leads to a naturalness problem, to zeroth approximation we expect the minimum to occur where the average value of $C_2(\mu_R)$ over the RG evolution is zero. Consider the case with only one portal coupling λ_{H1}. Then from Equation (3.24) our expectation requires $\lambda_{H1}(\mu_R)$ to take on values $\mathcal{O}(g^4/(4\pi)^2)$ (in order to cancel the pure gauge contribution), and for $C_2(\mu_R)$ to swap sign along its RG evolution. Indeed, we observe this to be the case in our numerical study, as we will demonstrate in Section 3.4. Now, λ_{H1} enters the one-loop dimensionless SM parameter RGEs only for the Higgs self-quartic λ, as $\sim \lambda_{H1}^2/(4\pi)^2$. Therefore its contribution to the evolution of λ (and all dimensionless SM parameters) is very small at the minimum, and we can say that $\partial\lambda(m_Z)/\partial\lambda_{H1}(\Lambda_h) \simeq 0$. As for the new quartic couplings $\lambda_{\Phi j}$, they do not directly enter any of the dimensionless SM parameter two-loop RGEs, therefore their effect is also very small. Extending to the case with two portal quartics, Equation (3.24) clearly implies that a contour in $(\lambda_{H1}, \lambda_{H2})$ space will satisfy $C_2(\mu_R) = 0$, so our argument for $\mathcal{O}(g^4/(4\pi)^2)$ quartics no longer holds. However the $\partial/\partial \log \lambda_{Hi}(\Lambda_h)$ terms in the sensitivity measure Equation (3.27) are proportional to $\lambda_{Hi}(\Lambda_h)$, so that the minimum will always prefer smaller values for these quartics. The dimensionless SM observables will then be insensitive to variations around $\lambda_{Hi}(\Lambda_h)$ for the reasons already argued.

[8]The full sensitivity measure Equation (3.27) should also involve a minimisation over the $\lambda_{\Phi j}$. However, we found that, after demanding $\lambda_{\Phi j}(M) \geq 0$ to ensure no non-trivial vacuum expectation value, the minimum always occurred for $\lambda_{\Phi j}(M) \simeq 0$. Thus in practice, to improve speed and numerical stability, we set $\lambda_{\Phi j}(M) = 0$ when evaluating the sensitivity measure and note that even varying this up to $\lesssim 0.5$ made little difference to our results. We also note that the $\lambda_{\Phi j}$ always evolve to positive values due to pure gauge contributions to their RGEs at one-loop, and therefore the potential does not become trivially unstable.

3.3 Results

The naturalness bounds for various vector-like fermionic and scalar GMs, derived according to the method detailed in Section 3.2, are presented in Tables 3.1 and 3.2 for $\Lambda_h = \{M^+, \Lambda_{Pl}\}$ and $\Delta(\Lambda_h) = \{10, 100, 1000\}$. Contour plots in (M, Δ) and (M, Λ_h) parameter space are also provided in Figures 3.4–3.7. These constitute the main result of this Chapter, and we hope that they will serve as a useful reference of naturalness benchmarks for phenomenological model builders.

Before we discuss them in more detail, let us briefly reiterate their meaning. The scale Λ_h corresponds to the input scale of $\overline{\text{MS}}$ parameters in the SM+GM EFT. The quantity $\Delta(\Lambda_h)$, defined in Equation (3.6), is a sensitivity measure for the Higgs mass parameter which can be interpreted as a Bayesian evidence on the Jeffreys scale or (more loosely) to a percentage fine-tuning in the Barbieri–Giudice sense. A stringent naturalness constraint is then $\Delta(\Lambda_{Pl}) < 10$, which (loosely) ensures $< 10\%$ sensitivity for $\mu^2(m_Z) \simeq -(88\,\text{GeV})^2$ when the $\overline{\text{MS}}$ parameters are defined at Λ_{Pl}. If a phenomenological model can satisfy this constraint then we would say it does not induce a Higgs naturalness problem. The bounds weaken in the limit $\Lambda_h \to M^+$. Still, rather remarkably, they remain finite in this limit, as we argued in Section 3.1. The $\Delta(M^+) < 10$ bound can therefore be interpreted as a conservative naturalness constraint on M. It is also of interest if $\Delta(\Lambda_{Pl})$ is not applicable, e.g. if new physics arises at a scale above M which markedly affects the $\mu^2(\mu_R)$ evolution, or if the EFT hits a Landau pole below Λ_{Pl}.

3.4 Discussion

Some aspects of our results can be understood by scaling relations. At fixed Λ_h, the bounds in Tables 3.1 and 3.2 scale approximately as $\sqrt{\Delta/C_2^{SM}}$, as one would expect from Equation (3.8) for the simple example discussed in Section 3.1. Where they are violated (particularly for the $\Delta(\Lambda_h)$ bounds) it is due to some cancellation between contributions: the contributions arising from $SU(3)$ charge are opposite in sign to those from $SU(2)$ and $U(1)_Y$ charge. The contour plots in Figures 3.4–3.7 make these cancellations more obvious, and we will discuss them shortly. Comparing bounds evaluated at disparate Λ_h is more involved. Indeed, this is why we have gone to the trouble of a two-loop RGE analysis! Still, some qualitative observations will be made presently.

For the fermionic GMs in Table 3.1, the rough scaling relation $\sim \sqrt{1/\sqrt{5}\log(\Lambda_{Pl}/M)}$ between bounds evaluated at $\Delta(M^+)$ and $\Delta(\Lambda_{Pl})$, as expected from Equation (3.8), is broken by the RG evolution of C_2. We observe that the naturalness bounds at Λ_{Pl} are more stringent than this relation would suggest for $\psi(1, 1, Q_1)$, and less stringent for $\psi(1, Q_2, 0)$ and $\psi(Q_3, 1, 0)$. This is

			$\Lambda_h = M^+$			$\Lambda_h = 10^{19}$ GeV		
$SU(3)$	$SU(2)_L$	$U(1)_Y$	$\Delta = 10$	$\Delta = 100$	$\Delta = 1000$	$\Delta = 10$	$\Delta = 100$	$\Delta = 1000$
1	1	$\pm\frac{1}{6}$	1400	4300	13000	130	420	1300
		$\pm\frac{1}{3}$	690	2200	6800	64	210	670
		$\pm\frac{2}{3}$	350	1100	3400	32	110	340
		±1	230	730	2300	22	72	230
		±2	120	370	1200	13	43	140
		±3	80	250	790	-	-	-
	2	0	70	230	740	11	35	110
		$\pm\frac{1}{2}$	69	220	720	10	34	110
		±1	65	210	670	9.7	32	100
		±2	54	170	550	-	-	-
	3	0	35	110	370	6.0	20	64
		±1	34	110	350	6.1	20	65
		±2	31	100	330	-	-	-
3	1	0	54	190	700	17	56	190
		$\pm\frac{1}{3}$	54	200	710	17	60	210
		$\pm\frac{2}{3}$	56	210	750	21	77	300
		±1	59	220	830	72	140	340
		±2	110	800	1600	-	-	-
	2	0	180	350	850	13	37	110
		±1	110	250	660	9.0	28	84
		±2	57	150	440	-	-	-
	3	0	29	86	260	-	-	-
		±1	27	82	250	-	-	-
		±2	24	72	220	-	-	-
8	1	0	20	74	270	7.3	25	86
		±1	21	77	280	-	-	-
		±2	23	91	360	-	-	-
	2	0	17	67	270	-	-	-
		±1	18	72	310	-	-	-
		±2	21	110	780	-	-	-
	3	0	63	110	270	-	-	-
		±1	50	98	240	-	-	-
		±2	32	72	190	-	-	-

TABLE 3.1: Naturalness bounds on the mass M (in TeV and to 2 significant figures) of various vector-like fermionic gauge multiplets for $\Lambda_h = \{M^+, 10^{19}\text{ GeV}\}$ and $\Delta(\Lambda_h) = \{10, 100, 1000\}$. The dashes indicate that a Landau pole arises below 10^{19} GeV along the $\Delta(\Lambda_h) = 10$ contour.

			$\Lambda_h = M^+$			$\Lambda_h = 10^{19}$ GeV		
$SU(3)$	$SU(2)_L$	$U(1)_Y$	$\Delta = 10$	$\Delta = 100$	$\Delta = 1000$	$\Delta = 10$	$\Delta = 100$	$\Delta = 1000$
1	1	$\pm\frac{1}{6}$	1300	4100	13000	29	96	310
		$\pm\frac{1}{3}$	670	2000	6400	14	47	150
		$\pm\frac{2}{3}$	340	1000	3200	6.8	23	75
		±1	230	690	2200	4.4	15	48
		±2	120	350	1100	2.0	6.5	21
		±3	77	240	740	-	-	-
	2	0	67	210	680	2.3	7.7	25
		$\pm\frac{1}{2}$	65	210	660	2.1	7.2	24
		±1	62	190	620	1.8	6.0	20
		±2	52	160	510	1.1	3.6	12
	3	0	33	100	340	1.1	3.6	12
		±1	32	100	330	0.95	3.2	10
		±2	30	94	300	0.45	1.7	6.7
3	1	0	220	820	2900	12	40	130
		$\pm\frac{1}{3}$	290	1200	5400	12	38	110
		$\pm\frac{2}{3}$	330	880	2500	4.2	14	45
		±1	160	470	1400	2.5	8.4	27
		±2	71	210	660	0.99	3.2	10
	2	±0	40	130	400	1.3	4.3	14
		±1	37	120	370	0.99	3.3	11
		±2	31	96	300	-	-	-
	3	±0	20	62	200	-	-	-
		±1	19	60	190	-	-	-
		±2	18	55	180	-	-	-

TABLE 3.2: Naturalness bounds on the mass M (in TeV and to 2 significant figures) of various scalar gauge multiplets for $\Lambda_h = \{M^+, 10^{19}\text{ GeV}\}$ and $\Delta(\Lambda_h) = \{10, 100, 1000\}$. The dashes indicate that a Landau pole arises below 10^{19} GeV along the $\Delta(\Lambda_h) = 10$ contour.

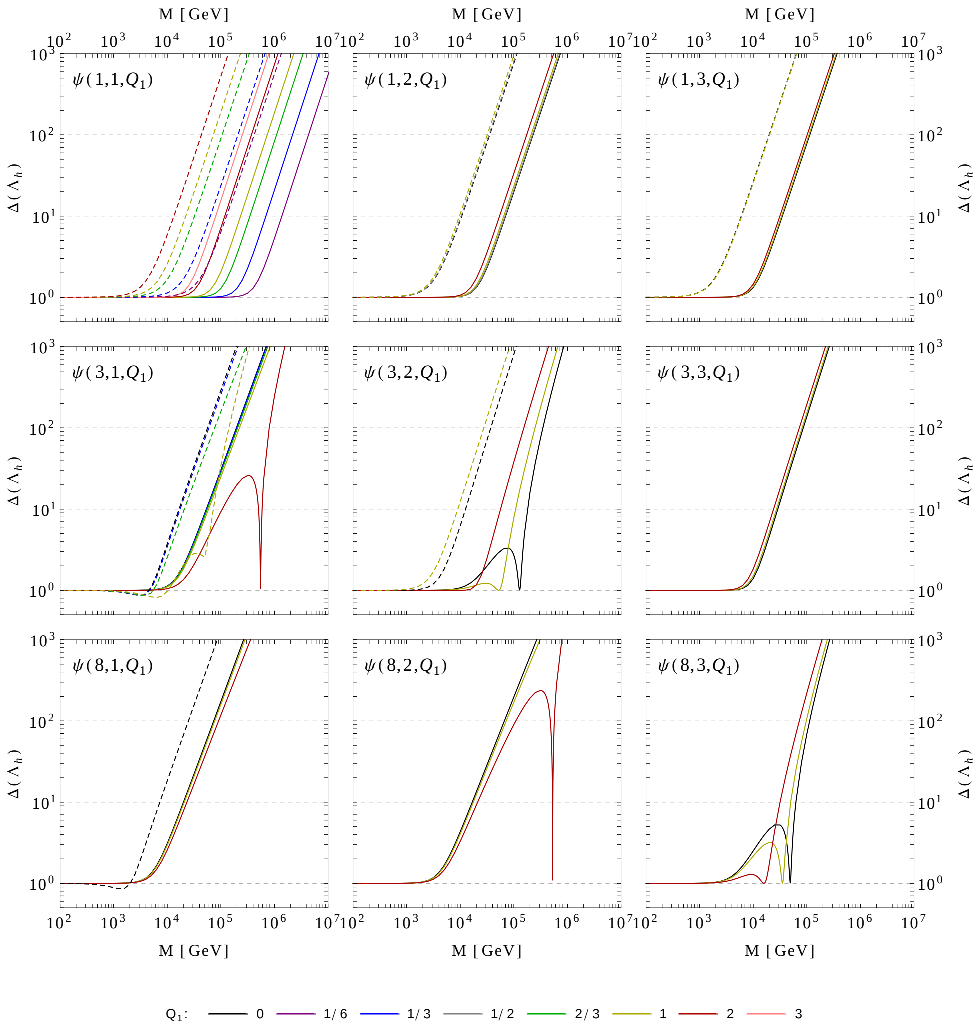

FIGURE 3.4: $\Lambda_h = \{M^+, \Lambda_{Pl}\}$ contours {solid, dashed} in the vector-like fermionic SM+GM EFT. The "throat" features are an artifact of the loop level to which we are working [see Section 3.1.3].

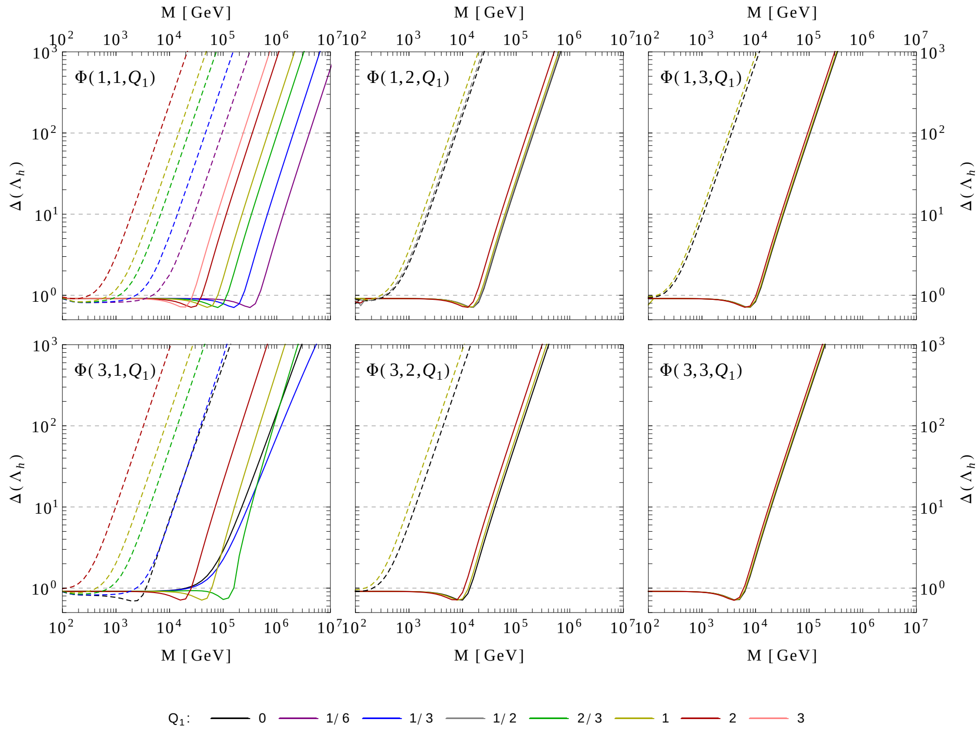

FIGURE 3.5: $\Lambda_h = \{M^+, \Lambda_{Pl}\}$ contours {solid, dashed} in the scalar SM+GM EFT.

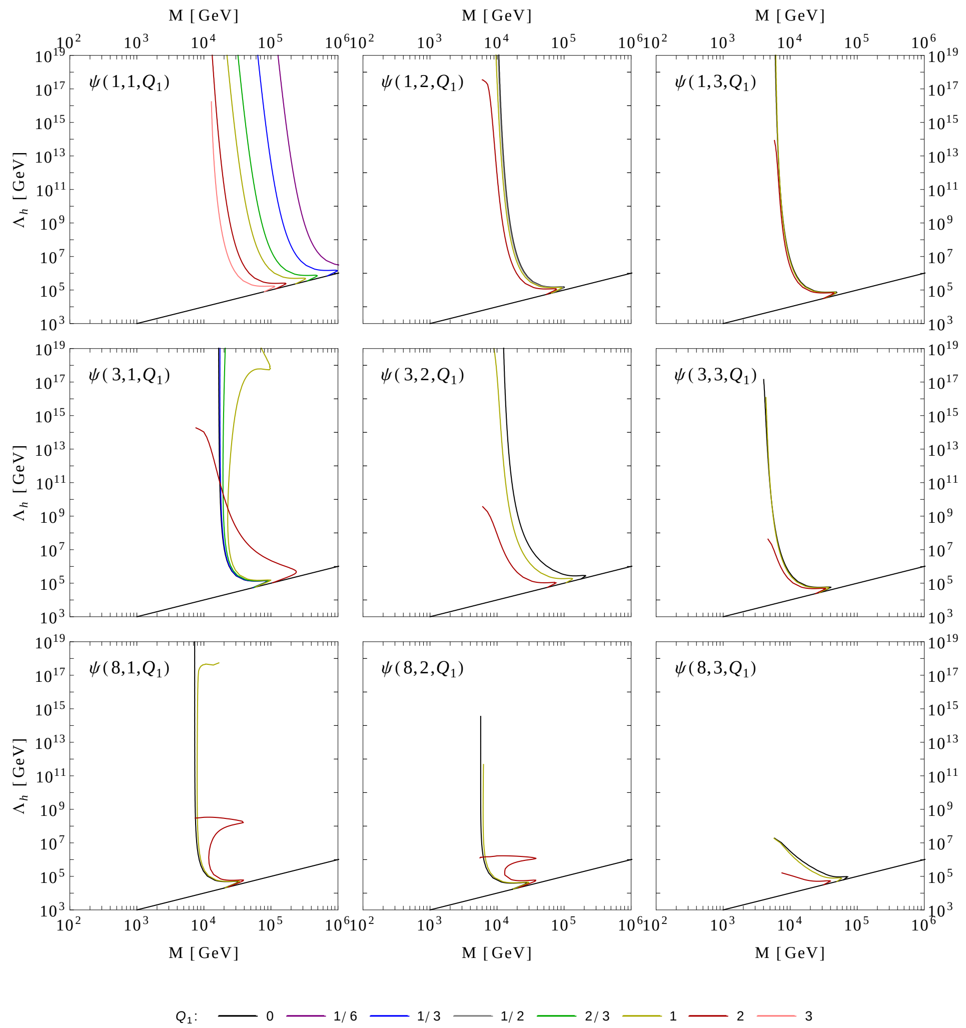

FIGURE 3.6: $\Delta(\Lambda_h) = 10$ contours in the vector-like fermionic SM+GM EFT. If a line ends it is because the system hits a Landau pole.

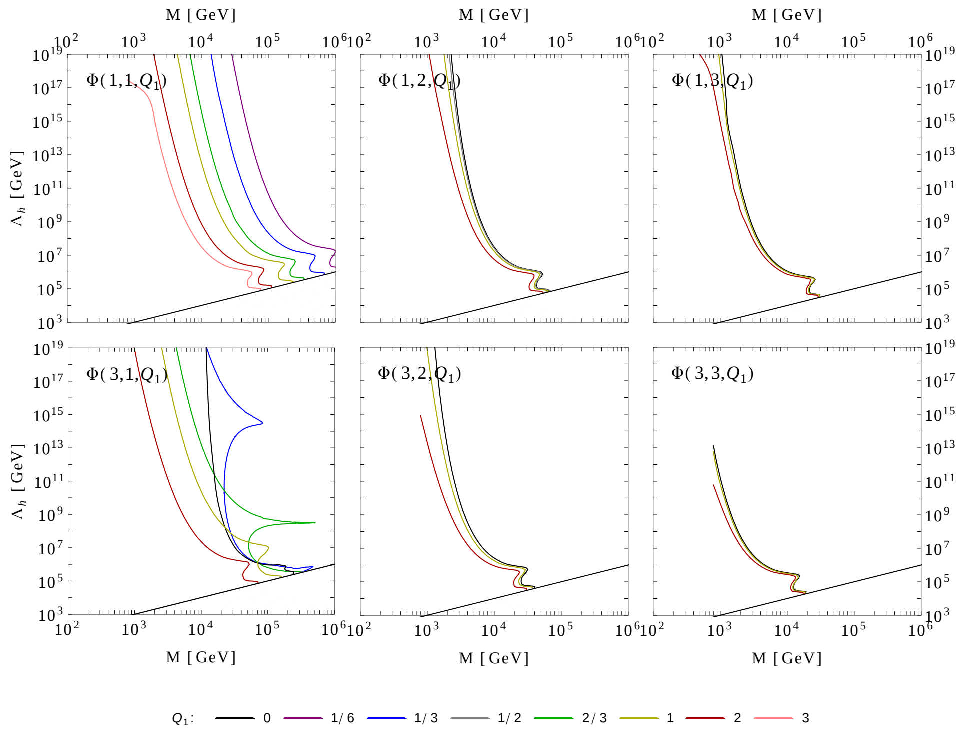

FIGURE 3.7: $\Delta(\Lambda_h) = 10$ contours in the scalar SM+GM EFT. If a line ends it is because the system hits a Landau pole.

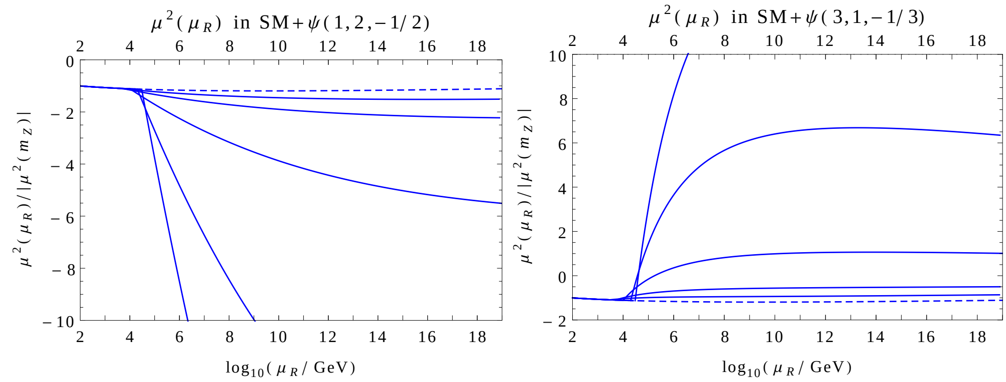

FIGURE 3.8: Example running of $\mu^2(\mu_R)$ in the SM+GM EFT for a heavy lepton doublet $\psi(1,2,-1/2)$ and a heavy down-type quark $\psi(3,1,-1/3)$ with $M = 3, 5, 10, 20, 30$ TeV. The dashed line is the SM-only case.

simply because $g_1^4(\mu_R)$ (and therefore C_2) grows at higher energy, whereas the opposite is true for $g_2^4(\mu_R)$ and $g_3^4(\mu_R)y_t^2(\mu_R)$. This effect can be observed in Figure 3.8, where we show the example RG evolution of $\mu^2(\mu_R)$ for gauge multiplets of increasing mass. The naturalness problem which broadly arises from a sensitivity to the high scale input $\mu^2(\Lambda_h)$ is self-evident for large masses.

For the scalar GMs in Table 3.2, there is no obvious scaling relation between naturalness bounds at different scales. One observation is that, although the $\Delta(M^+)$ bounds are similar[9] to those found in the fermionic GM case, the $\Delta(\Lambda_{Pl})$ bounds are much more stringent. This is because the sole one-loop term in the μ^2 RGE involves the portal quartic λ_{H1}, which is *itself* renormalised by pure gauge RG terms at one-loop. Thus the scaling relation is expected to more closely resemble $\sim 1/\log(\Lambda_{Pl}/M)$ [rather than $\sim \sqrt{1/\log(\Lambda_{Pl}/M)}$]. What actually happens is unfortunately quite opaque, since it is hidden by various complexities: a coupled set of RGEs; a non-trivial sensitivity measure Equation (3.27); and a minimisation procedure over the λ_{Hi}. Let us attempt to convey some intuition for what happens by considering the example of a two Higgs doublet model, i.e. the SM+$\Phi(1,2,1/2)$. To this end it is useful to define a reduced sensitivity measure

$$\Delta_{red}(M,\Lambda_h) = \left|\frac{\partial \log \mu^2(m_Z)}{\partial \log \mu^2(\Lambda_h)}\right|, \tag{3.28}$$

which is a subcomponent of the full measure Equation (3.27). This reduced measure vanishes in the limit $\mu^2(\Lambda_h) \to 0$. As we already argued in Section 3.2.2, it is always possible to choose the λ_{Hi} such that C_2 swaps sign over its RG evolution and $\mu^2(\Lambda_h) = 0$. Thus one expects a contour in λ_{Hi} space along which $\Delta_{red}(M,\Lambda_h)$ vanishes [5]. In Figure 3.9 we plot $\Delta_{red}(M,\Lambda_h)$ as a function of $(\lambda_{H1}(M), \lambda_{H2}(M))$ for $\Lambda_h = \Lambda_{Pl}$ and $M = 1$ TeV, where such a contour is readily

[9] The larger relative difference between the bounds for coloured states may be partly accounted for by the three-loop $g_3^4 y_t^2$ term which is not captured in our pure two-loop scalar analysis.

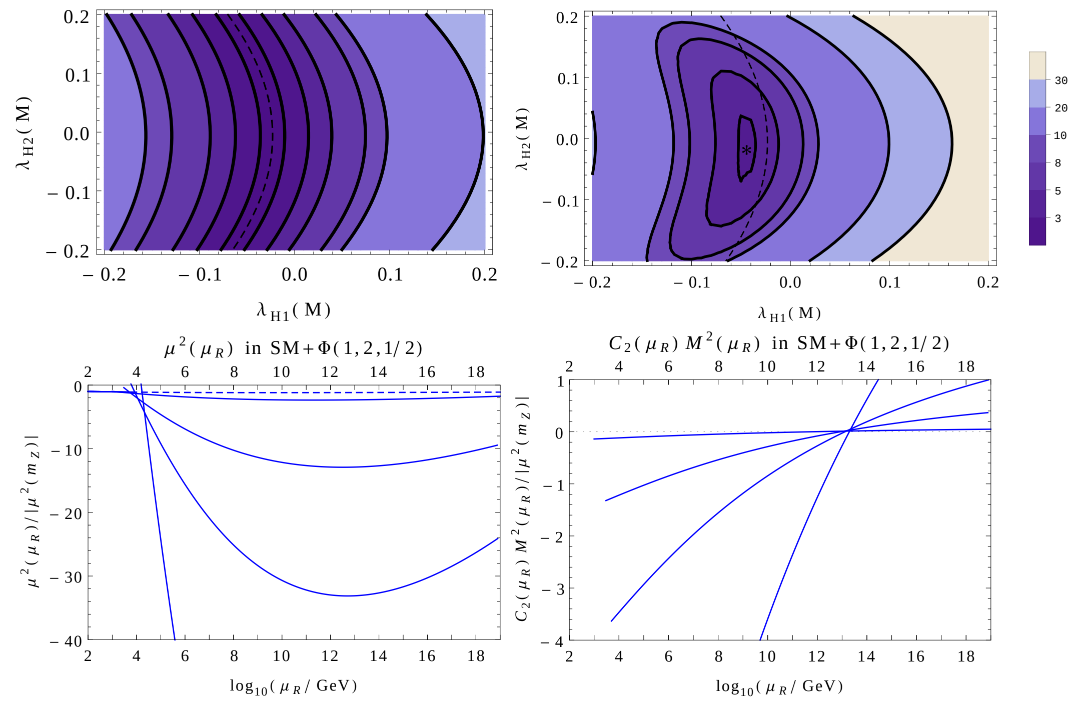

FIGURE 3.9: Sensitivity measure and RG evolution in the SM+$\Phi(1,2,1/2)$ (i.e. the 2HDM). Upper panel: The not-yet-minimised sensitivity measure for $M = 1$ TeV as a function of $(\lambda_{H1}(M), \lambda_{H2}(M))$ for: (left) $\Delta_{red}(\Lambda_{Pl})$ of Equation (3.28), and (right) $\Delta(\Lambda_{Pl})$ of Equation (3.27). The dashed line shows the $\mu^2(\Lambda_{Pl}) = 0$ contour and the star denotes the global minimum. Lower panel: RG evolution of $\mu^2(\mu_R)$ and $C_2(\mu_R)M^2(\mu_R)$ for $M = 1, 3, 5, 10$ TeV evaluated at the $(\lambda_{H1}, \lambda_{H2})$ points which minimise $\Delta(\Lambda_{Pl})$.

observed. Obviously this contour constitutes a fine-tuning in the λ_{Hi}, and we would hope that our full sensitivity measure captures this tuning and restores a finite naturalness bound. Indeed, it does; also shown in Figure 3.9 is the full sensitivity measure as a function of $(\lambda_{H1}(M), \lambda_{H2}(M))$, with a unique minimum of $\Delta(\Lambda_{Pl}) \simeq 2.7$ nearby the $\mu^2(\Lambda_h) = 0$ contour. In the lower panel of Figure 3.9 we also show the running of $\mu^2(\mu_R)$ and $C_2(\mu_R)M^2(\mu_R)$ at this minimum (and for other example masses). It is seen that C_2 does switch sign, as expected.

We will now briefly comment on some features in the (M, Δ) and (M, Λ_h) contour plots of Figures 3.4–3.7. In Figure 3.4 there is a sharp "Veltman throat" in the $\Delta(M^+)$ contours for coloured fermions. This occurs when the three-loop colour contribution cancels with the electroweak contributions such that $C_2(M) = 0$. It was already noted in Section 3.1.3 that this is only an artifact of the loop level to which we are working. The $\Delta(\Lambda_{Pl})$ contour for the $\psi(3,1,1)$ GM demonstrates how this feature is effectively removed when $\Lambda_h > M$. In Figure 3.5 the qualitative form of the contours in the $\Phi(3,1,Q_1)$ scalar case is seen to change as Q_1 is increased from 0 to 2. This is due to a transition in dominance between colour and hypercharge effects, which are opposite in sign.

In Figure 3.6 a cusp feature is observed when Λ_h is just above M. This can be understood from the toy model Equation (3.8): it is the point where $2\log(\Lambda_h/M) \simeq 1$ and the $\partial/\partial \log M^2$ sensitivity measure is minimised. Also, the "turn-around" features in the $\psi(3,1,Q_1)$, $\psi(8,1,Q_1)$, and $\psi(8,2,Q_1)$ plots can again be understood as a balance between the colour and electroweak contributions. In Figure 3.7 a number of cusp features are observed, mostly occuring at $\Lambda_h \sim 20M$. These features all have the same origin: they occur for solutions where $\mu^2(\Lambda_h) \approx 0$. For example, in the $\Phi(1,2,1/2)$ case at $\Lambda_h = \Lambda_{Pl}$ we saw that the λ_{Hi} took on values such that $\mu^2(\Lambda_{Pl}) < 0$ (see Figure 3.9). It turns out that, for $\Lambda_h \lesssim 20M$, the sensitivity measure is minimised for values such that $\mu^2(\Lambda_h) > 0$. At the transition point the reduced sensitivity measure Equation (3.28) vanishes, and hence the full sensitivity measure is somewhat reduced. Note that in the cases where Φ is coloured the transition occurs later due to the competiting contributions between gauge contributions.

Before concluding we would like to make a few comments about the applicability of these bounds in the context of extended models. First, in deriving our sensitivity measure we have made the assumption of flat priors on the logarithms of $\overline{\text{MS}}$ input parameters at scale Λ_h. This makes logical sense in a bottom-up approach where one would like to remain maximally agnostic to the higher scale UV theory. However, if one were to derive these priors as posteriors arising from a flat set of priors in the UV theory, they would almost certainly not be flat. Hence our results are only broadly applicable if those derived priors are approximately flat. In particular, some might argue that this is unlikely for $\log \mu^2(\Lambda_h)$ in the presence of gravity, but then some might choose to remain agnostic. Second, we have assumed no correlations between the high scale $\overline{\text{MS}}$ input parameters. Again, this makes sense from an agnostic bottom-up standpoint, but is not the general expectation if these parameters were derived from some UV theory. Third, one might contend that our bounds (especially the $\Delta(\Lambda_{Pl})$ bounds), which are only derived in the context of minimal SM+GM extensions, are not applicable in a realistic model with additional high scale states. This is true in a quantitative sense: the bounds are sure to change. Nonetheless, this does not imply that they are not qualitatively useful. It would take very special physics to ameliorate these bounds by a significant amount. For example, one could try to introduce new states with particular properties at $\Lambda_h \sim M$ such that loop contributions approximately cancel at this scale [298]. In the absence of a symmetry which introduces the appropriate correlations between parameters at this scale, and a symmetry which ensures the cancellation remains satisfied under RG evolution, naturalness bounds similar to those we have derived will be quickly reintroduced at $\Lambda_h > M$. Actually, such symmetry requirements are just those provided by supersymmetric theories, and herein lies the connection between our RG description and the usual naturalness arguments in the context of supersymmetry. In any case, the framework we have outlined in Appendix A.1 is fully generalisable to perturbative models with more states. Naturalness of the low scale Higgs mass parameter can be quantified by the Bayesian sensitivity measure Equation (A.7), as long as one is prepared to calculate and solve RGEs at least at two-loop order with one-loop matching between intermediate physical scales.

3.5 Conclusion

The aim of this Chapter was to confront the question, *at what mass does a heavy gauge multiplet introduce a physical Higgs naturalness problem?* In Section 3.1 we described a physical way to understand the Higgs naturalness problem which might be introduced when perturbative heavy new physics is added to the SM. The description is of particular interest in bottom-up extensions of the SM. The premise is essentially as follows. In any perturbative EFT, the low scale Higgs mass parameter $\mu^2(m_Z) \simeq -(88\,\mathrm{GeV})^2$ can be connected by renormalisation group equations to $\overline{\mathrm{MS}}$ "input" parameters defined at some high scale Λ_h. If $\mu^2(m_Z)$ is especially sensitive to these input parameters, then this signifies a Higgs naturalness problem. In particular, this can occur if a heavy particle of mass M is added to the SM.

In order to sensibly quantify this potential problem, we derived a sensitivity measure using Bayesian probabilistic arguments. The measure can be interpreted as a Bayesian model comparison [see Equation (3.4)] which captures the "naturalness price" paid for promoting the Higgs mass parameter to a high scale input parameter of the model as opposed to a purely phenomenological input parameter at low scale. It is fully generalisable to any perturbative QFT, with the details provided in Appendix A.1. The measure reduces in a certain (relevant) limit to an intuitively motivated Barbieri–Giudice-like fine-tuning measure [see Equation (3.5)]. The resulting sensitivity measure is generally a function of unknown high scale inputs. We conservatively projected these out by minimising over them, thereby obtaining the sensitivity measure Equation (3.6), which is a function of Λ_h and the mass M of a heavy new particle.

This sensitivity measure was used to set naturalness bounds on the masses of various gauge multiplets, using a full two-loop RGE analysis with one-loop matching. An interesting outcome is that, once RG effects are taken into account and finite threshold corrections are captured, a naturalness bound on M remains even in the limit $\Lambda_h \to M^+$. The resulting bounds are presented in Tables 3.1 and 3.2, and as contours in Figures 3.4–3.7. They form the main result of this Chapter, and we hope they are of interest to model builders. For $\Lambda_h = \Lambda_{Pl}$ we find "10% fine-tuning" bounds of $M < \mathcal{O}(1\text{–}10)$ TeV on the masses of various gauge multiplets, with the bounds on fermionic gauge multiplets significantly weaker than for scalars. In the limit $\Lambda_h \to M^+$ the bounds weaken to $M < \mathcal{O}(10\text{–}100)$ TeV; these can be considered as conservative naturalness bounds, of interest if new physics is expected to substantially alter the RG evolution of $\mu^2(\mu_R)$ above the scale M. We also found that the bounds on coloured multiplets are no more severe than on electroweak multiplets, since they correct the Higgs mass directly at three-loop order.

4 Neutrino Mass

This Chapter is based on the publication "Testing Radiative Neutrino Mass Models at the LHC," written in collaboration with Yi Cai, Michael A. Schmidt, and Raymond R. Volkas [2].

In Section 1.1.3 we motivated Majorana neutrino masses and described two generic generation mechanisms: tree-level seesaw mechanisms, and loop-level radiative mechanisms. The focus of this Chapter will be radiative mechanisms, in which the neutrino mass is suppressed by powers of loop factors $\sim 1/(4\pi)^2$ in addition to the mass suppression from heavy particles appearing in the loop. One reason to be interested in such models is that the new physics required might lie at a nearby scale, and therefore may be searched for at the LHC or in lepton-flavour-violation (LFV) experiments.

A challenge is that there are many viable radiative models, and one wishes to study them in as generic and inclusive a way as possible. One way to approach this task is to begin with gauge-invariant effective operators that violate lepton-number by two units ($\Delta L = 2$), constructed out of SM fields [305–307]. These operators, which Babu & Leung [305] systematically classified for mass dimensions 5, 7, 9, and 11, produce vertices that feature in loop-level graphs generating Majorana masses (and mixing angles and phases). By "opening up" the operators in all possible ways subject to some minimality assumptions, one may in principle construct all candidate renormalisable models that yield radiative Majorana neutrino masses consistent with those assumptions [307].

In this Chapter we first write down the candidate models implied by opening up all of the dimension 7 (D7) operators in the Babu–Leung list, restricting ourselves to tree-level ultraviolet (UV) completions subject to the following minimality assumptions: the gauge symmetry is that of the SM only, and effective operators containing gauge fields are excluded from consideration; the exotic particles that are integrated out to produce the effective operators are either scalars, vector-like fermions, or Majorana fermions. We predict vector-like quarks, vector-like leptons, scalar leptoquarks, a charged scalar, a scalar doublet, and a scalar quadruplet, whose properties are constrained by neutrino oscillation data. As well, a detailed collider study is presented for $\mathcal{O}_3 = LLQ\bar{d}H$ and $\mathcal{O}_8 = L\bar{d}\bar{e}^\dagger\bar{u}^\dagger H$ completions with a vector-like quark $\chi \sim (3, 2, -\frac{5}{6})$ and a leptoquark $\phi \sim (\bar{3}, 1, \frac{1}{3})$, taking account of LFV constraints in the process. The existing limits extracted from LHC searches for vector-like fermions and sbottoms/stops are $m_\chi \gtrsim 620$ GeV and $m_\phi \gtrsim 600$ GeV.

4.1 Minimal UV completions of D7 $\Delta L = 2$ operators

In Weyl-spinor notation, the D7 operators of interest, using the numbering system of Babu–Leung [305], are

$$\mathcal{O}_2 = LLL\bar{e}H, \quad \mathcal{O}_3 = LLQ\bar{d}H, \quad \mathcal{O}_4 = LLQ^\dagger\bar{u}^\dagger H, \quad \mathcal{O}_8 = L\bar{d}\bar{e}^\dagger\bar{u}^\dagger H, \tag{4.1}$$

and the Weinberg-like operator

$$\mathcal{O}_1' = LL\tilde{H}HHH. \tag{4.2}$$

The pertinent part of the SM Lagrangian is

$$\mathcal{L}_{SM,Y} = Y_e L\bar{e}\tilde{H} + Y_u Q\bar{u}H + Y_d Q\bar{d}\tilde{H} + H.c.\ , \tag{4.3}$$

where $\tilde{H} = i\tau_2 H^*$ is the charge conjugate of H. The Weinberg-like operator $\mathcal{O}_1'$ has not been explicitly shown in the list of Babu–Leung [305], but has been studied in Refs. [308, 309]. Note that this operator always induces the usual Weinberg operator $\mathcal{O}_1 = LLHH$ by connecting the two external legs H and $\tilde{H}$ via a Higgs boson to form a Higgs loop. This contribution dominates if the scale of new physics is large, much above the TeV scale.

We will consider minimal UV completions of these D7 operators using scalars and fermions, following the programme set out in Ref. [307]. We do not include models with new gauge bosons. Also, we only consider models which do not generate the dimension-5 Weinberg operator at tree-level. Hence we remove models in which one of the three seesaw mechanisms may operate, i.e. models containing SM singlet fermions, electroweak (EW) triplet scalars with unit hypercharge, and EW triplet fermions.

We group the completions by topology in Figures 4.1–4.3 and Tables 4.1–4.3, where quantum numbers are given with respect to $SU(3)_c \times SU(2)_L \times U(1)_Y$. More details can be found in the Appendix of our Ref. [2]. The contents of Tables 4.1–4.3 constitute a workable list of exotic particles relevant to D7 radiative neutrino mass models which may be searched for at the LHC or in LFV experiments.

It turns out that the operators $\mathcal{O}_2$ and $\mathcal{O}_{3b}$ lead to one-loop models, while the others only admit two-loop models. Generally for models with scalar leptoquarks and vector-like fermions, the radiatively generated neutrino mass is proportional to the quark or lepton mass in the loop (we will show this in detail in Section 4.2). Thus the exotic fermions dominantly mix with the third generation quarks or leptons, as the third generation masses dominate the neutrino mass

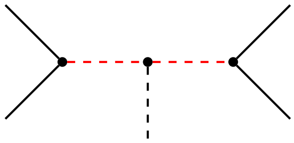

FIGURE 4.1: Scalar-only extension.

Scalar	Scalar	Operator
$(1, 2, \frac{1}{2})$	$(1, 1, 1)$	$\mathcal{O}_{2,3,4}$ [77]
$(3, 2, \frac{1}{6})$	$(3, 1, -\frac{1}{3})$	$\mathcal{O}_{3,8}$ [305, 310]
$(3, 2, \frac{1}{6})$	$(3, 3, -\frac{1}{3})$	$\mathcal{O}_{3}$

TABLE 4.1: Topology of Figure 4.1.

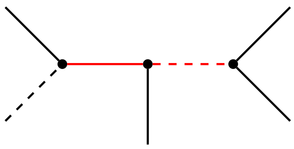

FIGURE 4.2: Extension by a scalar and a fermion.

Dirac fermion	Scalar	Operator
$(1, 2, -\frac{3}{2})$	$(1, 1, 1)$	$\mathcal{O}_2$
$(3, 2, -\frac{5}{6})$	$(1, 1, 1)$	$\mathcal{O}_3$
$(3, 1, \frac{2}{3})$	$(1, 1, 1)$	$\mathcal{O}_3$
$(3, 1, \frac{2}{3})$	$(3, 2, \frac{1}{6})$	$\mathcal{O}_3$ [311]
$(3, 2, -\frac{5}{6})$	$(3, 1, -\frac{1}{3})$	$\mathcal{O}_{3,8}{}^*$
$(3, 2, -\frac{5}{6})$	$(3, 3, -\frac{1}{3})$	$\mathcal{O}_3$
$(3, 3, \frac{2}{3})$	$(3, 2, \frac{1}{6})$	$\mathcal{O}_3$
$(3, 2, \frac{7}{6})$	$(1, 1, 1)$	$\mathcal{O}_4$
$(3, 1, -\frac{1}{3})$	$(1, 1, 1)$	$\mathcal{O}_4$
$(3, 2, \frac{7}{6})$	$(3, 2, \frac{1}{6})$	$\mathcal{O}_8$
$(1, 2, -\frac{1}{2})$	$(3, 2, \frac{1}{6})$	$\mathcal{O}_8$

TABLE 4.2: Topology of Figure 4.2. The completion marked with a * is studied in detail in Section 4.2.

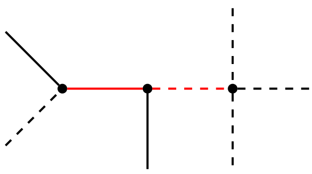

FIGURE 4.3: Extension by a scalar and a fermion.

Dirac fermion	Scalar	Operator
$(1, 3, -1)$	$(1, 4, \frac{3}{2})$	$\mathcal{O}'_1$ [312]

TABLE 4.3: Topology of Figure 4.3.

matrix unless there is an unnatural flavour structure for the various coupling constants.

The completions listed in Tables 4.1–4.3 each contain two fields beyond the SM, including vector-like quarks, vector-like leptons, scalar leptoquarks, charged scalars, EW scalar doublets and EW scalar quadruplets. In our Ref. [2] we discussed the pertinent LHC searches and limits for these exotic fields. We will not reproduce that discussion here. However, we would like to emphasise the generic predictivity of these minimal UV completions. The exotic particles are required to not only conform to existing flavour constraints, but also to fit low energy neutrino measurements. As a result it is common in these neutrino mass generation models to be able to predict the decay patterns of the exotic particles. Then for a specific model it is possible to extract the limit based on the decay patterns, either from existing searches, as we shall see in Section 4.2.4, or by carefully recasting relevant LHC searches, as in Section 4.2.5.

4.2 Detailed study of a specific model

4.2.1 An $\mathcal{O}_3$ and $\mathcal{O}_8$ completion

In order to demonstrate the LHC reach with regard to minimal UV completions of D7 $\Delta L = 2$ operators, we study a specific example model (marked in Table 4.2) with a scalar leptoquark ϕ and a vector-like quark χ with quantum numbers

$$\phi \sim \left(\bar{3}, 1, \frac{1}{3}\right), \qquad \chi \sim \left(3, 2, -\frac{5}{6}\right) . \tag{4.4}$$

These particles arise in the minimal UV completions of $\mathcal{O}_3 = LLQ\bar{d}H$ and $\mathcal{O}_8 = L\bar{d}\bar{e}^\dagger\bar{u}^\dagger H$ operators, whose SU(2)$_L$ structures are

$$L^\alpha L^\beta Q^\gamma \bar{d} H^\delta \epsilon_{\alpha\gamma}\epsilon_{\beta\delta}, \qquad\qquad L^\alpha \bar{d}\bar{e}^\dagger\bar{u}^\dagger H^\beta \epsilon_{\alpha\beta}, \tag{4.5}$$

respectively. The corresponding neutrino mass diagrams are shown in Figure 4.4. Their flavour structures are

$$\kappa^{\mathcal{O}_{3b}}_{ijkl} L^\alpha_i L^\beta_j Q^\gamma_k \bar{d}_l H^\delta \epsilon_{\alpha\gamma}\epsilon_{\beta\delta}, \qquad\qquad \kappa^{\mathcal{O}_8}_{ijkl} L^\alpha_i \bar{d}_j \bar{e}^\dagger_k \bar{u}^\dagger_l H^\beta \epsilon_{\alpha\beta}, \tag{4.6}$$

and the neutrino mass matrix $(m_\nu)_{ij}$ is

$$\kappa^{\mathcal{O}_{3b}}_{ijkl} (m_d)_{kl}\, I, \qquad\qquad \kappa^{\mathcal{O}_8}_{ijkl} (m_d^\dagger m_u)_{jl} m_{\ell_k}\, I, \tag{4.7}$$

with the loop integral I. Note that the proportionality on the SM mass matrices introduces a hierarchy.

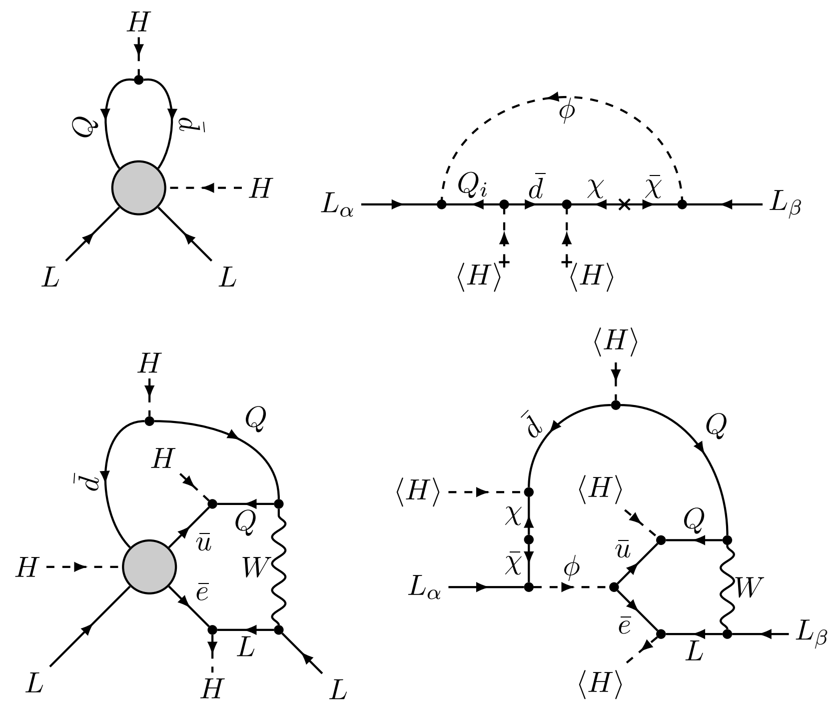

FIGURE 4.4: Neutrino mass via the $\mathcal{O}_{3b}$ (upper left) and $\mathcal{O}_8$ (lower left) operators, and their respective UV completions in our detailed study (right).

In our specific model, the Yukawa couplings of the new exotic particles are given by

$$\mathcal{L}_{Yuk} = Y_{ij}^{LQ\phi} L_i Q_j \phi + Y_{ij}^{\bar{e}\bar{u}\phi} \bar{e}_i \bar{u}_j \phi^\dagger + Y_{ij}^{\bar{d}\chi H} \bar{d}_i \chi_j H + Y_i^{L\bar{\chi}\phi} L_i \bar{\chi} \phi^\dagger + H.c.. \tag{4.8}$$

Besides the SM gauge symmetry group, we have to demand baryon-number conservation, in order to forbid the operators $Y_{ij}^{QQ\phi} Q_i Q_j \phi^\dagger$ and $Y_{ij}^{\bar{d}\bar{u}\phi} \bar{d}_i \bar{u}_j \phi$, which induce proton decay in analogy to Ref. [313].

4.2.2 Neutrino mass generation

The neutrino mass receives its dominant contribution from the loop diagrams in Figure 4.4. The two-loop $\mathcal{O}_8$ contribution (as well as the corresponding three-loop contribution obtained by connecting the two external Higgs lines) is generally subdominant to the one-loop $\mathcal{O}_{3b}$ contribution unless the coupling of the leptoquark ϕ to right-handed fermions is much larger, $|Y_{i3}^{\bar{e}\bar{u}\phi}| \gg |Y_{j3}^{LQ\phi}|$. The neutrino mass matrix is proportional to the down-type quark mass matrix, dominated by the bottom quark. For simplicity we will assume that the vector-like quark only mixes with the third generation quarks and set all couplings to the first two generation quarks to zero. In addition we will focus on the $\mathcal{O}_3$ contribution, neglect the $\mathcal{O}_8$ contributions, and assume $Y_{ij}^{\bar{e}\bar{u}\phi} = 0$.

Decomposing the vector-like quark χ and $\bar{\chi}$ into its components with respect to SU(2)$_L$, we write

$$\chi = \begin{pmatrix} B' \\ Y \end{pmatrix}, \qquad \bar{\chi} = \begin{pmatrix} \bar{Y} \\ \bar{B}' \end{pmatrix}. \tag{4.9}$$

$\bar{Y}$ and Y form a Dirac pair with mass $m_Y = m_\chi$ and $\bar{B}'$ and B' mix with the gauge eigenstate of the bottom quark b',

$$\begin{pmatrix} \bar{b} \\ \bar{B} \end{pmatrix} = \begin{pmatrix} c_1 & s_1 \\ -s_1 & c_1 \end{pmatrix}^\dagger \begin{pmatrix} \bar{b}' \\ \bar{B}' \end{pmatrix}, \quad \begin{pmatrix} b \\ B \end{pmatrix} = \begin{pmatrix} c_2 & s_2 \\ -s_2 & c_2 \end{pmatrix}^\dagger \begin{pmatrix} b' \\ B' \end{pmatrix}, \tag{4.10}$$

forming the mass eigenstates b and B. The physical masses are

$$m_b^2 = m_{b'}^2 - m_{bB}^2 \frac{m_\chi^2}{m_\chi^2 - m_{b'}^2}, \qquad m_B^2 = m_\chi^2 + m_{bB}^2 \frac{m_{b'}^2}{m_\chi^2 - m_{b'}^2}. \tag{4.11}$$

with $m_{bB} = Y_3^{\bar{d}\chi H} v/\sqrt{2}$, $m_{b'} = y_b v/\sqrt{2}$ and the mixing angles are given by

$$s_1 = \frac{m_{bB}\, m_\chi}{m_\chi^2 - m_{b'}^2}, \qquad s_2 = \frac{m_{bB}\, m_{b'}}{m_\chi^2 - m_{b'}^2}, \tag{4.12}$$

with $c_{1,2} = \sqrt{1 - s_{1,2}^2}$. After electroweak symmetry breaking, and in the $m_b \ll m_B, m_\phi$ limit, we calculate the radiatively generated neutrino mass as

$$(m_\nu)_{ij} = \frac{3}{16\pi^2} \left(Y_{i3}^{LQ\phi} Y_j^{L\bar{\chi}\phi} + (i \leftrightarrow j) \right) m_{bB} \frac{m_b m_B}{m_\phi^2 - m_B^2} \ln \frac{m_B^2}{m_\phi^2}. \tag{4.13}$$

This is a rank 2 matrix, thus there is one almost massless neutrino and two massive neutrinos.

Next we would like to use the low-energy parameters (the PMNS matrix as well as the neutrino masses) to determine the Yukawa couplings in terms of the high-scale parameters. The flavour structure of the neutrino mass matrix can be parameterised by vectors $a_\pm$ and a common factor α,

$$m_\nu = \alpha(a_+ a_-^T + a_- a_+^T), \tag{4.14}$$

i.e. the neutrino mass matrix is generated by multiplying two different vectors $a_\pm$ symmetrically. On the other hand it can be written in terms of the low-energy parameters for normal (NO) as well as inverted (IO) mass ordering,

$$m_\nu^{NO} = m_2 u_2^* u_2^\dagger + m_3 u_3^* u_3^\dagger, \qquad m_\nu^{IO} = m_1 u_1^* u_1^\dagger + m_2 u_2^* u_2^\dagger, \tag{4.15}$$

where m_i are the neutrino masses and $U = (u_1, u_2, u_3)$ is the PMNS matrix. We can rewrite the right-most expression of Equation (4.14) as

$$\alpha(a_+ a_-^T + a_- a_+^T) = \frac{\alpha}{2}\left[\left(\frac{a_+}{\zeta} + \zeta a_-\right)\left(\frac{a_+}{\zeta} + \zeta a_-\right)^T - \left(\frac{a_+}{\zeta} - \zeta a_-\right)\left(\frac{a_+}{\zeta} - \zeta a_-\right)^T\right] \tag{4.16}$$

and match it onto Equation (4.15) to obtain the vectors $a_\pm$ in terms of the low-energy parameters:

$$a_\pm^{\mathrm{NO}} = \frac{\zeta^{\pm 1}}{\sqrt{2\alpha}}\left(\sqrt{m_2} u_2^* \pm i\sqrt{m_3} u_3^*\right), \quad a_\pm^{\mathrm{IO}} = \frac{\zeta^{\pm 1}}{\sqrt{2\alpha}}\left(\sqrt{m_1} u_1^* \pm i\sqrt{m_2} u_2^*\right) . \tag{4.17}$$

The complex parameter ζ is a free parameter not determined by low-energy physics. In the following analysis we use the best fit values (v1.2) of the NuFIT collaboration [314][1] assuming normal ordering:

$$\begin{aligned} \sin^2\theta_{12} &= 0.306\,, & \Delta m_{21}^2 &= 7.45 \times 10^{-5}\ \mathrm{eV}^2\,, \\ \sin^2\theta_{13} &= 0.0231\,, & \Delta m_{31}^2 &= 2.417 \times 10^{-3}\ \mathrm{eV}^2\,, \\ \sin^2\theta_{23} &= 0.446\ . \end{aligned} \tag{4.18}$$

Furthermore we set the lightest neutrino mass to zero and assume vanishing CP phases in the PMNS matrix, i.e. $\delta = \varphi_1 = \varphi_2 = 0$.

4.2.3 Constraints from flavour physics and neutrinoless double-beta decay

Experimental constraints on flavour violating processes already constrain the parameter space. Similarly to the two-loop model in Ref. [313], we expect the most stringent constraints from LFV processes, in particular from the $\mu \to e$ transition. We calculated $\mu \to e\gamma$, $\mu \to eee$ as well as $\mu N \to eN$ conversion in nuclei and compared the results with the current experimental limits. We use the contributions calculated in Ref. [313] and add the contributions from the additional coupling of the leptoquark to the vector-like lepton (see the Appendix of Ref. [2] for details).

As all parameters are fixed by the leptonic mixing and the neutrino masses, the constraints directly translate to a constraint on the complex rescaling parameter ζ, more precisely on $|\zeta|$. The phase of ζ drops out in the flavour physics amplitudes, at least for the leading contributions, because they are of the form $Y_i^{L\bar{\chi}\phi *} Y_j^{L\bar{\chi}\phi}$ and $Y_i^{LQ\phi *} Y_j^{LQ\phi}$. We present the constraints on $|\zeta|$ while varying one of the masses $m_{\phi,\chi}$ in Figure 4.5. The other mass is fixed to 2 TeV. The grey

[1] The newest best fit values in v1.3 of the NuFIT collaboration are slightly changed. See [315, 316] for other global fits to the neutrino oscillation data.

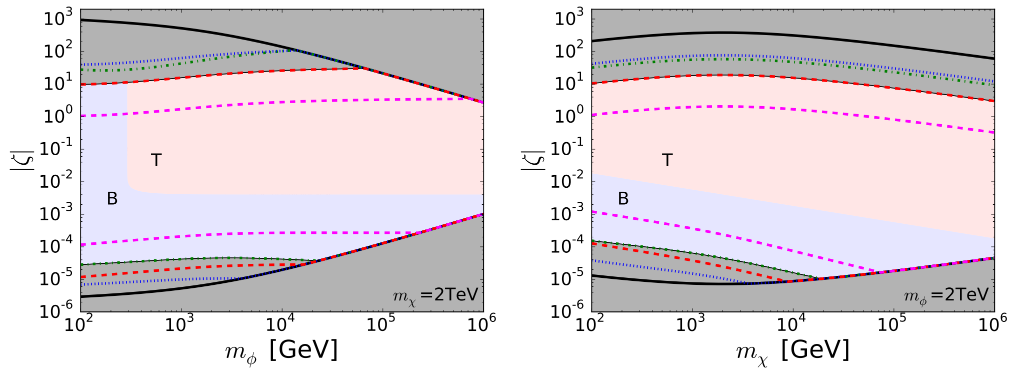

FIGURE 4.5: Constraints in $(m_{\{\phi,\chi\}}, |\zeta|)$ parameter space. The grey shaded region is excluded by: perturbativity of Yukawa couplings by requiring $\max(|Y_{ij}^{LQ\phi}|, |Y_{ij}^{L\bar{\chi}\phi}|) < 1$ (black solid); Br$(\mu \to e\gamma) < 5.7\times10^{-13}$ [317] (green dot-dashed); Br$(\mu \to eee) < 10^{-12}$ [318] (blue dotted); and Br$(\mu\mathrm{Au} \to e\mathrm{Au}) < 7 \times 10^{-13}$ [318] (red dashed). The magenta dashed line indicates the projected experimental sensitivity of $\mu\mathrm{Ti} \to e\mathrm{Ti}$ conversion in Mu2E at FNAL and COMET at J-PARC [319–321]. As well, we indicate two phenomenologically different experimental search regions for the leptoquark ϕ: the light blue region (B) has Br$(\phi \to b\nu) \approx 100\%$, while the light red region (T) has Br$(\phi \to b\nu) < 100\%$.

shaded region is excluded (see the caption for an explanation of the different exclusion lines). Within the bounds on $|\zeta|$ from LFV experiments there are two regions, separated by a sharp transition, with very different search strategies for the leptoquark ϕ. The light blue shaded region (region B) indicates the allowed region with Br$(\phi \to b\nu) \approx 100\%$. The light red shaded region (region T) has Br$(\phi \to b\nu) < 100\%$. We discuss both of these regions in Section 4.2.5.

In addition to constraints from flavor violating processes, there are constraints from lepton-number violating processes, like neutrinoless double beta decay. This specific model will lead to additional short-range contributions to neutrinoless double beta decay via couplings to the first generation of quarks. As neutrino mass does not depend on the coupling to the first generation of quarks, this bound can always be satisfied by setting these couplings to zero without affecting the mechanism of neutrino mass generation. This leaves the long-range contribution via an exchange of active neutrinos, which is controlled by the effective mass

$$\langle m_{ee} \rangle = \sum U_{ei}^2 m_i \, . \tag{4.19}$$

As the minimal framework leads to a strong mass hierarchy, there are currently no competitive constraints from neutrino-less double beta decay, similarly to the discussion in Ref. [313].

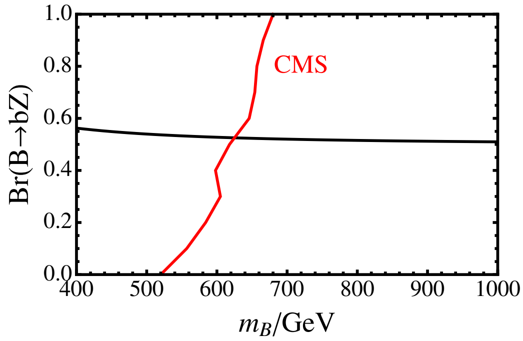

FIGURE 4.6: The branching ratio of $B \to bZ$ as a function of the heavy B mass with the observed limit from CMS.

4.2.4 Vector-like quark search

The mass eigenstate B will decay mainly through $B \to Zb$ and $B \to Hb$ while the third channel $B \to W^- t$ is highly suppressed due to the small mixing between the heavy vector-like quark B and the SM b-quark. The dominant branching ratios obey the relation

$$\frac{\mathrm{Br}(B \to Zb)}{\mathrm{Br}(B \to Hb)} = \frac{\lambda(1, r_b, r_Z)^{1/2}}{\lambda(1, r_b, r_H)^{1/2}} \frac{1 + r_Z^2 - 2r_b^2 - 2r_Z^4 + r_b^4 + r_Z^2 r_b^2}{1 + 6r_b^2 - r_H^2 + r_b^4 - r_b^2 r_H^2} , \qquad (4.20)$$

where $r_{b,H,Z} = m_{b,H,Z}/m_B$ and

$$\lambda(M, m_1, m_2) = (M^2 - (m_1 + m_2)^2)(M^2 - (m_1 - m_2)^2) . \qquad (4.21)$$

We can easily read our limit on the mass of B, $m_B \gtrsim 620$ GeV, from the exclusion curve provided by a dedicated CMS search [322], which is reproduced in Figure 4.6 as a function of the branching ratios.

4.2.5 Leptoquark searches

In the following subsection we take $L \equiv \{e, \mu, \tau\}$ and $l \equiv \{e, \mu\}$. The scalar leptoquark ϕ can be pair-produced at the LHC via gg fusion and $q\bar{q}$ annihilation. The cross section $\sigma(pp \to \phi\phi)$ is determined purely by colour charge and therefore depends only on the mass m_ϕ. We use NLO PROSPINO2 [323] cross sections for the LHC running at $\sqrt{s} = 8$ TeV, which gives $\sigma(pp \to \phi\phi) = 82$ (23.5) fb for $m_\phi = 500$ (600) GeV. We ignore the t-channel lepton exchange contribution and single production $qg \to \phi L$, since these will be suppressed by powers of small Yukawa couplings.

Upon pair production, the leptoquarks will decay with branching ratios dependent on the parameters $Y_{L3}^{LQ\phi}$ and $Y_3^{\bar{d}\chi H}$ relevant to neutrino mass generation.

The partial decay widths are

$$\Gamma(\phi \to Lt) = \frac{m_\phi}{8\pi} \left| Y_{L3}^{LQ\phi} \right|^2 f(m_\phi, m_L, m_t) \,, \tag{4.22}$$

$$\begin{aligned}\Gamma(\phi \to \nu_L b) = {} & \frac{m_\phi}{8\pi} \left(\left| Y_{L3}^{LQ\phi} c_2 \right|^2 + \left| Y_L^{L\bar{\chi}\phi} s_1 \right|^2 \right) f(m_\phi, m_{\nu_L}, m_b) \\ & - \frac{m_\phi}{4\pi} \mathrm{Re} \left(Y_{L3}^{LQ\phi} c_2 Y_L^{L\bar{\chi}\phi} s_1^* \right) f'(m_\phi, m_{\nu_L}, m_b) \,,\end{aligned} \tag{4.23}$$

$$\begin{aligned}\Gamma(\phi \to \nu_L B) = {} & \frac{m_\phi}{8\pi} \left(\left| Y_{L3}^{LQ\phi} s_2 \right|^2 + \left| Y_L^{L\bar{\chi}\phi} c_1 \right|^2 \right) f(m_\phi, m_{\nu_L}, m_B) \\ & + \frac{m_\phi}{4\pi} \mathrm{Re} \left(Y_{L3}^{LQ\phi} s_2 Y_L^{L\bar{\chi}\phi} c_1^* \right) f'(m_\phi, m_{\nu_L}, m_B) \,,\end{aligned} \tag{4.24}$$

$$\Gamma(\phi \to LY) = \frac{m_\phi}{8\pi} \left| Y_L^{L\bar{\chi}\phi} \right|^2 f(m_\phi, m_L, m_Y) \,, \tag{4.25}$$

where b, B are the two heaviest down-type quark mass eigenstates and the functions f, f' are defined as

$$f(M, m_1, m_2) = \frac{\left(M^2 - m_1^2 - m_2^2\right) \lambda(M, m_1, m_2)^{1/2}}{2\, M^4} \,, \tag{4.26}$$

$$f'(M, m_1, m_2) = \frac{m_1 m_2 \lambda(M, m_1, m_2)^{1/2}}{M^4} \,, \tag{4.27}$$

with λ given in Equation (4.21). The term in the second lines of Equation (4.23) and Equation (4.24) is neglible because it is suppressed by the neutrino mass. Note that the phase of ζ drops out in all decay widths. Non-zero couplings that are not constrained by the neutrino mass generation generally open extra decay channels. Since we are only interested in the consequences of neutrino mass generation, all these couplings are taken to be zero.

In the following we will concentrate on the region in parameter space with $m_Y, m_B \gg m_\phi$: each leptoquark may decay into either $b\nu$ or tL, resulting in $b\nu b\nu$, $b\nu tL$ or $tLtL$ after pair production. The branching ratios are determined by the single complex parameter ζ after fitting to low energy parameters as described in Section 4.2.2. There are two regions of interest:

- Region B where the branching ratio $\mathrm{Br}(\phi \to b\nu) \approx 100\%$, either because the other channels are kinematically not accessible for $m_\phi \lesssim m_t$ or $\left|Y^{LQ\phi}\right| \ll \left|Y^{L\bar{\chi}\phi}\right|$. It is shaded light blue in Figure 4.5.
- Region T in which all decay channels are open. It is shaded light red in Figure 4.5.

In region B we have $\mathrm{Br}(\phi \to \sum b\nu_L) \approx 1$, resulting in a $bb\not{E}_T$ final state for which sbottom pair searches can be directly applied [324, 325]. In this case m_ϕ is constrained to be $\gtrsim$ 730 GeV at 95% CL. Figure 4.7 shows branching ratios for region T in the case of normal ordering. The hierarchy between $\mathrm{Br}(\phi \to t\mu) \approx$

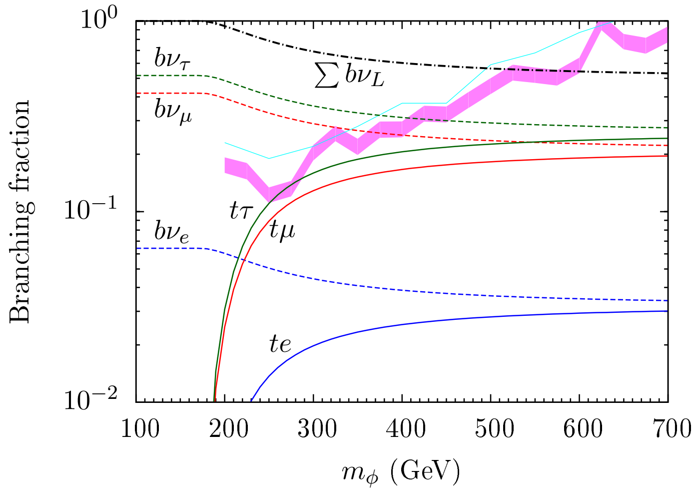

FIGURE 4.7: Branching fractions for ϕ as a function of m_ϕ in the region T. Also shown are limits on $\mathrm{Br}(\phi \to \sum_L b\nu_L)$ from sbottom pair searches of ATLAS (light blue) and CMS (the limit line lies somewhere within the magenta band).

$\mathrm{Br}(\phi \to t\tau)$ and $\mathrm{Br}(\phi \to te)$ is larger for normal compared to inverted mass ordering.[2] Hence there will be slightly more electrons in final states for the inverted mass ordering. The relative size of $\mathrm{Br}(\phi \to t\mu)$ and $\mathrm{Br}(\phi \to t\tau)$ is controlled by the atmospheric mixing angle θ_{23}, i.e. for $\theta_{23} > \pi/4$, $\mathrm{Br}(\phi \to t\mu) > \mathrm{Br}(\phi \to t\tau)$ and we expect the limits to get slightly stronger. In the limit of large m_ϕ it is apparent that $\mathrm{Br}(\phi \to \sum b\nu_L) \approx \mathrm{Br}(\phi \to \sum tL) \approx 0.5$.

In region T we can now calculate the branching fractions to LHC reconstructable final states.[3] The most frequent final state is $bb\not{E}_T$ at about 30%; as we will see, because $\mathrm{Br}(\phi \to \sum b\nu_L)$ is always greater than 50%, existing sbottom pair searches alone can provide a bound of $m_\phi > 500$ GeV. But can another final state compete? The next most frequent final state is $lbbjj\not{E}_T$ at about 22%; in this case, searches for top squark pairs in final states with one isolated lepton are applicable. About 8% of the time a two-lepton final state is produced; again, searches for top squark pairs are applicable. Three- and four-lepton final states are also predicted by this model in $\lesssim 1\%$ of events. For $m_\phi = 600$ GeV, where we will find the existing bound lies, one expects ≈ 500 leptoquark pair events in the $\sqrt{s} = 8$ TeV dataset. When compared to existing limits, it turns out there are simply not enough three- or four-lepton events to provide a competitive limit [327, 328]. However it is possible that, with more data at $\sqrt{s} = 13$ TeV, these final states can be competitive.

In the following subsections we will cover three final states of interest, namely $bb\not{E}_T$, $l\not{E}_T + (b\text{-})jets$, and $l^+l'^-\not{E}_T + jets$. Our aim is to recast LHC stop

[2] For example, at $m_\phi = 500$ GeV, normal ordering gives $(0.028, 0.183, 0.226)$ for $\mathrm{Br}(\phi \to te, t\mu, t\tau)$, whilst inverted ordering gives $(0.070, 0.165, 0.202)$.

[3] We do not attempt to reconstruct τ leptons since this will not improve sensitivity. CMS has performed a dedicated search for leptoquarks decaying to $t\tau$ [326]; the resulting bounds are not competitive with the bounds found henceforth.

searches [329, 330] in order to constrain m_ϕ.

Event samples and reconstruction

We generated two hadron-level signal samples[4] at $m_\phi = (500, 600)$ GeV using PYTHIA 8.180 with default tune [27, 28]; each contained 5×10^6 pair-produced leptoquark events where at least one leptoquark decays to tL. A validation set of 10^7 $t\bar{t}$ events where at least one t decays leptonically was also generated using PYTHIA, normalised to the predicted NNLO+NNLL cross section of $235 \times [1 - \mathrm{Br}(W \to \text{hadrons})^2]$ pb = 137 pb [331–336]. Lastly we used MADGRAPH5 V1.5.10 and PYTHIA to generate a validation set of 10^5 stop pair events, where the stops each decayed to a top and neutralino, $\tilde{t}_1 \to t\tilde{\chi}_1^0$; we took $m(\tilde{t}_1, \tilde{\chi}_1^0) = (600, 50)$ GeV.

The event samples were reconstructed after passing through the DELPHES 3.0.12 detector fast-simulation [29], both with and without simulated pileup. Jets were reconstructed with FASTJET 3.0.6 [337] using the anti-k_t clustering algorithm [338] with radius parameter 0.4, and were required to have $p_T > 20$ GeV. We used a flat b-tag rate of 70%, with a rejection factor of 5 (140) for jets initiated by charm (light) quarks. Electrons were considered isolated if $\sum p_T$, the scalar sum of the p_T of inner detector tracks with $p_T > 1$ GeV within a $\Delta R = 0.2$ cone surrounding the electron candidate, was less than 10% of the electron p_T. Muons were considered isolated if $\sum p_T$, defined as above, was less than 1.8 GeV. Otherwise, the default DELPHES ATLAS card was used. In the simulations with pileup we used a mean pileup $\mu = 21$, and pileup subtraction was performed using default parameters; the neutral pileup subtraction uses the jet area method [339, 340] with average contamination density ρ calculated using a k_t jet clustering algorithm with radius parameter 0.6. We note that this pileup subtraction method does not match that used in either of the ATLAS analyses. The results simulated with pileup therefore serve only as an indicator of pileup effects.

Further cuts were made with the aid of the MADANALYSIS5 v1.1.10beta SAMPLEANALYZER framework [271]. For preselection we required isolated leptons and

$$|\eta_e| < 2.47, \qquad |\eta_\mu| < 2.4, \qquad |\eta_j| < 2.5, \qquad p_T^l > 10\,\text{GeV}. \tag{4.28}$$

We rejected jets within $\Delta R = 0.2$ of a preselected electron, and leptons within $\Delta R = 0.4$ of remaining jets.

Each of the stop search analyses use variants of m_{T2}, known as the Cambridge m_{T2} or stransverse mass variable [341, 342], as a powerful discriminant of signal over background. For events where mother particles are pair produced and subsequently decay to two visible branches along with invisible momentum,

[4] We also used $m_\chi = 2$ TeV and $s_1 = 0.01$, but the branching ratios do not depend on the choice of m_χ and s_1 as long as $m_\chi > m_\phi$.

such as in leptonic or semi-leptonic $t\bar{t}$ decays, m_{T2} can be constructed to have an upper limit at the mother particle mass. It is defined as

$$m_{T2}(\vec{p}_T^{\,i}, \vec{p}_T^{\,j}, \not{\vec{p}}_T) = \min_{\vec{u}_T + \vec{v}_T = \not{\vec{p}}_T} \left\{ \max \left[m_T(\vec{p}_T^{\,i}, \vec{u}_T), m_T(\vec{p}_T^{\,j}, \vec{v}_T) \right] \right\}, \quad (4.29)$$

where $\not{\vec{p}}_T$ is the missing transverse momentum, $\vec{p}_T^{\,i}$ and $\vec{p}_T^{\,j}$ are the transverse momenta of two visible decay branches, and m_T is the usual transverse mass calculated assuming some mass for the invisible particle associated with that branch. It can be thought of as the minimum mother particle mass consistent with pair production, the decay hypothesis, and the observed kinematics. We calculated m_{T2} using the publicly available bisection method codes of Refs. [343, 344].

$bb\not{E}_T$

The $bb\not{E}_T$ final state arises primarily from the decay $\phi\phi \to b\nu b\nu$. There are also contributions from the other decay chains, where either leptons are missed or hadronically decaying taus are produced; these contributions will be subleading and additive, and will generally appear with extra hard jet activity in the event which may be vetoed in analyses. We will ignore them to obtain a slightly conservative limit.

Constraints on the production cross section of sbottom pairs decaying via $\tilde{b}_1 \to b\tilde{\chi}_1^0$ have been provided by both ATLAS and CMS [324, 325]. Along the contour $m_{\tilde{\chi}_1^0} = 0$, this provides a limit on the production cross section $\sigma(pp \to \phi\phi) \times \mathrm{Br}(\phi \to b\nu)^2$, and therefore on $\mathrm{Br}(\phi \to b\nu)$. These limits are reproduced in Figure 4.7.[5] The existing 95% CL limit from the CMS search for region T is somewhere between $m_\phi > 520$–600 GeV.

$l\not{E}_T + (b\text{-})jets$

The single lepton final state is produced primarily through the mixed decay $\phi\phi \to b\nu tL \to ljjbb\not{E}_T$, where the top decays hadronically. This final state is the same as for semi-leptonically decaying top pairs, which is the primary SM background. It can also be given by stop pairs decaying via the chains $\tilde{t}_1 \to b\tilde{\chi}_1^\pm \to bW^{(*)}\tilde{\chi}_1^0 \to bl\nu\tilde{\chi}_1^0$ or $\tilde{t}_1 \to t^{(*)}\tilde{\chi}_1^0 \to bl\nu\tilde{\chi}_1^0$. ATLAS and CMS have performed searches for stop pairs in the single lepton final state, with no significant excess observed [329, 345].[6] In this section we will recast the ATLAS analysis.

[5] The ATLAS limit on $\mathrm{Br}(\phi \to b\nu)$ can be read off the auxiliary Figure 5. The CMS limit on $\sigma(pp \to \phi\phi) \times \mathrm{Br}(\phi \to b\nu)^2$ can be read off Figure 6 and converted to a limit on $\mathrm{Br}(\phi \to b\nu)$ using the NLO value of $\sigma(pp \to \phi\phi)$ from PROSPINO2.

[6] In the time since this analysis was performed, ATLAS submitted a more detailed search in this channel [346].

		SRtN2	SRtN3	SRbC1	SRbC2	SRbC3
$m_{\tilde{t}_1} = 600$ GeV	$\mathcal{A}\varepsilon$ ATLAS (%)	2.7	2.3	5.7	1.7	0.84
$m_{\tilde{\chi}_1^0} = 50$ GeV	$\mathcal{A}\varepsilon$ obtained (%)	2.0 (2.1)	1.4 (1.5)	5.8 (5.6)	1.8 (1.6)	1.0 (0.83)
$m_\phi = 500$ GeV	N	21 (22)	14 (14)	75 (74)	28 (26)	16 (14)
$m_\phi = 600$ GeV	N	7.8 (8.3)	5.5 (5.7)	26 (26)	11 (10)	7.0 (6.4)
NP limit		10.7	8.5	83.2	19.5	7.6
Approximate m_ϕ limit (GeV)		567 (574)	553 (556)	490 (489)	537 (532)	589 (579)

TABLE 4.4: Acceptance times efficiency ($\mathcal{A}\varepsilon$) and total number of events (N) for three event samples without (with) pileup. The stop pair production sample is compared to the ATLAS result as a validation of our analysis. The 95% CL limit on new physics (NP) contributions are given; these limits are quoted ATLAS results. Lastly we provide an approximate limit on m_ϕ based on our results.

After preselection we demanded exactly two opposite sign leptons with the leading lepton having $p_T > 25$ GeV, at least four jets with $p_T > 80$, 60, 40, 25 GeV, and at least one tagged b-jet. We refer to Ref. [329] for the definitions of the remaining kinematical variables and of the signal regions (SRs) SRtN2-3 and SRbC1-3, designed for $\tilde{t}_1 \to t\tilde{\chi}_1^0$ and $\tilde{t}_1 \to b\tilde{\chi}_1^\pm$ topologies respectively (see their Table 1). Variables am_{T2} and m_{T2}^τ are variants of m_{T2} designed to reject leptonic and semi-leptonic $t\bar{t}$ background respectively: am_{T2} takes for its visible branches b and (bl), with a missing on-shell W associated with the b branch; m_{T2}^τ takes l and a jet for its visible branches, assuming massless invisible states. Both am_{T2} and m_{T2}^τ require two jets in the event to be chosen as b-jets, regardless of whether they are b-tagged. ATLAS are able to choose those jets which have the highest b-tag weight. However, DELPHES only outputs a boolean variable which identifies whether a jet is b-tagged or not. We must therefore find a way to choose two b-jets. We follow Ref. [344]. There are three cases:

- 2 b-tags: Take both as b-jets.
- 1 b-tag: Assume that second b-jet is in the leading two non-b-tagged jets.
- 0 or > 2 b-tags: Ignore b-tagging information and assume that b-jets are in leading three jets.

Then, to calculate am_{T2}, we take the $j_i(j_k l)$ permutation over the b-jet candidates which minimises am_{T2}. For m_{T2}^τ we assume that the τ-jet is in the leading three jets. We find the $j_i l$ combination over the candidate jets which minimises m_{T2}^τ. These methods are in the spirit of m_{T2} as the minimum mother particle mass consistent with the decay hypothesis and observed kinematics. Since the minimum plausible m_{T2} value is selected, the results after cuts are also conservative. We compared our obtained am_{T2} and m_{T2}^τ distributions for the $t\bar{t}$ sample at the preselection stage to Figure 3 in the ATLAS analysis [329] and found good agreement, particularly at large values where cuts are made.

The $N^{\text{iso-trk}}$ cut applied to the SRbC1-3 SRs cannot be replicated after our reconstruction has been performed. Cut-flows published in auxiliary Figures 112–117 of Ref. [346] suggest that after all other cuts, the $N^{\text{iso-trk}}$ requirement reduces the signal by 15–25%, consistent between the single-muon and single-electron channel. We therefore conservatively post-scale our results in the SRbC1-3 SRs by a factor 0.75 to take this into account.

The results of our analysis are shown in Table 4.4. The acceptance times efficiency ($\mathcal{A}\varepsilon$) for our stop pair validation sample agree well with ATLAS results in each of the signal regions; our predicted event rates are likely an underestimate for the SRtN2-3 SRs. We are confident that the discrepancies can be assigned to some combination of: different event generators, the third-party detector simulation, our b-tagging efficiency approximation, the necessary amendments to am_{T2} and m_{T2}^{τ} calculation methods, and our inability to recreate the pileup subtraction procedure. The predicted number of events in the 20.7 fb^{-1} of data for each of the signal samples are also given in Table 4.4.

Since the branchings of ϕ and the distribution shapes do not change significantly from masses 500 GeV to 600 GeV, and since $\log[\sigma(pp \to \phi\phi)]$ varies approximately linearly with mass m_ϕ, an approximate limit on m_ϕ can be determined by taking the published ATLAS new physics (NP) limits and assuming that, in each SR, the log of the number of accepted events scales linearly with m_ϕ. These results are also shown in Table 4.4. Since this is only a recast of the ATLAS results, these limits are not to be taken too seriously; they serve only as an indication of the present experimental reach.

We note that these limits are found using the sum of single electron and muon channels. In our model $\approx 75\%$ of accepted events are single muons, whereas an approximately even share is expected for the background (and stops). We would likely obtain stronger limits if ATLAS published a NP limit on each lepton channel separately.

$l^+l'^- \not{E}_T + jets$

The dilepton final state is produced primarily through the mixed decay $\phi\phi \to b\nu tL \to l^+l'^- bb\not{E}_T$. There is also a non-negligible contribution from $\phi\phi \to tLtL'$, where the top pair and possible τ lepton(s) decay such that only two leptons are detected. This final state is the same as for leptonically decaying top pairs or for stop pairs decaying via the same chains considered in the previous subsection. ATLAS has performed a search for stop pairs in the dilepton final state, with no significant excess observed [330]. In this section we will recast the analysis in order to place a constraint on m_ϕ.

After preselection we demanded exactly two opposite sign leptons with the leading lepton having $p_T > 25$ GeV. Any lepton pairs with invariant mass less than 20 GeV were rejected. We then defined three SRs in Table 4.5: L110, L100, and C1. We use the notation $p_T[1]$ ($p_T[2]$) to stand for the leading (subleading)

L110	L100	C1
$m(l^+l^-)^{<71}_{>111}$ GeV $\Delta\phi_b < 1.5$ $\Delta\phi_j > 1.0$		opposite flavour $m_{eff} > 300$ GeV $\not{E}_T > 50$ GeV
- -	$N(j) \geq 2$ $p_T^j[1] > 100$ GeV $p_T^j[2] > 50$ GeV	$N(j) \geq 2$ $p_T^j[1] > 50$ GeV
$m_{T2} > 110$ GeV	$m_{T2} > 100$ GeV	$m_{T2} > 150$ GeV

TABLE 4.5: Signal region selections after preselection requirements.

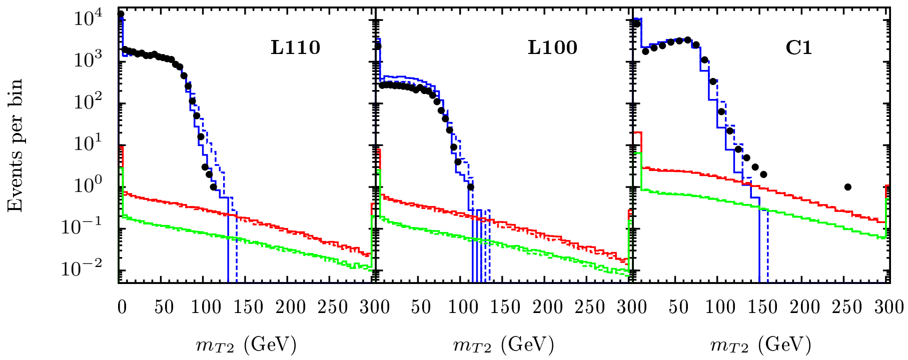

FIGURE 4.8: Distribution of m_{T2} opposite flavour events for the three SRs in $t\bar{t}$ and $m_\phi = 500, 600$ GeV event samples descending, simulated without (solid) and with (dashed) pileup. The ATLAS data, dominated by $t\bar{t}$ background for $m_{T2} \lesssim 100$ GeV, is overlaid as points. The apparent "excess" of $t\bar{t}$ events above $m_{T2} > 100$ GeV is only because we have not simulated subleading backgrounds (only $t\bar{t}$ is necessary for validation of our analysis). These can be compared with Figures 9, 10, and 3 respectively of Ref. [330].

p_T object. We refer to Ref. [330] for definitions of any unfamiliar variables. The most important is m_{T2}, which takes leptons for the visible branches and assumes massless missing particles. It is constructed to have a parton-level kinematic upper limit at m_W for the dominant $t\bar{t}$ background.

Plots of the number of events expected in 20.3 fb^{-1} of integrated luminosity for each SR are shown against m_{T2} for opposite flavour events in Figure 4.8. These are to be compared with Figures 3, 9, and 10 of the ATLAS analysis [330]. One can see that our analysis does a good job of reproducing the background distribution in the region $m_{T2} \lesssim 100$ GeV where $t\bar{t}$ dominates. We are confident that the discrepancies can be assigned to some combination of: an overall normalisation factor, the LO $t\bar{t}$ event generator, the third-party detector simulation, and our inability to recreate the pileup subtraction procedure. The number of events in the SRs are broken up by lepton flavour in Table 4.6.

The limits on the number of NP events summed over the lepton channels in SRs L110 and L100 are provided by ATLAS and reproduced in our Table 4.6. The limit from the C1 SR was not published, since this SR is subsequently filtered

	L110		L100		C1	
m_ϕ (GeV)	500	600	500	600	500	600
e^+e^-	0.93 (0.86)	0.34 (0.32)	0.79 (0.68)	0.30 (0.27)	-	-
$\mu^+\mu^-$	3.0 (2.8)	1.0 (0.93)	2.7 (2.3)	0.92 (0.81)	-	-
$\mu^\pm e^\mp$	4.6 (4.2)	1.5 (1.4)	3.9 (3.4)	1.4 (1.2)	7.5 (7.6)	2.8 (2.9)
$\sum_l l^+l'^-$	8.5 (7.8)	2.9 (2.7)	7.4 (6.3)	2.6 (2.3)	-	-
NP limit	9.0		5.6		2.3 *	
Approx. m_ϕ limit (GeV)	495 (487)		527 (512)		621 (622) *	

TABLE 4.6: Number of events in each SR without (with) pileup. The 95% CL limit on new physics contributions are also given; these limits are quoted ATLAS results for L110 and L100, and inferred from a plot for C1 (which is why we mark it with a *).

through a multivariate analysis. However, one can read off Figure 3 in Ref. [330] that three events were observed with $3.6^{+6.7}_{-?}$ expected before the multivariate analysis. It is therefore reasonable to model the probability density function for the expected number of events as a gamma distribution with shape parameter 1.3 and mean 3.6.[7] We performed toy Monte Carlo pseudoexperiments for different signal+background hypotheses (H_{s+b}) under this assumption, measuring

$$CL_s = \frac{Pr(n \leq n_{obs}|H_{s+b})}{Pr(n \leq n_{obs}|H_b)} \tag{4.30}$$

each time. We found $CL_s = 0.05$ for an expected new physics contribution of 2.3 events, corresponding to the observed 95% CL limit on the number of NP events determined using the CL_s method [347], the same as that used in the ATLAS analysis.

An approximate limit on m_ϕ can be derived in the same way described in the previous subsection, and the results are shown in Table 4.6. Again, since this is only a recast of the ATLAS analysis, these limits are not to be taken too seriously; they serve only as an indication of the present experimental reach.

The best limit is obtained from the C1 SR. There are three principal reasons for this. *(1)* The L110 and L100 limits are quoted on the sum over all flavour channels. In our model we expect greater than half of the events to be in the opposite-flavour channel. Simply requiring opposite flavour leptons reduces the background significantly (compare Figures 2 and 3 of Ref. [330]), so that one can afford to make softer cuts that keep more signal. *(2)* The L110 and L100 cuts on $\Delta\phi_b$ and $\Delta\phi_j$ are designed to reject background events with high m_{T2} arising from events with large $\not{E}_T$ from mismeasured jets. These cuts keep about 50% of the stop pair signals considered by ATLAS (see auxiliary Figures 24 and 25 of Ref. [330]). We found that only $\approx 35\%$ of events were kept for our model due to different kinematics. *(3)* The signal-to-background ratio and the limit is significantly improved if the cut on m_{T2} is slightly increased.

[7] The gamma distribution is the standard conjugate prior for rate parameters. A shape parameter of 1.3 ensures that $\int_{3.6}^{3.6+6.7} dx\, f(x; k = 1.3, \mu = 3.6) = 34.1\%$, corresponding to one half of the 68.2% confidence interval.

Summary

It is clear from these analyses that the existing constraints on the leptoquark from sbottom and stop searches are comparable, $m_\phi \gtrsim 600$ GeV. Inferred limits could be even stronger if the collaborations provided limits before combining lepton flavour channels. But this conclusion can be turned around: if the collaborations *were* to see a significant excess in any of the discussed final states, this model predicts that it should show up in all of them at around the same time, with a well-predicted, non-universal flavour signature and distinctive kinematics. Simple SUSY models might find this scenario difficult to accommodate.

4.3 Conclusion

In this Chapter we wrote down the minimal UV completions for all of the D7 $\Delta L = 2$ operators which could be responsible for radiatively generating a Majorana neutrino mass. These completions involve vector-like quarks, vector-like leptons, scalar leptoquarks, a charged scalar, a scalar doublet, and a scalar quadruplet. The properties of these particles are generally constrained by low-energy neutrino oscillation data, making the models predictive.

A detailed study of the collider bounds was presented for $\mathcal{O}_3 = LLQ\bar{d}H$ and $\mathcal{O}_8 = L\bar{d}\bar{e}^\dagger\bar{u}^\dagger H$ completions where a leptoquark $\phi \sim (\bar{3}, 1, \frac{1}{3})$ and a vector-like quark $\chi \sim (3, 2, -\frac{5}{6})$ are introduced. In the detailed study, we constrained the vector-like quark mass $m_\chi \gtrsim 620$ GeV using a dedicated LHC search. For the leptoquark ϕ we recast LHC sbottom/stop searches and explored in the parameter space allowed by the constraints from flavour physics. We found two distinct areas of parameter space, one where $\mathrm{Br}(\phi \to b\nu) \approx 100\%$, and the other where $\mathrm{Br}(\phi \to b\nu) < 100\%$. In the first case $m_\phi \gtrsim 520$–600 GeV, and in the second case we found $m_\phi \gtrsim 600$ GeV using three different final states.

Through this detailed analysis we have shown the powerful discovery and/or exclusion potential of the LHC for the radiative neutrino mass models based on $\Delta L = 2$ operators, and advanced a systematic approach to these searches.

5 Baryon Asymmetry of the Universe

This Chapter is based on the publications "Electroweak naturalness in the three-flavor type I seesaw model and implications for leptogenesis," and "Natural leptogenesis and neutrino masses with two Higgs doublets," each written in collaboration with Robert Foot and Raymond R. Volkas [3, 5]. See also the conference proceedings paper "How to avoid unnatural hierarchical thermal leptogenesis" [6].

The SM and the paradigm of electroweak symmetry breaking realised by the Higgs potential $V_{\text{SM}} = \mu^2\Phi^\dagger\Phi + \lambda\left(\Phi^\dagger\Phi\right)^2$, with $\mu^2(m_Z) \approx -(88\text{ GeV})^2$, has been extremely successful in explaining low energy phenomena. However it fails to explain neutrino masses and the baryon asymmetry of the Universe (BAU). A straightforward way to explain both, as introduced in Sections 1.1.3 and 1.1.4, is to add three heavy right-handed neutrinos: the minimal Type I seesaw model [72–74, 348]. Gauge invariance allows two additional renormalisable terms in the Yukawa Lagrangian,

$$-\Delta\mathcal{L}_Y = (y_\nu)_{ij}\overline{l_L^i}\tilde{\Phi}\nu_R^j + \frac{1}{2}M_i\overline{(\nu_R^i)^c}\nu_R^i + h.c., \tag{5.1}$$

where $l_L = (\nu_L, e_L)^T$, $\tilde{\Phi} = i\tau_2\Phi^*$, and M_i are the right-handed neutrino masses. After Φ gains a vev $\langle\Phi\rangle = v/\sqrt{2} \approx 174$ GeV the Type I seesaw model provides an elegant explanation for the smallness of the neutrino masses. If $y_\nu v \ll M_i$, the neutrino mass matrix is given by the seesaw formula

$$m_\nu = \frac{v^2}{2}y_\nu\mathcal{D}_M^{-1}y_\nu^T, \tag{5.2}$$

where $\mathcal{D}_M \equiv \text{diag}(M_1, M_2, M_3)$, suppressed by the presumably large right-handed neutrino mass scale. The BAU can be produced via hierarchical thermal leptogenesis [93]: the CP violating out-of-equilibrium decays of the lightest right-handed neutrino N_1 create a lepton asymmetry which is transferred to the baryon sector by electroweak sphalerons. The Davidson–Ibarra bound [96, 97], ensuring enough CP violation for successful hierarchical ($M_{N_1} \ll M_{N_2} \ll M_{N_3}$) thermal leptogenesis, is

$$M_{N_1} \gtrsim 5\times 10^8\text{ GeV}\left(\frac{v}{246\text{ GeV}}\right)^2, \tag{5.3}$$

where v is the vev that enters the seesaw Equation (5.2).

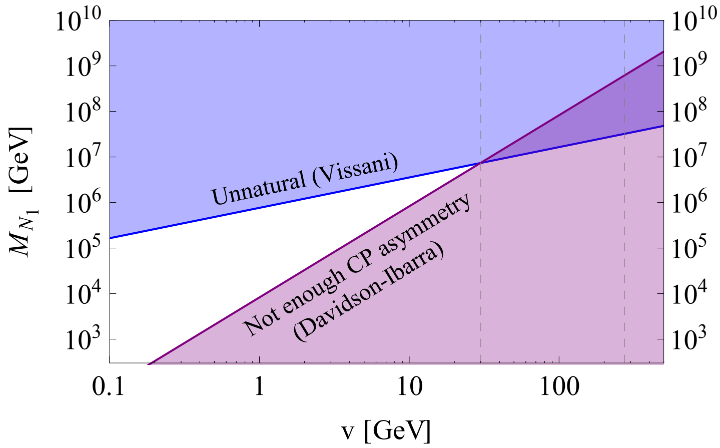

FIGURE 5.1: Bounds on hierarchical thermal leptogenesis as a function of v. Shown is the Davidson-Ibarra bound (purple), and the Vissani bound (blue). The dashed lines indicate $v = 246, 30$ GeV.

The ability of the minimal Type I seesaw model to simultaneously explain neutrino masses and the BAU is certainly intriguing. However, it appears to be incompatible with a naturalness argument for right-handed neutrinos made by Vissani [302] (see also Refs. [293, 296, 349–353]). In a *one-flavour* model, Vissani essentially bounded directly the induced μ^2 RGE term to obtain a naturalness bound on M_N:

$$\left|\frac{d\mu^2}{d\log\mu_R}\right| = \left|-\frac{1}{4\pi^2}y_\nu M_N^2 y_\nu^*\right| < 1\ \text{TeV}^2$$
$$\Rightarrow M_N \lesssim 3\times 10^7\ \text{GeV}\left(\frac{v}{246\ \text{GeV}}\right)^{\frac{2}{3}}, \tag{5.4}$$

where μ_R is the renormalisation scale, and the neutrino mass is $m_\nu = \frac{v^2}{2}\frac{y_\nu^2}{M_N} \approx 0.05$ eV. The incompatibility of leptogenesis and naturalness is exemplified in Figure 5.1; nowhere at $v = 246$ GeV is it possible to simultaneously fulfil the Davidson–Ibarra and Vissani bounds. Thus it appears that the minimal Type I seesaw model cannot explain both the observed neutrino masses and baryogenesis via standard thermal leptogenesis without ceding naturalness.

In Section 5.1 of this Chapter we address the following question: can three-flavour effects ameliorate this conflict? It is answered in the negative. We present a three-flavour treatment which generalises the Vissani result to obtain three naturalness bounds:

$$M_{N_1} \lesssim 4\times 10^7\ \text{GeV}, \tag{5.5}$$
$$M_{N_2} \lesssim 7\times 10^7\ \text{GeV}, \tag{5.6}$$
$$M_{N_3} \lesssim 3\times 10^7\ \text{GeV}\left(\frac{0.05\ \text{eV}}{m_{min}}\right)^{\frac{1}{3}}, \tag{5.7}$$

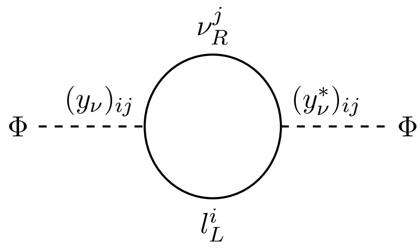

FIGURE 5.2: Loop diagram leading to $\delta\mu^2$.

where m_{min} is the lightest neutrino mass. We discuss how these bounds imply that natural N_1-, N_2-, or N_3-dominated hierarchical thermal leptogenesis is not possible in a minimal three-flavour Type I seesaw.

In Section 5.2 we address the logical follow-up question: in what minimal ways can this incompatibility be overcome? We list some solutions already existing in the liteature. We then focus on an apparently new solution motivated by the following observation: if $v \lesssim 30$ GeV in Equation (5.2), then Equations (5.3) and (5.4) become compatible, as is clear from Figure 5.1. Thus we expect that two-Higgs-doublet models with right-handed neutrinos (ν2HDMs) and $\tan\beta = v_1/v_2 \gtrsim 8$, where Φ_2 is responsible for a tree-level seesaw, can naturally accommodate leptogenesis and neutrino masses. Indeed, we discover viable natural models which predict a SM-like Higgs boson, (maximally) TeV-scale scalar states, and low to intermediate scale hierarchical leptogenesis with 10^3 GeV $\lesssim M_{N_1} \lesssim 10^8$ GeV.

5.1 Naturalness in the three-flavour Type I seesaw

5.1.1 Three-flavour Vissani bound

The neutrino mass matrix, entering the Lagrangian as $\frac{1}{2}\overline{\nu_L^i}(m_\nu)_{ij}(\nu_L^j)^c$, is given in Equation (5.2) and reproduced here: $m_\nu = \frac{v^2}{2} y_\nu \mathcal{D}_M^{-1} y_\nu^T$. One can diagonalise m_ν with a unitary matrix U,

$$\mathcal{D}_m \equiv \text{diag}(m_1, m_2, m_3) = U m_\nu U^T, \tag{5.8}$$

where m_i are the neutrino masses. Following Casas–Ibarra [94], it is possible to express y_ν as

$$y_\nu = \frac{\sqrt{2}}{v} U^\dagger \mathcal{D}_m^{\frac{1}{2}} R \mathcal{D}_M^{\frac{1}{2}}, \tag{5.9}$$

where R is a (possibly complex) orthogonal ($R^T R = R R^T = \mathbb{I}$) matrix. R is physically relevant and measurable in principle (e.g. by studying the production and decays of the ν_R^j), however measurements to date tell us nothing about it.

From Figure 5.2, we calculate the correction to μ^2 in $\overline{\text{MS}}$ scheme as

$$\delta\mu^2 = \frac{1}{(4\pi)^2}\left[-4y_\nu^{ij}M_j^2\left(\log\left[\frac{\mu_R}{M_j}\right]-\frac{1}{4}\right)y_\nu^{ij*}+\mathcal{O}\left(\mu^2\right)\right], \tag{5.10}$$

where μ_R is the renormalisation scale. The RGE for μ^2 therefore gains a contribution from all nine diagrams of

$$\frac{d\mu^2}{d\log\mu_R} \supset -\frac{4}{(4\pi)^2}\text{Tr}\left[y_\nu\mathcal{D}_M^2 y_\nu^\dagger\right]. \tag{5.11}$$

Upon substitution of the Casas–Ibarra form, this can be written

$$\frac{d\mu^2}{d\log\mu_R} \supset -\frac{4}{(4\pi)^2}\frac{2}{v^2}\text{Tr}\left[\mathcal{D}_m R\mathcal{D}_M^3 R^\dagger\right]. \tag{5.12}$$

Note that there is no explicit dependence on U, as one could anticipate, since all of U can be absorbed by $l_L \to Ul_L$, $y_\nu \to Uy_\nu$. One ends up with three corrections proportional to the cube of each heavy neutrino mass.

As argued in CHAPTER 3, if the new physics contribution in the $\mu^2(\mu_R)$ RGE is much larger than $\mu^2(m_Z)$ then this leads to a naturalness problem, manifesting as a sensitivity of the Higgs mass parameter to the high scale input parameters $\mu^2(\Lambda_h)$ and M_j. Naturalness demands that these corrections each be less than some scale not far above $\mu^2(m_Z) \simeq -(88\text{ GeV})^2$. Following Vissani, we bound each of the new contributions by 1 TeV^2:

$$\begin{aligned}&\frac{4}{(4\pi)^2}\frac{2}{v^2}M_j^3\sum_i m_i|R_{ij}|^2 < 1\text{ TeV}^2\\ &\qquad\Rightarrow M_j \lesssim 3\times 10^7\text{ GeV}\left(\frac{0.05\text{ eV}}{\sum_i m_i|R_{ij}|^2}\right)^{\frac{1}{3}},\end{aligned} \tag{5.13}$$

where R_{ij} are the entries of R. This equation reveals the Vissani result together with the three-flavour effects. Our results can be easily rescaled for a different naturalness criterion.

5.1.2 Extremising the bounds

Equation (5.13) results in three upper bounds on the right-handed neutrino masses. It says nothing about their mass ordering, since one can always append to R a permutation matrix. However we can always order the bounds by their size; we will call them B_j and take $B_1 \leq B_2 \leq B_3$.

We are interested in the values of B_j attainable from Equation (5.13). Thus all we have to do is extremise these bounds over R. We used the mass squared

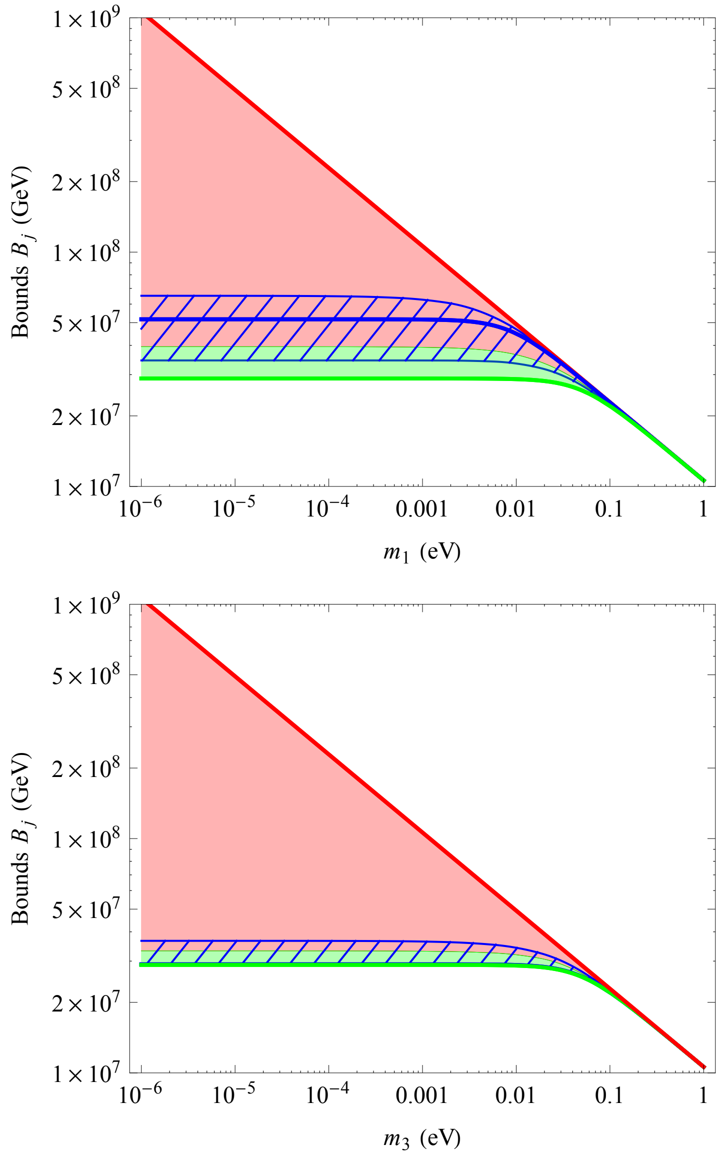

FIGURE 5.3: Region of attainable values for the $B_3 \geq B_2 \geq B_1$ (red/blue-hatched/green) right-handed neutrino mass naturalness bounds as a function of the lightest neutrino mass, by requiring their contribution to the $\mu^2(\mu_R)$ RGE be no greater than 1 TeV (Equation (5.13)). The upper (lower) panel is for NO (IO). The regions assume the orthogonal matrix R is real. Thick solid lines show the case when $R = \mathbb{I}$ (note that the thick blue line is obscured by the thick green line in the IO case). The case for complex R is similar, except there is no lower limit to the B_j (see text).

differences of NUFIT V2.0 [61],

$$\begin{aligned}\Delta m_{21}^2 &= 7.50 \times 10^{-5}\,\mathrm{eV}^2, \\ \Delta m_{3l}^2 &= \pm 2.46 \times 10^{-3}\,\mathrm{eV}^2,\end{aligned} \tag{5.14}$$

where $\Delta m_{3l}^2 = \Delta m_{31}^2 > 0$ for normal ordering (NO) and $\Delta m_{3l}^2 = \Delta m_{32}^2 < 0$ for inverted ordering (IO), and treat the lightest neutrino mass (m_1 for NO or m_3 for IO) as unknown. The B_j were numerically extremised over a parameterisation of R. The results were checked analytically and with scatterplots. Figure 5.3 show the cases for NO and IO when R is real. The solid lines are for $R = \mathbb{I}$.

The first thing to notice is that as the lightest neutrino mass tends to zero, the largest bound B_3 can potentially evaporate. This only happens in models where R is of a particular form, e.g. in NO, as is evident from Equation (5.13),

$$R = \begin{pmatrix} R_{11} & R_{12} & \pm 1 \\ R_{21} & R_{22} & 0 \\ R_{31} & R_{32} & 0 \end{pmatrix} \tag{5.15}$$

or some column permutation, where $R_{11} = R_{12} = 0$ if R is real. This corresponds to the Poincaré protected decoupling limit $y_\nu^{i3} \to 0$ and an effective two-flavour seesaw [354–356]. The maximisation of B_2 occurs when $B_2 = B_3$ and corresponds in NO to R of the form

$$R = \pm \begin{pmatrix} 0 & \frac{1}{\sqrt{2}} & -\frac{1}{\sqrt{2}} \\ 0 & \frac{1}{\sqrt{2}} & \frac{1}{\sqrt{2}} \\ \pm 1 & 0 & 0 \end{pmatrix}, \tag{5.16}$$

up to column permutations. Similarly the minimisation of B_2 occurs when $B_1 = B_2$, and corresponds to

$$R = \pm \begin{pmatrix} 0 & 0 & \pm 1 \\ \frac{1}{\sqrt{2}} & -\frac{1}{\sqrt{2}} & 0 \\ \frac{1}{\sqrt{2}} & \frac{1}{\sqrt{2}} & 0 \end{pmatrix}. \tag{5.17}$$

The maximisation (minimisation) of B_1 (B_3) occurs when $B_1 = B_2 = B_3$. This corresponds to a conspiratorial form of R.

Even though these arrangements are possible, it is clear from Figure 5.3 that it is not possible to construct a Type I seesaw model that changes the bounds B_1 and B_2 by more than a factor of 2 when R is real. Even if one does saturate these bounds, it is not possible then to place the right-handed neutrino masses at this bound and maintain a hierarchy which is a key assumption for the Davidson–Ibarra bound.

In the case of R complex the upper limits of the B_j are the same as the R real case. However the lower limits can potentially be much lower. The reason is that complex R with entries of arbitrarily large magnitude exist. Let us illustrate this in the two-flavour case. An example is

$$R = \begin{pmatrix} \cosh x & i \sinh x \\ -i \sinh x & \cosh x \end{pmatrix}. \tag{5.18}$$

In this case,

$$U y_\nu = \frac{\sqrt{2}}{v} \begin{pmatrix} \sqrt{m_1 M_1} \cosh x & -i\sqrt{m_1 M_2} \sinh x \\ i\sqrt{m_2 M_1} \sinh x & \sqrt{m_2 M_2} \cosh x \end{pmatrix}. \tag{5.19}$$

If $\cosh x \gg 1$, one need only calculate m_ν to see that the smallness of neutrino masses is only explained by fortuitous cancellations between entries of y_ν that constitute a fine tuning. If we demand that the entries of R have magnitude not exceeding 1, then the results for complex R are essentially the same as in the real case. In general, however, allowing complex R can only degrade the attainable region for the B_j.

5.1.3 Implications for leptogenesis

Corrections to the μ^2 parameter in the Type I seesaw model can be expressed in the concise form of Equation (5.12), as a function of an unknown (but in principle measurable) orthogonal matrix R. Requiring these corrections to be less than 1 TeV results in three bounds on the right-handed neutrino masses. Figure 5.3 reveals that, no matter what form R takes, there are three generic bounds:

$$M_{N_1} \lesssim 4 \times 10^7 \text{ GeV}, \tag{5.20a}$$

$$M_{N_2} \lesssim 7 \times 10^7 \text{ GeV}, \tag{5.20b}$$

$$M_{N_3} \lesssim 3 \times 10^7 \text{ GeV} \left(\frac{0.05 \text{ eV}}{m_{min}} \right)^{\frac{1}{3}}, \tag{5.20c}$$

where m_{min} is the lightest neutrino mass. For a given model, however, the bounds will be more stringent.

Baryogenesis via standard (N_1-dominated, hierarchical) leptogenesis requires $M_{N_1} \gtrsim 5 \times 10^8$ (2×10^9) GeV for N_1 with thermal (zero) initial abundancy [97][1], in conflict with Equation (5.20a).

In N_2 leptogenesis, it is possible to have $M_{N_1} \lesssim 10^7$ GeV. There are two scenarios. One is in the N_1-decoupling limit [359], and the other relies on special flavour alignments to protect an N_2-generated asymmetry from N_1 washout [360, 361]. Both are in conflict with Equation (5.20b), as such a light N_2 is unable to produce the required asymmetry for the usual reasons [96, 97].

[1]These bounds are unaffected by flavour considerations [357, 358].

One might think that there is still room left for N_3 leptogenesis. This turns out to not be the case. In order to naturally have $M_{N_3} \gtrsim 10^9$ GeV, one must have $m_{min} \lesssim 10^{-6}$ eV and R in a decoupling limit such as Equation (5.15). However in this limit the CP asymmetry from N_3 decays is [359]

$$\varepsilon_3 \sim 10^{-1} \sum_{i=1,2} \frac{2}{v^2} \frac{m_{min} M_i^2}{M_3} \mathrm{Im}\left(R_{1i}^2\right), \tag{5.21}$$

which is far too small.

Thus our results confirm that no minimal Type I seesaw model can explain the neutrino masses and baryogenesis via hierarchical (N_1-, N_2-, or N_3-dominated) thermal leptogenesis while remaining completely natural.

5.2 The ν2HDM

5.2.1 How to avoid unnatural hierarchical thermal leptogenesis

An obvious question is: in what minimal ways can we adapt the Type I seesaw to realise a natural BAU? Figure 5.1 suggests three conspicuous possibilities: (1) lowering the Davidson–Ibarra bound, e.g. by considering dominant initial N_1 abundancy [97][2], resonant leptogenesis [98], a different baryogenesis mechanism entirely (such as neutrino oscillations [362]), or by introducing new fields which allow increased CP violation in N_1 decays; (2) raising the naturalness bound, e.g. by partially cancelling right-handed neutrino corrections [352, 363], or removing it entirely by restoring low-scale supersymmetry; (3) lowering the (possibly effective) vev entering the seesaw Equation (5.2) so that the bounds of Equations (5.3) and (5.4) become consistent ($v \lesssim 30$ GeV).

In our Ref. [5] we implemented the latter possibility within a two-Higgs-doublet model with right-handed neutrinos (ν2HDM). The remainder of this Chapter is dedicated to describing such models. It is organised as follows. In Section 5.2.2 we build the ν2HDM models of interest, describe the scalar states, and briefly review the relevant experimental constraints. In Section 5.2.3 we pay particular attention to naturalness limits on the extra scalars; we verify that a natural ν2HDM of any Type is still allowed by experiment. We discuss neutrino masses in Section 5.2.4 and leptogenesis in Section 5.2.5. The region of parameter space which naturally achieves hierarchical leptogenesis is identified.

[2] The bound becomes $M_{N_1} \gtrsim 2 \times 10^7$ GeV, marginally consistent with the naturalness bound in Equation (5.7).

Model	u_R^i	d_R^i	e_R^i	ν_R^i
Type I	Φ_1	Φ_1	Φ_1	Φ_2
Type II	Φ_1	Φ_2	Φ_2	Φ_2
Lepton-specific (LS)	Φ_1	Φ_1	Φ_2	Φ_2
Flipped	Φ_1	Φ_2	Φ_1	Φ_2

TABLE 5.1: The four models with no tree-level flavour-changing neutral currents and allowing for a GeV-scale vev to provide the seesaw whilst preserving perturbativity of y_t.

5.2.2 Model

Lagrangian

The scalar content of the model contains two doublets $\Phi_{1,2}$ each with hypercharge +1. For simplicity we consider the softly broken, CP conserving, Z_2-symmetric potential (see e.g. Ref. [364])

$$
\begin{aligned}
V_{\text{2HDM}} = {} & m_{11}^2\, \Phi_1^\dagger \Phi_1 + m_{22}^2\, \Phi_2^\dagger \Phi_2 - m_{12}^2 \left(\Phi_1^\dagger \Phi_2 + \Phi_2^\dagger \Phi_1\right) \\
& + \frac{\lambda_1}{2} \left(\Phi_1^\dagger \Phi_1\right)^2 + \frac{\lambda_2}{2} \left(\Phi_2^\dagger \Phi_2\right)^2 \\
& + \lambda_3 \left(\Phi_1^\dagger \Phi_1\right)\left(\Phi_2^\dagger \Phi_2\right) + \lambda_4 \left(\Phi_1^\dagger \Phi_2\right)\left(\Phi_2^\dagger \Phi_1\right) \\
& + \frac{\lambda_5}{2} \left[\left(\Phi_1^\dagger \Phi_2\right)^2 + \left(\Phi_2^\dagger \Phi_1\right)^2\right],
\end{aligned} \tag{5.22}
$$

where all the parameters are real. To explain observations, at least one of these doublets must obtain a non-zero vev. We consider $m_{11}^2 < 0$ and a CP conserving vacuum,

$$
\langle \Phi_1 \rangle = \frac{1}{\sqrt{2}} \begin{pmatrix} 0 \\ v_1 \end{pmatrix}, \qquad \langle \Phi_2 \rangle = \frac{1}{\sqrt{2}} \begin{pmatrix} 0 \\ v_2 \end{pmatrix}, \tag{5.23}
$$

where $v_1 > 0$, $v_2 \geq 0$, and $v_1^2 + v_2^2 = v^2 \approx (246 \text{ GeV})^2$.

A general 2HDM will have flavour-changing neutral currents at tree-level. These can be avoided if right handed fermions of a given type (u_R^i, d_R^i, e_R^i) couple to only one of the doublets [365, 366]. Although not strictly necessary, we will assume that this is realised, and adopt the convention that only Φ_1 couples to the u_R^i. In a ν2HDM, if we assume this also applies for the ν_R^i, then there are eight possibilities. As mentioned in the Introduction, the seesaw constraint Equation (5.2) can be made consistent with naturalness and leptogenesis if the vev contributing to the seesaw is sufficiently small. Since we would like our model to remain perturbative, and already $y_t \approx 1$ for $v \approx 246$ GeV, we anticipate that Φ_2 obtains the small vev and thus we couple it to the ν_R^i. Remaining are four possible ν2HDMs which we refer to by their conventional Types as listed in

Table 5.1.[3] The Yukawa Lagrangian is then given by

$$\begin{aligned}-\mathcal{L}_Y = &+ y_u \overline{q_L}\tilde{\Phi}_1 u_R + y_d \overline{q_L}\Phi_I d_R \\ &+ y_e \overline{l_L}\Phi_J e_R + y_\nu \overline{l_L}\tilde{\Phi}_2 \nu_R \\ &+ \frac{1}{2} M_N \overline{(\nu_R)^c}\nu_R + h.c.,\end{aligned} \tag{5.24}$$

where I, J depend on the model Type, and family indices are implied.

Scalar masses and mixings

Consistency with experiments requires the extra scalar states to have masses at least $\gtrsim 80$ GeV. In order to construct models with potentially TeV-scale scalars with a naturally small v_2, we will consider $m_{22}^2 > 0$ and $m_{12}^2/m_{22}^2 \ll 1$ [367]. This is technically natural, since in the limit $m_{12}^2/m_{22}^2 \to 0$ a $U(1)$ or Z_2 symmetry is restored if $\lambda_5 = 0$ or $\lambda_5 \neq 0$, respectively.

For $m_{11}^2 < 0$, the vevs are given by

$$v_1 = \sqrt{\frac{2}{\lambda_1}\left[-m_{11}^2 + \frac{1}{\tan^2\beta}\left(m_{22}^2 + \frac{1}{2}\lambda_2 v_2^2\right)\right]} \tag{5.25}$$

$$v_2 \approx \frac{1}{1 + \frac{v_1^2}{2m_{22}^2}\lambda_{345}} \frac{m_{12}^2}{m_{22}^2} v_1, \tag{5.26}$$

In the limit $m_{22}^2 \gg v_1^2(\lambda_3 + \lambda_4)$, $\lambda_2 v_2^2$, we have $\tan\beta \equiv v_1/v_2 \approx m_{22}^2/m_{12}^2$ and $v_1 \approx \sqrt{\frac{2}{\lambda_1}\left(-m_{11}^2 + m_{22}^2/\tan^2\beta\right)}$. This implies a relevant condition,

$$m_{22}^2 \lesssim \frac{1}{2}\left(\lambda_1 v_1^2\right)\tan^2\beta, \tag{5.27}$$

to ensure $m_{11}^2 < 0$ and avoid a fine-tuning for v. Figure 5.4 illustrates how m_{11}^2 deviates from its standard value of $-(88\text{ GeV})^2$ as m_{22}^2 approaches this bound. For m_{22}^2 above this bound, m_{11}^2 very quickly grows to values $> v^2$, and $v \approx 246$ GeV is only explained by a miraculous balance of m_{11}^2 against $m_{22}^2/\tan^2\beta$, which constitutes a fine-tuning. Thus we adopt Equation (5.27) as a consistency condition. Typically we have $m_{22}^2/\tan^2\beta \ll |m_{11}^2|$ so that m_{11}^2 sets the mass of the Higgs (as does μ^2 in the SM).

The charged scalar and pseudoscalar (neutral scalar) mass-squared matrices are diagonalised by a mixing angle β (α). The neutral mass eigenstates are

$$\begin{aligned}h &= \rho_1\cos\alpha + \rho_2\sin\alpha, \\ H &= \rho_2\cos\alpha - \rho_1\sin\alpha, \\ A &= \eta_2\sin\beta - \eta_1\cos\beta,\end{aligned} \tag{5.28}$$

[3] Type I ν2HDMs with $v_2 \sim$ eV were considered in Refs. [367–370]. We will end up considering v_2 of $\mathcal{O}(0.1\text{–}10)$ GeV.

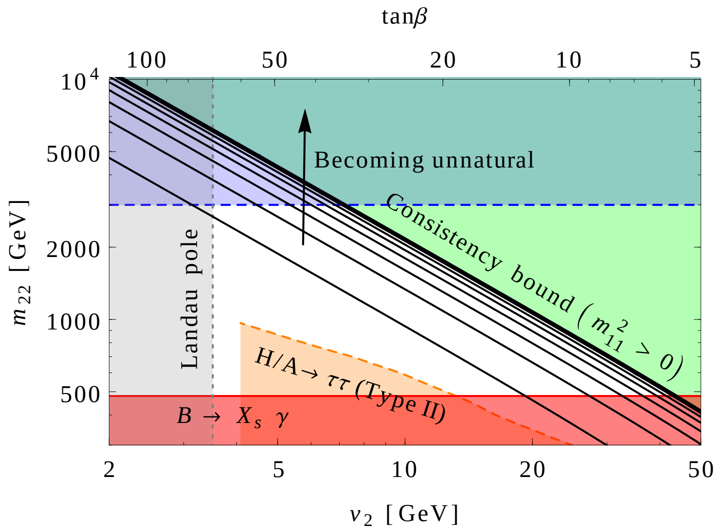

FIGURE 5.4: Constraints on m_{22}, as labelled. Solid black contours are $m_{11}^2/\mathrm{GeV}^2 = -80^2, -70^2$, and so on. The green shaded region has no solution for $m_{11}^2 < 0$. A subset of the models hit a Landau pole below M_{Pl} when $\tan\beta \gtrsim 70$. The $H/A \to \tau\tau$ bound is taken from the CMS search [371]. The naturalness bound is only illustrative, to be covered in Section 5.2.3.

where $\rho_i = \sqrt{2}\mathrm{Re}(\Phi_i^0) - v_i$ and $\eta_i = \sqrt{2}\mathrm{Im}(\Phi_i^0)$. The masses are given by

$$\begin{aligned}
m_h^2 &= \lambda_1 v_1^2 + \mathcal{O}\left(\frac{m_{12}^4}{m_{22}^4} v_1^2\right), \\
m_H^2 &= m_{22}^2 + \frac{1}{2}\lambda_{345} v_1^2 + \mathcal{O}\left(\frac{m_{12}^4}{m_{22}^4} m_{22}^2\right), \\
m_A^2 &= m_{22}^2 + \frac{1}{2}(\lambda_{345} - 2\lambda_5) v_1^2 + \mathcal{O}\left(\frac{m_{12}^4}{m_{22}^4} m_{22}^2\right), \\
m_{H^\pm}^2 &= m_{22}^2 + \frac{1}{2}\lambda_3 v_1^2 + \mathcal{O}\left(\frac{m_{12}^4}{m_{22}^4} m_{22}^2\right),
\end{aligned} \tag{5.29}$$

i.e. the same as in the inert doublet model [364] up to corrections proportional to m_{12}^4/m_{22}^4, which we provide in Appendix B.1. Clearly, if $m_{22}^2 \gg v^2$, the mass scale of extra scalar states is $\approx m_{22}$.

In the alignment limit $\cos(\alpha - \beta) \to 0$, the couplings of h to SM particles become SM-like. We calculate

$$\cos^2(\alpha - \beta) \approx \frac{m_{12}^4}{m_{22}^4}\frac{v_1^4}{m_{22}^4}\frac{(\lambda_1 - \lambda_{345})^2}{\left(1 - \frac{v_1^2}{2m_{22}^2}(2\lambda_1 - \lambda_{345})\right)^2 \left(1 + \frac{v_1^2}{2m_{22}^2}\lambda_{345}\right)^2}, \tag{5.30}$$

suppressed by the approximate $U(1)$ or Z_2 symmetry ($m_{12}^2/m_{22}^2 \ll 1$) as well as the usual decoupling limit suppression ($v_1^2/m_{22}^2 \ll 1$) [372]. Thus the model naturally accommodates a SM-like neutral scalar state.

Constraints

With $M_N > m_{22}$ the constraints (and search strategies) for a ν2HDM of given Type are largely identical to those for a 2HDM of the same Type, for which there is extensive literature (see references henceforth). The 2HDM potential Equation (6.4) is subject to a few standard theoretical constraints [364]. The necessary and sufficient conditions for positivity of the potential in all directions are [373–375]

$$\begin{aligned} \lambda_{1,2} &\geq 0, \\ \lambda_3 &\geq -\sqrt{\lambda_1\lambda_2}, \\ \lambda_3 + \lambda_4 - |\lambda_5| &\geq -\sqrt{\lambda_1\lambda_2}. \end{aligned} \tag{5.31}$$

Vacuum stability of the potential minimum is more difficult to evaluate. An inequality which ensures a global minimum, missing possible metastable vacua, is presented in Ref. [376]. Tree-level perturbative unitarity of scalar-scalar scattering is ensured by bounding the eigenvalues of the scattering matrix [364, 377–379]. Perturbativity of the λ_i can also be demanded [380]. At the very least these bounds should be implemented at the mass scale of the scalar states. In addition they may be demanded up to some high scale under the renormalisation group evolution, which results in non-trivial constraints on the parameter space (see e.g. Refs. [381–383][4]). Type II, LS, and Flipped 2HDMs are particularly susceptible to exclusion by such a demand at large $\tan\beta$; at one-loop, their Yukawa couplings hit a Landau pole before $M_{Pl} \sim 10^{18}$ GeV when $v_2 \lesssim 3.6, 2.3, 3.3$ GeV ($\tan\beta \gtrsim 68, 110, 75$) respectively [384]. These Landau poles merely indicate the breakdown of perturbativity.

The scalar boson discovered at the LHC is to be identified with the mass eigenstate h. Its couplings have been measured to be SM-like, which constrains the ν2HDM to lie in the alignment limit $\cos(\alpha-\beta) \approx 0$, particularly at large $\tan\beta$, and for Type II and Flipped 2HDMs.[5] As is evident from Equation (5.30), the alignment limit is automatically preferred in our model due to the approximate Z_2 or $U(1)$ symmetry. Thus we limit the following discussion on additional experimental limits to those that constrain moderate to large $\tan\beta$ models very close to the alignment limit.

In Type II and Flipped 2HDMs, the Φ_2 coupling to down-type quarks is $\tan\beta$ enhanced. The $H^\pm$ state then contributes significantly to radiative $B \to X_s\gamma$ decay; the experimental measurement [390] combined with a recent next-to-next-to-leading order SM calculation [391] bounds $m_{H^\pm} \gtrsim 480$ GeV at 95% CL for

[4]Note that some of the bounds derived in these papers do not apply to the softly broken Z_2-symmetric case, and also do not apply to the Z_2-symmetric case when one of the vevs vanishes.

[5]We refer the reader to Refs. [34, 383, 385–389] for allowed parameter space as a function of $\cos(\alpha-\beta)$ and $\tan\beta$ in all 2HDM Types.

$\tan\beta \gtrsim 2$. This bound along with the consistency condition Equation (5.27) implies $v_2 \lesssim 45$ GeV ($\tan\beta \gtrsim 5.4$) for these ν2HDMs. In the Type II 2HDM the Φ_2 coupling to e_R^i is also $\tan\beta$ enhanced, and the bound on $m_{H^\pm}$ from $B \to \tau\nu$ decays exceeds the radiative bound when $\tan\beta \gtrsim 60$ [364]. These bounds are depicted in Figure 5.4.

Direct searches at LEP constrain $m_{H^\pm} \gtrsim 80$ GeV assuming decay to SM particles [392]. At the LHC, searches for $H/A \to \tau\tau$ [371, 393] are particularly constraining in the Type II 2HDM. The 95% CL limit rises approximately linearly from $m_A \gtrsim 300$ GeV at $\tan\beta = 10$ to $m_A \gtrsim 1000$ GeV at $\tan\beta = 60$. Such searches can also be mildly constraining for the LS 2HDM at moderate $\tan\beta$. Searches for $H^\pm \to \tau\nu$ [394, 395] cannot compete with $B \to X_s\gamma$ for Type II/Flipped 2HDMs or with $H/A \to \tau\tau$ for the LS 2HDM. However, for $m_{H^\pm} < 160$ GeV, significant parameter space is ruled out in Type I 2HDMs with moderate $\tan\beta$.

The $(y_\nu)_{ij}\overline{l_L^i}\tilde{\Phi}_2\nu_R^j$ Yukawa term related to the neutrino masses can induce lepton flavour violating decays; these are suppressed by the small y_ν and the right-handed neutrino mass scale $M_N > m_{22}$. The processes of interest are $l_\alpha \to l_\beta\gamma$, $l_\alpha \to 3l_\beta$, and $\mu \to e$ conversion in nuclei (see Ref. [396] for expressions). As well, $b \to s l_\alpha \bar{l}_\beta$ decays are induced in Type II and Flipped ν2HDMs. In practice, lepton flavour violating measurements constrain linear combinations of $(y_\nu)_{ij}$ bi- and tri-linears as well as the M_{N_i}.

In summary, for moderate to large $\tan\beta$ and $\cos(\alpha - \beta) \approx 0$, experiments are most constraining for the Type II and Flipped 2HDMs, with $m_{22} \gtrsim 480$ GeV necessary (implying $v_2 \lesssim 45$ GeV). For Type I and LS 2HDMs, even additional scalars with masses down to 80 GeV may still have evaded detection.

5.2.3 Naturalness

In CHAPTER 3 we laid out our naturalness philosophy. A physical naturalness problem arises when the Higgs mass parameter $\mu^2(\mu_R)$ receives large corrections, $d\mu^2/d\log\mu_R \gg \mu^2(m_Z)$. Indeed, the Vissani bound of Section 5.1 is a direct bound of the μ^2 RGE contributions from the heavy right-handed neutrino. Below we present a discussion and a one-loop RG analysis within the ν2HDM.

In practice, the naturalness considerations can be divided into two distinct calculations: the influence of m_{22} on m_{11}, and the influence of M_N on m_{22}. These influences will be considered in turn.[6]

Corrections to m_{11}^2

If $m_{22}^2 \ll m_h^2 \tan^2\beta/2$, then m_{11}^2 sets the mass of the observed SM-like Higgs via Equations (5.26) and (5.29). The one-loop RGE for the m_{11}^2 parameter is [364] (see

[6]In the following we ignore the influence of the small y_ν Yukawas on m_{11}^2, and hence those results also hold in a general 2HDM.

Ref. [383] for a recent two-loop calculation)

$$\frac{dm_{11}^2}{d\ln\mu_R} = \frac{1}{(4\pi)^2}\left[(4\lambda_3 + 2\lambda_4)m_{22}^2 + \mathcal{O}(m_{11}^2)\right]. \tag{5.32}$$

The $\mathcal{O}(m_{11}^2)$ term contains gauge, λ_1, and Yukawa contributions, which, as in the SM case, do not induce a naturalness problem. However if $\lambda_{3,4}$ are non-zero then a naturalness problem is induced for sufficiently large m_{22}^2; we are interested in when this generically occurs. Even if $\lambda_{3,4} = 0$ at some scale, they will quickly be reintroduced by gauge interactions at one-loop. Their one-loop RGEs are given by

$$\begin{aligned}
\frac{d\lambda_3}{d\ln\mu_R} &= \frac{1}{(4\pi)^2}\left[\frac{3}{4}\left(g_Y^4 - 2g_Y^2 g_2^2 + 3g_2^4\right) + ...\right], \\
\frac{d\lambda_4}{d\ln\mu_R} &= \frac{1}{(4\pi)^2}\left[3g_Y^2 g_2^2 + ...\right],
\end{aligned} \tag{5.33}$$

where $g_2^2(m_Z) \approx 0.43$ and $g_Y^2(m_Z) \approx 0.13$ are the gauge couplings and the ellipses contain terms multiplicative in $\lambda_{3,4}$, terms proportional to λ_5^2, and terms related to the Yukawas. Let us ignore those effects for now and return to them later. Note that ignoring the contribution from λ_5^2 is equivalent to assuming $\lambda_5 \lesssim 0.2$, so that its contribution is subdominant to the gauge couplings. Typically, one would expect

$$\begin{aligned}
|\lambda_3(\mu_R)| &\gtrsim \frac{1}{(4\pi)^2}\frac{3}{4}\left(g_Y^4 - 2g_Y^2 g_2^2 + 3g_2^4\right), \\
|\lambda_4(\mu_R)| &\gtrsim \frac{1}{(4\pi)^2}3g_Y^2 g_2^2,
\end{aligned} \tag{5.34}$$

and thus

$$\left|\frac{dm_{11}^2}{d\ln\mu_R}\right| \gtrsim \frac{1}{(4\pi)^4}\left(3g_Y^4 + 9g_2^4\right)m_{22}^2. \tag{5.35}$$

This lower bound is of the same order as the two-loop pure gauge contribution [383].

Equation (5.35) represents a conservative bound on the running of the m_{11}^2 parameter above the scale $\sim m_{22}$. Naturalness demands that this running not be significantly larger than the value measured at a low scale, $|m_{11}| \approx 88$ GeV. A very conservative naturalness bound is therefore

$$\frac{1}{(4\pi)^4}\left(3g_Y^4 + 9g_2^4\right)m_{22}^2 < 1\ \text{TeV}^2, \tag{5.36}$$

$$\Rightarrow m_{22} \lesssim 1\times 10^5\ \text{GeV}. \tag{5.37}$$

Alternatively, we can try to bound a quantity which measures the fine-tuning in m_{11}^2 at some high scale Λ_h. A typical quantity is [288, 289]

$$\Delta\left(\Lambda_h\right) = \left| \frac{m_{11}^2(\Lambda_h)}{m_{11}^2(m_Z)} \frac{\partial m_{11}^2(m_Z)}{\partial m_{11}^2(\Lambda_h)} \right|, \tag{5.38}$$

which compares percentage variations of two (in principle) measurable parameters. Let us now estimate how such a bound might constrain m_{22}.

For simplicity, and anticipating that the m_{22} scale is not far above the electroweak scale, we will evolve the dimensionless parameters using the (ν)2HDM RGEs from the m_Z scale. First, the one-loop gauge coupling RGEs [364, 397] can be solved analytically. Upon substitution into the $\lambda_{3,4}$ RGEs (Equations (5.33)), and considering only the pure gauge contribution, the $\lambda_{3,4}$ running can be solved for given initial conditions. For simplicity we take $\lambda_3(m_{22}) = \lambda_4(m_{22}) \equiv \lambda_{3,4}(m_{22})$ and consider it a free parameter. Next we solve Equation (5.32) for $m_{11}^2(\mu_R)$ with the initial condition $m_{11}^2(m_{22}) = -(88 \text{ GeV})^2$ (neglecting any RGE evolution of m_{22}^2). With these simplifications $\partial m_{11}^2(m_Z)/\partial m_{11}^2(\Lambda_h) = 1$ and the fine-tuning measure is given simply by $\Delta(\Lambda_h) = \left|m_{11}^2(\Lambda_h)/(88 \text{ GeV})^2\right|$.

Note that in setting the initial condition $m_{11}^2(m_{22}) = -(88 \text{ GeV})^2$ we have implicitly assumed that $m_{22}^2 \ll m_h^2 \tan^2\beta/2$ (see Equation (5.27) and Figure 5.4). This is conservative for negative m_{11}^2, since $|m_{11}^2(m_{22})|$ shrinks as $m_{22}^2/\tan^2\beta \to m_h^2/2$ and the naturalness constraint would become more stringent. In some circumstances we will obtain naturalness bounds on m_{22}^2 which exceed $m_h^2 \tan^2\beta/2$, which just indicates that the naturalness constraint is weaker than the consistency condition Equation (5.27).

In Figure 5.5 we show $\Delta = 10$ and $\Delta = 100$ contours as a function of Λ_h and $\lambda_{3,4}(m_{22})$. These represent naturalness upper bounds on m_{22}. The cusp-like structures of apparently low fine-tuning in m_{11}^2 occur when m_{11}^2 runs negative before turning and passing through $m_{11}^2 = 0$, which just corresponds to a fine-tuning in $(\lambda_{3,4}, \Lambda_h)$, as discussed in CHAPTER 3. A stringent naturalness constraint is obtained by demanding $\Delta < 10$ at $\Lambda_h = M_{Pl}$; from Figure 5.5, it is clear that this implies

$$m_{22} \lesssim \text{few} \times 10^3 \text{ GeV}. \tag{5.39}$$

Indeed, in our two-loop study of CHAPTER 3 we obtained a similar bound of $M \lesssim 2.1$ TeV (see Table 3.2) for scalars in a minimal 2HDM (with $v_2 = 0$ and no Yukawa couplings). If any new physics comes in below M_{Pl} then the running of m_{11}^2 could change, and these bounds do not strictly apply. If that is the case then it is more appropriate to consider Λ_h at the scale of the new physics, which weakens the bound, as is clear from Figure 5.5. In the ν2HDM this new physics scale is the right-handed neutrino scale M_N, after which the right-handed neutrinos can contribute to the running of m_{11}^2 through m_{22}^2 at one-loop.

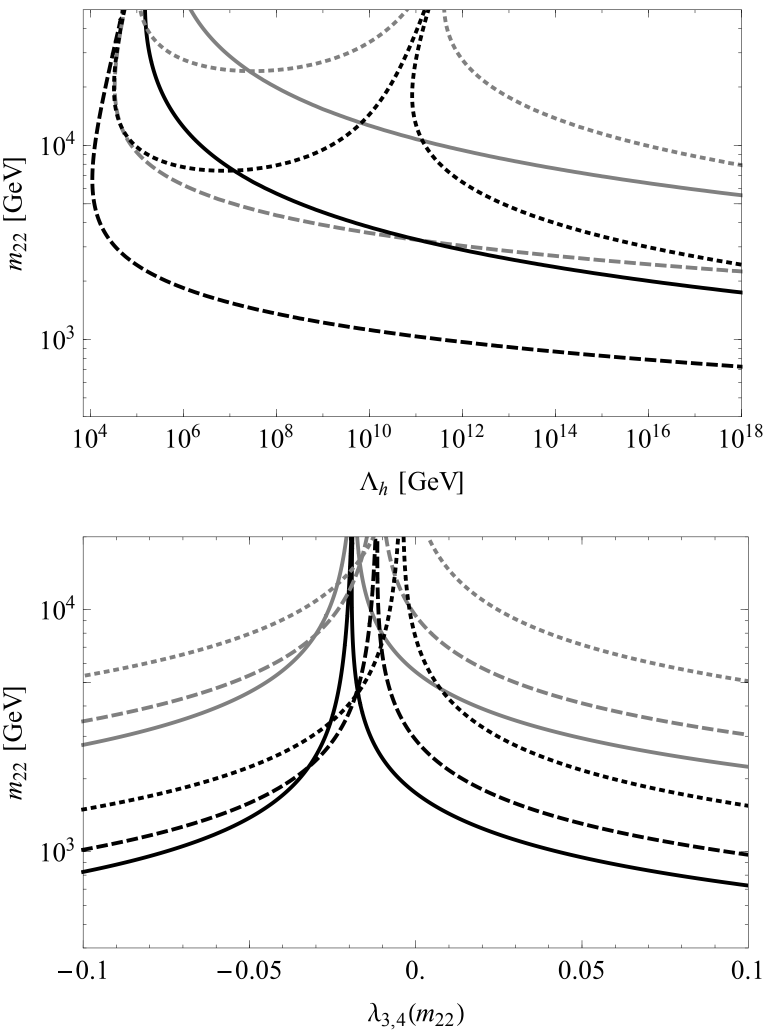

FIGURE 5.5: Contours of the fine-tuning measure $\Delta(\Lambda_h) = 10$ (100) in black (grey) as a function of (top) Λ_h for $\lambda_{3,4}(m_{22}) = 0.0, 0.1, -0.01$ (solid, dashed, dotted), and (bottom) $\lambda_{3,4}(m_{22})$ for $\Lambda_h = 10^{18}, 10^{12}, 10^7$ GeV (solid, dashed, dotted). See the text for the assumptions that accompany this plot.

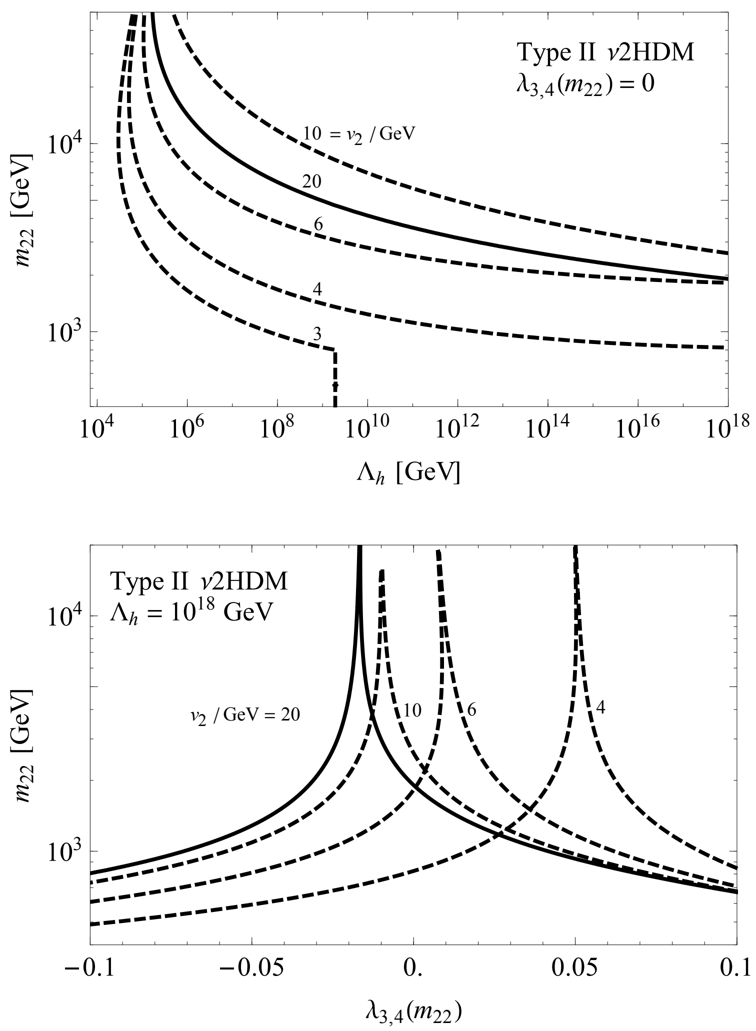

FIGURE 5.6: Contours of the fine-tuning measure $\Delta(\Lambda_h) = 10$ in an illustrative Type II ν2HDM (see text) for different values of v_2. The solid lines for $v_2 = 20$ GeV match approximately onto the solid lines in Figure 5.5.

We have so far ignored the RGE contributions from possibly large Yukawas. There are two situations in which the Yukawas play a significant role. The first is in Type II, LS, and Flipped ν2HDMs with $\tan\beta$ large enough such that an early Landau pole is induced (see Section 5.2.2), and the second is in Type II and Flipped ν2HDMs with moderate to large $\tan\beta$ when the pure Yukawa term $\pm\frac{1}{(4\pi)^2}12y_b^2y_t^2$ induced by a quark box diagram contributes significantly to the $\lambda_{3,4}$ RGEs (Equations (5.33)). In Figure 5.6 we show how the $\Delta = 10$ contours change as a function of v_2 in an example Type II ν2HDM. For this Figure we have numerically solved the full set of one-loop RGEs [383] including the top/bottom/tau Yukawas, taking the following values at the scale m_Z: $g_s^2 = 1.48$, $\lambda_1 = \lambda_2 = 0.26$, and $y_t = 0.96/\sin\beta$, $y_b = 0.017/\cos\beta$, $y_\tau = 0.010/\cos\beta$. Comparing to Figure 5.5, it can be seen that the pure Yukawa term has a noticeable effect when $v_2 \lesssim 20$ GeV. It is also apparent from Figure 5.6 that nearing $v_2 \approx 3.6$ GeV (below which a Landau pole is induced before M_{Pl}) can act to degrade *or* improve the naturalness bound. The $v_2 = 3$ GeV bound in Figure 5.6 shows the effect of hitting the Landau pole at $\sim 10^9$ GeV. We note that this only signals the breakdown of perturbation theory, and of our one-loop RGEs; we cannot calculate $m_{22}(\mu_R)$ above this scale though it is perfectly possible that the theory remains natural.

In a repeated full one-loop RGE analysis we found that the Flipped ν2HDM gave essentially the same results as the Type II ν2HDM in Figure 5.6, and there was no noticeable Yukawa effect in the LS ν2HDM until the Landau pole was reached. Thus we find that the stringent naturalness bounds of Equation (5.39) and Figure 5.5 are applicable at all times in the Type I ν2HDM, for $v_2 \gtrsim 2$ GeV in the LS ν2HDM, and for $v_2 \gtrsim 20$ GeV in the Type II and Flipped ν2HDMs. Otherwise Yukawa effects must be taken into account. Either way, the important point is now clear: a TeV scale m_{22} can be both completely natural and, as was discussed in the previous subsection, is experimentally allowed in all ν2HDM Types.

Corrections to m_{22}^2

Let us now consider the influence of the right-handed neutrinos. The one-loop RGE for m_{22}^2 is [3, 398]

$$\frac{dm_{22}^2}{d\ln\mu_R} = \frac{1}{(4\pi)^2}\left[-4\mathrm{Tr}[y_\nu\mathcal{D}_M^2 y_\nu^\dagger] + \mathcal{O}(m_{22}^2)\right]. \tag{5.40}$$

A conservative naturalness bound is obtained by bounding the running as we did in Equation (5.37),

$$\frac{1}{4\pi^2}\mathrm{Tr}[y_\nu\mathcal{D}_M^2 y_\nu^\dagger] < \Lambda_{bound}^2, \tag{5.41}$$

where taking $\Lambda_{bound} = 1$ TeV gives the Vissani bound on M_{N_1} of Equation (5.4) [3]. However, now we are bounding corrections to m_{22}^2 rather than m_{11}^2, which may be TeV scale. Thus, depending on the mass of the extra scalars, it is possible that we can sensibly take $\Lambda_{bound} > 1$ TeV, in which case the the naturalness bound is somewhat relaxed; in Figure 5.7 we show a Relaxed Vissani bound for $\Lambda_{bound} = \min(10\text{ TeV}, 10\sqrt{m_h^2 \tan^2\beta/2})$, where we have kept in mind the consistency condition Equation (5.27). The Vissani bound still represents the unnatural area of parameter space if m_{22} is closer to 100 GeV.

As before, we could instead bound a quantity which measures the fine-tuning in m_{22}^2 at some high scale Λ_h. In this case, the fine-tuning measure of Equation (5.38) is

$$\Delta(\Lambda_h) = 1 + \frac{1}{4\pi^2}\frac{\sum_{i,j}(y_\nu)_{ij}M_j^2(y_\nu^\dagger)_{ji}\ln(M_j/\Lambda_h)}{m_{22}^2(M_j)}. \tag{5.42}$$

Taking $m_{22}(M_j) \sim 1$ TeV and demanding $\Delta(M_{Pl}) < 10$ gives a similar bound to Vissani (Equation (5.41) with $\Lambda_{bound} = 1$ TeV). Note that there is no naturalness bound on M_N in the $y_\nu \to 0$ limit. This is the technically natural limit corresponding to an enhanced Poincaré symmetry in which ν_R decouples from the theory [37].

In summary, there are up to three scales in the ν2HDM: v, m_{22}, and M_N. We have described the conditions under which v^2 (or m_{11}^2) is protected from m_{22}^2, and m_{22}^2 from M_N^2. Under such conditions it follows that m_{11}^2 is also protected from M_N^2 and the model is entirely natural.

5.2.4 Neutrino masses

If $m_{12}^2 = 0$ and $\lambda_5 = 0$ then a $U(1)$ lepton number symmetry can be defined and neutrinos remain massless. Let us now consider turning each non-zero in turn.

$m_{12}^2 > 0,\ \lambda_5 = 0$

If $m_{12}^2 > 0$ then the $U(1)$ lepton number symmetry is softly broken, i.e. the breaking does not force us to insert a non-zero λ_5 term in order to introduce a divergent counterterm, and it is consistent to consider $m_{12}^2 > 0,\ \lambda_5 = 0$.

In this situation the neutrino mass matrix is given by the seesaw formula,

$$m_\nu = \frac{v_2^2}{2}y_\nu\mathcal{D}_M^{-1}y_\nu^T \approx \frac{1}{\tan^2\beta}\left(\frac{v^2}{2}y_\nu\mathcal{D}_M^{-1}y_\nu^T\right), \tag{5.43}$$

where $\tan\beta \approx m_{22}^2/m_{12}^2$ for $m_{22}^2 \gg \lambda_{345}v_1^2$, and we have bracketed the usual seesaw formula.

The analogous Davidson–Ibarra and Vissani bounds are given by the standard Equations (5.3) and (5.4) with the replacement $v \to v_2$. These bounds are depicted in Figure 5.7. If $v_2 \lesssim 30$ GeV ($\tan\beta \gtrsim 8$) then both bounds are satisfied.

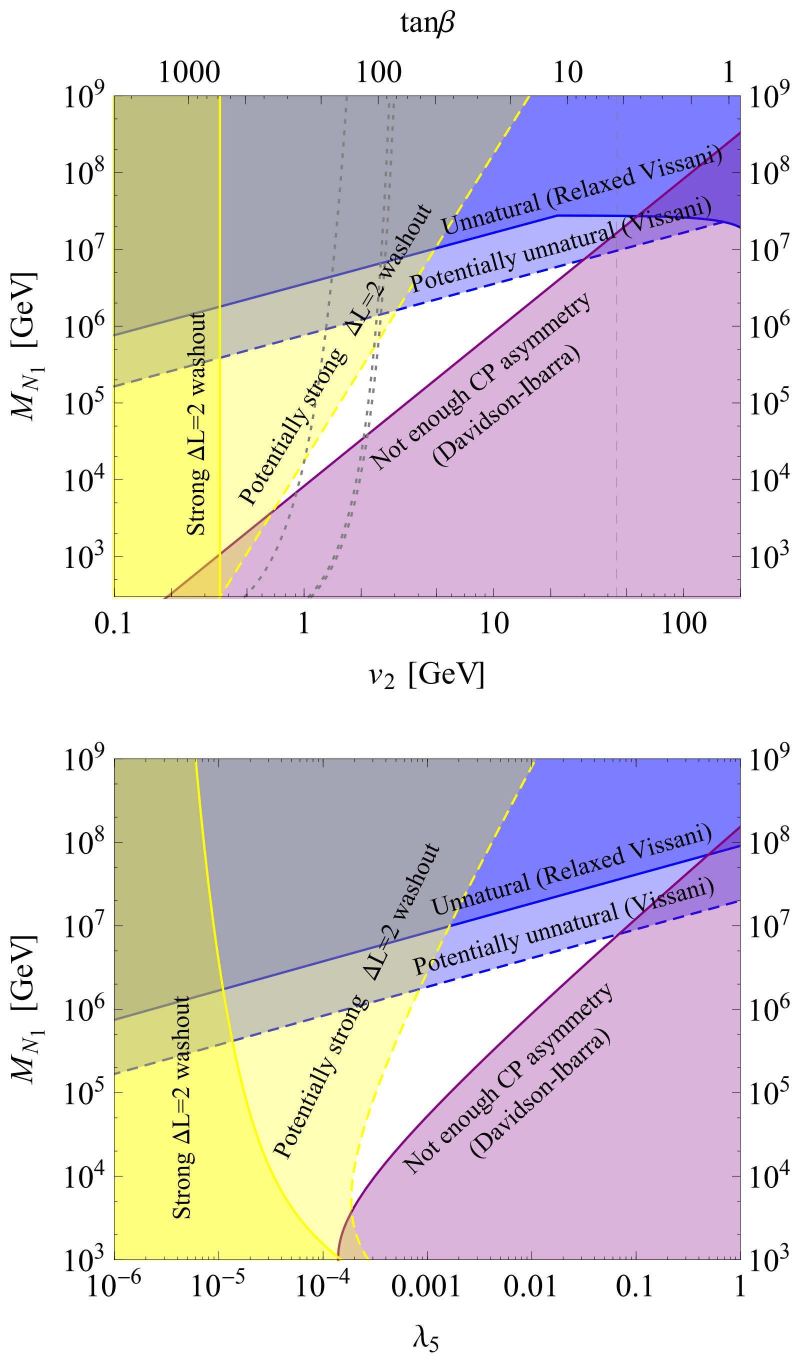

FIGURE 5.7: Upper: Bounds on the ν2HDM as a function of v_2. Shown (as labelled) are the Davidson-Ibarra bound, the Vissani and Relaxed Vissani naturalness bounds, and the areas of parameter space with strong $\Delta L = 2$ scattering washout. The Type II and Flipped ν2HDMs are excluded by $B \to X_s\gamma$ for values of v_2 greater than indicated by the grey dashed line (see Section 5.2.2). The grey dotted lines indicate the v_2 below which the Yukawas hit a Landau pole before M_{N_1} in the Type II, Flipped, and LS ν2HDMs right-to-left. Lower: As in Upper but for the Ma model. The Vissani and Relaxed Vissani bounds are evaluated at $m_{22} = 100, 1000$ GeV respectively. The Davidson-Ibarra bound and strong $\Delta L = 2$ washout region are shown for $m_{22} = 500$ GeV, though they are only mildly sensitive to m_{22}.

As well, as discussed in Section 5.2.3, if m_{22} is TeV scale the Vissani bound can be relaxed and the required CP asymmetry needed to reproduce the BAU via leptogenesis may be naturally achieved for $v_2 \lesssim 60$ GeV ($\tan\beta \gtrsim 4$). In the Type I ν2HDM, v_2 can be naturally $\ll$ GeV. Otherwise, requiring a perturbative theory up to M_{N_1} restricts $v_2 \gtrsim 1$ GeV ($v_2 \gtrsim 2$ GeV) for the LS (Type II/Flipped) ν2HDM in the parameter space region of interest, as depicted in Figure 5.7.

$m_{12}^2 = 0, \; \lambda_5 \neq 0$

In this situation $v_2 = 0$ and a Z_2 symmetry remains unbroken; this is the scenario of Ma [82]. The model yields a radiative neutrino mass and a dark matter candidate. This is only possible in the Type I ν2HDM, since in any other Type the unbroken Z_2 forbids a Dirac mass term for any charged fermion coupling to Φ_2. Note that the limit $\lambda_5 \to 0$ is technically natural, since in that limit the $U(1)$ lepton number symmetry is reinstated.

If $M_N^2 \gg m_{22}^2, v^2$ the radiatively induced neutrino mass matrix is

$$(m_\nu)_{ij} \approx \frac{v^2}{2} \frac{(y_\nu)_{ik}(y_\nu^T)_{kj}}{M_k} \frac{\lambda_5}{8\pi^2} \left(\ln \left[\frac{2M_k^2}{(m_H^2 + m_A^2)} \right] - 1 \right). \tag{5.44}$$

The analogous Davidson-Ibarra and Vissani bounds are given by the standard Equations (5.3) and (5.4) with the intuitive replacement $v^2 \to v^2 \frac{\lambda_5}{8\pi^2} \left(\ln \left[2M_{N_1}^2/(m_H^2 + m_A^2) \right] - 1 \right)$. This assumes that there is no fine-tuning in the complex y_ν parameters to reproduce the observed neutrino masses (see Appendix B.2 for details). These bounds are depicted in Figure 5.7, where the Davidson-Ibarra bound has been evaluated at $m_{22} = 500$ GeV as an illustrative example (the bound is only mildly sensitive to m_{22}). We find that the Ma model with $\lambda_5 \lesssim 0.5$ can naturally achieve the required CP asymmetry to reproduce the BAU via hierarchical leptogenesis.[7]

$m_{12}^2 > 0, \; \lambda_5 \neq 0$

In this case both the tree-level seesaw and the radiative mechanism will contribute to the neutrino mass. Both contributions are calculable, and either might dominate. Note that it is still technically natural to take $\lambda_5 \to 0$ in this case, since it restores a softly broken $U(1)$ symmetry. In other words, the λ_5 RGEs to all orders will be multiplicative in λ_5, indicative of the fact that the soft-breaking term can only generate finite $U(1)$-breaking corrections.

[7] A similar observation was made in a recent paper [353].

5.2.5 Leptogenesis

The observed BAU is achieved analogously to standard hierarchical thermal leptogenesis [93]; the out-of-equilibrium CP violating decays of the lightest right-handed neutrino $N_1 \to l\Phi_2$ create a lepton asymmetry which is transferred to the baryons by the electroweak sphalerons above $T \sim 100$ GeV.

The details of the leptogenesis are (as in the Type I seesaw case introduced in Section 1.1.4) largely defined (in the one-flavour approximation) by the decay parameter

$$K = \frac{\Gamma_D}{H|_{T=M_1}} = \frac{\tilde{m}_1}{m_*}, \tag{5.45}$$

comparing the rate for decays and inverse decays to the expansion rate at the time of departure from thermal equilibrium. Here, the rates

$$\Gamma_D = \frac{1}{8\pi}(y_\nu^\dagger y_\nu)_{11} M_1, \qquad\qquad H \approx \frac{17T^2}{M_{Pl}}, \tag{5.46}$$

are typically rescaled and expressed in terms of an effective neutrino mass $\tilde{m}_1$ and an equilibrium neutrino mass m_*,

$$\tilde{m}_1 = \frac{(y_\nu^\dagger y_\nu)_{11} v^2}{2M_1}, \qquad\qquad m_* \approx 1.1 \times 10^{-3}\ \text{eV} \left(\frac{v}{246\ \text{GeV}}\right)^2, \tag{5.47}$$

where v is the vev that enters the seesaw Equation (5.1). In the ν2HDM with $\lambda_5 = 0$ (with $m_{12}^2 = 0, \lambda_5 \neq 0$) the analogous definitions make the replacement $v^2 \to v_2^2$ ($v^2 \to v^2 \frac{\lambda_5}{8\pi^2}\left(\ln\left[2M_{N_1}^2/(m_H^2 + m_A^2)\right] - 1\right)$). Note that for the scenarios we are interested in (e.g. $v_2 \ll v$), m_* is smaller than its usual value in standard leptogenesis.

Let us briefly demonstrate that this picture is consistent. A simple example configuration which achieves maximal CP violation and saturates the Davidson–Ibarra bound is (assuming normal ordering) $m_1 \ll \tilde{m}_1$ and

$$R = \begin{pmatrix} \sqrt{1 - R_{31}^2} & 0 & R_{31} \\ 0 & 1 & 0 \\ R_{31} & 0 & -\sqrt{1 - R_{31}^2} \end{pmatrix}, \tag{5.48}$$

where $R_{31} \equiv \kappa \exp(i\pi/4)$. Here κ is related to the decay parameter by

$$\kappa \approx \frac{0.15\sqrt{K}}{\tan\beta}\left(\frac{0.05\ \text{eV}}{m_3}\right)^{\frac{1}{2}}, \tag{5.49}$$

and is typically $\lesssim 10^{-2}$ in the parameter range of interest. In the limit $m_1 = 0$, this corresponds to a Uy_ν which has one zero row, but is otherwise approximately diagonal. We note that, in this configuration, $\tilde{m}_1$ and the CP asymmetry are sufficiently stable under radiative corrections. The point is that, with three-flavour effects, it is possible to have $(y_\nu^\dagger y_\nu)_{11}$ arbitrarily small (in order that $K \sim 1$ and N_1 is sufficiently out of equilibrium) and still achieve maximal CP violation in its decays.

When only decays and inverse decays are considered, leptogenesis for given K proceeds exactly as in standard hierarchical thermal leptogenesis (see e.g. Ref. [95] for a review). In the weak washout regime $K \ll 1$, the baryon asymmetry strongly depends on the initial asymmetry and the initial N_1 abundance, with N_1 decays occuring at $T \ll M_1$. The strong washout regime $K \gg 1$ is independent of the initial conditions, and the asymmetry is generated as the N_1 fall out of thermal equilibrium.

The $2 \leftrightarrow 2$ scatterings with $\Delta L = 1$ (see e.g. Ref. [399]) provide a correction to the simple decays plus inverse decays picture; they act to increase N_1 production at $T > M_1$ and contribute to washout at $T < M_1$. In standard hierarchical thermal leptogenesis, the scattering contributions involving the top quark and the gauge bosons are roughly equal. In the present model the gauge boson contribution is the same as in the standard scenario. However, by construction, the Φ_2 involved here in leptogenesis does not couple directly to the top quark, and thus the usual s-channel ($Nl \leftrightarrow tq$) and t-channel ($Nt \leftrightarrow lq, Nq \leftrightarrow lt$) scattering contributions do not occur. Instead, at large $\tan\beta$ they can be replaced by the analogous contribution from other charged fermions, i.e. the bottom quark in Type II and Flipped ν2HDMs and/or the tau lepton in Type II and LS ν2HDMs. A large tau lepton Yukawa will also introduce new s-channel ($N\Phi_2 \leftrightarrow \tau\Phi_2$) and t-channel ($N\Phi_2 \leftrightarrow \tau\Phi_2, \tau N \leftrightarrow \Phi_2\bar{\Phi}_2$) scattering contributions. All of these processes are proportional to $(y_\nu^\dagger y_\nu)_{11}$ and hence $M_1\tilde{m}_1/v^2$, with the appropriate ν2HDM replacement for v^2. Therefore, they scale with the decays and inverse decays so that they represent only a minor (but obviously important) departure from the standard leptogenesis scenario.

The $2 \leftrightarrow 2$ scatterings with $\Delta L = 2$ mediated by the right-handed neutrinos ($\Phi_2 l \leftrightarrow \bar{\Phi}_2\bar{l}, \Phi_2\Phi_2 \leftrightarrow ll$) occur as they do in the standard scenario. These processes are proportional to $\mathrm{Tr}[(y_\nu y_\nu^T)(y_\nu y_\nu^T)^\dagger]$ and hence $M_1^2\overline{m}^2/v^4$ where $\overline{m}^2 = \sum m_i^2$ is the neutrino mass scale $\gtrsim (0.05\text{ eV})^2$. Comparing this rate to the decay/scattering rates $\propto M_1\tilde{m}_1/v^2$, it is easy to see that after making the appropriate ν2HDM replacement for v^2, e.g. $v^2 \to v_2^2 \ll v^2$, these scatterings will become comparatively more important than in the standard case. For $T \lesssim M_1/3$, and in the one-flavour approximation, the thermally averaged $\Delta L = 2$ scattering rate is well approximated by [95]

$$\frac{\Gamma_{\Delta L=2}}{H} \approx \frac{T}{2.2 \times 10^{13}\text{ GeV}} \left(\frac{246\text{ GeV}}{v}\right)^4 \left(\frac{\overline{m}}{0.05\text{ eV}}\right)^2, \tag{5.50}$$

where the previously described ν2HDM replacements for v^2 hold (see Appendix B.2). The upper (lower) panel of Figure 5.7 shows the region in the $\lambda_5 = 0$

($m_{12}^2 = 0, \lambda_5 \neq 0$) ν2HDM where these scatterings are still in equilibrium at $T \lesssim M_1/3$.[8] This is the region where strong $\Delta L = 2$ scatterings can potentially wash out the generated asymmetry, depending on the details of the leptogenesis (e.g. in a weak washout scenario with N_1 decays at $T \ll M_1$ this washout may be avoided). Demanding that the scatterings fall out of equilibrium before sphaleron freeze-out at $T \sim 100$ GeV provides a lower bound $v_2 \gtrsim 0.3$ or $\lambda_5 \gtrsim 10^{-5}$; this is represented by the strong $\Delta L = 2$ scattering washout regions in Figure 5.7. We note that this calculation has been performed in the context of a perturbative theory. This is reliable for the Type I ν2HDM but not for Type II, LS, or Flipped ν2HDMs with sufficiently small v_2, when perturbativity breaks down.

Since leptogenesis in this model will be occurring at temperatures below 10^9 GeV, the Yukawa couplings will be in equilibrium and flavour effects cannot be ignored (see e.g. Refs. [357, 406–409]). These departures from the standard scenario deserve further detailed study. Still, we do not expect the picture to be dramatically changed.

Putting this all together, we can now read off from Figure 5.7 the regions of parameter space which can achieve natural hierarchical thermal leptogenesis. For ν2HDMs with $m_{12}^2 > 0$ and $\lambda_5 = 0$, we find 10^3 GeV $\lesssim M_{N_1} \lesssim$ few $\times 10^7$ GeV is viable for Type I ν2HDMs, and 10^4 GeV $\lesssim M_{N_1} \lesssim$ few $\times$ 10^7 GeV for all other Types if they are to remain perturbative. For the Ma model with $m_{12}^2 = 0$ and $\lambda_5 \neq 0$, we find viable parameter space for 10^3 GeV $\lesssim M_{N_1} \lesssim 10^8$ GeV and $10^{-5} \lesssim \lambda_5 \lesssim 0.5$.

Lastly we note that the lightest scalar state in the Ma model is stable.[9] It is therefore possible that this state, if it is neutral, constitutes some or all of the observed dark matter. During the leptogenesis epoch, Φ_2 is produced in abundance in N_1 decays. Overproduction of dark matter is of no concern as long as Φ_2 efficiently thermalises at or below the temperatures when N_1 decays occur, which suggests $m_{22} \ll M_{N_1}$. In this case the lightest state is a thermal relic dark matter candidate.

5.3 Conclusion

The three-flavour Type I seesaw model is a simple way to explain neutrino masses and the BAU via hierarchical thermal leptogenesis. However, we proved in Section 5.1 that it cannot do so without introducing a naturalness problem.

[8] A similar plot to Figure 5.7 Upper appears in Ref. [400] in the context of the Type I ν2HDM with $v_2 > 0$. We are not aware of any plot similar to Figure 5.7 Lower in the literature, though see Refs. [401–405] for leptogenesis studies at points in the Ma model parameter space.

[9] The lifetimes of the heavier scalar states are governed by mass splittings Δ via $\Gamma \sim G_F^2 \Delta^5/(10^2\pi^3)$. In the parameter space of interest, one can check that Δ is typically already large enough at tree-level so that lifetimes remain well below $\mathcal{O}(1\text{ s})$ and therefore do not disturb big bang nucleosynthesis.

In Section 5.2 we listed some minimal ways to adapt the model to avoid this inconsistency: dominiant initial N_1 abundancy; resonant leptogenesis; neutrino oscillations; introducing an independent source of CP violation in N_1 decays; partial loop cancellations; supersymmetry; and reducing the (possibly effective) vev entering the seesaw. We described viable, natural ν2HDMs which utilise the latter mechanism. This can be done radiatively, or by having the second Higgs doublet provide a tree-level seesaw with a small vev v_2, kept natural by softly breaking a $U(1)$ or Z_2 symmetry.

The ν2HDMs accommodate a SM-like Higgs and predict the existence of approximately TeV scale extra scalar states in order to remain natural. We rediscovered the radiative Ma model as the only possibility when $v_2 = 0$; in that case we found 10^3 GeV $\lesssim M_{N_1} \lesssim 10^8$ GeV and $10^{-5} \lesssim \lambda_5 \lesssim 0.5$ could simultaneously explain neutrino masses and the BAU via leptogenesis while remaining natural. The $v_2 > 0$ models require $\tan\beta \gtrsim 4$; we found 10^3 GeV $\lesssim M_{N_1} \lesssim$ few $\times\, 10^7$ GeV was viable for Type I ν2HDMs, and 10^4 GeV $\lesssim M_{N_1} \lesssim$ few $\times\, 10^7$ GeV for all other Types if they are to remain perturbative up to M_N. The interesting areas of parameter space are well summarised in Figure 5.7.

6 Strong CP Problem

> This Chapter is based on the publication "Technically natural non-supersymmetric model of neutrino masses, baryogenesis, the strong CP problem, and dark matter," written in collaboration with Raymond R. Volkas [7].

The theme of this THESIS has been the inability of the SM to explain certain theoretical and phenomenological questions, such as neutrino masses, the BAU, the smallness of the neutron electric dipole moment (the strong CP problem), dark matter, and gravity. Whether nature realises these phenomena in a "natural" way, i.e. in such a way that μ^2 is (sufficiently) insensitive to physically meaningful quantum corrections, remains an open question. Still, motivated by aesthetics, the pursuit of a natural "theory of everything" has inspired much of modern particle physics.

In the same vein, this short Chapter describes a minimal extension of the SM by three right-handed neutrinos, a scalar doublet, and a scalar singlet, which serves as an existence proof that weakly coupled high scale physics can naturally explain phenomenological shortcomings of the SM. The model can be thought of as an extension of the Dine–Fischler–Srednicki-Zhitnitsky (DFSZ) invisible axion model [107, 108] by right-handed neutrinos, and is thus henceforth referred to as the νDFSZ. The νDFSZ can explain neutrino masses, baryogenesis, the strong CP problem, and dark matter, and remains calculably natural despite a hierarchy of scales up to $\sim 10^{11}$ GeV. This is achieved by a seesaw mechanism, intermediate scale hierarchical leptogenesis (10^5 GeV $\lesssim M_N \lesssim 10^7$ GeV), the Peccei–Quinn (PQ) mechanism, an invisible axion, and a technically natural decoupling limit, respectively. Much of the groundwork for the νDFSZ was laid in the ν2HDM of CHAPTER 5, so the discussion here will be kept brief.

This Chapter is organised as follows. We first detail the νDFSZ, its vacuum, and its scalar sector (and constraints). We then describe how it provides explanations for the strong CP problem, dark matter, neutrino masses, and the BAU. Penultimately, we identify the symmetries which protect each scale from quantum corrections, and study an example point in the parameter space.

6.1 The νDFSZ

6.1.1 Lagrangian

The scalar content of the model is a complex singlet S and two complex doublets $\Phi_{1,2}$ of hypercharge +1. The potential is[1]

$$\begin{aligned} V_{\nu\text{DFSZ}} = & M_{11}^2\, \Phi_1^\dagger \Phi_1 + M_{22}^2\, \Phi_2^\dagger \Phi_2 + M_{SS}^2\, S^* S \\ & + \frac{\lambda_1}{2} \left(\Phi_1^\dagger \Phi_1\right)^2 + \frac{\lambda_2}{2} \left(\Phi_2^\dagger \Phi_2\right)^2 + \frac{\lambda_S}{2} \left(S^* S\right)^2 \\ & + \lambda_3 \left(\Phi_1^\dagger \Phi_1\right)\left(\Phi_2^\dagger \Phi_2\right) + \lambda_4 \left(\Phi_1^\dagger \Phi_2\right)\left(\Phi_2^\dagger \Phi_1\right) \\ & + \lambda_{1S} \left(\Phi_1^\dagger \Phi_1\right)(S^* S) + \lambda_{2S} \left(\Phi_2^\dagger \Phi_2\right)(S^* S) \\ & - \epsilon \Phi_1^\dagger \Phi_2 S^2 - \epsilon \Phi_2^\dagger \Phi_1 S^{*2}, \end{aligned} \tag{6.1}$$

where $M_{SS}^2 \sim -\left(10^{11}\ \text{GeV}\right)^2 \equiv -M_{PQ}^2$ sets the PQ scale. Additional terms otherwise allowed by gauge symmetry are forbidden by a global $U(1)_{PQ}$ symmetry to be defined in Section 6.2.1, which is essential in solving the strong CP problem. The ϵ terms are necessary[2] to assign a PQ charge to S and help to generate neutrino masses once S obtains a vacuum expectation value (vev).

The only addition to the SM fermionic content is three right-handed neutrinos. The strong CP solution dictates that Φ_1 (Φ_2) couple to u_R (d_R), and our solution for natural neutrino masses and leptogenesis requires that Φ_2 couple to ν_R. The Yukawa Lagrangian is therefore

$$\begin{aligned} -\mathcal{L}_Y = & + y_u \overline{q_L} \tilde{\Phi}_1 u_R + y_d \overline{q_L} \Phi_2 d_R \\ & + y_e \overline{l_L} \Phi_J e_R + y_\nu \overline{l_L} \tilde{\Phi}_2 \nu_R \\ & + \frac{1}{2} y_N \overline{(\nu_R)^c} S \nu_R + H.c., \end{aligned} \tag{6.2}$$

where family indices are implied, $\tilde{\Phi}_i \equiv i\tau_2 \Phi_i^*$, and $J = 2$ (1) is a Type II (Flipped) ν-two-Higgs-doublet model (ν2HDM) arrangement. We will work in the basis where y_N is diagonal and real. Again, additional terms are forbidden by the $U(1)_{PQ}$ symmetry.[3]

We note here that each of $\epsilon \to 0$, $y_N \to 0$, and $y_\nu \to 0$ is a technically natural limit, since they lead to an extra $U(1)$ symmetry which can be identified with lepton number. As well, there are two apparent technically natural decoupling limits associated with enhanced Poincaré symmetries [37]: $\epsilon, \lambda_{1S}, \lambda_{2S}, y_N \to 0$

[1] As far as we are aware, the νDFSZ was first discussed in Ref. [36]. See Refs. [410–412] and references therein for other minimal approaches to connecting the PQ mechanism with neutrino masses.

[2] Another option is to have terms $-(\kappa \Phi_1^\dagger \Phi_2 S + H.c.)$ [413].

[3] In this model the right-handed neutrinos gain mass from the vev of S, but an alternative scenario with explicit Majorana masses is also possible.

decouples S, and $\epsilon, \lambda_{1S}, \lambda_{2S}, y_\nu \to 0$ decouples the (ν_R, S) subsystem. These limits will prove important in protecting the hierarchy of scales in the model.

6.1.2 Vacuum

The scalar fields acquire vevs $\langle S\rangle \equiv v_S/\sqrt{2}$, $\langle \Phi_i\rangle \equiv \left(0, v_i/\sqrt{2}\right)^T$. If $v_S \gg v_i$, then

$$v_S \approx \sqrt{\frac{-2M_{SS}^2}{\lambda_S}} \sim 10^{11}\ \text{GeV}. \tag{6.3}$$

Expanding around this vev, the right-handed neutrinos acquire Majorana masses $M_N = y_N\langle S\rangle$ and the scalar potential becomes

$$V_{\nu 2\text{HDM}} \approx m_{11}^2\, \Phi_1^\dagger \Phi_1 + m_{22}^2\, \Phi_2^\dagger \Phi_2 - m_{12}^2\, \left(\Phi_1^\dagger \Phi_2 + \Phi_2^\dagger \Phi_1\right) + \dots\,,$$

where $m_{ii}^2 = M_{ii}^2 + \lambda_{iS}\langle S\rangle^2$ and $m_{12}^2 = \epsilon\langle S\rangle^2$. Up to v/v_S corrections, at low scale the νDFSZ therefore just becomes the ν2HDM discussed in CHAPTER 5, with an additional very weakly coupled axion. We will adopt the same natural explanation of neutrino masses and baryogenesis detailed therein. This requires $v_2 \sim \mathcal{O}(1\text{–}10)$ GeV achieved with $m_{11}^2 < 0$, $m_{22}^2 > 0$, and $m_{12}^2/m_{22}^2 \ll 1$.[4] Anticipating $m_{22}^2 \gg v_1^2(\lambda_3+\lambda_4)$, $\lambda_2 v_2^2$, the Φ_i vevs can be written

$$v_2 \equiv \frac{v_1}{\tan\beta} \approx \frac{m_{12}^2}{m_{22}^2} v_1, \qquad\qquad v_1 \approx \sqrt{\frac{2}{\lambda_1}\left(-m_{11}^2 + \frac{m_{22}^2}{\tan^2\beta}\right)}, \tag{6.4}$$

where $\sqrt{v_1^2+v_2^2} = v \approx 246$ GeV and we have implicitly defined $\tan\beta$. The consistency condition Equation (5.27) applies in order to avoid a fine-tuning for v.

Typical values for the mass parameters are $m_{11}^2 \approx -(88\,\text{GeV})^2$, $m_{22} \sim 10^3$ GeV, and $m_{22}^2/\tan^2\beta \ll |m_{11}^2|$. Therefore, for no fine-tuning between M_{ii}^2 and m_{ii}^2, we already expect $\lambda_{1S} \lesssim 10^{-18}$, $\lambda_{2S} \lesssim 10^{-16}$, and $\epsilon \ll 10^{-18}$.

6.1.3 Scalar sector

The scalar mass eigenstates are, up to v_1/m_{22} and m_{12}^2/m_{22}^2 corrections (see Equation (5.29) for expressions), a CP even state (h) with $m_h^2 \approx \lambda_1 v_1^2$, three heavy scalar states ($H, A, H^\pm$) with masses $\approx m_{22}$, a PQ scale neutral scalar (s) with $m_s^2 = \lambda_S v_S^2$, and a very light pseudo-Goldstone boson (the invisible axion).

Owing to the approximate $U(1)$ symmetry due to $m_{12}^2/m_{22}^2 \ll 1$ and $v^2/m_{22}^2 \ll 1$, the state h closely resembles the SM Higgs. We refer to Figure 5.4 for the various constraints on m_{22}. These are the aforementioned consistency condition, measurements of $B \to X_s\gamma$ [390, 391], $H/A \to \tau\tau$ LHC searches (for the

[4] Note that, like $\epsilon \to 0$ in the original Lagrangian, $m_{12}^2/m_{22}^2 \to 0$ is a technically natural limit associated with $U(1)_L$ [367].

Field	$U(1)_{PQ}$	Value in [Type II, Flipped]
S	X_S	$\frac{1}{2}$
Φ_1	X_1	$\cos^2\beta$
Φ_2	X_2	$-\sin^2\beta$
q_L	X_q	0
u_R	X_u	$\cos^2\beta$
d_R	X_d	$\sin^2\beta$
l_L	X_l	$\frac{3}{4} - \cos^2\beta$
ν_R	X_ν	$-\frac{1}{4}$
e_R	X_e	$\left[\frac{7}{4}, \frac{3}{4}\right] - 2\cos^2\beta$

TABLE 6.1: Charges of νDFSZ fields under the PQ symmetry.

Type II model) [371, 393], perturbativity up to the Planck scale [384], and naturalness [5]. The naturalness bound was derived in Ref. [5] subject to the naturalness condition we describe in Section 6.3.1, and we refer the reader there for details.

6.2 Strong CP problem, dark matter, neutrino mass, and the BAU

6.2.1 Strong CP problem

In Section 1.1.5 we described the solution to the strong CP problem by PQ symmetry; let us now identify the global $U(1)_{PQ}$ symmetry in the νDFSZ. Defining the $U(1)_{PQ}$ charge names as in Table 6.1, we can (without loss of generality) set $X_q = 0$ and $X_u + X_d = 1$. Equations (6.1) and (6.2) set an additional six constraints on the charges, which brings the total to eight for nine unknown charges. They are completely defined by setting $X_1 = \alpha X_2$, as long as $\alpha \neq 1$; it is convention to choose $\alpha = -\cot^2\beta$ so that the PQ current does not couple to the field eaten by the Z boson. The resulting charge values are given in Table 6.1. This is enough to solve the strong CP problem, in the same spirit as the original DFSZ model.

A final comment before moving on. In the SM, if $\bar\theta$ is set to zero by hand at some high scale, renormalisation implies $\bar\theta \lesssim 10^{-17}$ [414, 415], well below the experimental bound. In this sense, in the SM, $\bar\theta \approx 0$ is *already* natural. Yet this explanation remains unsatisfying, since the limit $\bar\theta \to 0$ cannot be identified with a symmetry. The νDFSZ solution requires $\lambda_{iS} \lll 1$, and thus one could similarly ask: why are the $\lambda_{iS} \approx 0$? At least, here, this limit is identified with an increased Poincaré symmetry. As well, in the presence of CP violating new physics (such as the right-handed neutrinos), this solution *guarantees* $\bar\theta \approx 0$.

6.2.2 Dark matter

The νDFSZ axion gains a mass

$$m_a \approx 60\ \mu\text{eV}\left(\frac{10^{11}\ \text{GeV}}{f_a}\right) \tag{6.5}$$

due to the chiral anomaly [106, 416], where $f_a \approx \langle S \rangle$ is the axion decay constant, and inherits v/f_a suppressed couplings to nucleons, photons, and electrons (for expressions see e.g. Ref. [106]). Stellar energy loss constrains $f_a \gtrsim 4 \times 10^8$ GeV [106].[5]

The axion provides a cold dark matter candidate via the misalignment mechanism [420–422], wherein a significant amount of energy density is stored in coherent oscillations of the axion field, [423]

$$\Omega_a h^2 \sim 0.02 \left(\frac{f_a}{10^{11}\ \text{GeV}} \right)^{\frac{7}{6}} \left(\frac{\theta^2}{\pi^2/3} \right), \tag{6.6}$$

where $-\pi \leq \theta \leq \pi$ is the misalignment angle. The requirement that this quantity not exceed the measured cold dark matter energy density $\Omega_{\text{CDM}} h^2 \approx 0.12$ [69] implies

$$f_a \lesssim 6 \times 10^{11}\ \text{GeV} \left(\frac{\pi^2/3}{\theta^2} \right)^{\frac{6}{7}}, \tag{6.7}$$

with equality reproducing the observed density. If the PQ symmetry is broken after inflation, then the misalignment angle is the average value taken over many distinct patches, $\theta^2 \approx \pi^2/3$, and one obtains $f_a \lesssim 6 \times 10^{11}$ GeV [424].[6] Future projections of the ADMX and CAPP resonant microwave cavity experiments promise to probe this interesting region of parameter space [426, 427].

6.2.3 Neutrino mass and the BAU

Neutrino masses and the BAU are reproduced by the same mechanisms as in the ν2HDM detailed in Sections 5.2.4 and 5.2.5 of CHAPTER 5.

The neutrino mass matrix is given by Equation (5.43), and reproduced here for convenience:

$$m_\nu = \frac{v_2^2}{2} y_\nu \mathcal{D}_M^{-1} y_\nu^T \approx \frac{1}{\tan^2 \beta} \left(\frac{v^2}{2} y_\nu \mathcal{D}_M^{-1} y_\nu^T \right), \tag{6.8}$$

where the bracketed quantity is the typical Type I seesaw formula.

The BAU is produced analogously to standard hierarchical thermal leptogenesis, via the out-of-equilibrium, CP violating decays of the lightest right-handed neutrino: $N_1 \to l\Phi_2$. As argued in Section 5.2.5, there will be minor changes to the standard picture from extra $\Delta L = 1$ scatterings mediated by b quarks and (in Type II) τ leptons. The $\Delta L = 2$ scatterings can constitute a significant departure from the standard case, particularly in $K \ll 1$ scenarios dependent on

[5] In a Type II νDFSZ, red giants and white dwarfs constrain $f_a \gtrsim 8 \times 10^8 \sin^2 \beta$ GeV (the white dwarf cooling fit is actually improved for $f_a \approx 1 \times 10^9 \sin^2 \beta$) [106, 417–419].

[6] If inflation occurred after PQ symmetry breaking then a smaller θ can be anthropically chosen, allowing $f_a > 10^{12}$ GeV [425].

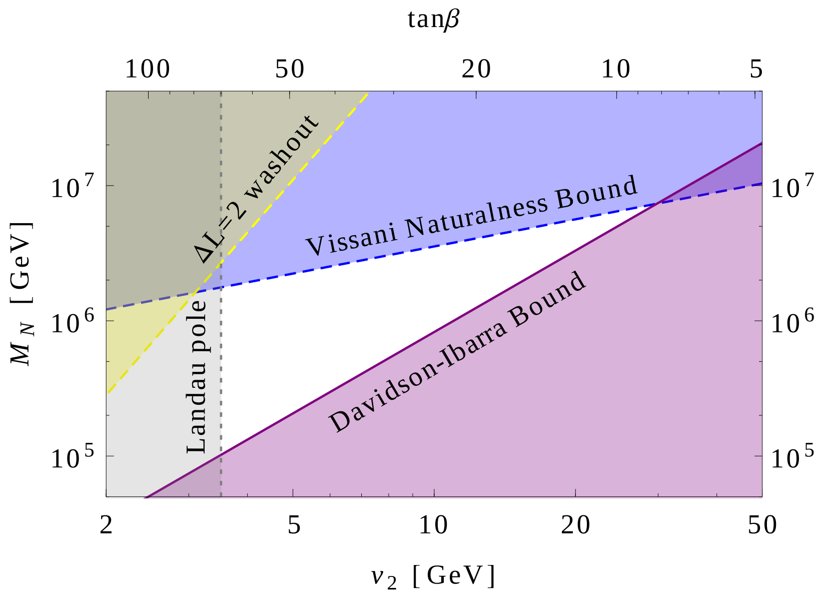

FIGURE 6.1: Constraints on the right-handed neutrino masses. The naturalness bound on M_N corresponds to the rough bound Equation (6.13) evaluated at $m_{22} = 1$ TeV.

initial conditions. However for the parameter space of interest to us, the generated asymmetry is safe from strong $\Delta L = 2$ scattering washout, as shown in Figure 6.1. An additional consideration in the νDFSZ is $N_1 N_1 \to aa$ annihilations; an estimate of the rate is $\Gamma_{N_1 N_1 \to aa} \sim 10^{-2} M_{N_1}^5 / \langle S \rangle^4$ at $T = M_{N_1}$, which implies the out-of-equilibrium condition $M_{N_1} \lesssim 10^9$ GeV, easily satisfied the parameter space of interest. As we noted in the ν2HDM picture, these departures from the standard scenario deserve further detailed study. Still, we do not expect the picture to be dramatically changed. In particular we expect the Davidson–Ibarra bound [96, 97] for successful hierarchical thermal leptogenesis, scaled for the differing vev in Equation (5.43), to approximately hold:

$$M_{N_1} \gtrsim \frac{5 \times 10^8 \text{ GeV}}{\tan^2 \beta}. \tag{6.9}$$

This bound is depicted in Figure 6.1.

6.3 Naturalness

6.3.1 Our naturalness philosophy

In CHAPTER 3 we explained why the RG formalism is a sensible way to quantify a physical naturalness problem in any perturbative quantum field theory. If the $\mu^2(\mu_R)$ RGE contains no large corrections then a model can be considered natural: $\mu^2(\mu_R)$ remains stable under RG evolution up to high scales. Extending this idea to other mass scales in the model, we can say that a model is natural if all scales remain stable under RG evolution. In that case, it follows intuitively that the low scale observables are not extremely sensitive to variations around their high scale inputs. In this Section we show that there exists a region of νDFSZ parameter space where our phenomenological goals can be achieved and the heavy PQ scale induces no naturalness problem.

6.3.2 Naturalness in the νDFSZ

Defining $\mathcal{D} \equiv (4\pi)^2 \frac{d}{d \ln \mu_R}$ and keeping only $y_{t,b,\tau,\nu}$ Yukawas, the one-loop RGEs for the [Type II, Flipped] ν2HDM mass parameters can be written [303]

$$\begin{aligned}
\mathcal{D} m_{12}^2 &= m_{12}^2 \bigg(-\frac{3}{2} g_1^2 - \frac{9}{2} g_2^2 + 2\lambda_3 + 4\lambda_4 + 2\lambda_S + 4\lambda_{1S} + 4\lambda_{2S} \\
&\quad + 3y_t^2 + 3y_b^2 + y_\tau^2 + \mathrm{Tr}\left(y_\nu^\dagger y_\nu \right) \bigg), && (6.10) \\
\mathcal{D} m_{11}^2 &= m_{11}^2 \left(-\frac{3}{2} g_1^2 - \frac{9}{2} g_2^2 + 6\lambda_1 + 6y_t^2 + \left[0, 2y_\tau^2\right] \right) \\
&\quad + m_{22}^2 \left(4\lambda_3 + 2\lambda_4\right) + \langle S \rangle^2 \lambda_{1S} \left(4\lambda_{1S} + 4\lambda_S\right) + M_{SS}^2 2\lambda_{1S}, && (6.11) \\
\mathcal{D} m_{22}^2 &= m_{22}^2 \left(-\frac{3}{2} g_1^2 - \frac{9}{2} g_2^2 + 6\lambda_2 + 6y_b^2 + \left[2y_\tau^2, 0\right] + 2\mathrm{Tr}\left(y_\nu^\dagger y_\nu \right) \right) \\
&\quad + m_{11}^2 \left(4\lambda_3 + 2\lambda_4\right) + \langle S \rangle^2 \lambda_{2S} \left(4\lambda_{2S} + 4\lambda_S\right) + M_{SS}^2 2\lambda_{2S} \\
&\quad - 4\mathrm{Tr}\left(y_\nu M_N^2 y_\nu^\dagger \right), && (6.12)
\end{aligned}$$

where $M_N^2 = y_N^\dagger y_N \langle S \rangle^2$ is the (diagonalised) right-handed neutrino mass matrix. The $\langle S \rangle^2$ and M_{SS}^2 terms correspond to the contribution from the heavy real singlet s in the broken phase. We provide the full list of RGEs in Appendix C.1.

These RGEs make manifest the decoupling limit ϵ, λ_{1S}, λ_{2S}, $\mathrm{Tr}(y_\nu^\dagger y_\nu y_N^\dagger y_N) \to 0$ which protects the scales from large corrections. First, corrections to m_{12}^2 are proportional to m_{12}^2, reflecting the fact that $\epsilon \to 0$ reinstates a $U(1)_L$ symmetry. Second, because the parameters $\lambda_{3,4}$ are reintroduced by gauge loops, m_{11}^2 can only be protected from m_{22}^2 by having m_{22}^2 not too much larger than m_{11}^2; in CHAPTER 3 it was shown that $m_{22} \lesssim 2.1$ TeV can accommodate a 10% fine-tuning measured at Λ_{Pl}. Third, m_{22}^2 is protected from the M_N by (roughly) $\mathrm{Tr}(y_\nu^\dagger y_\nu y_N^\dagger y_N)/(4\pi^2) \lesssim m_{22}^2/\langle S \rangle^2$; this translates to the sufficient condition (see Section 5.1)

$$M_N \lesssim \frac{3 \times 10^7 \text{ GeV}}{\tan^{\frac{2}{3}} \beta} \left(\frac{m_{22}}{\text{TeV}} \right)^{\frac{2}{3}}, \tag{6.13}$$

for all the right-handed neutrinos, illustrated in Figure 6.1. Last, the m_{ii}^2 are protected from the PQ scale by (again roughly) $\lambda_{iS} \lesssim m_{ii}^2/\langle S \rangle^2$. We note that there is a lepton box induced correction to λ_{2S}; this correction is also bounded by $m_{ii}^2/\langle S \rangle^2$ through Equation (6.13).

6.3.3 Explicit example

As a final demonstration we thought it illustrative to solve the coupled set of RGEs for an explicit example. We consider $\tan\beta = 30$ and neglect running in the following six quantities:

$$\begin{aligned} M_{SS}^2 &= -(10^{11}\ \text{GeV})^2, & M_{N_1} &= 6\times 10^5\ \text{GeV}, \\ \langle S\rangle^2 &= -M_{SS}^2/\lambda_S, & M_{N_2} &= M_{N_3} = 10^6\ \text{GeV}, \\ \lambda_S &= 0.26, & y_N &= M_N/\langle S\rangle. \end{aligned} \tag{6.14}$$

We have taken M_{N_1} at the Davidson–Ibarra bound and $M_{N_{2,3}}$ below the rough naturalness bound Equation (6.13). We take y_ν according to Equations (5.48) and (5.49) with $K = 1$, and neglect running here as well. A glance at the RGEs in Appendix C.1 will convince the reader that neglecting running in these parameters is a good approximation. Decoupling of the heavy degrees of freedom at m_s, M_{N_i}, and m_{22} should be accompanied by an associated shift in the λ_j parameters, matching to the effective theory below each threshold. However, in practice, since the λ_{iS}, y_ν are so small and m_{22} is not too much larger than m_Z, it makes little numerical difference to implement this shift. Therefore we evolve the following parameters under the νDFSZ RGEs:[7]

$$\begin{aligned} \lambda_3(m_{22}) &= \lambda_4(m_{22}) = 0.02, & \lambda_{1S}(m_s) &= 10^{-18}, \\ \lambda_1(m_Z) &= \lambda_2(m_Z) = 0.26 & \lambda_{2S}(m_s) &= 10^{-16}, \\ y_t(m_Z) &= 0.96/\sin\beta, & g_1^2(m_Z) &= 0.13, \\ y_b(m_Z) &= 0.017/\cos\beta, & g_2^2(m_Z) &= 0.43, \\ y_\tau(m_Z) &= 0.010/\cos\beta, & g_3^2(m_Z) &= 1.48. \end{aligned}$$

Their evolution is shown in Figure 6.3.[8]

To evolve the mass parameters we set $m_{11}^2(m_{22}) = -(88\ \text{GeV})^2$ and consider $m_{22}(m_{22}) = 0.6, 0.8, 1.0, 2.0$ TeV, with N_i and s decoupled by step functions at their thresholds. Their RG evolution is shown in Figure 6.2; it is plain that the mass parameters in this (viable) example remain relatively small up to high scales, and are therefore natural according to our philosophy.

6.4 Conclusion

We have described an extension of the SM (the "νDFSZ") by three right-handed neutrinos, a complex scalar doublet, and a complex scalar singlet. The νDFSZ

[7] For definiteness we take a Type II arrangement, but the Flipped arrangement gives very similar results.

[8] We note that the parameter λ_1 tends to run negative, threatening the stability of the electroweak vacuum; nevertheless we expect the problem to be no worse than in the SM, i.e. we expect a metastable vacuum.

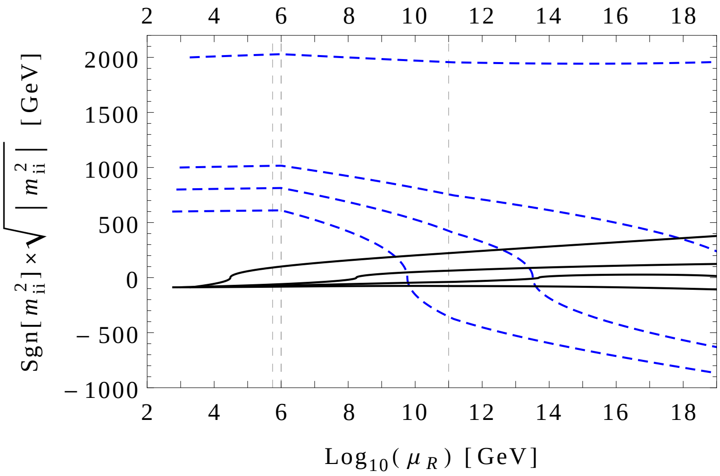

FIGURE 6.2: Example RG evolution (see text) of $m_{11}^2(\mu_R)$ (black solid) and $m_{22}^2(\mu_R)$ (blue dashed) for $m_{22} = 0.6, 0.8, 1.0, 2.0$ TeV bottom to top.

serves as an existence proof that weakly coupled high-scale physics can explain phenomenological shortcomings of the SM *without introducing a naturalness problem*. The model explains neutrino masses, the BAU, the strong CP problem, and dark matter, via a seesaw mechanism, hierarchical leptogenesis, the PQ mechanism, and a DFSZ invisible axion, respectively. It contains four scales: $|m_{11}| \approx 88$ GeV, $m_{22} \sim 10^3$ GeV, $M_N \sim 10^5$–10^7 GeV, and $M_{PQ} \sim 10^{11}$ GeV, each protected from quantum corrections by a technically natural decoupling limit. The $\sim$TeV scale scalars and the invisible axion of the model will be probed in upcoming experiments.

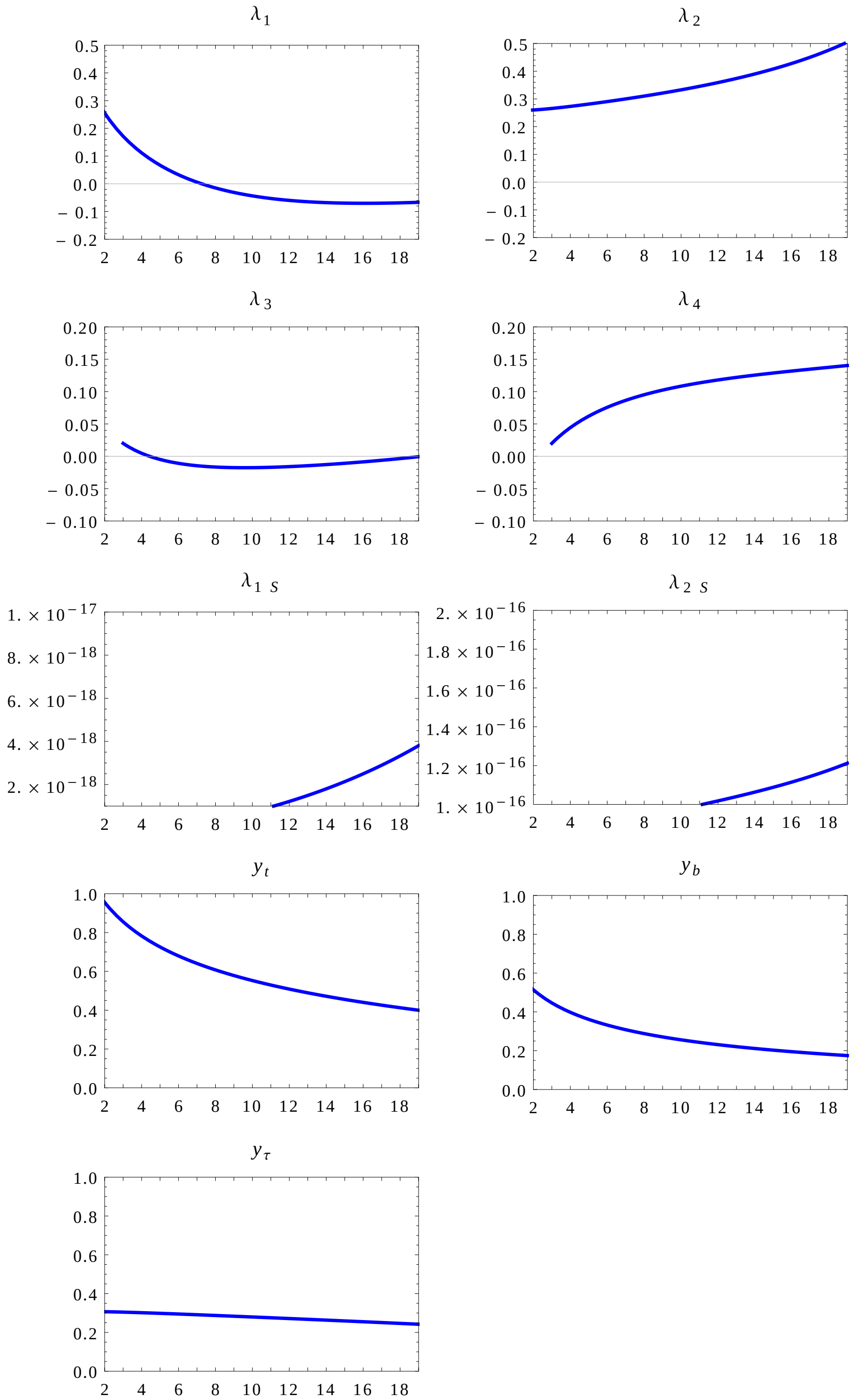

FIGURE 6.3: Example RG evolution of dimensionless parameters, as a function of $\log_{10}(\mu_R/\text{GeV})$.

7 Dark Matter

This Chapter is based on the publication "Plasma dark matter direct detection," written in collaboration with Robert Foot [8].

In Section 1.1.6 we introduced the overwhelming evidence for dark matter (DM). Still, its precise nature remains uncertain. Collisionless DM is a simple and well studied possibility, which works very well on large scales, but has some shortcomings on galactic scales (e.g. Refs. [120, 121, 428]). On the other hand, it is possible that DM has a very rich structure. This is especially natural if DM resides in a hidden sector with its own gauge interactions. In particular, DM might be multicomponent, charged under an unbroken dark $U(1)'$ gauge interaction, i.e. it interacts with itself via a massless "dark photon". It has been suggested that such self-interactions may even go some way toward ameliorating small scale structure problems (cf. Refs. [429–431]). Mirror dark matter (MDM) is a theoretically constrained example of such a theory [432] and there are many other scenarios considered in the literature (e.g. Refs. [433–444]). In such a framework, it is possible that the DM in the Universe exists primarily in a plasma state, as a macroscopically neutral "conductive gas" of ions with dark charge, broadly analogous to the state of much of the ordinary matter in the Universe. It is this "plasma dark matter" scenario that is the subject of this Chapter.

One important and distinctive property of a multicomponent plasma DM halo with light and heavy mass components is the following: energy equipartition implies light component velocities which are much larger than those expected under single component virialisation, and overall $U(1)'$ neutrality implies they can even be much larger than the galactic escape velocity. It has been pointed out [445] that this effect can give rise to observable keV electron recoils in direct detection experiments. It might even be possible to explain the DAMA annual modulation signal [143, 144, 446–448] in this manner, since the constraints on electron recoils provided by other experiments are generally much weaker than those of nuclear recoils. However, a detailed description of the plasma DM density and velocity distribution in the vicinity of the Earth is required. This is a highly non-trivial problem. If the dark plasma has interactions with ordinary matter then it will by captured by the Earth, forming an approximate "dark sphere" within. Understanding the interaction of the dark plasma with this dark sphere as the Earth moves through the halo is therefore of primary importance.

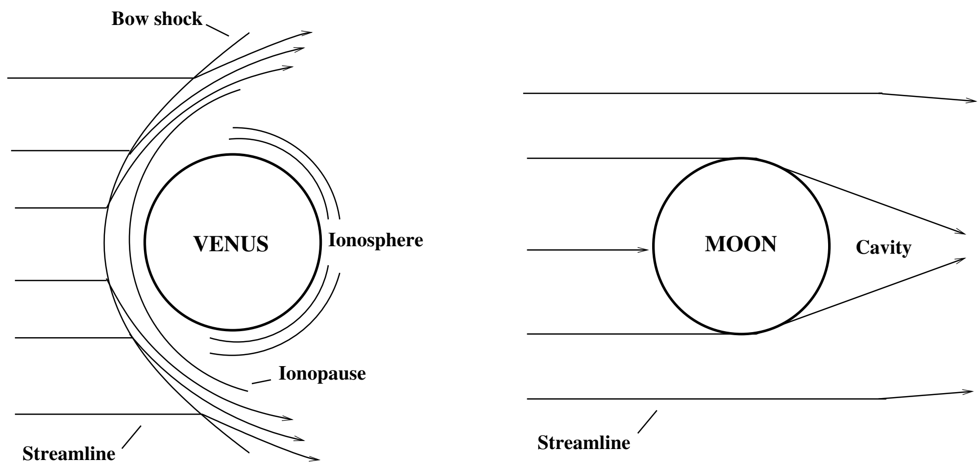

FIGURE 7.1: The solar wind interaction with Moon/Venus. These systems appear to represent useful analogues to the possible ways in which the dark plasma wind interacts with captured DM within the Earth.

The aim of this Chapter is to provide a consistent description of this interaction in order to qualitatively understand the implications for direct detection.

The captured dark sphere within the Earth forms an obstacle to the dark plasma wind. Two limiting cases can be envisaged: (1) if the captured DM is largely neutral, i.e. poorly conducting, then the dark plasma wind will be absorbed by the dark sphere, or; (2) if the captured DM is largely ionised, then the obstacle forms a conducting sphere which effectively deflects the dark plasma wind. Interestingly, these limiting cases appear analogous to the solar wind interaction with the Moon and Venus, respectively (e.g. Refs. [449, 450]); this is sketched in Figure 7.1. The Moon has no magnetic field and no atmosphere, so that the solar wind is largely absorbed at the lunar surface with very little upwind activity. Venus has no magnetic field, but forms an electrically conductive layer at the edge of its ionosphere, which at first approximation forms an impenetrable obstacle to the solar wind. These systems have been studied using magnetohydrodynamic (MHD) models, and this would seem to be an appropriate starting point for studying the dark plasma wind interaction with the captured DM within the Earth.

This Chapter is set out as follows. In Section 7.1 we provide a brief introduction to the plasma DM model and identify the parameter space of interest. In Section 7.2 we discuss some relevant properties of the dark sphere of DM captured within the Earth, and the DM plasma wind interaction with this dark sphere, modelled via magnetohydrodynamics. In Section 7.3 we consider the direct detection of plasma DM, identifying the general sources of event rate modulation, studying the modulation in a specific example (electron recoils in MDM), and describing the implications of our results in the light of the current experimental situation. In Section 7.4 our conclusions are drawn. In particular, the analysis presented here leaves open the intriguing possibility that the DAMA annual modulation signal is due primarily to electron recoils (or even a combination of electron recoils and nuclear recoils). The importance of diurnal modulation (in addition to annual modulation) as a means of probing this kind of DM is also emphasised.

7.1 Plasma dark matter

DM might reside in a hidden sector with its own gauge interactions. If the hidden sector contains an unbroken $U(1)'$ gauge interaction, then $U(1)'$ neutrality of the Universe implies a multicomponent self-interacting DM sector consisting of fermions and/or bosons carrying $U(1)'$ charge. In the following discussion we consider the minimal two-component case with fermionic DM. The DM consists of a "dark electron" (e_d) and a "dark proton" (p_d) with masses $m_{e_d} \leq m_{p_d}$ and $U(1)'$ charge ratio $Z' \equiv |Q'(p_d)/Q'(e_d)|$. The fundamental interactions are described by the hidden sector Lagrangian:

$$\mathcal{L} = \mathcal{L}_{SM}(e, \mu, u, d, A^{\mu}, ...) \ + \ \mathcal{L}_{dark}(e_d, p_d, A_d^{\mu}) \ + \ \mathcal{L}_{mix} \ . \tag{7.1}$$

Self-interactions of the dark electron and dark proton are mediated via the massless dark photon. These self-interactions can be defined in terms of the $U(1)'$ gauge coupling, g', or more conveniently by the dark electron fine structure constant, $\alpha_d \equiv [g'Q'(e_d)]^2/4\pi$. The dark sector is then fully described by the fundamental parameters: $m_{e_d}, m_{p_d}, Z', \alpha_d$.

One special case of this picture is a thermal relic DM scenario with particle–antiparticle DM [433].[1] In this case the parameters are constrained: $m_{e_d} = m_{p_d} \equiv m_{\chi}$, $Z' = 1$, and $\alpha_d \approx \ 4 \times \ 10^{-5} \ (m_{\chi}/\text{GeV})$. We will be more interested in the general asymmetric DM scenario in which $m_{e_d} \neq m_{p_d}$. A special case of this is MDM [432], where the hidden sector is exactly isomorphic to the standard model so that an exact discrete Z_2 symmetry swapping each ordinary particle with a "mirror" particle can be defined [132]. The interactions of the mirror electrons together with the dominant mass component, assumed to be mirror helium, is then described by: $m_{e_d} = m_e \simeq 0.511$ MeV, $m_{p_d} = m_{He} \simeq 3.76$ GeV, $Z' = 2$ and $\alpha_d = \alpha \simeq 1/137$.

The interactions of the dark sector with the standard sector are contained within the $\mathcal{L}_{mix}$ term in Equation (7.1). The only renormalisable (and non-gravitational) interaction allowed in the minimal setup is kinetic mixing of the $U(1)_Y$ and $U(1)'$ gauge bosons [451], which implies also photon - dark photon

[1] The particle-antiparticle case is also special because such DM can undergo annihilations into dark photons. DM annihilations are forbidden in the more general case assuming the minimal particle content ($A_d, \ e_d, \ p_d$), which can be viewed as a consequence of accidental $U(1)'$ dark lepton and dark baryon number global symmetries.

kinetic mixing:

$$\mathcal{L}_{mix} = \frac{\epsilon'}{2} F^{\mu\nu} F'_{\mu\nu} \, . \tag{7.2}$$

Here $F_{\mu\nu}$ and $F'_{\mu\nu}$ denote the field strength tensors for the photon and dark photon respectively and the dimensionless parameter ϵ' encodes the strength of the mixing interaction. The kinetic mixing interaction imbues the dark electron and dark proton with an ordinary electric charge, proportional to this kinetic mixing parameter, ϵ' [131]. It is convenient to introduce a new parameter, ϵ, such that the magnitude of the dark electron's ordinary electric charge is ϵe. Now, including the dark sector parameters, the fundamental physics is fully described by five parameters: $m_{e_d}, m_{p_d}, Z', \alpha_d, \epsilon$.

In this Chapter we are interested in the region of parameter space whereby the DM in spiral galaxies such as the Milky Way is in the form of a dark plasma. Typically this requires that the dark atomic binding energy be much smaller than (or of order) the temperature of the dark electrons (see [452] for more precise calculations). The binding energy of the hydrogen-like dark atom consisting of a dark proton and a dark electron is

$$I = \frac{1}{2} Z'^2 \alpha_d^2 \mu_d \, , \tag{7.3}$$

where $\mu_d = m_{e_d} m_{p_d}/(m_{e_d} + m_{p_d})$ is the reduced mass. The temperature of the dark electrons is more difficult to determine. Let us assume for now that the frequency of interactions of the dark electrons and dark protons is sufficiently great so that they have approximately the same temperature, and that this temperature is approximately the same throughout the halo (we will return to this condition shortly). The halo temperature can then be estimated from the virial theorem [453] and also by assuming hydrostatic equilibrium [432]:

$$T \sim \frac{1}{2} \bar{m} v_{rot}^2 \, , \tag{7.4}$$

where v_{rot} is the asymptotic value of the rotational velocity of the galaxy (for the Milky Way, $v_{rot} \approx 220$ km/s) and $\bar{m}$ is the mean mass of the particles in the halo.[2] For a fully ionised halo the mean mass can be determined from $U(1)'$ neutrality:

$$\bar{m} = \frac{m_{p_d} + Z' m_{e_d}}{Z' + 1} \, . \tag{7.5}$$

The plasma will be fully ionised if $I/T \ll 1$, a condition that reduces to:

$$\frac{I}{T} \simeq 0.20 \, Z'^2 (Z'+1) \left(\frac{\alpha_d}{10^{-2}}\right)^2 \left(\frac{\mu_d}{\text{MeV}}\right) \left(\frac{\text{GeV}}{m_{p_d} + Z' m_{e_d}}\right) \left(\frac{220 \text{ km/s}}{v_{rot}}\right)^2 \ll 1 \, . \tag{7.6}$$

[2]Unless otherwise stated we adopt natural units where $\hbar = c = k_B = 1$.

Of course with the dark photon massless this type of DM is dissipative. The plasma halo can radiatively cool via processes such as dark bremsstrahlung and potentially collapse onto a disk on a timescale less than the Hubble time. Thus, there is another condition for such a plasma to exist today, namely that the cooling timescale is longer than the Hubble time, or that a heating mechanism exists. The cooling timescale is given in e.g. [444] and requiring that this timescale be longer than the Hubble time for the Milky Way gives the approximate condition

$$m_{p_d} \gtrsim 20 \left(\frac{\mathrm{MeV}}{m_{e_d}}\right) \left(\frac{\alpha_d}{10^{-2}}\right)^2 Z'^{5/3}\ \mathrm{GeV}\ . \tag{7.7}$$

This was derived assuming that cooling is dominated by bremsstrahlung for the most stringent case of $m_{e_d} \ll m_{p_d}$. The alternative possibility is that the cooling rate is sufficiently high for the halo to have collapsed but is prevented from doing so due to heating [126, 444, 452–455]. If $\epsilon \sim 10^{-9}$–10^{-10} then sufficient heating of the halo can be provided by ordinary core-collapse supernovae [444, 453]. In that scenario, the halo is viewed as a dynamical object which evolves until an equilibrium configuration is reached where heating and cooling rates locally balance.

The conditions so far have been derived assuming that interactions were sufficiently rapid so that dark electrons and dark protons have approximately the same temperature. Let us briefly estimate the parameter space where this assumption is reasonable. If the mean kinetic energy of the dark electrons happened to be much greater than that of the dark protons, then the two body Rutherford scattering process ($e_d + p_d \leftrightarrow e_d + p_d$) would transfer net energy from the dark electrons to dark protons. Requiring that the timescale for which dark electrons are able to transfer all their excess energy to the dark protons is less than the Hubble time gives:

$$n_{e_d} n_{p_d} \int \frac{d\sigma}{dE_R}\, E_R v\, dE_R \gtrsim \frac{T n_{e_d}}{t_H}\ , \tag{7.8}$$

where T is the temperature of the dark electrons, $t_H \sim 14$ Gyr is the Hubble time and $d\sigma/dE_R$ is the differential cross section in terms of the recoil energy E_R of the scattered dark proton (approximated as initially at rest relative to the incoming dark electron of velocity, v). The cross section for this Rutherford scattering process is given by $d\sigma/dE_R = 2\pi Z'^2 \alpha_d^2/(m_{p_d} E_R^2 v^2)$. Equation (7.8) can be straightforwardly evaluated with the result depending logarithmically on the integration limits. The upper integration limit is obtained from kinematics: $E_R^{max} = 4E_i\mu_d/[m_{e_d} + m_{p_d}]$ (where $E_i \sim T$ is the initial energy of the dark electron) while the lower integration limit is given in terms of the Debye shielding length, $\lambda_D = \sqrt{T/(4\pi\alpha_d n_{e_d})}$, the scale over which the dark proton's charge is shielded by the dark electrons. Assuming T given by the estimate, Equation (7.4), and for typical Milky Way DM densities, $\rho_{DM} \sim 0.3\ \mathrm{GeV/cm^3}$, we find that Equation (7.8) reduces to the condition (for $m_{e_d} \ll m_{p_d}$):

$$m_{p_d} \lesssim 10^2 \, (Z'+1)^{3/7} \left(\frac{220 \text{ km/s}}{v_{rot}}\right)^{6/7} \left(\frac{Z'\alpha_d}{10^{-2}}\right)^{4/7} \left(\frac{m_{e_d}}{\text{MeV}}\right)^{1/7} \text{GeV} \,. \tag{7.9}$$

Strictly this derivation assumes the case of negligible dissipation and heating of the halo during the Hubble timescale, and modification is possible in the alternative case.

Equations (7.6), (7.7), and (7.9) give the rough conditions under which the DM is expected to take the form of a plasma in galaxies with the mean kinetic energy of the dark electrons comparable to that of the dark protons. It is clear that there is a significant region of parameter space available. In the limit where the dark electrons are much lighter than the dark protons, an important feature emerges: *the velocity dispersion of the dark electrons is much greater than that of the dark protons, and in fact can be even larger than the typical galactic escape velocity*. The dark electrons are prevented from escaping the galaxy due to $U(1)'$ neutrality; the plasma is highly conducting, and dark electric forces act to keep the plasma neutral over length scales larger than the Debye length. This is a distinctive feature of the plasma DM halo, indeed this behaviour is very different from weakly interacting massive particle (WIMP) DM or even a collisional gas of light and heavy neutral components.

Before proceeding further, we conclude this Section with a brief discussion relating to the bigger picture. Cosmological aspects of plasma DM have been discussed in the literature in the special case of MDM (e.g. Refs. [432, 456–461]). There is also a growing literature exploring more generic models with DM featuring unbroken $U(1)'$ (dark photon) gauge interactions (e.g. Refs. [433–435, 437, 438, 440–444, 462–466]). These studies demonstrate, among other things, that this type of self-interacting DM can reproduce the success of collisionless cold DM on very large scales with deviations expected on smaller scales. Indeed, the self-interactions might be important in addressing long-standing problems on small scales, including an explanation for cored DM profiles within galaxies. However, there are also upper bounds on the strength of such self-interactions. In particular, merging cluster systems have been used as a probe of DM self-interactions, the Bullet cluster system being one well studied example [124, 467]. Attempting to evaluate robust bounds on plasma DM from cluster collisions is, unfortunately, non-trivial. Firstly, the plasma DM self-interactions on cluster scales require careful modelling, as it is the collective plasma effects (i.e. not hard collisions) which potentially dominate [468]. Secondly, the plasma DM distribution within the cluster is required but is very uncertain. If the DM is sufficiently "clumpy" then the DM associated with each cluster can pass through each other essentially unimpeded, thereby consistent with the observations [469]. This depends on the fraction of the DM bound to individual galaxy halos compared to the diffuse cluster component, which is difficult to determine as it depends on the detailed properties of the cluster and its history, as well as the properties of the dark plasma. In short, despite the fact that such cluster mergers do in principle constrain the plasma DM parameters, it is not yet possible to write down any reliable and caveat-free bounds.

7.2 Plasma dark matter and the Earth

7.2.1 Within the Earth

The physical properties of the halo DM in the vicinity of the Earth are influenced by the way in which the halo DM interacts with the DM bound within the Earth. It is therefore pertinent to try to understand some of the relevant features of this "dark sphere" of influence. Some aspects of this problem have already been discussed for the specific cases of MDM [470] and for more generic dissipative DM models [471]. The discussion below draws on this work and extends it to the more general plasma case.

How does DM within the Earth arise? The kinetic mixing induced interaction with standard matter will occasionally trap some halo DM particles within the Earth during its formation phase and subsequently. Eventually sufficient DM accumulates so that further DM capture is primarily facilitated by self-interactions of halo DM with this captured DM. Once captured, it is expected to quickly thermalise with the ordinary matter within the Earth via the kinetic mixing interactions, to a temperature $T_E \sim 5000$ K (0.4 eV). If $m_{p_d} \gg$ MeV, this is much cooler than the halo temperature and the dark protons and dark electrons can potentially combine into neutral dark atoms. The dark sphere will be largely neutral (ionised) if $T_E \ll I$ ($T_E \gg I$), where I is the dark atomic binding energy given already in Equation (7.3). This motivates two limiting cases: a neutral "Moon-like" case in which the dark sphere largely absorbs the dark plasma wind, and; an ionised "Venus-like" case in which the dark sphere largely deflects the dark plasma wind by way of a current-carrying sheet at the "dark ionopause" (located where the plasma wind and "dark ionosphere" pressures equilibrate). In addition to its ionisation state, the other defining feature of the dark sphere is its effective size. Let us define a parameter, R_{DM}, which corresponds to the dark plasma wind stopping radius for the Moon-like case, and the dark ionopause radius for the Venus-like case. We will now attempt to estimate R_{DM} in terms of the fundamental plasma parameters.

If the dark sphere is Moon-like, then the (relatively stationary) dark protons accumulate at the "geometric" rate

$$\frac{dN_{p_d}}{dt} \approx \pi R_{DM}^2 v_{rot} n_{p_d} \ . \tag{7.10}$$

Dark electrons will be captured at a similar rate: $dN_{e_d}/dt = Z' dN_{p_d}/dt$ given the expected approximate $U(1)'$ charge neutrality of the Earth.[3] This represents an upper bound for the accumulation rate in the Venus-like case, though it might still be a useful estimate so long as a significant fraction ($\gtrsim 1\%$) of the halo wind is stopped within the Earth. Loss rates due to mechanisms such as thermal escape and dark atmospheric stripping are difficult to evaluate. Naturally, any estimate of the total amount of DM captured within the Earth is uncertain. Fortunately, it turns out that R_{DM} depends only weakly on the total number of Earth bound DM particles.

If we equate the radial temperature profile of the dark sphere gas/plasma with that of the Earth [472], the dark thermal pressure is given by $p(r) = \rho_{DM}(r)T_E(r)/\bar{m}$. Here $\bar{m}$ is the mean mass taking into account the ionisation state of the captured DM at the temperature $T_E(r)$. Assuming $m_{p_d} \gg m_{e_d}$, then $p(r) \simeq \xi \rho_{DM}(r) T_E(r)/m_{p_d}$ where $\xi = 1$ ($\xi = Z'+1$) for the Moon-like (Venus-like) case. The mass density profile $\rho_{DM}(r)$ of the captured DM can then be estimated from the hydrostatic equilibrium condition (with spherical symmetry assumed):

$$\frac{dp(r)}{dr} = -\rho_{DM}(r) g(r) \,, \tag{7.11}$$

where $g(r) \simeq G_N \int_0^r \rho_E 4\pi r'^2 dr'/r^2$ is the local gravitational acceleration within the Earth, almost entirely due to the ordinary matter component. Numerical work [470, 471] indicates that $\rho_{DM}(r)$ falls exponentially, with a scale length inversely proportional to the square root of m_{p_d}. This behaviour can be understood via simple analytical considerations. For radially constant T, ρ_E, and assuming $m_{p_d} \gg m_{e_d}$, the hydrostatic equilibrium condition has the analytic solution:

$$\rho_{DM}(r) = \rho_{DM}(0)\, e^{-r^2/R_h^2} \,, \tag{7.12}$$

where

$$\begin{aligned} R_h &= \left(\frac{3T_E\xi}{G_N \rho_E 2\pi m_{p_d}}\right)^{\frac{1}{2}} \\ \Rightarrow \frac{R_E}{R_h} &\simeq 1.2 \left(\frac{5000\ \mathrm{K}}{T_E}\right)^{\frac{1}{2}} \left(\frac{\rho_E}{10\ \mathrm{g/cm^3}}\right)^{\frac{1}{2}} \left(\frac{m_{p_d}/\xi}{\mathrm{GeV}}\right)^{\frac{1}{2}} \,. \end{aligned} \tag{7.13}$$

Evidently the DM density profile depends only on the mass and ionisation state of the DM particles. Here, R_h is the dark sphere scale length, which can be viewed as a rough estimate for R_{DM}. If $m_{p_d} \gtrsim$ few GeV, then R_h is expected to be within the Earth. In the alternative case which suggests $R_E/R_h < 1$, the thermal equilibrium assumption used in this calculation breaks down, and we would expect thermal escape and dark atmospheric stripping effects to act to

[3] This corresponds to a captured mass of $\sim 10^{15}(R_{DM}/R_E)^2$ kg if R_{DM} has remained roughly constant throughout Earth's history; note that this is much smaller than $M_E \sim 10^{24}$ kg.

keep $R_E/R_{DM} \gtrsim 1$, though it is difficult to say much more than this without detailed calculations.

For the Venus-like case, R_h can only provide a rough estimate for the location of the dark ionopause, as the ram pressure of the dark plasma wind and the pressure of the captured dark sphere can typically vary by many orders of magnitude. For the Moon-like case the stopping radius R_{DM} scales with R_h but also depends on the DM self-interaction cross section and hence on the other fundamental parameters. In fact, the R_{DM} value for dark electrons is not the same as that for dark protons as their self-interaction cross sections are different. For now, we shall ignore this subtlety and focus on the R_{DM} scale relevant for dark protons. Explicit calculations [471] that take into account the Earth's temperature and density profiles indicate that R_{DM} for dark protons is roughly:

$$\frac{R_E}{R_{DM}} \approx \left(\frac{10^{-2}}{\alpha_d}\right)^{0.06} \left(\frac{m_{p_d}/\xi}{5\text{ GeV}}\right)^{0.55} \left(\frac{1}{Z'}\right)^{0.14}, \tag{7.14}$$

which is approximately valid for $5 \times 10^{-4} \lesssim \alpha_d \lesssim 5 \times 10^{-2}$, 5 GeV $\lesssim m_{p_d}/\xi \lesssim$ 300 GeV, $1 \lesssim Z' \lesssim 40$. Again, if the plasma parameters suggested $R_E/R_{DM} < 1$, we expect that dark sphere interactions with the dark plasma wind will keep $R_E/R_{DM} \gtrsim 1$.

In the next Section we proceed to describe the interaction of the halo DM with the dark sphere. We model the halo DM using the MHD equations. Specifically we shall consider single fluid equations describing the system in terms of the total density, temperature, bulk velocity, and dark magnetic field. Such a description is only valid over distance scales larger than the Debye length: $\lambda_D = \sqrt{T/(4\pi\alpha_d n_{e_d})}$. For the dark plasma near the Earth, i.e. for $v_{rot} \approx 220$ km/s and $\rho_{DM} \approx 0.3\text{ GeV/cm}^3$,

$$\lambda_D \sim 0.2\,[Z'(Z'+1)]^{-1/2} \left(\frac{m_{p_d} + Z' m_{e_d}}{\text{GeV}}\right) \left(\frac{10^{-2}}{\alpha_d}\right)^{\frac{1}{2}} \text{ km.} \tag{7.15}$$

Requiring $\lambda_D/R_{DM} \ll 1$ imposes only a very mild restriction on parameter space.

7.2.2 Near-Earth environment

The interaction of the dark plasma wind with a macroscopic obstacle (length scale $\gg \lambda_D$) may be modelled via the magnetohydrodynamic (MHD) equations. It is a remarkable fact that the MHD equations can be derived as the moment equations of dark ion distribution functions obeying the kinetic Vlasov equations for a collisionless plasma; thus, even in the absence of hard collisions, collective effects of the long-range Coulomb force give rise to a fluid-like behaviour. For a perfectly conducting ideal fluid, the MHD equations take the form (in cgs units)

$$\begin{aligned}
\frac{\partial \rho}{\partial t} + \nabla \cdot (\rho \mathbf{v}) &= 0, \\
\frac{\partial (\rho \mathbf{v})}{\partial t} + \nabla \cdot \left[\rho \mathbf{v}\mathbf{v} + \mathbf{I}\left(p + \frac{B^2}{2}\right) - \mathbf{B}\mathbf{B} \right] &= 0, \\
\frac{\partial E}{\partial t} + \nabla \cdot \left[\left(E + p + \frac{B^2}{2}\right)\mathbf{v} - \mathbf{B}\left(\mathbf{v}\cdot\mathbf{B}\right) \right] &= 0, \\
\frac{\partial \mathbf{B}}{\partial t} + \nabla \cdot (\mathbf{v}\mathbf{B} - \mathbf{B}\mathbf{v}) &= 0, \qquad (7.16)
\end{aligned}$$

where ρ is the mass density, p is the thermal pressure, $\mathbf{v}$ is the bulk velocity, $\mathbf{B}$ is the (dark) magnetic field (a factor of $1/\sqrt{4\pi}$ has been absorbed), and $E = \rho v^2/2 + B^2/2 + p/(\gamma - 1)$ is the energy density, where we take an ideal gas equation of state with a ratio of specific heats $\gamma = 5/3$.

In practice the MHD equations are solved in a dimensionless form by setting $\tilde{\rho} = \rho/\rho_0$, $\tilde{L} = L/L_0$, $\tilde{\mathbf{v}} = \mathbf{v}/v_0$, $\tilde{p} = p/(\rho_0 v_0^2)$, $\tilde{t} = t/(L_0/v_0)$, $\tilde{\mathbf{B}} = \mathbf{B}/\sqrt{4\pi\rho_0 v_0^2}$. For the dark plasma wind it is convenient to take $\rho_0 = 0.3\,\mathrm{GeV/cm^3}$, $L_0 = R_{DM}$, and $v_0 = c_s$, where c_s is the sound speed in the plasma far from the Earth ($r \gg R_E$),

$$c_s = \sqrt{\frac{\gamma p}{\rho}} = \sqrt{\frac{\gamma T}{\bar{m}}} \sim \sqrt{\frac{\gamma}{2}} v_{rot}. \qquad (7.17)$$

Once these dark plasma units are set, the (quasi-)stable steady state solutions we are interested in will only depend on the wind mach number $M = v_\infty/c_s$ and the magnetic field strength $\tilde{B}_\infty$ far from the Earth. The quantity v_∞ is the plasma wind speed (as measured in the Earth frame) far from the Earth, which is a time-dependent quantity due to the Earth's orbital motion:

$$v_\infty = v_\odot + \Delta v_E \cos\omega(t - t_0) \qquad (7.18)$$

where $\omega = 2\pi/\mathrm{year}$, $v_\odot = v_{rot} + 12$ km/s (the 12 km/s correction is due to the Sun's peculiar velocity) and $\Delta v_E \simeq 15$ km/s results from the Earth's orbital motion. Evidently, v_∞ varies by $\pm\Delta v_E$ during the year with a maximum at $t = t_0 \simeq 153$ days (June 2^{nd}).

As suggested by the tilde in Equation (7.17), the local sound speed is not known precisely [cf. the temperature Equation (7.4)]. It is worth remarking here that the phenomenology is rather sensitive to the value of c_s that is realised. This is because c_s lies very close to the plasma wind speed v_∞, so that the Mach number straddles $M \sim 1$ throughout the year. Three distinct regimes can immediately be identified: the supersonic regime $c_s \lesssim v_\odot - \Delta v_E$; the subsonic regime $c_s \gtrsim v_\odot + \Delta v_E$, and; the intermediate regime $v_\odot - \Delta v_E \lesssim c_s \lesssim v_\odot + \Delta v_E$. In order to explore a representative range of possibilities in these models we choose to study Mach numbers $M \approx 0.74$–1.77 (i.e. $c_s = 140$–290 km/s for $v_{rot} = 220$ km/s).

As discussed in the previous Section, if the plasma DM has some interaction(s) with the standard matter then it will be captured within the Earth, forming an approximate "dark sphere" of dark protons and dark electrons which may or may not have recombined into dark atoms. For simulations we consider two limiting cases:

1. "Moon-like": the large majority of the captured dark plasma is in the form of dark atoms, and therefore cannot carry a significant dark current. In this case, to first approximation, the dark sphere acts as a perfect absorber of the dark plasma wind, much like the Moon in the solar wind.

2. "Venus-like": if a sufficient proportion of the captured dark plasma is ionised, then an ionospheric surface layer exists on the dark sphere. A current-carrying sheet then forms at the ionopause and, to first approximation, the dark sphere acts as a perfect spherical conductor which deflects all of the dark plasma wind, much like Venus in the solar wind.

We emphasise that these are first approximations of limiting cases. Satellite experiments have shown that MHD simulations employing these approximations give good descriptions of the Moon [473, 474] and Venus [475–478] solar wind systems, and we adapt them here as well-motivated paradigm cases in order to gain useful insight.[4]

We solve the MHD equations numerically within the PLUTO V4.2 simulation framework [479] utilising CHOMBO V3.2 [480] for adaptive mesh refinement.[5] The coordinate system is defined in the frame of the dark sphere, with the origin at the dark sphere centre and the $\mathbf{z}$ axis pointing in the wind direction. We consider the yz plane (assuming azimuthal symmetry) on a polar 2048×2048 equivalent grid with spatial extent $1 \leq \tilde{r} \leq 12$ and $0 \leq \theta \leq \pi$. Simulations were performed with inflowing dark plasma Mach numbers $M = 0.74$–1.77 (in steps of 0.01) and $B = 0$. These unmagnetised simulations are relevant when the thermal pressure dominates over the magnetic pressure, i.e. when the plasma beta $\beta = p/(B^2/2) \gg 1$. Far from the Earth, $\beta = 2c_s^2\rho_0/(\gamma B^2)$, implying the rough requirement $\tilde{B}_\infty \ll 1$. For $\alpha_d = \alpha$ this translates to $B_\infty \ll 5\ [c_s/(200\text{ km/s})]$ nT, to be compared with typical values within the galactic (intergalactic) medium of ~ 0.1–10 nT (~ 0.1 nT). Note that the existence of a significant magnetic field will

[4] In the Moon-like limiting case, the dark sphere consists predominately of neutral dark atoms, that is, a poorly conducting medium. Since the dark electron and dark proton stopping distances within the Earth are in general not equal due to their differing interaction cross sections in the Earth frame, significant dark charge separation within the Earth is possible and hence current flows. While dark electric fields are not expected to directly influence the halo DM distribution at the Earth's surface ($r = R_E$) where conductivity is expected to be high and effective Debye screening should occur, there remains the possibility that dark magnetic fields generated due to the current flows could have important implications for the distribution of halo DM at the Earth's surface. Unfortunately, such effects are very difficult to estimate, and no attempt to model them has been undertaken here.

[5] We make the relevant code and some example datasets publicly available at `http://github.com/jdclarke5/DarkSphere`; see the `readme.md` file therein for more information.

generally break the azimuthal symmetry of the system and potentially change the phenomenology appreciably. Some tests showed that our results are valid for the field-aligned case with $\tilde{\mathbf{B}}_\infty \lesssim 0.6\,\mathbf{z}$, after which we saw a sharp change in the system's behaviour. Study of the magnetised case is left for potential future work.

All simulations are initialised with a flat density and are allowed to evolve to a steady state. The dark plasma wind inflows at the $\tilde{r} = 12$ boundary when $\theta > \pi/2$, and outflows when $\theta < \pi/2$. In the Moon-like case we take the $\tilde{r} = 1$ surface boundary condition as absorbing ($v_r \leq 0$) for the windward side and reflective ($v_r = 0$) for the leeward side. This boundary condition was adopted for Moon simulations in previous works [474, 481]. For the Venus-like case the $\tilde{r} = 1$ surface boundary condition is fully reflective ($v_r = 0$). Our simulations were validated against the Moon and Venus simulations of Refs. [474, 477, 481] for solar wind parameters ($k_p \approx 10$ cm$^{-3}, M \approx 7, \tilde{B} \approx 1$).

The solutions for a collection of Mach numbers are shown in Figures 7.2 and 7.3. We show the distributions for the density ρ, temperature $T = \bar{m}p/\rho$, and absolute velocity $|v|$, normalised to their values far from the Earth. The solutions are characterised by the existence of various shocks (i.e. abrupt discontinuities), where the local bulk velocity exceeds the local sound speed. There are three dominant features: the downwind wake region of underdense hot plasma; the tail shock, which detaches from the sphere just below $\theta = \pi/2$ and recedes with increasing Mach number, and; the upwind bow shock, which is only present in the Venus-like case (there is very little upwind activity in the Moon-like case), defining the edge of an induced magnetosphere [449, 450].

These distributions illustrate the non-trivial (and time-dependent) dark plasma environment which surrounds the captured dark sphere and encompasses the Earth. It is clear that there are implications for direct detection experiments, and we will discuss these presently.

7.3 Plasma dark matter direct detection

7.3.1 General considerations

Plasma DM can potentially be probed by both nuclear and electron recoils. Kinematic considerations suggest that dark electrons scattering off electrons (dark protons scattering off nuclei) would be of relevance if $m_{e_d} \sim m_e$ ($m_{p_d} \sim$ 10–100 GeV). As already emphasised, plasma DM has the distinctive feature that the dark electrons and the dark protons have comparable kinetic energies given by Equation (7.4). Consequently, if the dark proton is sufficiently heavy ($\gtrsim$ GeV), electron recoils in the keV range are possible, making DM scattering off electrons (in addition to nuclear recoils) an important means of probing this type of DM.

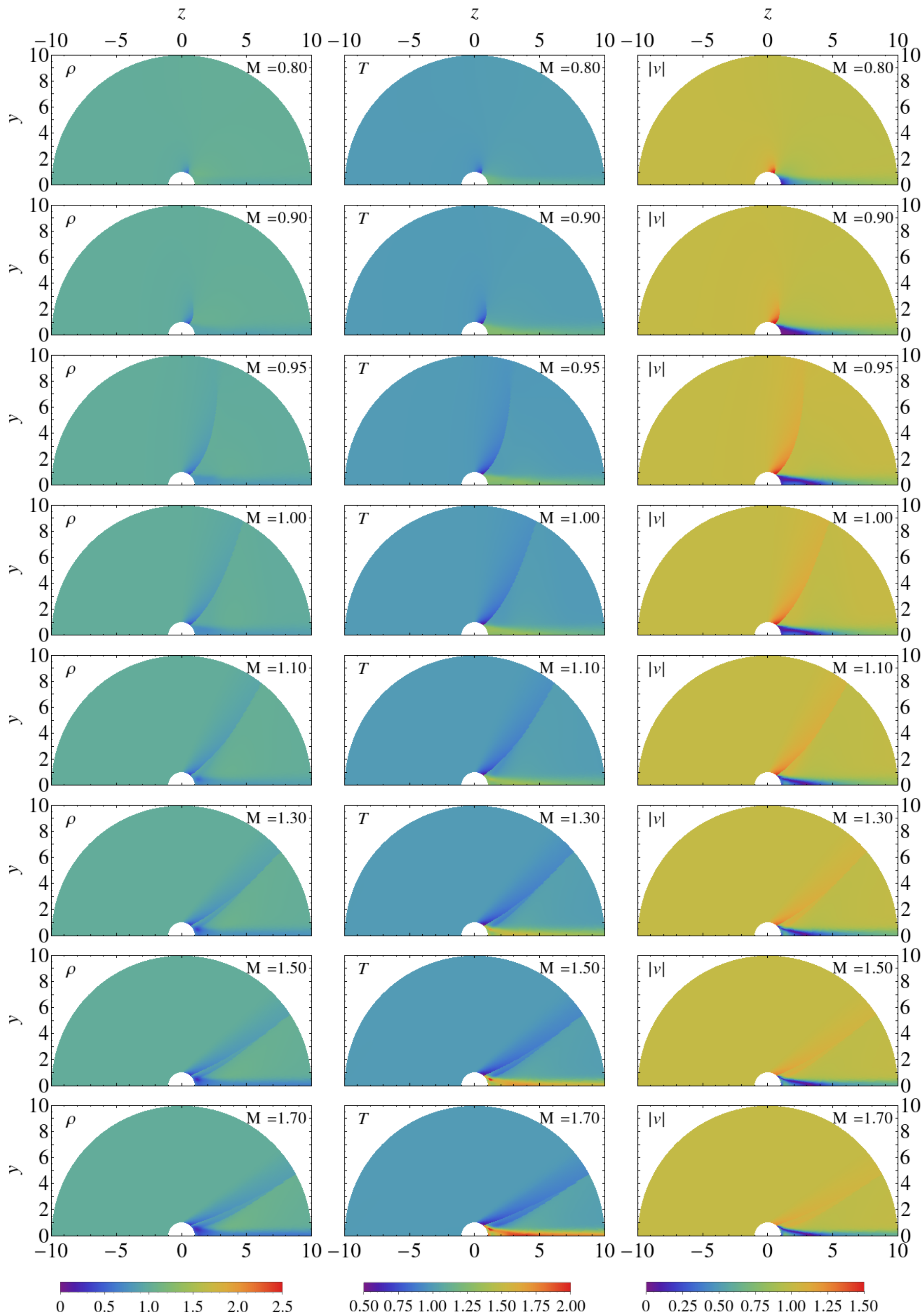

FIGURE 7.2: Moon-like ($B = 0$): normalised density, temperature, and absolute velocity solutions for various Mach numbers.

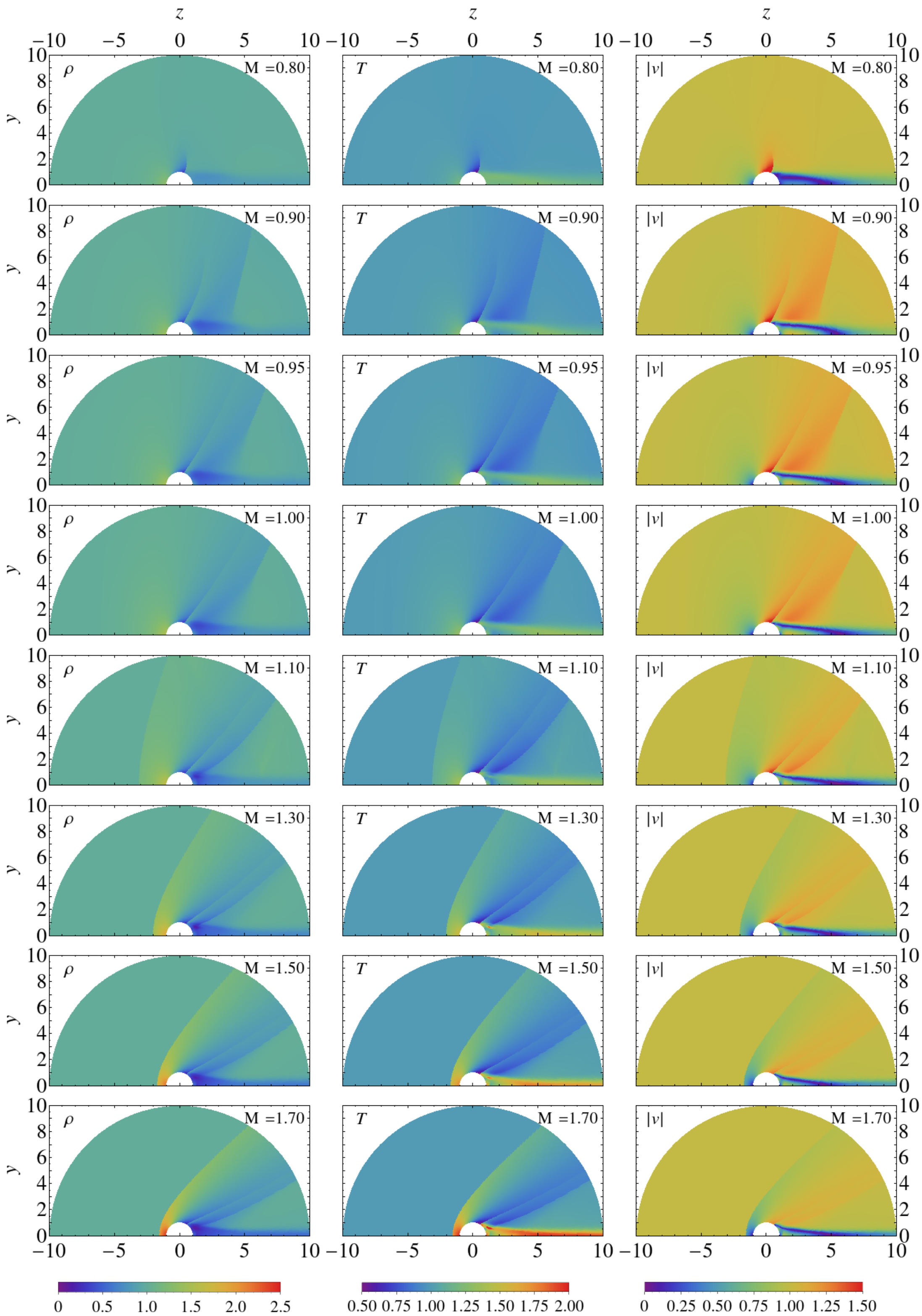

FIGURE 7.3: Venus-like ($B = 0$): normalised density, temperature, and absolute velocity solutions for various Mach numbers.

The rate of DM interactions in a direct detection experiment depends on both the properties (density and velocity distribution) of the DM particles and the interaction cross section. Let us define the dark electron and dark proton velocity probability density functions as $f_{e_d}(\mathbf{v})$ and $f_{p_d}(\mathbf{v})$ in the Earth frame. It is generally expected that these functions are both space and time dependent. The time dependence arises from the velocity of the Earth with respect to the DM halo, $\mathbf{v}_E(t)$, given by Equation (7.18). To make this dependence explicit we rewrite $f_{e_d}(\mathbf{v}) \to f_{e_d}(\mathbf{v};\mathbf{x},\mathbf{v}_E(t))$ and $f_{p_d}(\mathbf{v}) \to f_{p_d}(\mathbf{v};\mathbf{x},\mathbf{v}_E(t))$. The local number densities are also generally space and time dependent: $k_{e_d} \to n_{e_d}(\mathbf{x},\mathbf{v}_E(t))$, $k_{p_d} \to n_{p_d}(\mathbf{x},\mathbf{v}_E(t))$. The *local* differential interaction rate (i.e. at some point, $\mathbf{x}$, in space near the Earth) for dark electron scattering off electrons is then:

$$\frac{dR_e}{dE_R}(\mathbf{x},t) = N_e n_{e_d}(\mathbf{x},\mathbf{v}_E(t)) \int_{|\mathbf{v}|>v_{min}}^{\infty} \frac{d\sigma}{dE_R} f_{e_d}(\mathbf{v};\mathbf{x},\mathbf{v}_E(t))\,|\mathbf{v}|\,d^3v\,, \tag{7.19}$$

where E_R is the recoil energy of the target particle (electron). Also, N_e is the number of target electrons in the detector, $d\sigma/dE_R$ the relevant cross section, and the lower velocity limit $v_{min}(E_R)$ is given by the kinematic relation

$$v_{min} = \frac{\sqrt{m_e E_R/2}}{\mu} \tag{7.20}$$

with $\mu = m_e m_{e_d}/(m_e + m_{e_d})$ the reduced mass (the target electrons are approximated as being at rest). The rate of dark proton - nuclei scattering has a similar form.

What the detector will actually measure is the rate Equation (7.19) time-averaged over its position $\mathbf{x}(t)$ in space. In the well studied WIMP annual modulation scenario [482, 483], there is no spatial dependence. The mass (and number) density is neither space nor time dependent, and is estimated to be $\rho_0 \approx 0.3$ GeV/cm^3 near the Earth. All of the modulation arises from $\mathbf{v}_E(t)$, understood simply as the time variation of a Galilean boost through a Maxwellian velocity distribution. The plasma DM scenario is distinctly different. Far from the Earth, and for a fully ionised plasma, the velocity distributions are (ideally) expected to be described by boosted Maxwellians in the Earth frame with number densities:

$$n_{e_d} = \frac{Z'\rho_0}{Z' m_{e_d} + m_{p_d}}, \quad n_{p_d} = \frac{n_{e_d}}{Z'}\,. \tag{7.21}$$

However, this will not be the case in the vicinity of the Earth, where the detector is located. As is evident from Figures 7.2 and 7.3, both the number density and the velocity distributions are expected to display strong and non-trivial space and time dependence. It is therefore necessary to time-average the rate over the detector path $\mathbf{x}(t)$, and this will introduce an important new source of modulation. We will now describe this detector path.

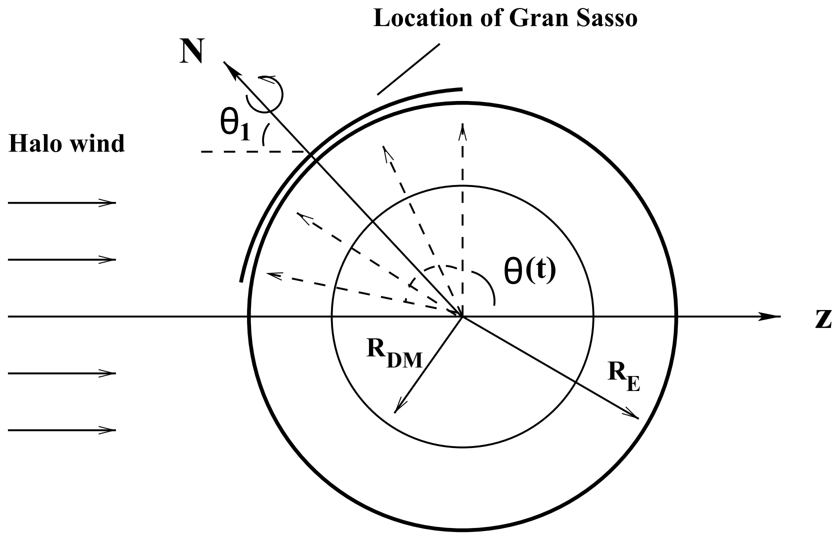

FIGURE 7.4: The relevant geometry (r, θ projection) of the dark halo wind interaction with the dark sphere (of radius R_{DM}) within the Earth. The variation of the location of an example detector (Gran Sasso) due to the Earth's daily rotation is indicated.

Consider the spherical coordinate system with its origin at the Earth's center and with $\mathbf{z}$ axis pointing in the direction of the halo wind as shown in Figure 7.4. Assuming azimuthal symmetry around the $\mathbf{z}$ axis, the position of the detector is given in polar coordinates by $\mathbf{x}(t) = (R_E, \theta(t))$, where $\theta(t)$ is the angle between the direction of the halo wind and the zenith at the detector's location. The time variation of the angle $\theta(t)$ is due to the Earth's daily rotation and motion around the sun. This angle has been evaluated previously [470] and is given by

$$\cos\theta(t) = -\sin\theta_1(t)\cos\theta_{lat}\cos\left(\frac{2\pi t}{T_{day}}\right) - \cos\theta_1(t)\sin\theta_{lat}\ , \tag{7.22}$$

where $T_{day} = 1$ *sidereal* day, and the phase is such that $\theta(t)$ is maximised at $t = 0$. Here, θ_{lat} is the latitude of the detector's location, which anticipates the important feature that *the measured rate and modulation will depend on the latitude of the detector*. The parameter $\theta_1(t)$ is the angle subtended by the direction of the Earth's motion through the halo with respect to the Earth's spin axis, which varies during the year due to the Earth's motion around the sun:

$$\begin{aligned}\cos\theta_1(t) \simeq \cos\bar{\theta}_1 + y\Bigg[&\cos\bar{\theta}_1\cos\gamma\sin\left(\frac{2\pi(t-T_1)}{\text{year}}\right)\\ &+ \sin\theta_{tilt}\sin\left(\frac{2\pi(t-T_2)}{\text{year}}\right)\Bigg],\end{aligned} \tag{7.23}$$

where $\theta_{tilt} = 23.5°$ is the angle between of the Earth's spin axis and the normal of the ecliptic plane, $\gamma = 60°$ is the angle between the normal of the ecliptic plane and the direction of the halo wind, $T_1 = t_0 + 0.25$ years $\simeq 244$ days, $T_2 \simeq 172$

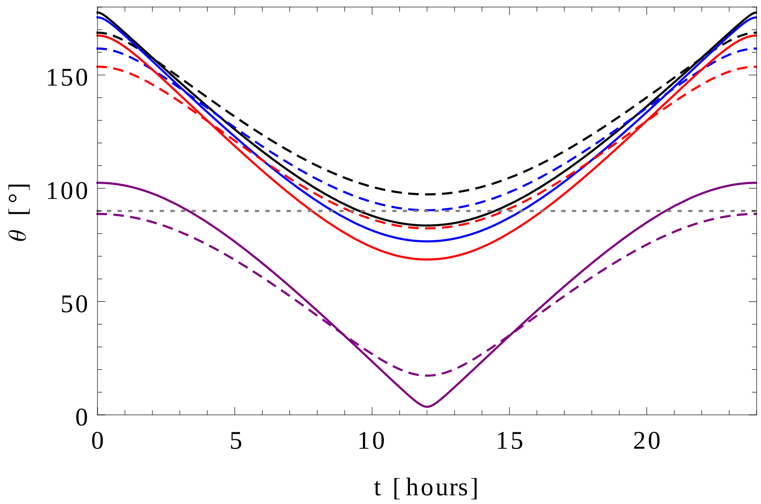

FIGURE 7.5: The time variation in sidereal hours of $\theta(t)$, the angle between the direction of the halo wind and the zenith at the detector's location. The time variation of the angle $\theta(t)$ is due to the Earth's daily rotation and motion around the sun [Equations (7.22) and (7.23)]. Shown are results for four detector locations, for April 25 (solid-curves), October 25 (dashed-curves). The four detector locations are, from top to bottom: Gran Sasso (black curves), Kamioka (blue curves), Jin-Ping (red curves), and Stawell (purple curves). The $90°$ line is also shown, which is the demarcation between the upwind and downwind regions.

days (northern summer solstice), and $y = v_\oplus/v_\odot \approx 30/232 \approx 0.13$. Evidently the angle $\theta_1(t)$ varies during the year with an average value of $\bar{\theta}_1 \simeq 43°$, a maximum of around $49°$ on April 25^{th} (115 days), and a minimum of around $36°$ six months later (297 days).

In Figure 7.5 we show the time variation of θ for four detector locations of interest: Gran Sasso [139, 142] or Sanford [141], Kamioka [140], China Jin-Ping [484], and Stawell [485], which correspond to $\theta_{lat} \approx 43°, 36°, 28°, -37°$, respectively. Also shown in Figure 7.5 is the $\theta = 90°$ line which is the demarcation between the upwind and downwind regions. In this region, the ρ, T, $|v|$ quantities can vary significantly due to the tail shock feature, evident in Figures 7.2 and 7.3. Interestingly the Gran Sasso laboratory spends most of its time in the near upwind region, while the Kamioka and Jin-Ping laboratories loiter in the near downwind region. Thus, even the relatively small latitude difference between these laboratories might be important, leading (potentially) to different DM interaction rates for detectors at these locations. Note that the Southern Hemisphere detector traverses a very different path compared to the Northern Hemisphere detectors, and can potentially probe the downwind wake region for part of the day.

Let us summarise the origin of modulation signals in plasma DM models:

1. Annual modulation with phase around June 2^{nd} (153 days) due to the variation of the Earth's speed relative to the DM halo. This variation not only

acts to provide a Galilean boost with respect to the halo, as in the well studied WIMP scenario, but also to change the non-trival density and velocity distributions in the vicinity of the Earth. In the previous Section we used MHD simulations to describe some features of these distributions for two idealised scenarios, as shown in Figures 7.2 and 7.3.[6]

2. Annual modulation with phase around April 25^{th} (115 days) due to the variation of the Earth's spin axis relative to the wind direction. This effect changes the detector's daily path through the DM distribution according to Equation (7.22), and can be the dominant source of annual modulation.

3. Sidereal daily modulation due to the rotation of the Earth with respect to the direction of the plasma wind and the subsequent time-dependent position of the detector throughout the day, again according to Equation (7.22). This is an extremely distinctive feature which can be probed with direct detection experiments. It is difficult to conceive any background which modulates with sidereal day.

The latter two effects are, of course, generic predictions of any spatially dependent near-Earth DM density/velocity distribution. Including, for example, models with DM subcomponents with sufficient interactions with the ordinary matter within the Earth to be stopped (or at least impeded) [486–488]. In the plasma DM case the spatial dependence arises from the complex interaction between the dark plasma wind with the captured dark sphere within the Earth. In the next Section we will explore these modulation effects in an example model.

7.3.2 Example: electron recoils in mirror dark matter

So far we have only outlined the origin of direct detection modulation signals in plasma DM models. In this Section we will explore more explicitly, based on our MHD simulation results of Section 7.2, the range of possible annual and diurnal modulations. The aim is to gain insight into where and how direct detection experiments should be searching for plasma DM. To facilitate this we will consider an explicit example: the MDM model.

The mirror model has fundamental plasma DM parameters $m_{e_d} = m_e \simeq 0.511$ MeV, $m_{p_d} = m_{He} \simeq 3.76$ GeV, $Z' = 2$, and $\alpha_d = \alpha \simeq 1/137$. Then, in the Milky Way, $T \sim 0.35$ keV and $I/T \sim 0.16$, so that the DM exists primarily in a plasma state. DM–SM interactions are due to the photon - dark photon kinetic mixing term Equation (7.2), which induces Coulomb scattering of dark electrons (dark protons) against electrons (nuclei). At 3.76 GeV, the dark proton is just light enough so that nuclear recoil rates are strongly kinematically suppressed

[6]There are additional contributions to the annual modulation with phase June 2^{nd}, which we haven't considered, and may be important. Among these are the variation of the physical properties of the dark sphere: variation of the effective R_{DM}, the surface ionisation fraction, "dark atmosphere" interactions, etcetera.

in current experiments.[7] Of most interest, therefore, is dark electron - electron scattering.

Coulomb scattering of dark electrons off electrons ($e_d e \to e_d e$) is a spin-independent process with cross section:

$$\frac{d\sigma}{dE_R} = \frac{\lambda}{E_R^2 v^2}, \tag{7.24}$$

where

$$\lambda \equiv \frac{2\pi\epsilon^2\alpha^2}{m_e}, \tag{7.25}$$

and E_R is the recoil energy of the scattered electron, approximated as being free and at rest relative to the incoming dark electron of speed v. Naturally this approximation can only be valid for the loosely bound atomic electrons, i.e. those with binding energy much less than E_R.

To proceed, we need to determine the local scattering rate as a function of position in the vicinity of the Earth. To do this we have to evaluate Equation (7.19), i.e. we have to integrate over the local velocity distribution. Unfortunately our MHD simulations only tell us the local moments of this distribution. Thus, without making a further assumption, we are stuck. In order to continue, *we will assume that the velocity distribution is everywhere locally given by a (boosted) Maxwellian*, i.e.

$$f_{e_d}(\mathbf{v}) = \left(\frac{1}{\pi v_0^2}\right)^{\frac{3}{2}} \exp\left(\frac{-(\mathbf{v}-\mathbf{v}_B)^2}{v_0^2}\right), \tag{7.26}$$

where $v_0 = (2T/m_{e_d})^{\frac{1}{2}} \approx 11200\ (T/0.35\,\text{keV})^{\frac{1}{2}}$ km/s, $\mathbf{v}_B$ is the bulk velocity in the Earth (i.e. detector) frame, and the space and time dependence is implied. We do not expect this to be a good assumption in general. Nevertheless, it will reproduce naive expectations that the scattering rate scales positively with temperature and bulk velocity. Due in a large part to this assumption we warn that our results should be interpreted only as qualitative. With this caveat acknowledged, the local differential rate Equation (7.19) can be evaluated for the (boosted) Maxwellian dark electron velocity distribution:

$$\frac{dR_e}{dE_R} = \frac{N_T g_T n_{e_d}\lambda}{2E_R^2|\mathbf{v}_B|}\left[\text{erf}\left(\frac{v_{min}+|\mathbf{v}_B|}{v_0}\right) - \text{erf}\left(\frac{v_{min}-|\mathbf{v}_B|}{v_0}\right)\right]. \tag{7.27}$$

Here N_T is the number of target particles (e.g. NaI pairs for DAMA, and Xe

[7] The MDM model can have heavier, mirror metal halo (sub)components, of known masses but uncertain abundances. Several works (e.g. Refs. [489, 490]) have explored the possibility that these components might lead to observable nuclear recoils in existing experiments. However, these studies used a very simplified picture for the halo distribution function, i.e. without considering the modifications due to the interaction of the plasma wind with the dark sphere within the Earth as discussed here.

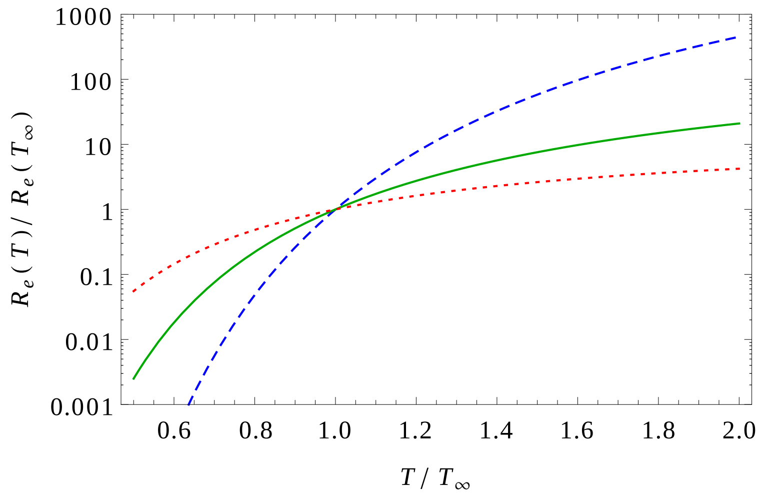

FIGURE 7.6: Rate dependence on temperature for $T_\infty = 0.17, 0.35, 0.73$ keV (or $c_s = 140, 200, 290$ km/s) as blue dashed, green solid, red dotted, respectively. A low energy threshold of $E_t = 2$ keV is assumed.

for the xenon experiments), g_T is the effective number of "free" electrons (binding energy $\lesssim$ 1 keV) per target particle ($g_{\rm NaI} \approx 54$, $g_{\rm Xe} \approx 44$), and $v_{min} \approx 26500\ (E_R/2\ {\rm keV})^{\frac{1}{2}}$ km/s [from Equation (7.20)].[8]

For electron recoils in the MDM model, $|\mathbf{v}_B| \ll v_0$, and in the limit $|\mathbf{v}_B|/v_0 \to 0$ Equation (7.27) can be integrated from a threshold energy, E_t, to give:

$$R_e = N_T g_T n_{e_d} \lambda \left(\frac{2m_{e_d}}{\pi T}\right)^{\frac{1}{2}} \left(\frac{e^{-\frac{E_t}{T}}}{E_t} - \frac{\Gamma\left[0, \frac{E_t}{T}\right]}{T}\right), \tag{7.28}$$

where $\Gamma[0, z]$ is the upper incomplete Gamma function. Corrections due to non-zero $\mathbf{v}_B$ are $\mathcal{O}(|\mathbf{v}_B|^2/v_0^2)$ and remain below one per cent for all cases considered. We note here that this rate is dominated by low energy recoils, and is therefore very sensitive to the lower limit of integration, E_t. For $E_t = 2$ keV (DAMA value), it is also a rather sensitive function of T, since $E_R > 2$ keV requires $v_{e_d} > 26500$ km/s, in the tail of the dark electron velocity distribution. In Figure 7.6 we illustrate this sensitivity for the range of T_∞ we consider. These sensitivities are further reasons to interpret our results only qualitatively.

The local differential rate, Equation (7.27), is a function of the local T, ρ, and $|\mathbf{v}_B|$ (the rate depends on ρ via its dependence on k_{e_d}). In particular these space

[8]The differential event rate evaluates (for a NaI detector) to:

$$\frac{dR}{dE_R} \approx 0.6 \left(\frac{n_{e_d}}{0.16\ {\rm cm}^{-3}}\right)\left(\frac{\epsilon}{10^{-9}}\right)^2 \left(\frac{2\ {\rm keV}}{E_R}\right)^2 \left(\frac{0.35\ {\rm keV}}{T}\right)^{\frac{1}{2}}$$
$$\times \exp\left[-\frac{2}{0.35}\left(\frac{E_R/2{\rm keV}}{T/0.35{\rm keV}} - 1\right)\right]\ {\rm cpd/kg/keV}.$$

This can be compared with the rough limit from DAMA that the differential rate should be less than about 0.25 cpd/kg/keV at $E_R \simeq 2$ keV [491]. Evidently ϵ in the range $10^{-9} - 10^{-10}$ is being probed in direct detection experiments via electron recoils in the mirror model, which coincides with the range of interest for small scale structure [432, 444, 453].

and time dependent quantities were obtained in Section 7.2, as shown in Figures 7.2 and 7.3. Fixing $v_{rot} = 220$ km/s to give the time-dependent dark plasma wind velocity in the Earth frame [Equation (7.18)], the space and time dependence of the differential rate throughout the year will depend only on the plasma sound speed c_s, or equivalently $T_\infty \ = \ 0.35\ [c_s/(200\,\mathrm{km/s})]^2$ keV. Then for a given detector latitude θ_{lat} and dark sphere size R_{DM} it is possible to determine the quantities of interest: the rate as a function of time of year averaged over the day (the annual modulation), and; the rate as a function of time of sidereal day averaged over the year (the diurnal modulation). This average includes the variation throughout the year of dark plasma wind Mach number and position of the detector according to Equations (7.18) and (7.22), respectively.

For the numerical work, we set $E_t = 2$ keV (current DAMA threshold) and considered an idealised detector with 100% detection efficiency and perfect resolution. We give our results in Figures 7.7–7.10 under each of the scenarios previously considered, i.e. Moon-like/Venus-like dark sphere with unmagnetised plasma wind. We consider sound speeds $c_s = 140$–290 km/s, encompassing the supersonic to subsonic dark plasma wind regimes, and $\theta_{lat} = 43°, 36°, 28°, -37°$, which correspond to detectors at Gran Sasso [139, 142] or Sanford [141], Kamioka [140], China Jin-Ping [484], and Stawell [485], respectively. We leave the size of the Earth with respect to the dark sphere, R_E/R_{DM}, as a free parameter which is assumed to remain constant throughout the averaging procedure. Strictly, the particle physics should dictate the nature and size of the dark sphere. Indeed, for MDM, the procedure described in Section 7.2 suggests a Moon-like scenario with $R_E/R_{DM} \approx 1$–1.5 . Still, it is possible that effects such as surface ionisation and dark atmospheric stripping significantly change this picture. Thus it is sensible to consider each scenario and a range of dark sphere radii, and this agnosticism anyway coincides with our aim to explore the range of modulation possibilities in plasma DM models in general.

In the next Section we will make some qualitative observations from these results and deduce the implications for direct detection experiments.

7.3.3 Implications for direct detection

In the previous Section we presented results for the annual and diurnal modulation of electron recoils in the mirror dark mater model. Here we gather some comments on these results and discuss the current experimental situation.

The behaviour exhibited in Figures 7.7–7.10 is clearly quite diverse, and we make the following observations:

1. The annual modulation fraction can be large, even $> 90\%$.

2. There are situations where the modulation is approximately sinusoidal, but this is not the general case. Interplay with various shocks may produce sharp transitions in the rate.

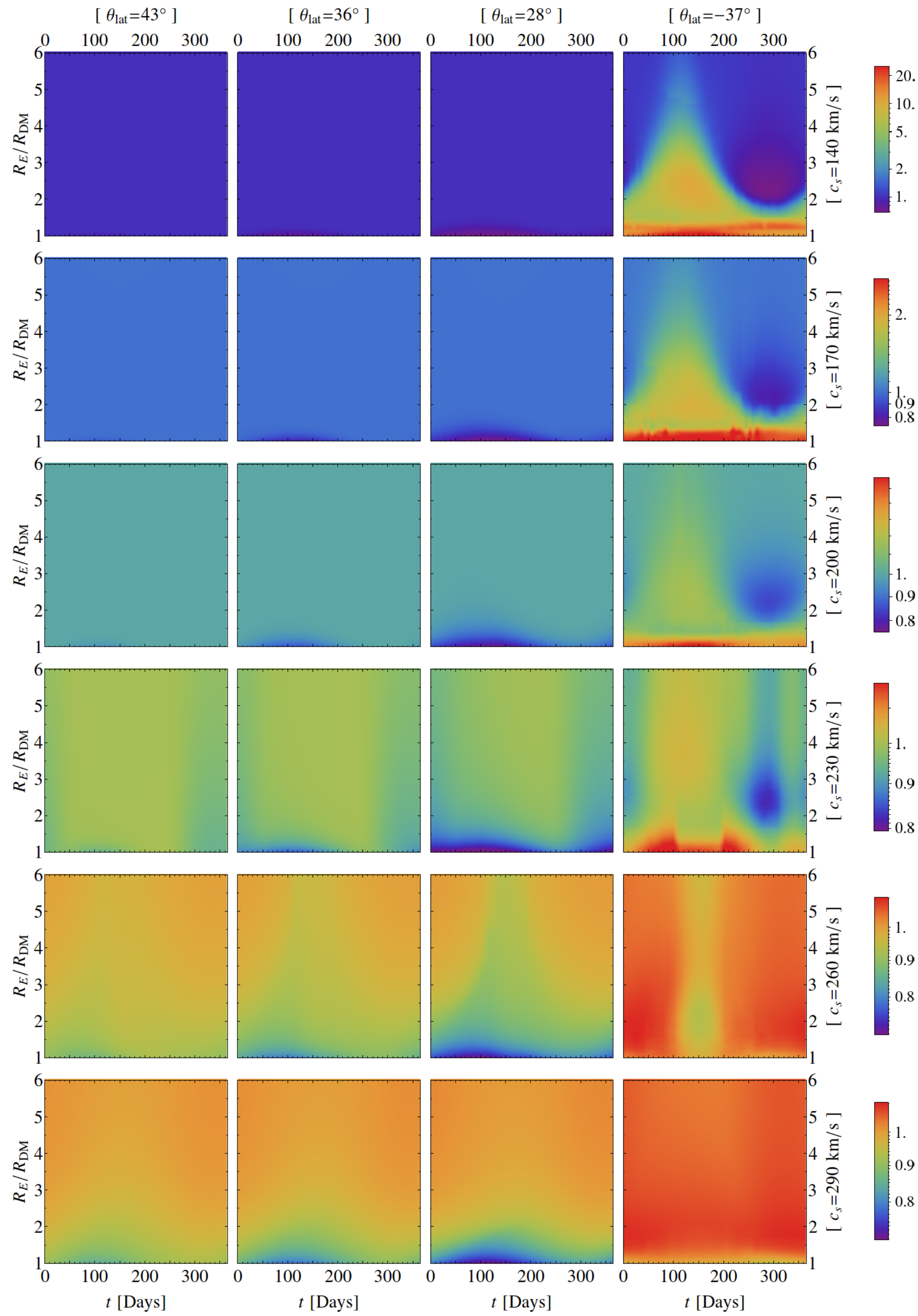

FIGURE 7.7: Moon-like ($B = 0$) annual modulation: R_e/R_e^∞ as a function of time of year plotted for example detector locations [Gran Sasso, Kamioka, Jin-Ping, and Stawell] (columns) and sound speeds (rows).

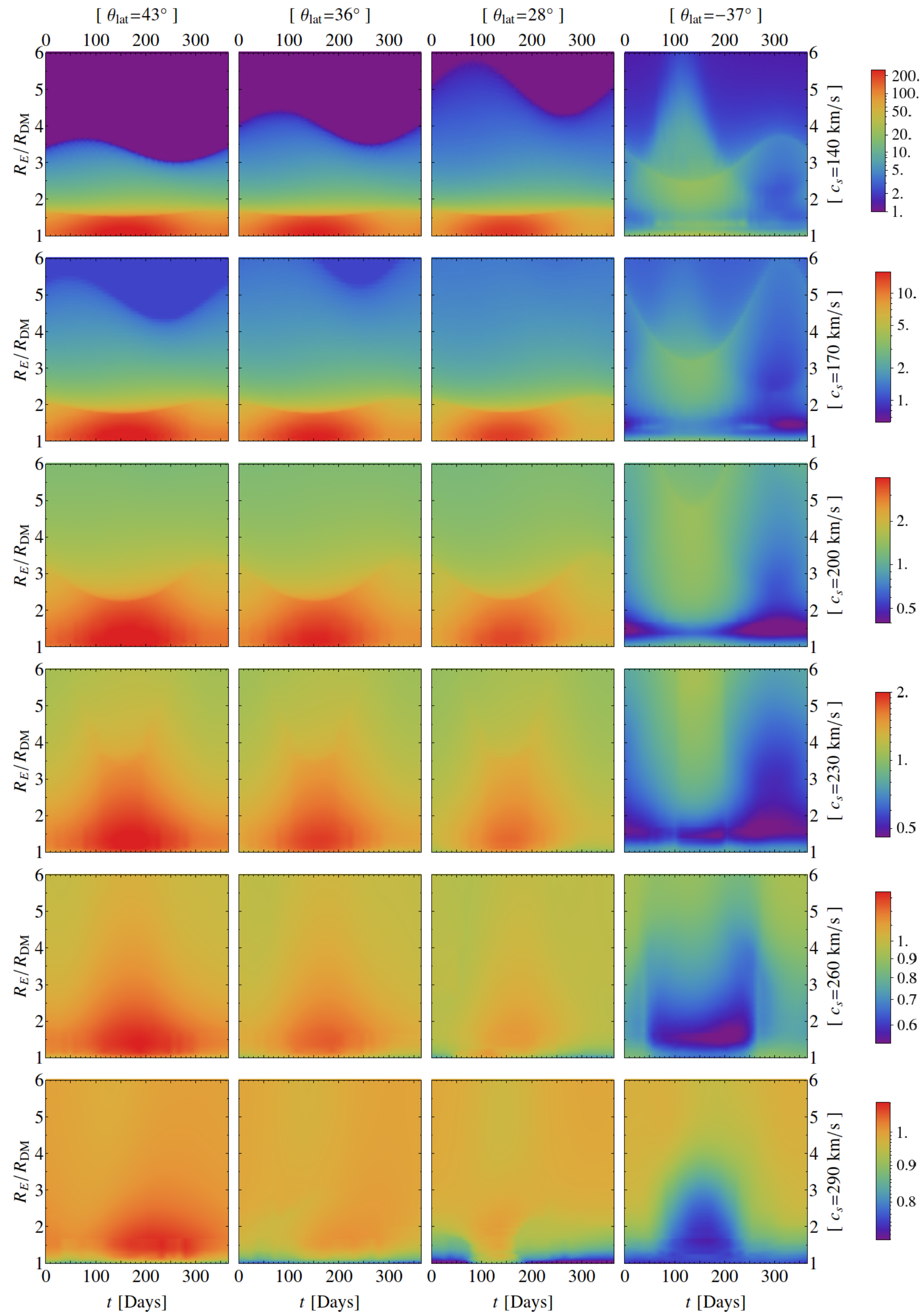

FIGURE 7.8: Venus-like ($B = 0$) annual modulation: R_e/R_e^∞ as a function of time of year plotted for example detector locations [Gran Sasso, Kamioka, Jin-Ping, and Stawell] (columns) and sound speeds (rows).

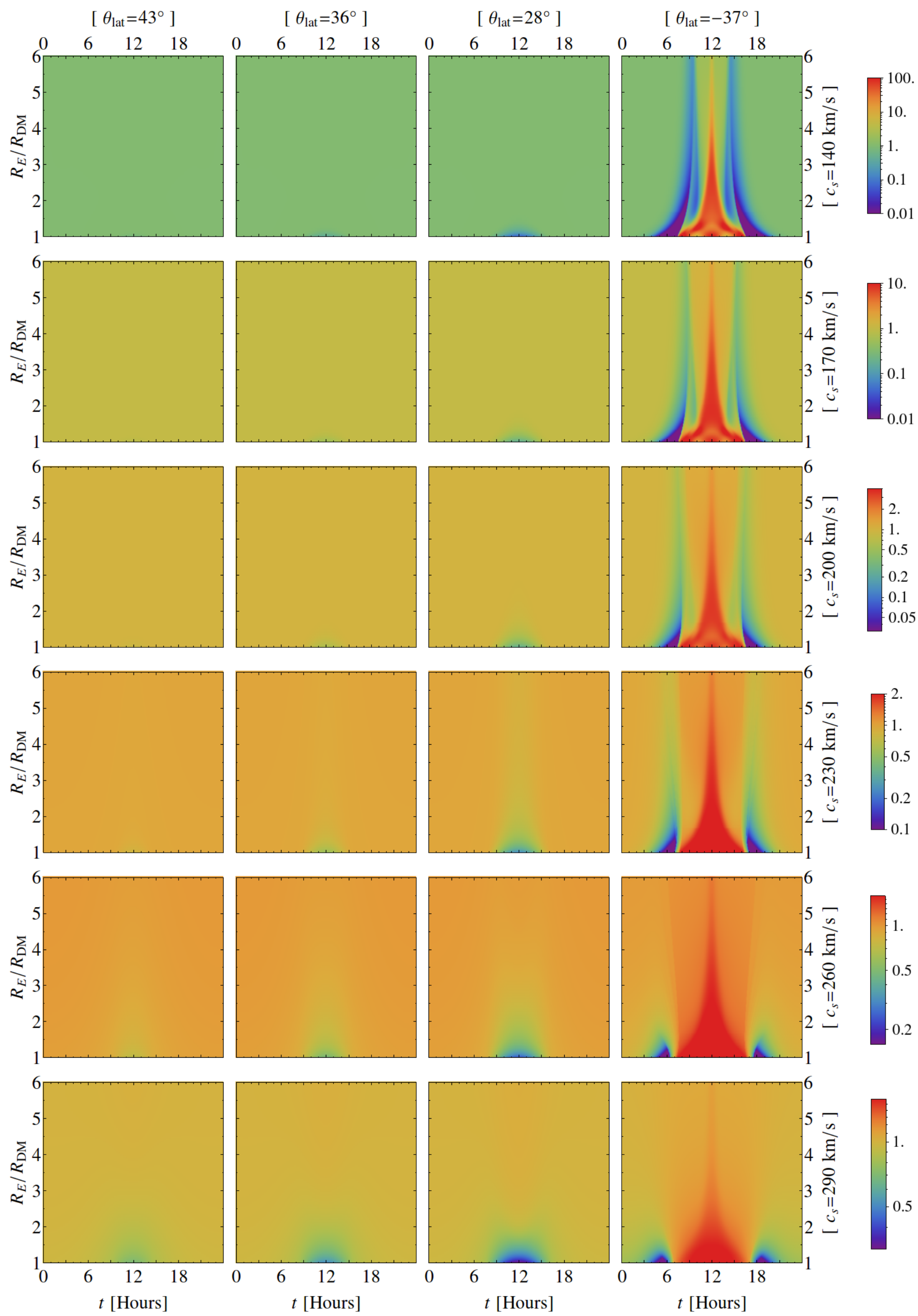

FIGURE 7.9: Moon-like ($B = 0$) diurnal modulation: R_e/R_e^{∞} as a function of sidereal hours plotted for example detector locations [Gran Sasso, Kamioka, Jin-Ping, and Stawell] (columns) and sound speeds (rows).

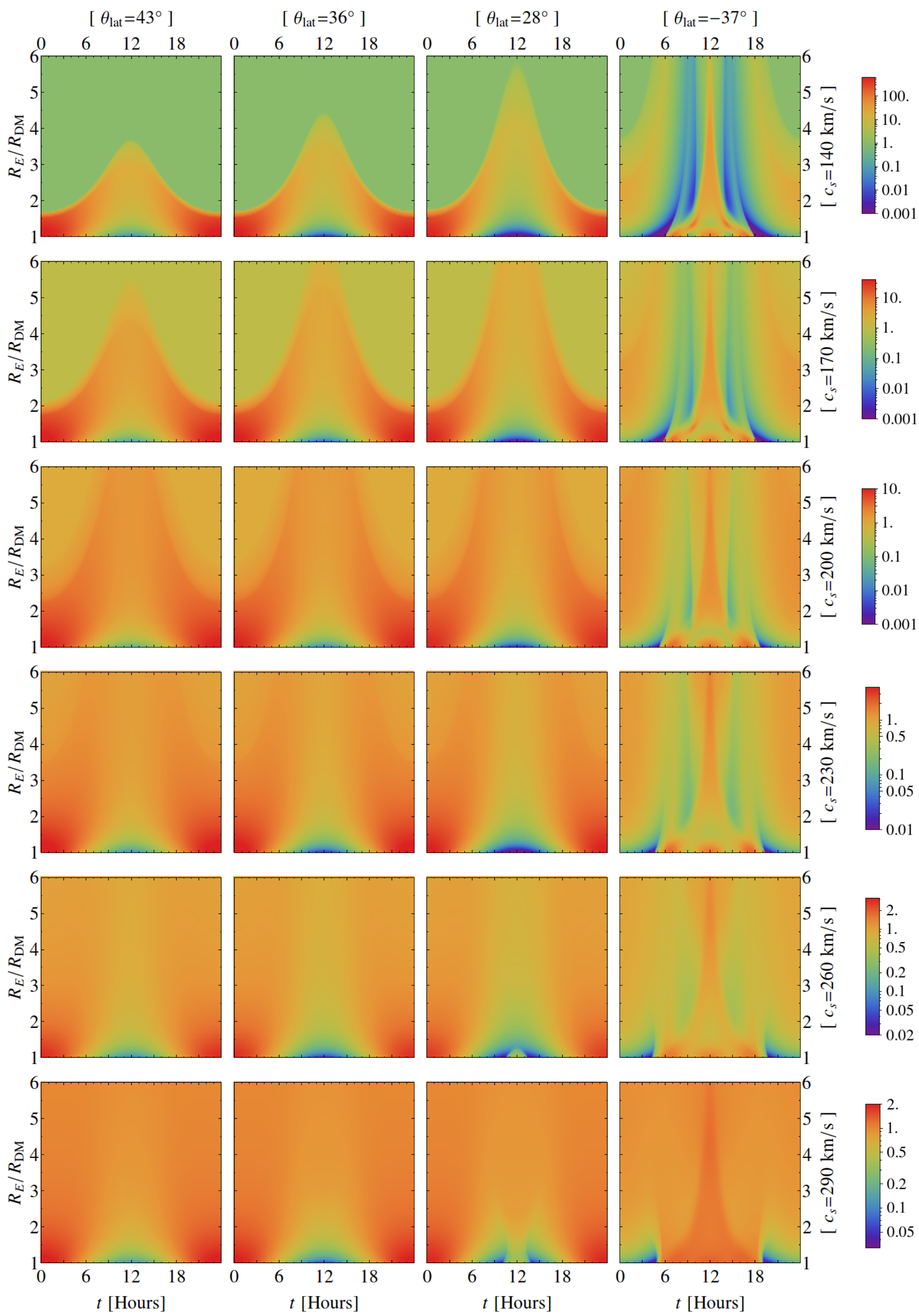

FIGURE 7.10: Venus-like ($B = 0$) diurnal modulation: R_e/R_e^∞ as a function of sidereal hours plotted for example detector locations [Gran Sasso, Kamioka, Jin-Ping, and Stawell] (columns) and sound speeds (rows).

3. The two annual modulation contributions, with phases of 153 days and 115 days, can be seen by eye, e.g. Moon-like $c_s \geq 260$ km/s (Figure 7.7) or Venus-like $c_s \leq 170$ km/s (Figure 7.8). The contributions can be different sign and either might dominate.

4. The dependence on θ_{lat} is obvious. In particular, the Stawell detector gives very different results since it probes the downwind wake region. Still, even between Northern Hemisphere detectors, significant changes in the modulation can be observed. For example, in the Moon-like case with c_s in the intermediate region ($c_s \approx 230$ km/s) with $R_E/R_{DM} \lesssim 2$ we observe a change in the effective sign between Northern Hemisphere detectors. This is due to the interplay of the wind speed pushing the tail shock back around 155 days, and the detector moving further into the shock at 115 days.

5. It is possible to see modulation effects in a detector at one latitude which would escape detection in an identical detector at a different latitude.

6. The diurnal modulation fraction can be large, typically of order the annual modulation, or larger. It is in general not sinusoidal and can display sharp transitions.

7. The azimuthal symmetry (in the unmagnetised case) implies that diurnal modulation is symmetric about $t = 12$ hours (with our phase convention). This motivates combining data from $0 \leq t/\text{hours} \leq 12$ with data from $24 \geq t/\text{hours} \geq 12$. As well, the average rate during the middle half of the day (6–18 hours) often differs markedly from the average rate during than the other half. This motivates a far/near ratio measurement,

$$R_{\text{far/near}} = \frac{R(6 \leq t/\text{hours} \leq 18)}{R(0 \leq t/\text{hours} \leq 6 \ \cup \ 18 \leq t/\text{hours} \leq 24)} \ , \tag{7.29}$$

looking for deviations from unity.

Nuclear recoils arising from dark proton scattering are, in principle, also very interesting. Although we haven't given any results for nuclear recoils, qualitatively they are expected to follow a similar pattern to the electron recoil results of Figures 7.7–7.10. Indeed, the nuclear recoil rate has a similar form to Equation (7.27), and in particular, the rate depends on the same variables $\rho,\ T,\ |\mathbf{v}_B|$ (in the single fluid approximation). The principle difference is the nuclear recoil kinematics, which depend on the mass of the dark proton. In general we expect nuclear recoils to show similar sensitivity to variation in ρ, comparable or smaller sensitivity to variation in T (depending on the mass of the dark proton), and more sensitivity to variation in $|\mathbf{v}_B|$ (since $|\mathbf{v}_B|/v_0$ is larger by a factor $\sqrt{m_{p_d}/m_{e_d}}$).

Let us here add somewhat of a disclaimer. We have sketched what we believe to be a sound general picture of modulation effects in plasma DM models. However, there is great difficulty involved in modelling the interaction of the dark plasma wind with the captured dark sphere. We have made a first attempt at a consistent description using MHD simulations. Obviously there are shortcomings. Notably, we have only studied two idealised dark sphere scenarios in the special unmagnetised case, and we have also made the questionable assumption of locally Maxwellian distributions in order to explore the modulation signals for an example model. Quantitative results for the actual realised case may be very different. Nonetheless, we believe that the above qualitative observations should still hold.

We have yet to discuss the current experimental situation with regard to DM direct detection. A variety of experiments, employing different techniques, are probing DM interactions with nuclei and electrons. Stringent limits on DM nuclear recoils have been found, with XENON100 [492], LUX [493], CRESST-II [494], and CDMS [495] among the most sensitive. By contrast, a positive hint for DM interactions has been obtained by the DAMA and DAMA/LIBRA experiments in the Gran Sasso Laboratory (latitude: 43° N) [143, 144, 446–448]. The DAMA experiments were designed to search for DM via the annual modulation signal and indeed such a modulation (with phase: $t_0 = 144 \pm 7$ days) was observed in their measured event rate at around $\sim 9\sigma$ C.L.. The DAMA and DAMA/LIBRA experiments feature a sodium iodine target with sensitivity to both nuclear and electron recoils in the keV recoil energy range. The stringent limits on nuclear recoils obtained by other experiments (as mentioned above) appears to indicate that electron recoils is the most likely DM option.

There are only a few experiments with sufficient sensitivity to probe electron recoils as the source of the DAMA annual modulation signal. At the present time, three such experiments have published results: CoGeNT, XENON100, and XMASS, all of which have some, albeit statistically weak, evidence for an annually modulated event rate. Consider first the CoGeNT experiment. This experiment involves p-type point contact germanium detectors operating in the Soudan Underground Laboratory (latitude: 48° N). Analysis of three years of data found evidence for an annual modulation at 2.2σ C.L. with phase consistent with that of DAMA [496]. The XENON100 experiment, located at Gran Sasso, recently analysed data collected over a 13 month period, observing an annually modulated electron recoil event rate at 2.8σ C.L. with phase consistent with that of DAMA [145]. The XENON100 experiment also obtained strong limits on the average electron recoil event rate, thereby suggesting that DM interactions with electrons could only be the source of the DAMA annual modulation if the modulation fraction was large: $\gtrsim 50\%$ [145, 497]. Most recently, the XMASS experiment at Kamioka Observatory (latitude: 36° N), also utilising a xenon target, has searched for DM–electron interactions [146]. Their data shows a possible hint

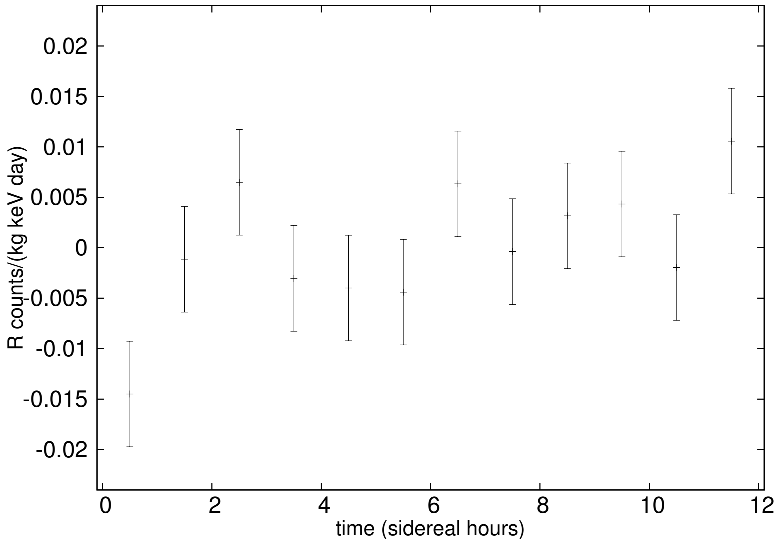

FIGURE 7.11: The DAMA [498] measured rate: $R - \langle R \rangle$ versus sidereal time, where the data has been replotted here with $24 \geq t \geq 12$ hours combined with $0 \leq t \leq 12$ hours.

of annual modulation with opposite sign to that of DAMA (i.e. approximately six months out of phase). Naturally it is difficult to directly compare DAMA's annual modulation signal with the results of these other experiments, as they differ in their recoil energy range, energy resolution, and low energy cutoff. The CoGeNT and XMASS experiments are also at different latitudes.

Of these experiments, only DAMA has given results for their event rate binned into 24 sideral hours (i.e. diurnal modulation). Taking our phase convention, where $t = 0$ is the time of day when θ is maximised, and motivated by azimuthal symmetry, it is sensible to combine the data from $0 \leq t/\text{hours} \leq 12$ with data from $24 \geq t/\text{hours} \geq 12$. We plot the data [498] combined in this way in Figure 7.11. The figure does show some modest evidence for a rising event rate toward $t = 12$ hours. The far/near ratio Equation (7.29) can be evaluated as:

$$R_{\text{far/near}} = 1.0072 \pm 0.0031 \; . \tag{7.30}$$

That is, $R_{\text{far/near}}$ is different from unity at approximately 2.3σ C.L..

The current experimental situation is rather intriguing, especially when viewed in the context of plasma DM. Indeed, plasma DM appears to have the potential to resolve the diverse results of the different experiments. In particular, our analysis leaves open the interesting possibility that the DAMA annual modulation signal might be due to electron recoils (or even a combination of electron and nuclear recoils). This modulation fraction can be large, thus potentially satisfying the constraints on electron recoils from XENON100. Similarly, constraints on nuclear recoils (such as those in [492–495]) are considerably weakened if the modulation fraction is large. Also, the results of XMASS might not be inconsistent with DAMA given the difference in latitude between the locations of these two experiments.

Clearly further work is required to clarify this situation. More experiments could analyse their data for possible DM interactions with electrons, in addition to nuclear recoils. Diurnal modulation in addition to annual modulation should be searched for. Experiments at different latitudes are important, and more experiments in the Southern Hemisphere would be helpful.

7.4 Conclusion

DM may have non-trivial particle properties leading to all sorts of interesting effects on small scales. The particular situation studied here is that DM in spiral galaxies like the Milky Way takes the form of a dark plasma. Hidden sector DM charged under an unbroken $U(1)'$ gauge interaction provides a simple and well defined particle physics model realising this possibility. The assumed $U(1)'$ neutrality of the Universe then implies (at least) two oppositely charged DM components with self-interactions mediated via a massless "dark photon" (the $U(1)'$ gauge boson). We considered the simplest case of two such DM components, the "dark electron" and the "dark proton", with $m_{e_d} \leq m_{p_d}$.

Various astrophysical and cosmological aspects of this type of DM have been explored in the literature previously, but there have been relatively few attempts to understand the implications for direct detection experiments. This seems to be particularly relevant at the present time in view of the rapidly progressing experimental activity in the field of DM direct detection. Moreover, plasma DM is quite unique in that it can potentially lead to both nuclear and electron recoils in the keV energy range; this is because energy equipartition implies a potentially large dark electron velocity dispersion, and $U(1)'$ neutrality prevents dark electrons from escaping the galaxy. In fact, previous work has speculated that plasma DM might possibly be able to explain the DAMA annual modulation signal via electron recoils, as the constraints on electron recoils from other experiments are generally much weaker than those for nuclear recoils.

To properly examine this idea, and the implications for direct detection experiments more generally, requires a detailed description of the plasma DM density and velocity distribution in the vicinity of the Earth. This is a rather complex problem as any assumed interaction with ordinary matter will inevitably lead to DM being captured by the Earth, forming an approximate "dark sphere" within. This dark sphere provides an obstacle to the halo DM wind, the nature of which depends on whether the captured DM is largely neutral or ionised. We considered these two limiting cases, referred to as "Moon-like" or "Venus-like," making use of analogy with the solar wind interactions with the Moon and Venus. We studied these limiting cases using single fluid magnetohydrodynamic equations.

We numerically solved the magnetohydrodynamic equations to obtain the space and time dependent dark plasma density, temperature, and bulk velocity in the vicinity of the Earth. We identified two distinct sources of annual modulation: the first arises from the variation of the Earth's speed relative to the DM halo, and; the second arises from the variation of the Earth's spin axis relative to the wind direction. While both effects are due to the Earth's orbital motion around the Sun, their phases are different: June 2^{nd} versus April 25^{th}. In addition, the variation of the location of a given detector relative to the wind direction due to the Earth's daily rotation leads to a diurnal modulation (i.e. with period of one sidereal day). The latter two modulation effects are a direct consequence of the spatially dependent near-Earth DM density and velocity distributions, and are expected to be an important consideration in general self-interacting DM models capable of giving a direct detection signal. Importantly, they imply latitudinal dependence of the measured event rate.

In order to make predictions for direct detection experiments, a kinetic description of the plasma dark electron and dark proton components is required. This is a challenging and unsolved problem. To make progress, we modelled the velocity distribution locally in terms of a Maxwellian distribution. Although this is rather unsatisfactory, it is hoped that such a description will provide useful insight. We considered mirror DM as an example, and evaluated the annual and diurnal modulations, focusing on the distinctive electron recoil interaction. Several relevant qualitative observations were made from the results.

Plasma DM is very different from e.g. weakly interacting DM. Large annual and diurnal modulations can arise. These modulations need not be sinusoidal and may contain sharp features. Moreover, the spatial dependence of the local event rate in the vicinity of the Earth implies that experiments at different latitudes will not necessarily find the same thing (even qualitatively). This is especially true for a Southern Hemisphere detector, but is even true for varying latitudes in the Northern Hemisphere. The analysis presented here leaves open the interesting possibility that the DAMA annual modulation signal might be due primarily to electron recoils (or even a combination of electron and nuclear recoils). The modulation fraction can be large, thus potentially satisfying constraints from other experiments. Furthermore, the results of XMASS might not be inconsistent with DAMA given the difference in latitude between the locations of these two experiments. Much more experimental activity is required. A greater emphasis on electron recoils would be helpful and we encourage all experiments to present results for diurnal variation.

8 Conclusion

The Standard Model (SM) is an enigma. On the one hand it has proven to be an extremely successful effective field theory for describing particle physics phenomenology at energy scales $\lesssim$ TeV, and even remains theoretically consistent when extrapolated to the Planck scale. On the other hand it leaves unanswered a number of theoretical and phenomenological questions. In this THESIS we presented a collection of original pieces of work pertaining to six of the major questions, which were introduced in Section 1.1: the Higgs sector; naturalness; neutrino masses; the baryon asymmetry of the Universe (BAU); the strong CP problem; and dark matter (DM). Since the SM is already so successful, a logical (and tractable) way to study these questions is by so-called "bottom-up" extensions, whereby new physics is minimally added to the SM framework in order to address and/or to understand the implications of those questions. This was the general philosophy embraced throughout the THESIS.

In CHAPTER 2: HIGGS SECTOR we explored the phenomenological implications of extending the SM Higgs sector by a very light real singlet scalar s (100 MeV $< m_s < m_h/2$). Constraints on this scenario from collider, meson decay, and fixed target experiments were derived; they are summarised in Figure 2.4. Three distinct regions of parameter space exist for LHC phenomenology. First, for $m_s \gtrsim m_B$, future searches for parton-level production via Vs can potentially probe parameter space beyond existing constraints. Second, for $m_s \lesssim m_B$, we found that s production via the decay of B mesons could have resulted in up to thousands of potentially background free moderate p_T displaced dimuons within the detector volumes of ATLAS/CMS or at LHCb during the 8 TeV run. This motivates a search for $B \to s + X \to (\mu^+\mu^-) + X$ displaced dimuons at ATLAS/CMS and/or LHCb. Indeed, as a result of that work, a search was later performed at LHCb which excludes a large region of previously unexplored parameter space. Third, when s is long-lived, production via Higgs decays $h \to ss$ result in a spectacular signature in the LHC detectors. We demonstrated a simple Monte Carlo method to reinterpret displaced searches utilising efficiency tables, which we hope goes some way to motivating the LHC Collaborations to publish relevant multidimensional efficiency tables along with their displaced searches.

In CHAPTER 3: NATURALNESS we considered the question, at what mass does a heavy gauge multiplet introduce a physical Higgs naturalness problem?

We motivated a renormalisation group description of naturalnes, of particular interest for bottom-up extensions of the SM. The Higgs mass is interpreted as a derived quantity of high scale $\overline{\mathrm{MS}}$ "input" parameters. If $\mu^2(m_Z)$ is especially sensitive to these input parameters, then this signifies a Higgs naturalness problem. It was shown how a Higgs sensitivity measure can be rigorously derived using Bayesian probabilistic arguments. The derived measure captures, in essence, the "naturalness price" paid for promoting the Higgs mass parameter to a high scale input parameter of the model. We used this measure to set naturalness bounds on the masses of various gauge multiplets in a full two-loop RGE analysis with one-loop matching. The resulting bounds are presented in Tables 3.1 and 3.2, and as contours in Figures 3.4–3.7; they lie in the range $M < \mathcal{O}(1\text{–}100)$ TeV, depending on the gauge multiplet and the naturalness criterion considered. Bounds on fermionic gauge multiplets are weaker than for scalars, and bounds on coloured multiplets are no more severe than on electroweak multiplets, since they correct the Higgs mass directly only at three-loop.

In CHAPTER 4: NEUTRINO MASS we wrote down minimal UV completions for all of the dimension 7, $\Delta L = 2$ SM operators which could be responsible for radiatively generating a Majorana neutrino mass. These completions predict a plethora of particles whose properties are constrained by low-energy neutrino oscillation data, and form the basis of a systematic approach to testing radiative neutrino mass models at the LHC. A detailed collider study was presented for a $LLQ\bar{d}H$ completion with a leptoquark $\phi \sim (\bar{3}, 1, \frac{1}{3})$ and a vector-like quark $\chi \sim (3, 2, -\frac{5}{6})$. The analysis constrained $m_\chi \gtrsim 620$ GeV and $m_\phi \gtrsim 600$ GeV.

In CHAPTER 5: BARYON ASYMMETRY OF THE UNIVERSE we proved that the three-flavour Type I seesaw model cannot explain neutrino masses and the BAU via hierarchical leptogenesis without introducing a Higgs naturalness problem. We then described a model with a second Higgs doublet (the "ν2HDM") which can avoid this conclusion. Neutrino masses are generated radiatively, or by a tree-level seesaw with small vev insertions. The ν2HDM accommodates a SM-like Higgs, predicts approximately TeV scale scalar states, and low to intermediate scale leptogenesis (10^3 GeV $\lesssim M_{N_1} \lesssim$ few $\times\, 10^7$ GeV). The interesting areas of parameter space are summarised in Figure 5.7.

In CHAPTER 6: STRONG CP PROBLEM we wrote down a simple model (the "νDFSZ") which serves as an existence proof that weakly coupled high-scale physics can explain phenomenological shortcomings of the SM *without introducing a naturalness problem*. Neutrino masses, the BAU, the strong CP problem, and DM are explained via a seesaw mechanism, hierarchical leptogenesis, the PQ mechanism, and a DFSZ invisible axion, respectively. The νDFSZ contains four scales: $|m_{11}| \approx 88$ GeV, $m_{22} \sim 10^3$ GeV, $M_N \sim 10^5$–10^7 GeV, and $M_{PQ} \sim 10^{11}$ GeV, which are protected from large corrections by a technically natural decoupling limit. Furthermore there are testable predictions: TeV scale scalar states, and axionic DM.

Lastly, in CHAPTER 7: DARK MATTER we considered the implications of the "plasma dark matter" scenario for direct detection experiments. Plasma DM is type of hidden sector DM which is minimally composed of a "dark electron," a "dark proton," and a massless "dark photon" which mediates a dark electromagnetism. An interesting consequence is that, if $m_{e_d} \ll m_{p_d}$, energy equipartition and $U(1)'$ neutrality in the galactic halo imply a much larger dark electron velocity dispersion than in standard single component models. Plainly this has implications for direct detection experiments. As well, if this DM interacts with standard matter, then some amount will be captured inside the Earth. There, since the DM is self-interacting, it will form an obstacle to the DM wind, implying a spatially dependent near-Earth DM density and velocity distribution. This has a number of implications for direct detection signals: a new source of annual modulation (from annual modulation of the Earth rotation axis direction); modulation with sidereal day; and latitudinal dependence. We studied the interaction of plasma DM with the captured DM in certain limiting cases using numerical magnetohydrodynamic simulations. The specific example of electron recoils in mirror DM was then studied under simplifying assumptions. Several qualitative implications were identified from the results, as summarised in Section 7.3.3. The analysis leaves open the interesting possibility that the DAMA annual modulation signal might be due primarily to electron recoils. We hope that, since this picture can be abstracted to general self-interacting DM scenarios, the analysis encourages direct detection experiments to search for sidereal modulation.

If an overarching conclusion is to be made from this THESIS, then perhaps it would be the following. As we have discussed, the SM leaves open a number of questions. These questions can be answered by physics beyond the SM, featuring a huge variety of phenomenologically distinct predictions, some within the reach of existing or soon-to-be existing experiments. Exactly which of these questions will be resolved first, or even if they will be resolved at all, is not clear. In the mean time, it is vitally important to probe nature in all the ways it could plausibly be probed. This requires dilligence from the full spectrum of particle physicists: theorists, phenomenologists, and experimentalists. After all, nature has only one manifestation, and it is our job to find out which one that is.

A Appendix A

A.1 Sensitivity measure as a Bayesian model comparison

In this Appendix we show how a Barbieri–Giudice-like fine-tuning measure for $\mu^2(m_Z)$ arises in a certain limit of our Bayesian model comparison. Similar connections have been made in earlier works, e.g. Refs. [279, 283].

Bayesian probability allows one to assign a degree of belief to some hypothesis, in our case a particle physics model. The model $\mathcal{M}$ consists of a set of input parameters $\mathcal{I}$ and a rule for connecting these to a set of observables $\mathcal{O}$. Let us assume that there are n fundamental input parameters $\mathcal{I} = \{\mathcal{I}_1, \ldots, \mathcal{I}_n\}$ and $m \leq n$ independent observables $\mathcal{O} = \{\mathcal{O}_1, \ldots, \mathcal{O}_m\}$. The rule is just a map $\mathcal{R} : \mathcal{I} \to \mathcal{O}$ from input space to observable space with $(\mathcal{I}_1, \ldots, \mathcal{I}_n) \mapsto \mathcal{R}(\mathcal{I}_1, \ldots, \mathcal{I}_n) = (\mathcal{O}_1, \ldots, \mathcal{O}_m)$. In CHAPTER 3 the models consist of the SM plus a new gauge multiplet of mass M, with inputs as the logarithms of $\overline{\text{MS}}$ parameters of the full Lagrangian defined at scale Λ_h, observables as the logarithms of $\overline{\text{MS}}$ SM Lagrangian parameters at scale m_Z, and $\mathcal{R}$ given by the RGEs. The logarithms are taken to avoid dependence on units or rescalings of the Lagrangian.[1]

The Bayesian evidence B for $\mathcal{M}$ is the probability that the observables $\mathcal{O}$ attain their experimentally observed values $\mathcal{O}_{ex}$, assuming $\mathcal{M}$ is true:

$$B(\mathcal{M}) := p(\mathcal{O} = \mathcal{O}_{ex}|\mathcal{M}) = \int p(\mathcal{O} = \mathcal{O}_{ex}|\mathcal{I})\, p(\mathcal{I})\, d\mathcal{I} \,, \tag{A.1}$$

where $p(\mathcal{O} = \mathcal{O}_{ex}|\mathcal{I})$ is also called the likelihood function $\mathcal{L}(\mathcal{I})$, and $p(\mathcal{I})$ is the prior density for the model parameters. The prior density represents the degree of belief in the values of the input parameters before any observations are made. In the absence of any knowledge about the complete UV theory, we should assume priors which are maximally agnostic. This corresponds to a flat prior in the n-dimensional input space $\mathcal{I}$. The mapping $\mathcal{R}$ can be used to express some point in input space $(\mathcal{I}_1, \ldots, \mathcal{I}_n)$ in terms of a new set of coordinates $(\mathcal{O}, \mathcal{I}') \equiv (\mathcal{O}_1, \ldots, \mathcal{O}_m, \mathcal{I}_{m+1}, \ldots, \mathcal{I}_n)$ simply by $\mathcal{I} \mapsto \mathcal{R}'(\mathcal{I}) \equiv (\mathcal{R}(\mathcal{I}), \mathcal{I}')$. We assume that this is a one-to-one mapping (indeed, it is for RGEs in the perturbative regime). If we assume perfectly measured observables, then Equation (A.1)

[1] Absolute values inside the logarithms are implied. The signs of the parameters can be considered as separate inputs. Explicitly including them with a flat prior probability mass function does not change the final result, and we ignore them henceforth for clarity.

becomes

$$B(\mathcal{M}) \propto \int \delta(\mathcal{O} - \mathcal{O}_{ex})\, p \circ \mathcal{R}'^{-1}(\mathcal{O}, \mathcal{I}') \times \left| \begin{pmatrix} \frac{\partial \mathcal{I}_1}{\partial \mathcal{O}_1} & \cdots & \frac{\partial \mathcal{I}_1}{\partial \mathcal{O}_m} \\ \vdots & \ddots & \vdots \\ \frac{\partial \mathcal{I}_m}{\partial \mathcal{O}_1} & \cdots & \frac{\partial \mathcal{I}_m}{\partial \mathcal{O}_m} \end{pmatrix} \right| d\mathcal{O}_1 \cdots d\mathcal{O}_m d\mathcal{I}_{m+1} \cdots d\mathcal{I}_n \,, \tag{A.2}$$

where the likelihood has become a delta function multiplied by a constant term, and $|(\,\cdot\,)| \equiv |\det[(\,\cdot\,)]|$ is the determinant of the Jacobian associated with the coordinate transformation. Performing the integration over the observables,

$$B(\mathcal{M}) \propto \int p'(\mathcal{I}') \left| \begin{pmatrix} \frac{\partial \mathcal{I}_1}{\partial \mathcal{O}_1} & \cdots & \frac{\partial \mathcal{I}_1}{\partial \mathcal{O}_m} \\ \vdots & \ddots & \vdots \\ \frac{\partial \mathcal{I}_m}{\partial \mathcal{O}_1} & \cdots & \frac{\partial \mathcal{I}_m}{\partial \mathcal{O}_m} \end{pmatrix} \right| d\mathcal{I}_{m+1} \cdots d\mathcal{I}_n \Bigg|_{\mathcal{O}=\mathcal{O}_{ex}} \,, \tag{A.3}$$

where $p'(\mathcal{I}') \equiv p \circ \mathcal{R}^{-1}(\mathcal{O}_{ex}, \mathcal{I}')$. The requirement $\mathcal{O} = \mathcal{O}_{ex}$ has carved out an experimentally allowed $(n - m)$ dimensional submanifold within the original n dimensional input space. We know that, since the original prior was flat in n dimensions, the prior on the submanifold must be flat with respect to the induced volume element (as opposed to the volume element $d\mathcal{I}_{m+1} \cdots d\mathcal{I}_n$). We can rescale the existing volume element to write, equivalently,

$$B(\mathcal{M}) \propto \int p'(\mathcal{I}') \frac{\left| \begin{pmatrix} \frac{\partial \mathcal{I}_1}{\partial \mathcal{O}_1} & \cdots & \frac{\partial \mathcal{I}_1}{\partial \mathcal{O}_m} \\ \vdots & \ddots & \vdots \\ \frac{\partial \mathcal{I}_m}{\partial \mathcal{O}_1} & \cdots & \frac{\partial \mathcal{I}_m}{\partial \mathcal{O}_m} \end{pmatrix} \right|}{\sqrt{\left| \begin{pmatrix} \frac{\partial \mathcal{I}_1}{\partial \mathcal{I}_{m+1}} & \cdots & \frac{\partial \mathcal{I}_1}{\partial \mathcal{I}_n} \\ \vdots & \ddots & \vdots \\ \frac{\partial \mathcal{I}_n}{\partial \mathcal{I}_{m+1}} & \cdots & \frac{\partial \mathcal{I}_n}{\partial \mathcal{I}_n} \end{pmatrix}^T \begin{pmatrix} \frac{\partial \mathcal{I}_1}{\partial \mathcal{I}_{m+1}} & \cdots & \frac{\partial \mathcal{I}_1}{\partial \mathcal{I}_n} \\ \vdots & \ddots & \vdots \\ \frac{\partial \mathcal{I}_n}{\partial \mathcal{I}_{m+1}} & \cdots & \frac{\partial \mathcal{I}_n}{\partial \mathcal{I}_n} \end{pmatrix} \right|}} d\Sigma \Bigg|_{\mathcal{O}=\mathcal{O}_{ex}} \,, \tag{A.4}$$

where the quantity under the square root is the determinant of the induced metric, $d\Sigma$ is the induced volume element, and the prior $p'(\mathcal{I}')$ is constant with respect to this volume element. This reduces to

$$B(\mathcal{M}) \propto \int \frac{p'(\mathcal{I}')}{\sqrt{|JJ^T|}} \, d\Sigma \Bigg|_{\mathcal{O}=\mathcal{O}_{ex}} \,, \tag{A.5}$$

where J is the $m \times n$ matrix defined by $J_{ij} = \partial \mathcal{O}_i / \partial \mathcal{I}_j$ [283]. Additionally, by taking a delta function prior on $\mathcal{I}'$ we can evaluate (and compare) Bayesian evidence for the model $\mathcal{M}$ with unconstrained input parameters $(\mathcal{I}_{m+1}, \ldots, \mathcal{I}_n)$ taking on specific values:

$$B(\mathcal{M};\mathcal{I}') \propto \left.\frac{1}{\sqrt{|JJ^T|}}\right|_{\substack{\mathcal{O}_{ex}\\ \mathcal{I}'}} . \tag{A.6}$$

Let us now put this in the context of minimal extensions of the SM by a gauge multiplet of mass M. We take $\mathcal{I}_1 = \log\mu^2(\Lambda_h)$ and $\mathcal{O}_1 = \log\mu^2(m_Z)$. The remaining inputs and observables are logarithms of the $\overline{\text{MS}}$ Lagrangian parameters. The Bayesian evidence Equation (A.6) is not enough by itself; it can only be interpreted with respect to some reference model. We will, after all, be interested in the sensitivity of $\mu^2(m_Z)$ to the input parameters, and we have not so far treated the μ^2 parameter in any special way. The reference model we choose to compare to is the model $\mathcal{M}_0$ in which the Higgs mass parameter is instead taken as a "phenomenological" input parameter at scale m_Z, i.e. $\mathcal{I}_1 = \mathcal{O}_1 = \log\mu^2(m_Z)$. In $\mathcal{M}_0$ we have that $J_{11} = 1$ and $J_{1j} = 0$ for $j > 1$. The Bayes factor between these two models is then

$$K(\mathcal{M};\mathcal{I}') := \left.\frac{B(\mathcal{M}_0;\mathcal{I}')}{B(\mathcal{M};\mathcal{I}')}\right|_{\substack{\mathcal{O}_{ex}\\ \mathcal{I}'}} . \tag{A.7}$$

Since the dimensionful parameter $\mu^2(\mu_R)$ does not enter the (mass independent) RGEs of the remaining dimensionless observables, we have that $J_{i1} = \partial\mathcal{O}_i/\partial\mathcal{I}_1 = 0$ for $i > 1$. Additionally, in the special case that the dimensionless observables are approximately insensitive to the unconstrained inputs, i.e. $J_{ij} \simeq 0$ for $i > 1$ and $j \geq m+1$, Equation (A.6) becomes

$$B(\mathcal{M};\mathcal{I}') \propto \left.\frac{\left|\begin{pmatrix} \frac{\partial\mathcal{O}_2}{\partial\mathcal{I}_2} & \cdots & \frac{\partial\mathcal{O}_2}{\partial\mathcal{I}_m} \\ \vdots & \ddots & \vdots \\ \frac{\partial\mathcal{O}_m}{\partial\mathcal{I}_2} & \cdots & \frac{\partial\mathcal{O}_m}{\partial\mathcal{I}_m} \end{pmatrix}\right|^{-1}}{\sqrt{\left(\frac{\partial\log\mu^2(m_Z)}{\partial\mathcal{I}_1}\right)^2 + \sum_{j\geq m+1}\left(\frac{\partial\log\mu^2(m_Z)}{\partial\mathcal{I}_j}\right)^2}}\right|_{\substack{\mathcal{O}_{ex}\\ \mathcal{I}'}} . \tag{A.8}$$

We can see that a Barbieri–Giudice-like fine-tuning measure has appeared in the denominator. In this case the quantity $B(\mathcal{M}_0;\mathcal{I}')$ becomes independent of $\mathcal{I}'$, and the Bayes factor Equation (A.7) is

$$K(\mathcal{M};\mathcal{I}') = \left.\sqrt{\left(\frac{\partial\log\mu^2(m_Z)}{\partial\log\mu^2(\Lambda_h)}\right)^2 + \sum_{j\geq m+1}\left(\frac{\partial\log\mu^2(m_Z)}{\partial\mathcal{I}_j}\right)^2}\right|_{\substack{\mathcal{O}_{ex}\\ \mathcal{I}'}} . \tag{A.9}$$

This is reminiscent of the Barbieri–Giudice fine-tuning measure. We observe the interesting emergence of additional terms quantifying Higgs mass sensitivity only to the unconstrained parameters of the model. Conceptually, K is a comparison between a flat prior in $\log \mu^2(m_Z)$ and the RG devolved (to m_Z) flat prior in $\log \mu^2(\Lambda_h)$, in the vicinity $\mu^2(m_Z) \simeq -(88\,\mathrm{GeV})^2$. A Bayes factor of $K > 10$ corresponds to the onset of strong evidence (on the Jeffreys scale) for $\mathcal{M}_0$ over $\mathcal{M}$.

Lastly, note that the Bayes factor K is still a function of the unknown parameters $\mathcal{I}'$. In order to write down a sensitivity measure for the model $\mathcal{M}$ as a function of a subset of these unknown parameters (e.g. the gauge multiplet mass M), we might want some way of projecting out the nuisance unknowns. One way is to integrate over some region of $\mathcal{I}'$, i.e. evaluate Equation (A.5). However, in CHAPTER 3 we instead choose the following conservative projection:

$$\Delta(\mathcal{M}) = \min_{\mathcal{I}'} \Big\{ K(\mathcal{M};\mathcal{I}') \Big\}. \tag{A.10}$$

This identifies the best case scenario for Higgs mass naturalness in $\mathcal{M}$ by finding the point in $\mathcal{I}'$ with the lowest Bayes factor.

B Appendix B

B.1 ν2HDM squared scalar masses at $\mathcal{O}(m_{12}^4/m_{22}^4)$

To order m_{12}^4/m_{22}^4, the scalar masses Equations (5.29) are given by

$$\begin{aligned}
m_h^2 &\approx v_1^2\left[\lambda_1 + \frac{m_{12}^4}{m_{22}^4}\frac{2\lambda_{345} - \lambda_1 - \frac{v_1^2}{2m_{22}^2}\lambda_1\lambda_{345}}{\left(1+\frac{v_1^2}{2m_{22}^2}\left(\lambda_{345}-2\lambda_1\right)\right)\left(1+\frac{v_1^2}{2m_{22}^2}\lambda_{345}\right)^2}\right], \\
m_H^2 &\approx m_{22}^2\left[1+\lambda_{345}\frac{v_1^2}{2m_{22}^2}\right. \\
&\qquad\left. + \frac{m_{12}^4}{m_{22}^4}\frac{1-\frac{v_1^2}{2m_{22}^2}\left(2\lambda_{345}-3\lambda_2\right)+\frac{v_1^4}{4m_{22}^4}\left(\lambda_{345}^2+3\lambda_2\lambda_{345}-6\lambda_1\lambda_2\right)}{\left(1+\frac{v_1^2}{2m_{22}^2}\left(\lambda_{345}-2\lambda_1\right)\right)\left(1+\frac{v_1^2}{2m_{22}^2}\lambda_{345}\right)^2}\right], \\
m_A^2 &\approx m_{22}^2\left[1+\left(\lambda_{345}-2\lambda_5\right)\frac{v_1^2}{2m_{22}^2} + \frac{m_{12}^4}{m_{22}^4}\frac{1+\frac{v_1^2}{2m_{22}^2}\left(\lambda_{345}+\lambda_2-2\lambda_5\right)}{\left(1+\frac{v_1^2}{2m_{22}^2}\lambda_{345}\right)^2}\right], \\
m_{H^\pm}^2 &\approx m_{22}^2\left[1+\lambda_3\frac{v_1^2}{2m_{22}^2} + \frac{m_{12}^4}{m_{22}^4}\frac{1+\frac{v_1^2}{2m_{22}^2}\left(\lambda_2+\lambda_3\right)}{\left(1+\frac{v_1^2}{2m_{22}^2}\lambda_{345}\right)^2}\right].
\end{aligned} \tag{B.1}$$

B.2 Bounds for more general m_ν

We consider the seesaw Lagrangian as in Eq. 5.1 and a neutrino mass matrix of the form

$$m_\nu = \frac{v^2}{2}y_\nu \mathcal{D}_M^{-1}\mathcal{D}_{f(M)}y_\nu^T, \tag{B.2}$$

where $\mathcal{D}_x \equiv \mathrm{diag}(x_1, x_2, x_3)$. Note that in the ν2HDM with $\lambda_5 = 0$ we have $f(M_j) = v_2^2/v^2$, and in the Ma model with $M_N \gg m_{22}$ we have

$$f(M_j) = \frac{\lambda_5}{8\pi^2}\left(\ln\left[\frac{M_j^2}{(m_H^2+m_A^2)/2}\right]-1\right). \tag{B.3}$$

Following Casas-Ibarra [94], it is possible to write

$$y_\nu = \frac{\sqrt{2}}{v} U^\dagger \mathcal{D}_m^{\frac{1}{2}} R \mathcal{D}_M^{\frac{1}{2}} \mathcal{D}_{f(M)}^{-\frac{1}{2}}, \tag{B.4}$$

where R is a (possibly complex) orthogonal ($RR^T = R^T R = \mathbb{I}$) matrix. The Vissani bound on each right-handed neutrino mass becomes [3]

$$\begin{aligned} &\frac{1}{4\pi^2} \frac{2}{v^2} \frac{M_j^3}{f(M_j)} \sum_i m_i |R_{ij}|^2 < 1 \text{ TeV}^2 \\ &\Rightarrow M_{N_1} \lesssim 3 \times 10^7 \text{ GeV} \times f(M_{N_1})^{\frac{1}{3}}. \end{aligned} \tag{B.5}$$

The CP asymmetry for hierarchical neutrinos [96] becomes

$$\begin{aligned} |\epsilon_1| &= \frac{6}{16\pi} \frac{M_1}{v^2} \frac{\text{Im}[(R^\dagger \mathcal{D}_m (R \mathcal{D}_{f(M)}^{-1} R^T) \mathcal{D}_m R^*)_{11}]}{(R^\dagger \mathcal{D}_m R)_{11}} \\ &\lesssim \frac{6}{16\pi} \frac{m_3 M_{N_1}}{v^2} \frac{1}{\min[f(M_j)]}, \end{aligned} \tag{B.6}$$

where the approximate inequality holds for $\max(|R_{ij}|) \leq 1$. For larger $\max(|R_{ij}|)$ the inequality can be exceeded, but this corresponds to a fine-tuning (see Ref. [3]). With this caveat, the Davidson-Ibarra bound for $\min[f(M_i)] = f(M_{N_1})$ therefore becomes

$$M_{N_1} \gtrsim 5 \times 10^8 \text{ GeV} \times f(M_{N_1}). \tag{B.7}$$

The $\Delta L = 2$ scatterings are proportional to [95, 499]

$$\begin{aligned} &\sum_{i,j} \text{Re}[(y_\nu^\dagger y_\nu)_{ij} (y_\nu^\dagger y_\nu)_{ij}] \frac{1}{M_i M_j} \\ &\quad = \text{Tr}[(y_\nu \mathcal{D}_M^{-1} y_\nu^T)(y_\nu \mathcal{D}_M^{-1} y_\nu^T)^\dagger] \\ &\quad = \frac{4}{v^4} \text{Tr}[\mathcal{D}_m (R \mathcal{D}_{f(M)}^{-1} R^T) \mathcal{D}_m (R \mathcal{D}_{f(M)}^{-1} R^T)^\dagger] \\ &\quad \lesssim \frac{4}{v^4} \frac{\overline{m}^2}{\min[f(M_j)]^2}, \end{aligned} \tag{B.8}$$

where the last line is an exact equality for $f(M_1) = f(M_2) = f(M_3)$, an exact inequality when R is real, and an approximate inequality (as indicated) if R is complex with $\max(|R_{ij}|) \leq 1$. Again, for larger $\max(|R_{ij}|)$ the inequality can be exceeded. Then for $\min[f(M_i)] = f(M_{N_1})$, the $\Delta L = 2$ scattering Eq. 5.50 becomes

$$\frac{\Gamma_{\Delta L=2}}{H} \lesssim \frac{T}{2.2 \times 10^{13} \text{ GeV}} \frac{1}{f(M_{N_1})^2} \left(\frac{\overline{m}}{0.05 \text{ eV}} \right)^2. \tag{B.9}$$

C Appendix C

C.1 νDFSZ RGEs

Following is the full list of RGEs in the [Type II, Flipped] model, found using PyR@TE [303]. Underlined are those parameters which, for simplicity, we did not evolve in our RGE analysis.

$$\mathcal{D}M_{11}^2 = M_{11}^2\left(6\lambda_1 - \frac{3}{2}g_1^2 - \frac{9}{2}g_2^2 + 6y_t^2 + \left[0, 2y_\tau^2\right]\right) + M_{22}^2\left(4\lambda_3 + 2\lambda_4\right) + M_{SS}^2 2\lambda_{1S}, \tag{C.1}$$

$$\mathcal{D}M_{22}^2 = M_{22}^2\left(6\lambda_2 - \frac{3}{2}g_1^2 - \frac{9}{2}g_2^2 + 6y_b^2 + \left[2y_\tau^2, 0\right] + 2\mathrm{Tr}\left(y_\nu^\dagger y_\nu\right)\right) + M_{11}^2\left(4\lambda_3 + 2\lambda_4\right) + M_{SS}^2 2\lambda_{2S}, \tag{C.2}$$

$$\underline{\mathcal{D}M_{SS}^2} = M_{SS}^2\left(4\lambda_S + \mathrm{Tr}\left(y_N^\dagger y_N\right)\right) + M_{11}^2 4\lambda_{1S} + M_{22}^2 4\lambda_{2S}, \tag{C.3}$$

$$\underline{\mathcal{D}\langle S\rangle^2} = -\,\mathrm{Tr}\left(y_N^\dagger y_N\right)\langle S\rangle^2 \quad \text{[i.e. the wave function renormalisation]}, \tag{C.4}$$

$$\mathcal{D}g_{\{1,2,3\}} = \{7, -3, -7\}g_{\{1,2,3\}}^3, \tag{C.5}$$

$$\mathcal{D}\lambda_1 = \frac{3}{4}g_1^4 + \frac{3}{2}g_1^2 g_2^2 + \frac{9}{4}g_2^4 - \lambda_1\left(3g_1^2 + 9g_2^2\right) + 12\lambda_1^2 + 4\lambda_3\lambda_4 + 4\lambda_3^2 + 2\lambda_4^2 + 2\lambda_{1S}^2 + 12\lambda_1 y_t^2 - 12y_t^4 + \left[0, 4\lambda_1 y_\tau^2 - 4y_\tau^4\right], \tag{C.6}$$

$$\mathcal{D}\lambda_2 = \frac{3}{4}g_1^4 + \frac{3}{2}g_1^2 g_2^2 + \frac{9}{4}g_2^4 - \lambda_2\left(3g_1^2 + 9g_2^2\right) + 12\lambda_2^2 + 4\lambda_3\lambda_4 + 4\lambda_3^2 + 2\lambda_4^2 + 2\lambda_{2S}^2 + 12\lambda_1 y_b^2 - 12y_b^4 + \left[4\lambda_1 y_\tau^2 - 4y_\tau^4, 0\right] + 4\lambda_2\mathrm{Tr}\left(y_\nu^\dagger y_\nu\right) - 4\mathrm{Tr}\left(y_\nu^\dagger y_\nu y_\nu^\dagger y_\nu\right), \tag{C.7}$$

$$\mathcal{D}\lambda_3 = \frac{3}{4}g_1^4 - \frac{3}{2}g_1^2 g_2^2 + \frac{9}{4}g_2^4 - \lambda_3\left(3g_1^2 + 9g_2^2\right) + \left(6\lambda_3 + 2\lambda_4\right)\left(\lambda_1 + \lambda_2\right) + 4\lambda_3^2 + 2\lambda_4^2 + 2\lambda_{1S}\lambda_{2S} + \lambda_3\left(6y_t^2 + 6y_b^2 + 2y_\tau^2 + 2\mathrm{Tr}\left(y_\nu^\dagger y_\nu\right)\right) - 12y_t^2 y_b^2 - \left[0, 4\left(y_\nu^\dagger y_\nu\right)_{33} y_\tau^2\right], \tag{C.8}$$

$$\mathcal{D}\lambda_4 = 3g_1^2 g_2^2 - \lambda_4\left(3g_1^2 + 9g_2^2\right) + 2\lambda_4\left(\lambda_1 + \lambda_2\right) + 8\lambda_4\lambda_3 + 4\lambda_4^2 + \lambda_4\left(6y_t^2 + 6y_b^2 + 2y_\tau^2 + 2\mathrm{Tr}\left(y_\nu^\dagger y_\nu\right)\right) + 12y_t^2 y_b^2 + \left[0, 4\left(y_\nu^\dagger y_\nu\right)_{33} y_\tau^2\right], \tag{C.9}$$

$$\underline{\mathcal{D}\lambda_S} = 10\lambda_S^2 + 2\lambda_S\mathrm{Tr}\left(y_N^\dagger y_N\right) + 4\lambda_{1S}^2 + 4\lambda_{2S}^2 - 2\mathrm{Tr}\left(y_N^\dagger y_N y_N^\dagger y_N\right), \tag{C.10}$$

$$\mathcal{D}\lambda_{1S} = \lambda_{1S}\left(-\frac{3}{2}g_1^2 - \frac{9}{2}g_2^2 + 4\lambda_{1S} + 4\lambda_S + 6\lambda_1\right) + \lambda_{2S}\left(4\lambda_3 + 2\lambda_4\right) + \lambda_{1S}\left(6y_t^2 + \left[0, 2y_\tau^2\right] + \mathrm{Tr}\left(y_N^\dagger y_N\right)\right), \tag{C.11}$$

$$\mathcal{D}\lambda_{2S} = \lambda_{2S}\left(-\frac{3}{2}g_1^2 - \frac{9}{2}g_2^2 + 4\lambda_{2S} + 4\lambda_S + 6\lambda_2\right) + \lambda_{1S}\left(4\lambda_3 + 2\lambda_4\right) + \lambda_{2S}\left(6y_b^2 + \left[2y_\tau^2, 0\right] + 2\mathrm{Tr}\left(y_\nu^\dagger y_\nu\right) + \mathrm{Tr}\left(y_N^\dagger y_N\right)\right) - 4\mathrm{Tr}\left(y_\nu^\dagger y_\nu y_N^\dagger y_N\right), \tag{C.12}$$

$$\mathcal{D}\epsilon = \epsilon\Big(-\frac{3}{2}g_1^2 - \frac{9}{2}g_2^2 + 2\lambda_3 + 4\lambda_4 + 2\lambda_S + 4\lambda_{1S} + 4\lambda_{2S} + 3y_t^2 + 3y_b^2 + y_\tau^2 + \mathrm{Tr}\left(y_\nu^\dagger y_\nu\right) + \mathrm{Tr}\left(y_N^\dagger y_N\right)\Big), \tag{C.13}$$

$$\mathcal{D}y_t = y_t\left(-\frac{17}{12}g_1^2 - \frac{9}{4}g_2^2 - 8g_3^2 + \frac{9}{2}y_t^2 + \frac{1}{2}y_b^2 + \left[0, y_\tau^2\right]\right), \tag{C.14}$$

$$\mathcal{D}y_b = y_b\left(-\frac{5}{12}g_1^2 - \frac{9}{4}g_2^2 - 8g_3^2 + \frac{9}{2}y_b^2 + \frac{1}{2}y_t^2 + \left[y_\tau^2, 0\right]\right), \tag{C.15}$$

$$\mathcal{D}y_\tau = y_\tau\left(-\frac{15}{4}g_1^2 - \frac{9}{4}g_2^2 + \frac{5}{2}y_\tau^2 + \left[3y_b^2, 3y_t^2\right]\right), \tag{C.16}$$

$$\underline{\mathcal{D}y_\nu} = y_\nu\left(-\frac{3}{4}g_1^2 - \frac{9}{4}g_2^2 + 3y_b^2 + \mathrm{Tr}\left(y_\nu^\dagger y_\nu\right)\right) + \left[y_\nu y_\tau^2 - \frac{3}{2}\mathrm{Diag}\left(0, 0, y_\tau^2\right)y_\nu, 0\right] + \frac{3}{2}y_\nu y_\nu^\dagger y_\nu + \frac{1}{2}y_\nu y_N^\dagger y_N, \tag{C.17}$$

$$\underline{\mathcal{D}y_N} = \frac{1}{2}\mathrm{Tr}\left(y_N^\dagger y_N\right)y_N + y_N y_N^\dagger y_N + y_N y_\nu^\dagger y_\nu + y_\nu^T y_\nu^* y_N. \tag{C.18}$$

Bibliography

[1] J. D. Clarke, R. Foot, and R. R. Volkas. "Phenomenology of a very light scalar (100 MeV $< m_h <$ 10 GeV) mixing with the SM Higgs". *JHEP* 1402 (2014), p. 123. DOI: 10.1007/JHEP02(2014)123. arXiv: 1310.8042 [hep-ph].

[2] Y. Cai et al. "Testing Radiative Neutrino Mass Models at the LHC". *JHEP* 02 (2015), p. 161. DOI: 10.1007/JHEP02(2015)161. arXiv: 1410.0689 [hep-ph].

[3] J. D. Clarke, R. Foot, and R. R. Volkas. "Electroweak naturalness in the three-flavor type I seesaw model and implications for leptogenesis". *Phys. Rev.* D91.7 (2015), p. 073009. DOI: 10.1103/PhysRevD.91.073009. arXiv: 1502.01352 [hep-ph].

[4] J. D. Clarke. "Constraining portals with displaced Higgs decay searches at the LHC". *JHEP* 10 (2015), p. 061. DOI: 10.1007/JHEP10(2015)061. arXiv: 1505.00063 [hep-ph].

[5] J. D. Clarke, R. Foot, and R. R. Volkas. "Natural leptogenesis and neutrino masses with two Higgs doublets". *Phys. Rev.* D92.3 (2015), p. 033006. DOI: 10.1103/PhysRevD.92.033006. arXiv: 1505.05744 [hep-ph].

[6] J. D. Clarke. "How to avoid unnatural hierarchical thermal leptogenesis". *PoS* PLANCK2015 (2015), p. 026. arXiv: 1509.07242 [hep-ph].

[7] J. D. Clarke and R. R. Volkas. "Technically natural nonsupersymmetric model of neutrino masses, baryogenesis, the strong CP problem, and dark matter". *Phys. Rev.* D93.3 (2016), p. 035001. DOI: 10.1103/PhysRevD.93.035001. arXiv: 1509.07243 [hep-ph].

[8] J. D. Clarke and R. Foot. "Plasma dark matter direct detection". *JCAP* 1601.01 (2016), p. 029. DOI: 10.1088/1475-7516/2016/01/029. arXiv: 1512.06471 [astro-ph.GA].

[9] Y. Cai et al. "TeV-scale pseudo-Dirac seesaw mechanisms in an E_6 inspired model". *Phys. Rev.* D94.3 (2016), p. 033003. DOI: 10.1103/PhysRevD.94.033003. arXiv: 1605.02743 [hep-ph].

[10] J. D. Clarke and R. Foot. "Mirror dark matter will be confirmed or excluded by XENON1T" (2016). arXiv: 1606.09063 [hep-ph].

[11] J. D. Clarke and P. Cox. "Naturalness made easy: two-loop naturalness bounds on minimal SM extensions" (2016). arXiv: 1607.07446 [hep-ph].

[12] H. Weyl. "Electron and Gravitation. 1. (In German)". *Z. Phys.* 56 (1929). [Surveys High Energ. Phys.5,261(1986)], pp. 330–352. DOI: 10.1007/BF01339504.

[13] J. Goldstone. "Field Theories with Superconductor Solutions". *Nuovo Cim.* 19 (1961), pp. 154–164. DOI: 10.1007/BF02812722.

[14] J. Goldstone, A. Salam, and S. Weinberg. "Broken Symmetries". *Phys. Rev.* 127 (1962), pp. 965–970. DOI: 10.1103/PhysRev.127.965.

[15] P. W. Anderson. "Plasmons, Gauge Invariance, and Mass". *Phys. Rev.* 130 (1963), pp. 439–442. DOI: 10.1103/PhysRev.130.439.

[16] F. Englert and R. Brout. "Broken Symmetry and the Mass of Gauge Vector Mesons". *Phys.Rev.Lett.* 13 (1964), pp. 321–323. DOI: 10.1103/PhysRevLett.13.321.

[17] P. W. Higgs. "Broken Symmetries and the Masses of Gauge Bosons". *Phys.Rev.Lett.* 13 (1964), pp. 508–509. DOI: 10.1103/PhysRevLett.13.508.

[18] G. Guralnik, C. Hagen, and T. Kibble. "Global Conservation Laws and Massless Particles". *Phys.Rev.Lett.* 13 (1964), pp. 585–587. DOI: 10.1103/PhysRevLett.13.585.

[19] S. Weinberg. "A Model of Leptons". *Phys. Rev. Lett.* 19 (1967), pp. 1264–1266. DOI: 10.1103/PhysRevLett.19.1264.

[20] A. Salam. "Weak and Electromagnetic Interactions". *Conf. Proc.* C680519 (1968), pp. 367–377.

[21] S. L. Glashow. "Partial Symmetries of Weak Interactions". *Nucl. Phys.* 22 (1961), pp. 579–588. DOI: 10.1016/0029-5582(61)90469-2.

[22] T. D. Lee and C.-N. Yang. "Question of Parity Conservation in Weak Interactions". *Phys. Rev.* 104 (1956), pp. 254–258. DOI: 10.1103/PhysRev.104.254.

[23] C. S. Wu et al. "Experimental Test of Parity Conservation in Beta Decay". *Phys. Rev.* 105 (1957), pp. 1413–1414. DOI: 10.1103/PhysRev.105.1413.

[24] R. Barate et al. "Search f the standard model Higgs boson at LEP". *Phys.Lett.* B565 (2003), pp. 61–75. DOI: 10.1016/S0370-2693(03)00614-2. arXiv: hep-ex/0306033 [hep-ex].

[25] "Updated Combination of CDF and D0 Searches for Standard Model Higgs Boson Production with up to 10.0 fb^{-1} of Data". 2012. arXiv: 1207.0449 [hep-ex].

[26] J. Alwall et al. "MadGraph 5 : Going Beyond". *JHEP* 1106 (2011), p. 128. DOI: `10.1007/JHEP06(2011)128`. arXiv: `1106.0522 [hep-ph]`.

[27] T. Sjostrand, S. Mrenna, and P. Z. Skands. "PYTHIA 6.4 Physics and Manual". *JHEP* 0605 (2006), p. 026. DOI: `10.1088/1126-6708/2006/05/026`. arXiv: `hep-ph/0603175 [hep-ph]`.

[28] T. Sjostrand, S. Mrenna, and P. Z. Skands. "A Brief Introduction to PYTHIA 8.1". *Comput.Phys.Commun.* 178 (2008), pp. 852–867. DOI: `10.1016/j.cpc.2008.01.036`. arXiv: `0710.3820 [hep-ph]`.

[29] J. de Favereau et al. "DELPHES 3, A modular framework for fast simulation of a generic collider experiment". *JHEP* 1402 (2014), p. 057. DOI: `10.1007/JHEP02(2014)057`. arXiv: `1307.6346 [hep-ex]`.

[30] G. Aad et al. "Observation of a new particle in the search for the Standard Model Higgs boson with the ATLAS detector at the LHC". *Phys.Lett.* B716 (2012), pp. 1–29. DOI: `10.1016/j.physletb.2012.08.020`. arXiv: `1207.7214 [hep-ex]`.

[31] S. Chatrchyan et al. "Observation of a new boson at a mass of 125 GeV with the CMS experiment at the LHC". *Phys.Lett.* B716 (2012), pp. 30–61. DOI: `10.1016/j.physletb.2012.08.021`. arXiv: `1207.7235 [hep-ex]`.

[32] G. Aad et al. "Measurements of the Higgs boson production and decay rates and constraints on its couplings from a combined ATLAS and CMS analysis of the LHC pp collision data at $\sqrt{s} = 7$ and 8 TeV" (2016). arXiv: `1606.02266 [hep-ex]`.

[33] G. Aad et al. "Combined Measurement of the Higgs Boson Mass in pp Collisions at $\sqrt{s} = 7$ and 8 TeV with the ATLAS and CMS Experiments". *Phys. Rev. Lett.* 114 (2015), p. 191803. DOI: `10.1103/PhysRevLett.114.191803`. arXiv: `1503.07589 [hep-ex]`.

[34] G. Belanger et al. "Global fit to Higgs signal strengths and couplings and implications for extended Higgs sectors". *Phys.Rev.* D88 (2013), p. 075008. DOI: `10.1103/PhysRevD.88.075008`. arXiv: `1306.2941 [hep-ph]`.

[35] K. Cheung, J. S. Lee, and P.-Y. Tseng. "Higgs precision analysis updates 2014". *Phys.Rev.* D90 (2014), p. 095009. DOI: `10.1103/PhysRevD.90.095009`. arXiv: `1407.8236 [hep-ph]`.

[36] R. Volkas, A. Davies, and G. Joshi. "Naturalness of the invisible axion model". *Phys.Lett.* B215 (1988), p. 133. DOI: `10.1016/0370-2693(88)91084-2`.

[37] R. Foot et al. "Poincare Protection for a Natural Electroweak Scale". *Phys.Rev.* D89 (2014), p. 115018. DOI: `10.1103/PhysRevD.89.115018`. arXiv: `1310.0223 [hep-ph]`.

[38] B. Pontecorvo. "Mesonium and anti-mesonium". *Sov. Phys. JETP* 6 (1957). [Zh. Eksp. Teor. Fiz.33,549(1957)], p. 429.

[39] Z. Maki, M. Nakagawa, and S. Sakata. "Remarks on the unified model of elementary particles". *Prog.Theor.Phys.* 28 (1962), pp. 870–880. DOI: 10.1143/PTP.28.870.

[40] G. Bellini et al. "Neutrino oscillations". *Adv. High Energy Phys.* 2014 (2014), p. 191960. DOI: 10.1155/2014/191960. arXiv: 1310.7858 [hep-ph].

[41] K. S. Hirata et al. "Experimental Study of the Atmospheric Neutrino Flux". *Phys. Lett.* B205 (1988). [,447(1988)], p. 416. DOI: 10.1016/0370-2693(88)91690-5.

[42] K. S. Hirata et al. "Observation of a small atmospheric muon-neutrino / electron-neutrino ratio in Kamiokande". *Phys. Lett.* B280 (1992), pp. 146–152. DOI: 10.1016/0370-2693(92)90788-6.

[43] Y. Fukuda et al. "Atmospheric muon-neutrino / electron-neutrino ratio in the multiGeV energy range". *Phys. Lett.* B335 (1994), pp. 237–245. DOI: 10.1016/0370-2693(94)91420-6.

[44] R. Becker-Szendy et al. "The Electron-neutrino and muon-neutrino content of the atmospheric flux". *Phys. Rev.* D46 (1992), pp. 3720–3724. DOI: 10.1103/PhysRevD.46.3720.

[45] R. Becker-Szendy et al. "Neutrino measurements with the IMB detector". *Nucl.Phys.Proc.Suppl.* 38 (1995), pp. 331–336. DOI: 10.1016/0920-5632(94)00765-N.

[46] Y. Fukuda et al. "Evidence for oscillation of atmospheric neutrinos". *Phys.Rev.Lett.* 81 (1998), pp. 1562–1567. DOI: 10.1103/PhysRevLett.81.1562. arXiv: hep-ex/9807003 [hep-ex].

[47] B. Cleveland et al. "Measurement of the solar electron neutrino flux with the Homestake chlorine detector". *Astrophys.J.* 496 (1998), pp. 505–526. DOI: 10.1086/305343.

[48] L. Wolfenstein. "Neutrino Oscillations in Matter". *Phys. Rev.* D17 (1978), pp. 2369–2374. DOI: 10.1103/PhysRevD.17.2369.

[49] S. P. Mikheev and A. Yu. Smirnov. "Resonance Amplification of Oscillations in Matter and Spectroscopy of Solar Neutrinos". *Sov. J. Nucl. Phys.* 42 (1985). [Yad. Fiz.42,1441(1985)], pp. 913–917.

[50] K. S. Hirata et al. "Observation of B-8 Solar Neutrinos in the Kamiokande-II Detector". *Phys. Rev. Lett.* 63 (1989), p. 16. DOI: 10.1103/PhysRevLett.63.16.

[51] K. S. Hirata et al. "Results from one thousand days of real time directional solar neutrino data". *Phys. Rev. Lett.* 65 (1990), pp. 1297–1300. DOI: 10.1103/PhysRevLett.65.1297.

[52] W. Hampel et al. "GALLEX solar neutrino observations: Results for GALLEX IV". *Phys.Lett.* B447 (1999), pp. 127–133. DOI: 10.1016/S0370-2693(98)01579-2.

[53] J. N. Abdurashitov et al. "Measurement of the solar neutrino capture rate with gallium metal". *Phys. Rev.* C60 (1999), p. 055801. DOI: 10.1103/PhysRevC.60.055801. arXiv: astro-ph/9907113 [astro-ph].

[54] Q. Ahmad et al. "Measurement of the rate of $\nu_e + d \to p + p + e^-$ interactions produced by ^8B solar neutrinos at the Sudbury Neutrino Observatory". *Phys.Rev.Lett.* 87 (2001), p. 071301. DOI: 10.1103/PhysRevLett.87.071301. arXiv: nucl-ex/0106015 [nucl-ex].

[55] Q. Ahmad et al. "Direct evidence for neutrino flavor transformation from neutral current interactions in the Sudbury Neutrino Observatory". *Phys.Rev.Lett.* 89 (2002), p. 011301. DOI: 10.1103/PhysRevLett.89.011301. arXiv: nucl-ex/0204008 [nucl-ex].

[56] K. Eguchi et al. "First results from KamLAND: Evidence for reactor anti-neutrino disappearance". *Phys.Rev.Lett.* 90 (2003), p. 021802. DOI: 10.1103/PhysRevLett.90.021802. arXiv: hep-ex/0212021 [hep-ex].

[57] M. Ahn et al. "Measurement of Neutrino Oscillation by the K2K Experiment". *Phys.Rev.* D74 (2006), p. 072003. DOI: 10.1103/PhysRevD.74.072003. arXiv: hep-ex/0606032 [hep-ex].

[58] D. Michael et al. "Observation of muon neutrino disappearance with the MINOS detectors and the NuMI neutrino beam". *Phys.Rev.Lett.* 97 (2006), p. 191801. DOI: 10.1103/PhysRevLett.97.191801. arXiv: hep-ex/0607088 [hep-ex].

[59] N. Cabibbo. "Unitary Symmetry and Leptonic Decays". *Phys. Rev. Lett.* 10 (1963). [,648(1963)], pp. 531–533. DOI: 10.1103/PhysRevLett.10.531.

[60] M. Kobayashi and T. Maskawa. "CP Violation in the Renormalizable Theory of Weak Interaction". *Prog. Theor. Phys.* 49 (1973), pp. 652–657. DOI: 10.1143/PTP.49.652.

[61] M. Gonzalez-Garcia, M. Maltoni, and T. Schwetz. "Updated fit to three neutrino mixing: status of leptonic CP violation". *JHEP* 1411 (2014), p. 052. DOI: 10.1007/JHEP11(2014)052. arXiv: 1409.5439 [hep-ph].

[62] K. Hirata et al. "Observation of a Neutrino Burst from the Supernova SN 1987a". *Phys. Rev. Lett.* 58 (1987). [,727(1987)], pp. 1490–1493. DOI: 10.1103/PhysRevLett.58.1490.

[63] R. M. Bionta et al. "Observation of a Neutrino Burst in Coincidence with Supernova SN 1987a in the Large Magellanic Cloud". *Phys. Rev. Lett.* 58 (1987), p. 1494. DOI: 10.1103/PhysRevLett.58.1494.

[64] E. N. Alekseev et al. "Detection of the Neutrino Signal From SN1987A in the LMC Using the Inr Baksan Underground Scintillation Telescope". *Phys. Lett.* B205 (1988), pp. 209–214. DOI: 10.1016/0370-2693(88)91651-6.

[65] T. J. Loredo and D. Q. Lamb. "Bayesian analysis of neutrinos observed from supernova SN-1987A". *Phys. Rev.* D65 (2002), p. 063002. DOI: 10.1103/PhysRevD.65.063002. arXiv: astro-ph/0107260 [astro-ph].

[66] G. Pagliaroli, F. Rossi-Torres, and F. Vissani. "Neutrino mass bound in the standard scenario for supernova electronic antineutrino emission". *Astropart. Phys.* 33 (2010), pp. 287–291. DOI: 10.1016/j.astropartphys.2010.02.007. arXiv: 1002.3349 [hep-ph].

[67] C. Kraus et al. "Final results from phase II of the Mainz neutrino mass search in tritium beta decay". *Eur. Phys. J.* C40 (2005), pp. 447–468. DOI: 10.1140/epjc/s2005-02139-7. arXiv: hep-ex/0412056 [hep-ex].

[68] V. N. Aseev et al. "An upper limit on electron antineutrino mass from Troitsk experiment". *Phys. Rev.* D84 (2011), p. 112003. DOI: 10.1103/PhysRevD.84.112003. arXiv: 1108.5034 [hep-ex].

[69] P. Ade et al. "Planck 2015 results. XIII. Cosmological parameters" (2015). arXiv: 1502.01589 [astro-ph.CO].

[70] A. Gando et al. "Search for Majorana Neutrinos near the Inverted Mass Hierarchy region with KamLAND-Zen" (2016). arXiv: 1605.02889 [hep-ex].

[71] S. Weinberg. "Baryon and Lepton Nonconserving Processes". *Phys. Rev. Lett.* 43 (1979), pp. 1566–1570. DOI: 10.1103/PhysRevLett.43.1566.

[72] P. Minkowski. "$\mu \to e\gamma$ at a Rate of One Out of 1-Billion Muon Decays?" *Phys.Lett.* B67 (1977), p. 421. DOI: 10.1016/0370-2693(77)90435-X.

[73] T. Yanagida. "Horizontal symmetry and masses of neutrinos". *Conf.Proc.* C7902131 (1979), pp. 95–99.

[74] M. Gell-Mann, P. Ramond, and R. Slansky. "Complex Spinors and Unified Theories". *Conf.Proc.* C790927 (1979), pp. 315–321. arXiv: 1306.4669 [hep-th].

[75] J. Schechter and J. Valle. "Neutrino Masses in SU(2) x U(1) Theories". *Phys.Rev.* D22 (1980), p. 2227. DOI: 10.1103/PhysRevD.22.2227.

[76] R. Foot et al. "Seesaw Neutrino Masses Induced by a Triplet of Leptons". *Z.Phys.* C44 (1989), p. 441. DOI: 10.1007/BF01415558.

[77] A. Zee. “A Theory of Lepton Number Violation, Neutrino Majorana Mass, and Oscillation”. *Phys. Lett.* B93 (1980), p. 389. DOI: 10.1016/0370-2693(80)90349-4.

[78] T. Cheng and L.-F. Li. “Neutrino Masses, Mixings and Oscillations in SU(2) x U(1) Models of Electroweak Interactions”. *Phys.Rev.* D22 (1980), p. 2860. DOI: 10.1103/PhysRevD.22.2860.

[79] A. Zee. “QUANTUM NUMBERS OF MAJORANA NEUTRINO MASSES”. *Nucl.Phys.* B264 (1986), p. 99. DOI: 10.1016/0550-3213(86)90475-X.

[80] K. Babu. “Model of ’Calculable’ Majorana Neutrino Masses”. *Phys.Lett.* B203 (1988), p. 132. DOI: 10.1016/0370-2693(88)91584-5.

[81] L. M. Krauss, S. Nasri, and M. Trodden. “A Model for neutrino masses and dark matter”. *Phys.Rev.* D67 (2003), p. 085002. DOI: 10.1103/PhysRevD.67.085002. eprint: hep-ph/0210389.

[82] E. Ma. “Verifiable radiative seesaw mechanism of neutrino mass and dark matter”. *Phys. Rev.* D73 (2006), p. 077301. DOI: 10.1103/PhysRevD.73.077301. eprint: hep-ph/0601225.

[83] A. G. Cohen, A. De Rujula, and S. L. Glashow. “A Matter - antimatter universe?” *Astrophys. J.* 495 (1998), pp. 539–549. DOI: 10.1086/305328. arXiv: astro-ph/9707087 [astro-ph].

[84] B. Fields and S. Sarkar. “Big-Bang nucleosynthesis (2006 Particle Data Group mini-review)” (2006). arXiv: astro-ph/0601514 [astro-ph].

[85] W. M. Yao et al. “Review of Particle Physics”. *J. Phys.* G33 (2006), pp. 1–1232. DOI: 10.1088/0954-3899/33/1/001.

[86] G. Hinshaw et al. “Nine-year Wilkinson Microwave Anisotropy Probe (WMAP) Observations: Cosmological Parameter Results”. *The Astrophysical Journal Supplement* 208, 19 (Oct. 2013), p. 19. DOI: 10.1088/0067-0049/208/2/19. arXiv: 1212.5226.

[87] H.-Y. Chiu. “Symmetry between particle and anti-particle populations in the universe”. *Phys. Rev. Lett.* 17 (1966), p. 712. DOI: 10.1103/PhysRevLett.17.712.

[88] A. D. Sakharov. “Violation of CP Invariance, c Asymmetry, and Baryon Asymmetry of the Universe”. *Pisma Zh. Eksp. Teor. Fiz.* 5 (1967). [Usp. Fiz. Nauk161,61(1991)], pp. 32–35. DOI: 10.1070/PU1991v034n05ABEH002497.

[89] G. ’t Hooft. “Symmetry Breaking Through Bell-Jackiw Anomalies”. *Phys. Rev. Lett.* 37 (1976), pp. 8–11. DOI: 10.1103/PhysRevLett.37.8.

[90] F. R. Klinkhamer and N. S. Manton. "A Saddle Point Solution in the Weinberg-Salam Theory". *Phys. Rev.* D30 (1984), p. 2212. DOI: 10.1103/PhysRevD.30.2212.

[91] L. Canetti, M. Drewes, and M. Shaposhnikov. "Matter and Antimatter in the Universe". *New J. Phys.* 14 (2012), p. 095012. DOI: 10.1088/1367-2630/14/9/095012. arXiv: 1204.4186 [hep-ph].

[92] M. E. Shaposhnikov. "Structure of the High Temperature Gauge Ground State and Electroweak Production of the Baryon Asymmetry". *Nucl. Phys.* B299 (1988), pp. 797–817. DOI: 10.1016/0550-3213(88)90373-2.

[93] M. Fukugita and T. Yanagida. "Baryogenesis Without Grand Unification". *Phys.Lett.* B174 (1986), p. 45. DOI: 10.1016/0370-2693(86)91126-3.

[94] J. Casas and A. Ibarra. "Oscillating neutrinos and $\mu \to e\gamma$". *Nucl.Phys.* B618 (2001), pp. 171–204. DOI: 10.1016/S0550-3213(01)00475-8. arXiv: hep-ph/0103065 [hep-ph].

[95] W. Buchmuller, P. Di Bari, and M. Plumacher. "Leptogenesis for pedestrians". *Annals Phys.* 315 (2005), pp. 305–351. DOI: 10.1016/j.aop.2004.02.003. arXiv: hep-ph/0401240 [hep-ph].

[96] S. Davidson and A. Ibarra. "A Lower bound on the right-handed neutrino mass from leptogenesis". *Phys.Lett.* B535 (2002), pp. 25–32. DOI: 10.1016/S0370-2693(02)01735-5. arXiv: hep-ph/0202239 [hep-ph].

[97] G. Giudice et al. "Towards a complete theory of thermal leptogenesis in the SM and MSSM". *Nucl.Phys.* B685 (2004), pp. 89–149. DOI: 10.1016/j.nuclphysb.2004.02.019. arXiv: hep-ph/0310123 [hep-ph].

[98] A. Pilaftsis and T. E. Underwood. "Resonant leptogenesis". *Nucl.Phys.* B692 (2004), pp. 303–345. DOI: 10.1016/j.nuclphysb.2004.05.029. arXiv: hep-ph/0309342 [hep-ph].

[99] S. L. Adler. "Axial vector vertex in spinor electrodynamics". *Phys. Rev.* 177 (1969), pp. 2426–2438. DOI: 10.1103/PhysRev.177.2426.

[100] J. S. Bell and R. Jackiw. "A PCAC puzzle: pi0 –> gamma gamma in the sigma model". *Nuovo Cim.* A60 (1969), pp. 47–61. DOI: 10.1007/BF02823296.

[101] W. A. Bardeen. "Anomalous Ward identities in spinor field theories". *Phys. Rev.* 184 (1969), pp. 1848–1857. DOI: 10.1103/PhysRev.184.1848.

[102] W. A. Bardeen. "Anomalous Currents in Gauge Field Theories". *Nucl. Phys.* B75 (1974), pp. 246–258. DOI: 10.1016/0550-3213(74)90546-X.

[103] C. Baker et al. "An Improved experimental limit on the electric dipole moment of the neutron". *Phys.Rev.Lett.* 97 (2006), p. 131801. DOI: 10.1103/PhysRevLett.97.131801. arXiv: hep-ex/0602020 [hep-ex].

[104] R. Peccei and H. R. Quinn. "CP Conservation in the Presence of Instantons". *Phys.Rev.Lett.* 38 (1977), pp. 1440–1443. DOI: 10.1103/PhysRevLett.38.1440.

[105] R. D. Peccei and H. R. Quinn. "Constraints Imposed by CP Conservation in the Presence of Instantons". *Phys. Rev.* D16 (1977), pp. 1791–1797. DOI: 10.1103/PhysRevD.16.1791.

[106] G. Raffelt. "Astrophysical axion bounds". *Lect.Notes Phys.* 741 (2008), pp. 51–71. DOI: 10.1007/978-3-540-73518-2_3. arXiv: hep-ph/0611350 [hep-ph].

[107] M. Dine, W. Fischler, and M. Srednicki. "A Simple Solution to the Strong CP Problem with a Harmless Axion". *Phys.Lett.* B104 (1981), p. 199. DOI: 10.1016/0370-2693(81)90590-6.

[108] A. Zhitnitsky. "On Possible Suppression of the Axion Hadron Interactions. (In Russian)". *Sov.J.Nucl.Phys.* 31 (1980), p. 260.

[109] G. Hinshaw et al. "Nine-Year Wilkinson Microwave Anisotropy Probe (WMAP) Observations: Cosmological Parameter Results". *Astrophys. J. Suppl.* 208 (2013), p. 19. DOI: 10.1088/0067-0049/208/2/19. arXiv: 1212.5226 [astro-ph.CO].

[110] P. A. R. Ade et al. "Planck 2013 results. XVI. Cosmological parameters". *Astron. Astrophys.* 571 (2014), A16. DOI: 10.1051/0004-6361/201321591. arXiv: 1303.5076 [astro-ph.CO].

[111] V. Springel et al. "Simulating the joint evolution of quasars, galaxies and their large-scale distribution". *Nature* 435 (2005), pp. 629–636. DOI: 10.1038/nature03597. arXiv: astro-ph/0504097 [astro-ph].

[112] G. R. Blumenthal et al. "Formation of Galaxies and Large Scale Structure with Cold Dark Matter". *Nature* 311 (1984), pp. 517–525. DOI: 10.1038/311517a0.

[113] M. Tegmark et al. "The 3-D power spectrum of galaxies from the SDSS". *Astrophys. J.* 606 (2004), pp. 702–740. DOI: 10.1086/382125. arXiv: astro-ph/0310725 [astro-ph].

[114] S. Cole et al. "The 2dF Galaxy Redshift Survey: Power-spectrum analysis of the final dataset and cosmological implications". *Mon. Not. Roy. Astron. Soc.* 362 (2005), pp. 505–534. DOI: 10.1111/j.1365-2966.2005.09318.x. arXiv: astro-ph/0501174 [astro-ph].

[115] D. J. Eisenstein et al. "Detection of the baryon acoustic peak in the large-scale correlation function of SDSS luminous red galaxies". *Astrophys. J.* 633 (2005), pp. 560–574. DOI: 10.1086/466512. arXiv: astro-ph/0501171 [astro-ph].

[116] V. Springel, C. S. Frenk, and S. D. M. White. "The large-scale structure of the Universe". *Nature* 440 (2006), p. 1137. DOI: 10.1038/nature04805. arXiv: astro-ph/0604561 [astro-ph].

[117] D. Harvey et al. "The non-gravitational interactions of dark matter in colliding galaxy clusters". *Science* 347 (2015), pp. 1462–1465. DOI: 10.1126/science.1261381. arXiv: 1503.07675 [astro-ph.CO].

[118] V. C. Rubin, N. Thonnard, and W. K. Ford Jr. "Extended rotation curves of high-luminosity spiral galaxies." *Astrophysical Journal* 225 (Nov. 1978), pp. L107–L111. DOI: 10.1086/182804.

[119] Y. Sofue and V. Rubin. "Rotation curves of spiral galaxies". *Ann. Rev. Astron. Astrophys.* 39 (2001), pp. 137–174. DOI: 10.1146/annurev.astro.39.1.137. arXiv: astro-ph/0010594 [astro-ph].

[120] W. J. G. de Blok. "The Core-Cusp Problem". *Advances in Astronomy* 2010, 789293 (2010), p. 789293. DOI: 10.1155/2010/789293. arXiv: 0910.3538.

[121] J. S. Bullock. "Notes on the Missing Satellites Problem". *ArXiv e-prints* (Sept. 2010). arXiv: 1009.4505 [astro-ph.CO].

[122] M. Boylan-Kolchin, J. S. Bullock, and M. Kaplinghat. "Too big to fail? The puzzling darkness of massive Milky Way subhaloes". *Monthly Notices of the Royal Astronomical Society* 415 (July 2011), pp. L40–L44. DOI: 10.1111/j.1745-3933.2011.01074.x. arXiv: 1103.0007 [astro-ph.CO].

[123] A. Pontzen and F. Governato. "Cold dark matter heats up". *Nature* 506 (2014), pp. 171–178. DOI: 10.1038/nature12953. arXiv: 1402.1764 [astro-ph.CO].

[124] M. Markevitch et al. "Direct constraints on the dark matter self-interaction cross-section from the merging galaxy cluster 1E0657-56". *Astrophys. J.* 606 (2004), pp. 819–824. DOI: 10.1086/383178. arXiv: astro-ph/0309303 [astro-ph].

[125] S. W. Randall et al. "Constraints on the Self-Interaction Cross-Section of Dark Matter from Numerical Simulations of the Merging Galaxy Cluster 1E 0657-56". *Astrophys. J.* 679 (2008), pp. 1173–1180. DOI: 10.1086/587859. arXiv: 0704.0261 [astro-ph].

[126] R. Foot. "Dissipative dark matter and the rotation curves of dwarf galaxies" (2015). arXiv: 1506.01451 [astro-ph.GA].

[127] A. Mahdavi et al. "A Dark Core in Abell 520". *Astrophys. J.* 668 (2007), pp. 806–814. DOI: 10.1086/521383. arXiv: 0706.3048 [astro-ph].

[128] M. J. Jee et al. "Hubble Space Telescope/Advanced Camera for Surveys Confirmation of the Dark Substructure in A520". *Astrophys. J.* 783 (2014), p. 78. DOI: 10.1088/0004-637X/783/2/78. arXiv: 1401.3356 [astro-ph.CO].

[129] R. Massey et al. "The behaviour of dark matter associated with four bright cluster galaxies in the 10 kpc core of Abell 3827". *Mon. Not. Roy. Astron. Soc.* 449.4 (2015), pp. 3393–3406. DOI: 10.1093/mnras/stv467. arXiv: 1504.03388 [astro-ph.CO].

[130] K. Petraki and R. R. Volkas. "Review of asymmetric dark matter". *Int. J. Mod. Phys.* A28 (2013), p. 1330028. DOI: 10.1142/S0217751X13300287. arXiv: 1305.4939 [hep-ph].

[131] B. Holdom. "Two U(1)'s and Epsilon Charge Shifts". *Phys.Lett.* B166 (1986), p. 196. DOI: 10.1016/0370-2693(86)91377-8.

[132] R. Foot, H. Lew, and R. Volkas. "A Model with fundamental improper space-time symmetries". *Phys.Lett.* B272 (1991), pp. 67–70. DOI: 10.1016/0370-2693(91)91013-L.

[133] B. Patt and F. Wilczek. "Higgs-field portal into hidden sectors" (2006). arXiv: hep-ph/0605188 [hep-ph].

[134] A. M. Green. "Astrophysical uncertainties on direct detection experiments". *Mod. Phys. Lett.* A27 (2012), p. 1230004. DOI: 10.1142/S0217732312300042. arXiv: 1112.0524 [astro-ph.CO].

[135] J. D. Sloane et al. "Assessing Astrophysical Uncertainties in Direct Detection with Galaxy Simulations" (2016). arXiv: 1601.05402 [astro-ph.GA].

[136] C. Kelso et al. "The impact of baryons on the direct detection of dark matter" (2016). arXiv: 1601.04725 [astro-ph.GA].

[137] N. Bozorgnia et al. "Simulated Milky Way analogues: implications for dark matter direct searches". *JCAP* 1605.05 (2016), p. 024. DOI: 10.1088/1475-7516/2016/05/024. arXiv: 1601.04707 [astro-ph.CO].

[138] T. Marrodán Undagoitia and L. Rauch. "Dark matter direct-detection experiments". *J. Phys.* G43.1 (2016), p. 013001. DOI: 10.1088/0954-3899/43/1/013001. arXiv: 1509.08767 [physics.ins-det].

[139] E. Aprile et al. "The XENON100 dark matter experiment". *Astroparticle Physics* 35 (Apr. 2012), pp. 573–590. DOI: 10.1016/j.astropartphys.2012.01.003. arXiv: 1107.2155 [astro-ph.IM].

[140] K. Abe et al. "XMASS detector". *Nucl. Instrum. Meth.* A716 (2013), pp. 78–85. DOI: 10.1016/j.nima.2013.03.059. arXiv: 1301.2815 [physics.ins-det].

[141] D. S. Akerib et al. "The Large Underground Xenon (LUX) Experiment". *Nucl. Instrum. Meth.* A704 (2013), pp. 111–126. DOI: 10.1016/j.nima.2012.11.135. arXiv: 1211.3788 [physics.ins-det].

[142] R. Bernabei et al. "The DAMA/LIBRA apparatus". *Nucl. Instrum. Meth.* A592 (2008), pp. 297–315. DOI: 10.1016/j.nima.2008.04.082. arXiv: 0804.2738 [astro-ph].

[143] R. Bernabei et al. "First results from DAMA/LIBRA and the combined results with DAMA/NaI". *Eur. Phys. J.* C56 (2008), pp. 333–355. DOI: 10.1140/epjc/s10052-008-0662-y. arXiv: 0804.2741 [astro-ph].

[144] R. Bernabei et al. "Final model independent result of DAMA/LIBRA-phase1". *Eur. Phys. J.* C73 (2013), p. 2648. DOI: 10.1140/epjc/s10052-013-2648-7. arXiv: 1308.5109 [astro-ph.GA].

[145] E. Aprile et al. "Search for Event Rate Modulation in XENON100 Electronic Recoil Data". *Phys. Rev. Lett.* 115.9 (2015), p. 091302. DOI: 10.1103/PhysRevLett.115.091302. arXiv: 1507.07748 [astro-ph.CO].

[146] K. Abe et al. "Direct dark matter search by annual modulation in XMASS-I" (2015). arXiv: 1511.04807 [astro-ph.CO].

[147] *Measurements of the Higgs boson production and decay rates and constraints on its couplings from a combined ATLAS and CMS analysis of the LHC pp collision data at $\sqrt{s}$ = 7 and 8 TeV*. Tech. rep. ATLAS-CONF-2015-044. Geneva: CERN, 2015.

[148] S. Coleman and E. Weinberg. "Radiative Corrections as the Origin of Spontaneous Symmetry Breaking". *Phys. Rev. D* 7 (6 1973), pp. 1888–1910. DOI: 10.1103/PhysRevD.7.1888.

[149] R. Hempfling. "The Next-to-minimal Coleman-Weinberg model". *Phys.Lett.* B379 (1996), pp. 153–158. DOI: 10.1016/0370-2693(96)00446-7. arXiv: hep-ph/9604278 [hep-ph].

[150] K. A. Meissner and H. Nicolai. "Conformal Symmetry and the Standard Model". *Phys.Lett.* B648 (2007), pp. 312–317. DOI: 10.1016/j.physletb.2007.03.023. arXiv: hep-th/0612165 [hep-th].

[151] W.-F. Chang, J. N. Ng, and J. M. Wu. "Shadow Higgs from a scale-invariant hidden U(1)(s) model". *Phys.Rev.* D75 (2007), p. 115016. DOI: 10.1103/PhysRevD.75.115016. arXiv: hep-ph/0701254 [HEP-PH].

[152] R. Foot, A. Kobakhidze, and R. R. Volkas. "Electroweak Higgs as a pseudo-Goldstone boson of broken scale invariance". *Phys.Lett.* B655 (2007), pp. 156–161. DOI: 10.1016/j.physletb.2007.06.084. arXiv: 0704.1165 [hep-ph].

[153] R. Foot et al. "A Solution to the hierarchy problem from an almost decoupled hidden sector within a classically scale invariant theory". *Phys.Rev.* D77 (2008), p. 035006. DOI: 10.1103/PhysRevD.77.035006. arXiv: 0709.2750 [hep-ph].

[154] L. Alexander-Nunneley and A. Pilaftsis. "The Minimal Scale Invariant Extension of the Standard Model". *JHEP* 1009 (2010), p. 021. DOI: 10.1007/JHEP09(2010)021. arXiv: 1006.5916 [hep-ph].

[155] C. Englert et al. "Emergence of the Electroweak Scale through the Higgs Portal". *JHEP* 1304 (2013), p. 060. DOI: 10.1007/JHEP04(2013)060. arXiv: 1301.4224 [hep-ph].

[156] T. Hambye and A. Strumia. "Dynamical generation of the weak and Dark Matter scale". *Phys.Rev.* D88 (2013), p. 055022. DOI: 10.1103/PhysRevD.88.055022. arXiv: 1306.2329 [hep-ph].

[157] M. Heikinheimo et al. "Twin Peak Higgs" (2013). arXiv: 1307.7146 [hep-ph].

[158] E. Gildener and S. Weinberg. "Symmetry breaking and scalar bosons". *Phys. Rev. D* 13 (12 1976), pp. 3333–3341. DOI: 10.1103/PhysRevD.13.3333.

[159] R. Foot and A. Kobakhidze. "Electroweak Scale Invariant Models with Small Cosmological Constant" (2011). arXiv: 1112.0607 [hep-ph].

[160] F. Bezrukov and D. Gorbunov. "Light inflaton Hunter's Guide". *JHEP* 1005 (2010), p. 010. DOI: 10.1007/JHEP05(2010)010. arXiv: 0912.0390 [hep-ph].

[161] F. Bezrukov and D. Gorbunov. "Light inflaton after LHC8 and WMAP9 results". *JHEP* 1307 (2013), p. 140. DOI: 10.1007/JHEP07(2013)140. arXiv: 1303.4395 [hep-ph].

[162] R. Foot, A. Kobakhidze, and R. R. Volkas. "Cosmological constant in scale-invariant theories". *Phys.Rev.* D84 (2011), p. 075010. DOI: 10.1103/PhysRevD.84.075010. arXiv: 1012.4848 [hep-ph].

[163] V. Silveira and A. Zee. "SCALAR PHANTOMS". *Phys.Lett.* B161 (1985), p. 136. DOI: 10.1016/0370-2693(85)90624-0.

[164] J. F. Gunion et al. *The Higgs Hunter's Guide*. Frontiers in Physics. Later reprinted under the 'Frontiers in Physics' series from Perseus Publishing in 2000. Boulder, CO: Westview, 1990.

[165] M. Voloshin. "Once Again About the Role of Gluonic Mechanism in Interaction of Light Higgs Boson with Hadrons". *Sov.J.Nucl.Phys.* 44 (1986), p. 478.

[166] B. Grinstein, L. J. Hall, and L. Randall. "Do B meson decays exclude a light Higgs?" *Phys.Lett.* B211 (1988), pp. 363–369. DOI: 10.1016/0370-2693(88)90916-1.

[167] S. Raby and G. B. West. "THE BRANCHING RATIO FOR A LIGHT HIGGS TO DECAY INTO $\mu^+\mu^-$ PAIRS". *Phys.Rev.* D38 (1988), p. 3488. DOI: 10.1103/PhysRevD.38.3488.

[168] E. Duchovni, E. Gross, and G. Mikenberg. "MOTIVATION AND TECHNIQUE FOR LIGHT HIGGS BOSON SEARCH". *Phys.Rev.* D39 (1989), pp. 365–367. DOI: 10.1103/PhysRevD.39.365.

[169] S. Narison. "GLUONIA ENHANCEMENTS OF THE HIGGS BOSON HADRONIC WIDTHS". *Phys.Lett.* B228 (1989), p. 513. DOI: 10.1016/0370-2693(89)90984-2.

[170] T. N. Truong and R. Willey. "BRANCHING RATIOS FOR DECAYS OF LIGHT HIGGS BOSONS". *Phys.Rev.* D40 (1989), p. 3635. DOI: 10.1103/PhysRevD.40.3635.

[171] J. F. Donoghue, J. Gasser, and H. Leutwyler. "THE DECAY OF A LIGHT HIGGS BOSON". *Nucl.Phys.* B343 (1990), pp. 341–368. DOI: 10.1016/0550-3213(90)90474-R.

[172] S. Bethke. "Experimental tests of asymptotic freedom". *Prog.Part.Nucl.Phys.* 58 (2007), pp. 351–386. DOI: 10.1016/j.ppnp.2006.06.001. arXiv: hep-ex/0606035 [hep-ex].

[173] E. Gross and P. Yepes. "SM Higgs boson hunting at LEP". *Int.J.Mod.Phys.* A8 (1993), pp. 407–454. DOI: 10.1142/S0217751X93000175.

[174] M. Acciarri et al. "Search for neutral Higgs boson production through the process $e^+e^- \to Z^*H0$". *Phys.Lett.* B385 (1996), pp. 454–470. DOI: 10.1016/0370-2693(96)00987-2.

[175] D. Buskulic et al. "Search for a nonminimal Higgs boson produced in the reaction $e^+e^- \to hZ^*$". *Phys.Lett.* B313 (1993), pp. 312–325. DOI: 10.1016/0370-2693(93)91228-F.

[176] G. Abbiendi et al. "Search for invisibly decaying Higgs bosons in $e^+e^- \to Z0h0$ production at $\sqrt{s} = 183$ GeV - 209 GeV". *Phys.Lett.* B682 (2010), pp. 381–390. DOI: 10.1016/j.physletb.2009.09.010. arXiv: 0707.0373 [hep-ex].

[177] *Searches for invisible Higgs bosons: Preliminary combined results using LEP data collected at energies up to 209-GeV*. Tech. rep. LHWG-NOTE-2001-06, ALEPH-2001-036, DELPHI-2001-116, L3-NOTE-2702, OPAL-TN-694. 2001. arXiv: hep-ex/0107032 [hep-ex].

[178] D. Decamp et al. "Searches for new particles in Z decays using the ALEPH detector". *Phys.Rept.* 216 (1992), pp. 253–340. DOI: 10.1016/0370-1573(92)90177-2.

[179] A. Sopczak. "Status of Higgs hunting at the Z resonance and its prospects at LEP-200". *Nucl.Phys.Proc.Suppl.* 37C (1995), p. 168.

[180] H. Leutwyler and M. A. Shifman. "LIGHT HIGGS PARTICLE IN DECAYS OF K AND η MESONS". *Nucl.Phys.* B343 (1990), pp. 369–397. DOI: 10.1016/0550-3213(90)90475-S.

[181] B. Batell, M. Pospelov, and A. Ritz. "Multi-lepton Signatures of a Hidden Sector in Rare B Decays". *Phys.Rev.* D83 (2011), p. 054005. DOI: 10.1103/PhysRevD.83.054005. arXiv: 0911.4938 [hep-ph].

[182] P. Ball and R. Zwicky. "New results on $B \to \pi, K, \eta$ decay formfactors from light-cone sum rules". *Phys.Rev.* D71 (2005), p. 014015. DOI: 10.1103/PhysRevD.71.014015. arXiv: hep-ph/0406232 [hep-ph].

[183] J. Batley et al. "New measurement of the $K^{\pm} \to \pi^{\pm}\mu^{+}\mu^{-}$ decay". *Phys.Lett.* B697 (2011), pp. 107–115. DOI: 10.1016/j.physletb.2011.01.042. arXiv: 1011.4817 [hep-ex].

[184] S. Friot, D. Greynat, and E. De Rafael. "Rare kaon decays revisited". *Phys.Lett.* B595 (2004), pp. 301–308. DOI: 10.1016/j.physletb.2004.05.069. arXiv: hep-ph/0404136 [hep-ph].

[185] A. Dubnickova et al. "Kaon decay probe of the weak static interaction". *Phys.Part.Nucl.Lett.* 5 (2008), pp. 76–84. DOI: 10.1007/s11497-008-2003-9. arXiv: hep-ph/0611175 [hep-ph].

[186] E. Goudzovski. private communication.

[187] A. Artamonov et al. "Study of the decay $K^{+} \to \pi^{+}\nu\bar{\nu}$ in the momentum region 140 < P(pi) < 199-MeV/c". *Phys.Rev.* D79 (2009), p. 092004. DOI: 10.1103/PhysRevD.79.092004. arXiv: 0903.0030 [hep-ex].

[188] S. Adler et al. "Measurement of the $K^{+} \to \pi^{+}\nu\nu$ branching ratio". *Phys.Rev.* D77 (2008), p. 052003. DOI: 10.1103/PhysRevD.77.052003. arXiv: 0709.1000 [hep-ex].

[189] R Aaij et al. "Differential branching fraction and angular analysis of the $B^{+} \to K^{+}\mu^{+}\mu^{-}$ decay". *JHEP* 1302 (2013), p. 105. DOI: 10.1007/JHEP02(2013)105. arXiv: 1209.4284 [hep-ex].

[190] A. Ali et al. “Improved model independent analysis of semileptonic and radiative rare B decays”. *Phys.Rev.* D66 (2002), p. 034002. DOI: 10.1103/PhysRevD.66.034002. arXiv: hep-ph/0112300 [hep-ph].

[191] J.-T. Wei et al. “Measurement of the Differential Branching Fraction and Forward-Backword Asymmetry for $B \to K^{(*)}l^+l^-$”. *Phys.Rev.Lett.* 103 (2009), p. 171801. DOI: 10.1103/PhysRevLett.103.171801. arXiv: 0904.0770 [hep-ex].

[192] B. Aubert et al. “Direct CP, Lepton Flavor and Isospin Asymmetries in the Decays $B \to K^{(*)}\ell^+\ell^-$”. *Phys.Rev.Lett.* 102 (2009), p. 091803. DOI: 10.1103/PhysRevLett.102.091803. arXiv: 0807.4119 [hep-ex].

[193] K.-F. Chen et al. “Search for $B \to h(*)\nu\bar{\nu}$ decays at Belle”. *Phys.Rev.Lett.* 99 (2007), p. 221802. DOI: 10.1103/PhysRevLett.99.221802. arXiv: 0707.0138 [hep-ex].

[194] P. del Amo Sanchez et al. “Search for the Rare Decay $B \to K\nu n\bar{u}$”. *Phys.Rev.* D82 (2010), p. 112002. DOI: 10.1103/PhysRevD.82.112002. arXiv: 1009.1529 [hep-ex].

[195] H. Hyun et al. “Search for a Low Mass Particle Decaying into $\mu^+\mu^-$ in $B^0 \to K^{*0}X$ and $B^0 \to \rho^0 X$ at Belle”. *Phys.Rev.Lett.* 105 (2010), p. 091801. DOI: 10.1103/PhysRevLett.105.091801. arXiv: 1005.1450 [hep-ex].

[196] M. Freytsis, Z. Ligeti, and J. Thaler. “Constraining the Axion Portal with $B \to Kl^+l^-$”. *Phys.Rev.* D81 (2010), p. 034001. DOI: 10.1103/PhysRevD.81.034001. arXiv: 0911.5355 [hep-ph].

[197] K. Schmidt-Hoberg, F. Staub, and M. W. Winkler. “Constraints on light mediators: confronting dark matter searches with B physics”. *Phys.Lett.* B727 (2013), pp. 506–510. DOI: 10.1016/j.physletb.2013.11.015. arXiv: 1310.6752 [hep-ph].

[198] J. Lees et al. “Search for Long-Lived Particles in e^+e^- Collisions” (2015). arXiv: 1502.02580 [hep-ex].

[199] R. Aaij et al. “Search for hidden-sector bosons in $B^0 \to K^{*0}\mu^+\mu^-$ decays” (2015). arXiv: 1508.04094 [hep-ex].

[200] J. Lees et al. “Search for di-muon decays of a low-mass Higgs boson in radiative decays of the $\Upsilon(1S)$”. *Phys.Rev.* D87.3 (2013), p. 031102. DOI: 10.1103/PhysRevD.87.031102. arXiv: 1210.0287 [hep-ex].

[201] J. Lees et al. “Search for a Low-Mass Scalar Higgs Boson Decaying to a Tau Pair in Single-Photon Decays of $\Upsilon(1S)$” (2012). arXiv: 1210.5669 [hep-ex].

[202] J. Lees et al. "Search for a light Higgs boson decaying to two gluons or ss-bar in the radiative decays of $\Upsilon(1S)$". *Phys.Rev.* D88 (2013), p. 031701. DOI: 10.1103/PhysRevD.88.031701. arXiv: 1307.5306 [hep-ex].

[203] P. del Amo Sanchez et al. "Search for Production of Invisible Final States in Single-Photon Decays of $\Upsilon(1S)$". *Phys.Rev.Lett.* 107 (2011), p. 021804. DOI: 10.1103/PhysRevLett.107.021804. arXiv: 1007.4646 [hep-ex].

[204] D. McKeen. "Constraining Light Bosons with Radiative Upsilon(1S) Decays". *Phys.Rev.* D79 (2009), p. 015007. DOI: 10.1103/PhysRevD.79.015007. arXiv: 0809.4787 [hep-ph].

[205] F. Bergsma et al. "SEARCH FOR AXION LIKE PARTICLE PRODUCTION IN 400-GeV PROTON-COPPER INTERACTIONS". *Phys.Lett.* B157 (1985), p. 458. DOI: 10.1016/0370-2693(85)90400-9.

[206] A. M. Cooper-Sarkar et al. "Search for Heavy Neutrino Decays in the BEBC Beam Dump Experiment". *Phys.Lett.* B160 (1985), p. 207. DOI: 10.1016/0370-2693(85)91493-5.

[207] J. Badier et al. "Mass and Lifetime Limits on New Longlived Particles in 300-GeV/$c\pi^-$ Interactions". *Z.Phys.* C31 (1986), p. 21. DOI: 10.1007/BF01559588.

[208] G. Bernardi et al. "FURTHER LIMITS ON HEAVY NEUTRINO COUPLINGS". *Phys.Lett.* B203 (1988), p. 332. DOI: 10.1016/0370-2693(88)90563-1.

[209] E. Gallas et al. "Search for neutral weakly interacting massive particles in the Fermilab Tevatron wideband neutrino beam". *Phys. Rev. D* 52 (1 1995), pp. 6–14. DOI: 10.1103/PhysRevD.52.6.

[210] J. Adams et al. "Search for light gluinos via the spontaneous appearance of $\pi^+\pi^-$ pairs with an 800-GeV/c proton beam at Fermilab". *Phys.Rev.Lett.* 79 (1997), pp. 4083–4087. DOI: 10.1103/PhysRevLett.79.4083. arXiv: hep-ex/9709028 [hep-ex].

[211] B. Batell, M. Pospelov, and A. Ritz. "Exploring Portals to a Hidden Sector Through Fixed Targets". *Phys.Rev.* D80 (2009), p. 095024. DOI: 10.1103/PhysRevD.80.095024. arXiv: 0906.5614 [hep-ph].

[212] R. Essig et al. "Discovering New Light States at Neutrino Experiments". *Phys.Rev.* D82 (2010), p. 113008. DOI: 10.1103/PhysRevD.82.113008. arXiv: 1008.0636 [hep-ph].

[213] P. deNiverville, M. Pospelov, and A. Ritz. "Observing a light dark matter beam with neutrino experiments". *Phys.Rev.* D84 (2011), p. 075020. DOI: 10.1103/PhysRevD.84.075020. arXiv: 1107.4580 [hep-ph].

[214] P. deNiverville, D. McKeen, and A. Ritz. "Signatures of sub-GeV dark matter beams at neutrino experiments". *Phys.Rev.* D86 (2012), p. 035022. DOI: 10.1103/PhysRevD.86.035022. arXiv: 1205.3499 [hep-ph].

[215] C. Lourenco and H. Wohri. "Heavy flavour hadro-production from fixed-target to collider energies". *Phys.Rept.* 433 (2006), pp. 127–180. DOI: 10.1016/j.physrep.2006.05.005. arXiv: hep-ph/0609101 [hep-ph].

[216] M. Anelli et al. "A facility to Search for Hidden Particles (SHiP) at the CERN SPS" (2015). arXiv: 1504.04956 [physics.ins-det].

[217] S. Alekhin et al. "A facility to Search for Hidden Particles at the CERN SPS: the SHiP physics case" (2015). arXiv: 1504.04855 [hep-ph].

[218] J. Pumplin et al. "New generation of parton distributions with uncertainties from global QCD analysis". *JHEP* 0207 (2002), p. 012. arXiv: hep-ph/0201195 [hep-ph].

[219] H. Lai et al. "Global QCD analysis of parton structure of the nucleon: CTEQ5 parton distributions". *Eur.Phys.J.* C12 (2000), pp. 375–392. DOI: 10.1007/s100529900196. arXiv: hep-ph/9903282 [hep-ph].

[220] *A Search for Light CP-Odd Higgs Bosons Decaying to $\mu^+\mu^-$ in ATLAS*. Tech. rep. ATLAS-CONF-2011-020, ATLAS-COM-CONF-2011-036. Geneva: CERN, 2011.

[221] S. Chatrchyan et al. "Search for a light pseudoscalar Higgs boson in the dimuon decay channel in pp collisions at $\sqrt{s} = 7$ TeV". *Phys.Rev.Lett.* 109 (2012), p. 121801. DOI: 10.1103/PhysRevLett.109.121801. arXiv: 1206.6326 [hep-ex].

[222] S. Chatrchyan et al. "Search for Light Resonances Decaying into Pairs of Muons as a Signal of New Physics". *JHEP* 1107 (2011), p. 098. DOI: 10.1007/JHEP07(2011)098. arXiv: 1106.2375 [hep-ex].

[223] *Measurement of the production cross section of prompt J/ψ mesons in association with a $W^\pm$ boson in pp collisions at $\sqrt{s} = 7$ TeV*. Tech. rep. ATLAS-CONF-2013-042. Geneva: CERN, 2013.

[224] M. Cacciari et al. "Theoretical predictions for charm and bottom production at the LHC". *JHEP* 1210 (2012), p. 137. DOI: 10.1007/JHEP10(2012)137. arXiv: 1205.6344 [hep-ph].

[225] G. Aad et al. "Measurement of the differential cross-section of B^+ meson production in pp collisions at $\sqrt{s}$ = 7 TeV at ATLAS" (2013). arXiv: 1307.0126 [hep-ex].

[226] R Aaij et al. "Measurement of B meson production cross-sections in proton-proton collisions at $\sqrt{s}$ = 7 TeV". *JHEP* 1308 (2013), p. 117. DOI: 10.1007/JHEP08(2013)117. arXiv: 1306.3663 [hep-ex].

[227] G. Aad et al. “Search for displaced muonic lepton jets from light Higgs boson decay in proton-proton collisions at $\sqrt{s} = 7$ TeV with the ATLAS detector”. *Phys.Lett.* B721 (2013), pp. 32–50. DOI: 10.1016/j.physletb.2013.02.058. arXiv: 1210.0435 [hep-ex].

[228] *Muon Reconstruction Performance*. Tech. rep. ATLAS-CONF-2010-064. Geneva: CERN, 2010.

[229] G. Aad et al. “Search for Higgs bosons decaying to aa in the $\mu\mu\tau\tau$ final state in pp collisions at $\sqrt{s} = 8$ TeV with the ATLAS experiment”. *Phys. Rev.* D92.5 (2015), p. 052002. DOI: 10.1103/PhysRevD.92.052002. arXiv: 1505.01609 [hep-ex].

[230] G. Aad et al. “Search for new light gauge bosons in Higgs boson decays to four-lepton final states in pp collisions at $\sqrt{s} = 8$ TeV with the ATLAS detector at the LHC”. *Phys. Rev.* D92.9 (2015), p. 092001. DOI: 10.1103/PhysRevD.92.092001. arXiv: 1505.07645 [hep-ex].

[231] G. Aad et al. “A search for prompt lepton-jets in pp collisions at $\sqrt{s} = 8$ TeV with the ATLAS detector”. *JHEP* 02 (2016), p. 062. DOI: 10.1007/JHEP02(2016)062. arXiv: 1511.05542 [hep-ex].

[232] V. Khachatryan et al. “A search for pair production of new light bosons decaying into muons”. *Phys. Lett.* B752 (2016), pp. 146–168. DOI: 10.1016/j.physletb.2015.10.067. arXiv: 1506.00424 [hep-ex].

[233] M. J. Strassler and K. M. Zurek. “Discovering the Higgs through highly-displaced vertices”. *Phys.Lett.* B661 (2008), pp. 263–267. DOI: 10.1016/j.physletb.2008.02.008. arXiv: hep-ph/0605193 [hep-ph].

[234] N. Arkani-Hamed and N. Weiner. “LHC Signals for a SuperUnified Theory of Dark Matter”. *JHEP* 0812 (2008), p. 104. DOI: 10.1088/1126-6708/2008/12/104. arXiv: 0810.0714 [hep-ph].

[235] G. Aad et al. “Search for a light Higgs boson decaying to long-lived weakly-interacting particles in proton-proton collisions at $\sqrt{s} = 7$ TeV with the ATLAS detector”. *Phys.Rev.Lett.* 108 (2012), p. 251801. DOI: 10.1103/PhysRevLett.108.251801. arXiv: 1203.1303 [hep-ex].

[236] *Search for pair produced long-lived neutral particles decaying in the ATLAS hadronic calorimeter in pp collisions at $\sqrt{s} = 8$ TeV*. Tech. rep. ATLAS-CONF-2014-041. Geneva: CERN, 2014.

[237] G. Aad et al. “Search for pair-produced long-lived neutral particles decaying in the ATLAS hadronic calorimeter in pp collisions at $\sqrt{s} = 8$ TeV” (2015). arXiv: 1501.04020 [hep-ex].

[238] G. Aad et al. “Search for long-lived, weakly interacting particles that decay to displaced hadronic jets in proton-proton collisions at $\sqrt{s} = 8$ TeV with the ATLAS detector” (2015). arXiv: 1504.03634 [hep-ex].

[239] G. Aad et al. "Search for long-lived neutral particles decaying into lepton jets in proton-proton collisions at $\sqrt{s} = 8$ TeV with the ATLAS detector". *JHEP* 1411 (2014), p. 088. DOI: 10.1007/JHEP11(2014)088. arXiv: 1409.0746 [hep-ex].

[240] S. Chatrchyan et al. "Search in leptonic channels for heavy resonances decaying to long-lived neutral particles". *JHEP* 1302 (2013), p. 085. DOI: 10.1007/JHEP02(2013)085. arXiv: 1211.2472 [hep-ex].

[241] V. Khachatryan et al. "Search for long-lived neutral particles decaying to quark-antiquark pairs in proton-proton collisions at sqrt(s) = 8 TeV". *Phys.Rev.* D91 (2015), p. 012007. DOI: 10.1103/PhysRevD.91.012007. arXiv: 1411.6530 [hep-ex].

[242] V. Khachatryan et al. "Search for long-lived particles that decay into final states containing two electrons or two muons in proton-proton collisions at $\sqrt{s}$ = 8 TeV" (2014). arXiv: 1411.6977 [hep-ex].

[243] *Search for Higgs-like bosons decaying into long-lived exotic particles*. Tech. rep. LHCb-CONF-2012-014. Geneva: CERN, 2012.

[244] R. Aaij et al. "Search for long-lived particles decaying to jet pairs" (2014). arXiv: 1412.3021 [hep-ex].

[245] S. Gopalakrishna, S. Jung, and J. D. Wells. "Higgs boson decays to four fermions through an abelian hidden sector". *Phys.Rev.* D78 (2008), p. 055002. DOI: 10.1103/PhysRevD.78.055002. arXiv: 0801.3456 [hep-ph].

[246] C.-F. Chang, E. Ma, and T.-C. Yuan. "Multilepton Higgs Decays through the Dark Portal". *JHEP* 1403 (2014), p. 054. DOI: 10.1007/JHEP03(2014)054. arXiv: 1308.6071 [hep-ph].

[247] D. Curtin et al. "Exotic decays of the 125 GeV Higgs boson". *Phys.Rev.* D90.7 (2014), p. 075004. DOI: 10.1103/PhysRevD.90.075004. arXiv: 1312.4992 [hep-ph].

[248] B. Batell, M. Pospelov, and A. Ritz. "Probing a Secluded U(1) at B-factories". *Phys.Rev.* D79 (2009), p. 115008. DOI: 10.1103/PhysRevD.79.115008. arXiv: 0903.0363 [hep-ph].

[249] D. Curtin et al. "Illuminating Dark Photons with High-Energy Colliders" (2014). arXiv: 1412.0018 [hep-ph].

[250] M. L. Graesser. "Broadening the Higgs boson with right-handed neutrinos and a higher dimension operator at the electroweak scale". *Phys.Rev.* D76 (2007), p. 075006. DOI: 10.1103/PhysRevD.76.075006. arXiv: 0704.0438 [hep-ph].

[251] M. L. Graesser. "Experimental Constraints on Higgs Boson Decays to TeV-scale Right-Handed Neutrinos" (2007). arXiv: 0705.2190 [hep-ph].

[252] D. G. Cerdeño, V. Martín-Lozano, and O. Seto. "Displaced vertices and long-lived charged particles in the NMSSM with right-handed sneutrinos". *JHEP* 1405 (2014), p. 035. DOI: 10.1007/JHEP05(2014)035. arXiv: 1311.7260 [hep-ph].

[253] A. Maiezza, M. Nemevsek, and F. Nesti. "Lepton Number Violation in Higgs Decay" (2015). arXiv: 1503.06834 [hep-ph].

[254] L. M. Carpenter, D. E. Kaplan, and E.-J. Rhee. "Reduced fine-tuning in supersymmetry with R-parity violation". *Phys.Rev.Lett.* 99 (2007), p. 211801. DOI: 10.1103/PhysRevLett.99.211801. arXiv: hep-ph/0607204 [hep-ph].

[255] D. E. Kaplan and K. Rehermann. "Proposal for Higgs and superpartner searches at the LHCb experiment". *JHEP* 0710 (2007), p. 056. DOI: 10.1088/1126-6708/2007/10/056. arXiv: 0705.3426 [hep-ph].

[256] D. Aristizabal Sierra et al. "Novel Higgs decay signals in R-parity violating models". *Phys.Rev.* D78 (2008), p. 015015. DOI: 10.1103/PhysRevD.78.015015. arXiv: 0804.1907 [hep-ph].

[257] P. W. Graham et al. "Displaced Supersymmetry". *JHEP* 1207 (2012), p. 149. DOI: 10.1007/JHEP07(2012)149. arXiv: 1204.6038 [hep-ph].

[258] P. Ghosh et al. "Probing the $\mu\nu$SSM with light scalars, pseudoscalars and neutralinos from the decay of a SM-like Higgs boson at the LHC" (2014). arXiv: 1410.2070 [hep-ph].

[259] Y. F. Chan et al. "LHC Signatures of a Minimal Supersymmetric Hidden Valley". *JHEP* 1205 (2012), p. 155. DOI: 10.1007/JHEP05(2012)155. arXiv: 1112.2705 [hep-ph].

[260] A. Falkowski et al. "Hidden Higgs Decaying to Lepton Jets". *JHEP* 1005 (2010), p. 077. DOI: 10.1007/JHEP05(2010)077. arXiv: 1002.2952 [hep-ph].

[261] A. Falkowski et al. "Discovering Higgs Decays to Lepton Jets at Hadron Colliders". *Phys.Rev.Lett.* 105 (2010), p. 241801. DOI: 10.1103/PhysRevLett.105.241801. arXiv: 1007.3496 [hep-ph].

[262] M. J. Strassler and K. M. Zurek. "Echoes of a hidden valley at hadron colliders". *Phys.Lett.* B651 (2007), pp. 374–379. DOI: 10.1016/j.physletb.2007.06.055. arXiv: hep-ph/0604261 [hep-ph].

[263] J. E. Juknevich. "Pure-glue hidden valleys through the Higgs portal". *JHEP* 08 (2010), p. 121. DOI: 10.1007/JHEP08(2010)121. arXiv: 0911.5616 [hep-ph].

[264] M. J. Strassler. "Possible effects of a hidden valley on supersymmetric phenomenology" (2006). arXiv: hep-ph/0607160 [hep-ph].

[265] T. Han et al. "Phenomenology of hidden valleys at hadron colliders". *JHEP* 0807 (2008), p. 008. DOI: 10.1088/1126-6708/2008/07/008. arXiv: 0712.2041 [hep-ph].

[266] P. Schwaller, D. Stolarski, and A. Weiler. "Emerging Jets" (2015). arXiv: 1502.05409 [hep-ph].

[267] N. Craig et al. "Naturalness in the Dark at the LHC" (2015). arXiv: 1501.05310 [hep-ph].

[268] D. Curtin and C. B. Verhaaren. "Discovering Uncolored Naturalness in Exotic Higgs Decays" (2015). arXiv: 1506.06141 [hep-ph].

[269] C. Csaki et al. "Searching for Displaced Higgs Decays" (2015). arXiv: 1508.01522 [hep-ph].

[270] Y. Cui and B. Shuve. "Probing Baryogenesis with Displaced Vertices at the LHC". *JHEP* 1502 (2015), p. 049. DOI: 10.1007/JHEP02(2015)049. arXiv: 1409.6729 [hep-ph].

[271] E. Conte, B. Fuks, and G. Serret. "MadAnalysis 5, A User-Friendly Framework for Collider Phenomenology". *Comput.Phys.Commun.* 184 (2013), pp. 222–256. DOI: 10.1016/j.cpc.2012.09.009. arXiv: 1206.1599 [hep-ph].

[272] Z. Liu and B. Tweedie. "The Fate of Long-Lived Superparticles with Hadronic Decays after LHC Run 1" (2015). arXiv: 1503.05923 [hep-ph].

[273] G. Aad et al. *Triggering on Long-Lived Neutral Particles in the ATLAS Detector*. Tech. rep. 2009.

[274] G. Aad et al. "Triggers for displaced decays of long-lived neutral particles in the ATLAS detector". *JINST* 8 (2013), P07015. DOI: 10.1088/1748-0221/8/07/P07015. arXiv: 1305.2284 [hep-ex].

[275] A. Strumia. "Naturalness of supersymmetric models". *Proceedings, 34th Rencontres de Moriond, 99 electroweak interactions and unified theories*. 2001, pp. 441–446. arXiv: hep-ph/9904247 [hep-ph].

[276] B. C. Allanach. "Naturalness priors and fits to the constrained minimal supersymmetric standard model". *Phys. Lett.* B635 (2006), pp. 123–130. DOI: 10.1016/j.physletb.2006.02.052. arXiv: hep-ph/0601089 [hep-ph].

[277] B. C. Allanach et al. "Natural priors, CMSSM fits and LHC weather forecasts". *JHEP* 08 (2007), p. 023. DOI: 10.1088/1126-6708/2007/08/023. arXiv: 0705.0487 [hep-ph].

[278] P. Athron and D. J. Miller. "A New Measure of Fine Tuning". *Phys. Rev.* D76 (2007), p. 075010. DOI: 10.1103/PhysRevD.76.075010. arXiv: 0705.2241 [hep-ph].

[279] M. E. Cabrera, J. A. Casas, and R. Ruiz de Austri. “Bayesian approach and Naturalness in MSSM analyses for the LHC”. *JHEP* 03 (2009), p. 075. DOI: 10.1088/1126-6708/2009/03/075. arXiv: 0812.0536 [hep-ph].

[280] S. S. AbdusSalam et al. “Fitting the Phenomenological MSSM”. *Phys. Rev.* D81 (2010), p. 095012. DOI: 10.1103/PhysRevD.81.095012. arXiv: 0904.2548 [hep-ph].

[281] M. E. Cabrera, J. A. Casas, and R. Ruiz d Austri. “MSSM Forecast for the LHC”. *JHEP* 05 (2010), p. 043. DOI: 10.1007/JHEP05(2010)043. arXiv: 0911.4686 [hep-ph].

[282] D. M. Ghilencea, H. M. Lee, and M. Park. “Tuning supersymmetric models at the LHC: A comparative analysis at two-loop level”. *JHEP* 07 (2012), p. 046. DOI: 10.1007/JHEP07(2012)046. arXiv: 1203.0569 [hep-ph].

[283] S. Fichet. “Quantified naturalness from Bayesian statistics”. *Phys. Rev.* D86 (2012), p. 125029. DOI: 10.1103/PhysRevD.86.125029. arXiv: 1204.4940 [hep-ph].

[284] D. Kim et al. “Bayesian naturalness of the CMSSM and CNMSSM”. *Phys. Rev.* D90.5 (2014), p. 055008. DOI: 10.1103/PhysRevD.90.055008. arXiv: 1312.4150 [hep-ph].

[285] A. Fowlie. “CMSSM, naturalness and the “fine-tuning price” of the Very Large Hadron Collider”. *Phys. Rev.* D90 (2014), p. 015010. DOI: 10.1103/PhysRevD.90.015010. arXiv: 1403.3407 [hep-ph].

[286] A. Fowlie. “Is the CNMSSM more credible than the CMSSM?” *Eur. Phys. J.* C74.10 (2014), p. 3105. DOI: 10.1140/epjc/s10052-014-3105-y. arXiv: 1407.7534 [hep-ph].

[287] A. Fowlie et al. “Naturalness of the relaxion mechanism” (2016). arXiv: 1602.03889 [hep-ph].

[288] R. Barbieri and G. Giudice. “Upper Bounds on Supersymmetric Particle Masses”. *Nucl.Phys.* B306 (1988), p. 63. DOI: 10.1016/0550-3213(88)90171-X.

[289] J. Ellis et al. “Observables in Low-Energy Superstring Models”. *Mod.Phys.Lett.* A1 (1986), p. 57. DOI: 10.1142/S0217732386000105.

[290] C. Wetterich. “Fine Tuning Problem and the Renormalization Group”. *Phys. Lett.* B140 (1984), pp. 215–222. DOI: 10.1016/0370-2693(84)90923-7.

[291] W. Bardeen. “On naturalness in the standard model”. *Conf.Proc.* FERMILAB-CONF-95-391-T, C95-08-27.3 (1995).

[292] H. Aoki and S. Iso. "Revisiting the Naturalness Problem – Who is afraid of quadratic divergences? –". *Phys. Rev.* D86 (2012), p. 013001. DOI: 10.1103/PhysRevD.86.013001. arXiv: 1201.0857 [hep-ph].

[293] M. Farina, D. Pappadopulo, and A. Strumia. "A modified naturalness principle and its experimental tests". *JHEP* 08 (2013), p. 022. DOI: 10.1007/JHEP08(2013)022. arXiv: 1303.7244 [hep-ph].

[294] M. Heikinheimo et al. "Physical Naturalness and Dynamical Breaking of Classical Scale Invariance". *Mod. Phys. Lett.* A29 (2014), p. 1450077. DOI: 10.1142/S0217732314500771. arXiv: 1304.7006 [hep-ph].

[295] L. Bian. "Renormalization group equation, the naturalness problem, and the understanding of the Higgs mass term". *Phys. Rev.* D88.5 (2013), p. 056022. DOI: 10.1103/PhysRevD.88.056022. arXiv: 1308.2783 [hep-ph].

[296] A. de Gouvea, D. Hernandez, and T. M. P. Tait. "Criteria for Natural Hierarchies". *Phys. Rev.* D89.11 (2014), p. 115005. DOI: 10.1103/PhysRevD.89.115005. arXiv: 1402.2658 [hep-ph].

[297] A. Kobakhidze and K. L. McDonald. "Comments on the Hierarchy Problem in Effective Theories". *JHEP* 07 (2014), p. 155. DOI: 10.1007/JHEP07(2014)155. arXiv: 1404.5823 [hep-ph].

[298] M. Fabbrichesi and A. Urbano. "Naturalness redux: The case of the neutrino seesaw mechanism". *Phys. Rev.* D92 (2015), p. 015028. DOI: 10.1103/PhysRevD.92.015028. arXiv: 1504.05403 [hep-ph].

[299] K. Fujikawa. "Dimensional regularization is generic". *Conference on New Physics at the Large Hadron Collider Singapore, Singapore, February 29-March 4, 2016*. 2016. arXiv: 1605.05813 [hep-th].

[300] H. Jeffreys. *The Theory of Probability*. Oxford Classic Texts in the Physical Sciences. 1939. ISBN: 9780198503682.

[301] M. J. G. Veltman. "The Infrared - Ultraviolet Connection". *Acta Phys. Polon.* B12 (1981), p. 437.

[302] F. Vissani. "Do experiments suggest a hierarchy problem?" *Phys.Rev.* D57 (1998), pp. 7027–7030. DOI: 10.1103/PhysRevD.57.7027. arXiv: hep-ph/9709409 [hep-ph].

[303] F. Lyonnet et al. "PyR@TE: Renormalization Group Equations for General Gauge Theories". *Comput. Phys. Commun.* 185 (2014), pp. 1130–1152. DOI: 10.1016/j.cpc.2013.12.002. arXiv: 1309.7030 [hep-ph].

[304] M. Steinhauser. "MATAD: A Program package for the computation of MAssive TADpoles". *Comput. Phys. Commun.* 134 (2001), pp. 335–364. DOI: 10.1016/S0010-4655(00)00204-6. arXiv: hep-ph/0009029 [hep-ph].

[305] K. S. Babu and C. N. Leung. "Classification of effective neutrino mass operators". *Nucl. Phys.* B619 (2001), pp. 667–689. DOI: 10.1016/S0550-3213(01)00504-1. eprint: hep-ph/0106054.

[306] A. de Gouvea and J. Jenkins. "A Survey of Lepton Number Violation Via Effective Operators". *Phys.Rev.* D77 (2008), p. 013008. DOI: 10.1103/PhysRevD.77.013008. arXiv: 0708.1344 [hep-ph].

[307] P. W. Angel, N. L. Rodd, and R. R. Volkas. "Origin of neutrino masses at the LHC: $\Delta L = 2$ effective operators and their ultraviolet completions". *Phys.Rev.* D87.7 (2013), p. 073007. DOI: 10.1103/PhysRevD.87.073007. arXiv: 1212.6111 [hep-ph].

[308] F. Bonnet et al. "Neutrino masses from higher than d=5 effective operators". *JHEP* 0910 (2009), p. 076. DOI: 10.1088/1126-6708/2009/10/076. arXiv: 0907.3143 [hep-ph].

[309] M. B. Krauss et al. "Neutrino Mass from a d=7 Effective Operator in an SU(5) SUSY-GUT Framework" (Jan. 2013). eprint: 1301.4221.

[310] K. Babu and J. Julio. "Two-Loop Neutrino Mass Generation through Leptoquarks". *Nucl.Phys.* B841 (2010), pp. 130–156. DOI: 10.1016/j.nuclphysb.2010.07.022. arXiv: 1006.1092 [hep-ph].

[311] K. Babu and J. Julio. "Radiative Neutrino Mass Generation through Vector-like Quarks". *Phys.Rev.* D85 (Dec. 2012), p. 073005. DOI: 10.1103/PhysRevD.85.073005. eprint: 1112.5452.

[312] K. Babu, S. Nandi, and Z. Tavartkiladze. "New Mechanism for Neutrino Mass Generation and Triply Charged Higgs Bosons at the LHC". *Phys.Rev.* D80 (2009), p. 071702. DOI: 10.1103/PhysRevD.80.071702. arXiv: 0905.2710 [hep-ph].

[313] P. W. Angel et al. "Testable two-loop radiative neutrino mass model based on an $LLQd^cQd^c$ effective operator". *JHEP* 1310 (2013), p. 118. DOI: 10.1007/JHEP10(2013)118. arXiv: 1308.0463 [hep-ph].

[314] M. Gonzalez-Garcia et al. "Global fit to three neutrino mixing: critical look at present precision". *JHEP* 1212 (2012), p. 123. DOI: 10.1007/JHEP12(2012)123. arXiv: 1209.3023 [hep-ph].

[315] D. Forero, M. Tortola, and J. Valle. "Global status of neutrino oscillation parameters after Neutrino-2012". *Phys.Rev.* D86 (2012), p. 073012. DOI: 10.1103/PhysRevD.86.073012. arXiv: 1205.4018 [hep-ph].

[316] G. Fogli et al. "Global analysis of neutrino masses, mixings and phases: entering the era of leptonic CP violation searches". *Phys.Rev.* D86 (2012), p. 013012. DOI: 10.1103/PhysRevD.86.013012. arXiv: 1205.5254 [hep-ph].

[317] J. Adam et al. "New constraint on the existence of the $\mu^+ \to e^+\gamma$ decay". *Phys.Rev.Lett.* 110.20 (2013), p. 201801. DOI: 10.1103/PhysRevLett.110.201801. arXiv: 1303.0754 [hep-ex].

[318] J. Beringer *et. al.* "Review of Particle Physics". *Phys. Rev. D* 86 (1 2012), p. 010001. DOI: 10.1103/PhysRevD.86.010001.

[319] R. Carey et al. "Proposal to search for $\mu^- N \to e^- N$ with a single event sensitivity below 10^{-16}" (2008).

[320] R. K. Kutschke. "The Mu2e Experiment at Fermilab" (2011). arXiv: 1112.0242 [hep-ex].

[321] Y. Cui et al. "Conceptual design report for experimental search for lepton flavor violating mu- - e- conversion at sensitivity of 10**(-16) with a slow-extracted bunched proton beam (COMET)" (2009).

[322] CMS Collaboration. *Search for Vector-Like b′ Pair Production with Multilepton Final States in pp collisions at sqrt(s) = 8 TeV*. Tech. rep. CMS-PAS-B2G-13-003. 2013.

[323] M. Kramer et al. "Pair production of scalar leptoquarks at the CERN LHC". *Phys.Rev.* D71 (2005), p. 057503. DOI: 10.1103/PhysRevD.71.057503. arXiv: hep-ph/0411038 [hep-ph].

[324] G. Aad et al. "Search for direct third-generation squark pair production in final states with missing transverse momentum and two b-jets in $\sqrt{s} =$ 8 TeV pp collisions with the ATLAS detector". *JHEP* 1310 (2013), p. 189. DOI: 10.1007/JHEP10(2013)189. arXiv: 1308.2631 [hep-ex].

[325] CMS Collaboration. *Search for direct production of bottom squark pairs*. Tech. rep. CMS-PAS-SUS-13-018. Geneva: CERN, 2014.

[326] CMS Collaboration. *Search for Third Generation Scalar Leptoquarks Decaying to Top Quark - Tau Lepton Pairs in pp Collisions*. Tech. rep. CMS-PAS-EXO-12-030. Geneva: CERN, 2014.

[327] G. Aad et al. "Search for supersymmetry at $\sqrt{s}$=8 TeV in final states with jets and two same-sign leptons or three leptons with the ATLAS detector" (2014). arXiv: 1404.2500 [hep-ex].

[328] G. Aad et al. "Search for supersymmetry in events with four or more leptons in $\sqrt{s}$ = 8 TeV pp collisions with the ATLAS detector" (2014). arXiv: 1405.5086 [hep-ex].

[329] ATLAS Collaboration. *Search for direct top squark pair production in final states with one isolated lepton, jets, and missing transverse momentum in $sqrts = 8$,TeV pp collisions using 21 fb^{-1} of ATLAS data*. Tech. rep. ATLAS-CONF-2013-037. Geneva: CERN, 2013.

[330] G. Aad et al. "Search for direct top-squark pair production in final states with two leptons in pp collisions at $\sqrt{s}$=8 TeV with the ATLAS detector" (2014). arXiv: 1403.4853 [hep-ex].

[331] M. Cacciari et al. "Top-pair production at hadron colliders with next-to-next-to-leading logarithmic soft-gluon resummation". *Phys.Lett.* B710 (2012), pp. 612–622. DOI: 10.1016/j.physletb.2012.03.013. arXiv: 1111.5869 [hep-ph].

[332] P. Bernreuther, M. Czakon, and A. Mitov. "Percent Level Precision Physics at the Tevatron: First Genuine NNLO QCD Corrections to $q\bar{q} \to t\bar{t} + X$". *Phys.Rev.Lett.* 109 (2012), p. 132001. DOI: 10.1103/PhysRevLett.109.132001. arXiv: 1204.5201 [hep-ph].

[333] M. Czakon and A. Mitov. "NNLO corrections to top-pair production at hadron colliders: the all-fermionic scattering channels". *JHEP* 1212 (2012), p. 054. DOI: 10.1007/JHEP12(2012)054. arXiv: 1207.0236 [hep-ph].

[334] M. Czakon and A. Mitov. "NNLO corrections to top pair production at hadron colliders: the quark-gluon reaction". *JHEP* 1301 (2013), p. 080. DOI: 10.1007/JHEP01(2013)080. arXiv: 1210.6832 [hep-ph].

[335] M. Czakon, P. Fiedler, and A. Mitov. "Total Top-Quark Pair-Production Cross Section at Hadron Colliders Through $O(\alpha_S^4)$". *Phys.Rev.Lett.* 110.25 (2013), p. 252004. DOI: 10.1103/PhysRevLett.110.252004. arXiv: 1303.6254 [hep-ph].

[336] M. Czakon and A. Mitov. "Top++: A Program for the Calculation of the Top-Pair Cross-Section at Hadron Colliders" (2011). arXiv: 1112.5675 [hep-ph].

[337] M. Cacciari, G. P. Salam, and G. Soyez. "FastJet User Manual". *Eur.Phys.J.* C72 (2012), p. 1896. DOI: 10.1140/epjc/s10052-012-1896-2. arXiv: 1111.6097 [hep-ph].

[338] M. Cacciari, G. P. Salam, and G. Soyez. "The Anti-k(t) jet clustering algorithm". *JHEP* 0804 (2008), p. 063. DOI: 10.1088/1126-6708/2008/04/063. arXiv: 0802.1189 [hep-ph].

[339] M. Cacciari and G. P. Salam. "Pileup subtraction using jet areas". *Phys.Lett.* B659 (2008), pp. 119–126. DOI: 10.1016/j.physletb.2007.09.077. arXiv: 0707.1378 [hep-ph].

[340] M. Cacciari, G. P. Salam, and G. Soyez. "The Catchment Area of Jets". *JHEP* 0804 (2008), p. 005. DOI: 10.1088/1126-6708/2008/04/005. arXiv: 0802.1188 [hep-ph].

[341] C. Lester and D. Summers. "Measuring masses of semiinvisibly decaying particles pair produced at hadron colliders". *Phys.Lett.* B463 (1999), pp. 99–103. DOI: 10.1016/S0370-2693(99)00945-4. arXiv: hep-ph/9906349 [hep-ph].

[342] A. Barr, C. Lester, and P. Stephens. "m(T2): The Truth behind the glamour". *J.Phys.* G29 (2003), pp. 2343–2363. DOI: 10.1088/0954-3899/29/10/304. arXiv: hep-ph/0304226 [hep-ph].

[343] H.-C. Cheng and Z. Han. "Minimal Kinematic Constraints and m(T2)". *JHEP* 0812 (2008), p. 063. DOI: 10.1088/1126-6708/2008/12/063. arXiv: 0810.5178 [hep-ph].

[344] Y. Bai et al. "Stop the Top Background of the Stop Search". *JHEP* 1207 (2012), p. 110. DOI: 10.1007/JHEP07(2012)110. arXiv: 1203.4813 [hep-ph].

[345] S. Chatrchyan et al. "Search for top-squark pair production in the single-lepton final state in pp collisions at $\sqrt{s}$ = 8 TeV". *Eur.Phys.J.* C73 (2013), p. 2677. DOI: 10.1140/epjc/s10052-013-2677-2. arXiv: 1308.1586 [hep-ex].

[346] G. Aad et al. "Search for top squark pair production in final states with one isolated lepton, jets, and missing transverse momentum in $\sqrt{s} = 8$ TeV pp collisions with the ATLAS detector" (2014). arXiv: 1407.0583 [hep-ex].

[347] A. L. Read. "Presentation of search results: The CL(s) technique". *J.Phys.* G28 (2002), pp. 2693–2704. DOI: 10.1088/0954-3899/28/10/313.

[348] R. Mohapatra and G. Senjanovic. "Neutrino Mass and Spontaneous Parity Violation". *Phys.Rev.Lett.* 44 (1980), p. 912. DOI: 10.1103/PhysRevLett.44.912.

[349] J. Casas, J. Espinosa, and I. Hidalgo. "Implications for new physics from fine-tuning arguments. 1. Application to SUSY and seesaw cases". *JHEP* 0411 (2004), p. 057. DOI: 10.1088/1126-6708/2004/11/057. arXiv: hep-ph/0410298 [hep-ph].

[350] A. Abada et al. "Low energy effects of neutrino masses". *JHEP* 0712 (2007), p. 061. DOI: 10.1088/1126-6708/2007/12/061. arXiv: 0707.4058 [hep-ph].

[351] Z.-z. Xing. "Naturalness and Testability of TeV Seesaw Mechanisms". *Prog.Theor.Phys.Suppl.* 180 (2009), pp. 112–127. DOI: 10.1143/PTPS.180.112. arXiv: 0905.3903 [hep-ph].

[352] F. Bazzocchi and M. Fabbrichesi. "Little hierarchy problem for new physics just beyond the LHC". *Phys.Rev.* D87.3 (2013), p. 036001. DOI: 10.1103/PhysRevD.87.036001. arXiv: 1212.5065 [hep-ph].

[353] H. Davoudiasl and I. Lewis. "Right-Handed Neutrinos as the Origin of the Electroweak Scale". *Phys.Rev.* D90.3 (2014), p. 033003. DOI: 10.1103/PhysRevD.90.033003. arXiv: 1404.6260 [hep-ph].

[354] P. Frampton, S. Glashow, and T. Yanagida. "Cosmological sign of neutrino CP violation". *Phys.Lett.* B548 (2002), pp. 119–121. DOI: 10.1016/S0370-2693(02)02853-8. arXiv: hep-ph/0208157 [hep-ph].

[355] M. Raidal and A. Strumia. "Predictions of the most minimal seesaw model". *Phys.Lett.* B553 (2003), pp. 72–78. DOI: 10.1016/S0370-2693(02)03124-6. arXiv: hep-ph/0210021 [hep-ph].

[356] W.-l. Guo, Z.-z. Xing, and S. Zhou. "Neutrino Masses, Lepton Flavor Mixing and Leptogenesis in the Minimal Seesaw Model". *Int.J.Mod.Phys.* E16 (2007), pp. 1–50. DOI: 10.1142/S0218301307004898. arXiv: hep-ph/0612033 [hep-ph].

[357] S. Blanchet and P. Di Bari. "Flavor effects on leptogenesis predictions". *JCAP* 0703 (2007), p. 018. DOI: 10.1088/1475-7516/2007/03/018. arXiv: hep-ph/0607330 [hep-ph].

[358] F. Josse-Michaux and A. Abada. "Study of flavour dependencies in leptogenesis". *JCAP* 0710 (2007), p. 009. DOI: 10.1088/1475-7516/2007/10/009. arXiv: hep-ph/0703084 [HEP-PH].

[359] P. Di Bari. "Seesaw geometry and leptogenesis". *Nucl.Phys.* B727 (2005), pp. 318–354. DOI: 10.1016/j.nuclphysb.2005.08.032. arXiv: hep-ph/0502082 [hep-ph].

[360] O. Vives. "Flavor dependence of CP asymmetries and thermal leptogenesis with strong right-handed neutrino mass hierarchy". *Phys.Rev.* D73 (2006), p. 073006. DOI: 10.1103/PhysRevD.73.073006. arXiv: hep-ph/0512160 [hep-ph].

[361] G. Engelhard et al. "The Importance of N2 leptogenesis". *Phys.Rev.Lett.* 99 (2007), p. 081802. DOI: 10.1103/PhysRevLett.99.081802. arXiv: hep-ph/0612187 [hep-ph].

[362] E. Akhmedov, V. Rubakov, and A. Smirnov. "Baryogenesis via neutrino oscillations". *Phys.Rev.Lett.* 81 (1998), pp. 1359–1362. DOI: 10.1103/PhysRevLett.81.1359. arXiv: hep-ph/9803255 [hep-ph].

[363] M. Fabbrichesi and A. Urbano. "Naturalness redux" (2015). arXiv: 1504.05403 [hep-ph].

[364] G. Branco et al. "Theory and phenomenology of two-Higgs-doublet models". *Phys.Rept.* 516 (2012), pp. 1–102. DOI: 10.1016/j.physrep.2012.02.002. arXiv: 1106.0034 [hep-ph].

[365] E. Paschos. "Diagonal Neutral Currents". *Phys.Rev.* D15 (1977), p. 1966. DOI: 10.1103/PhysRevD.15.1966.

[366] S. Glashow and S. Weinberg. "Natural Conservation Laws for Neutral Currents". *Phys.Rev.* D15 (1977), p. 1958. DOI: 10.1103/PhysRevD.15.1958.

[367] E. Ma. "Naturally small seesaw neutrino mass with no new physics beyond the TeV scale". *Phys.Rev.Lett.* 86 (2001), pp. 2502–2504. DOI: 10.1103/PhysRevLett.86.2502. arXiv: hep-ph/0011121 [hep-ph].

[368] F. Wang, W. Wang, and J. Yang. "Split two-Higgs-doublet model and neutrino condensation". *Europhys.Lett.* 76 (2006), pp. 388–394. DOI: 10.1209/epl/i2006-10293-3. arXiv: hep-ph/0601018 [hep-ph].

[369] S. Gabriel and S. Nandi. "A New two Higgs doublet model". *Phys.Lett.* B655 (2007), pp. 141–147. DOI: 10.1016/j.physletb.2007.04.062. arXiv: hep-ph/0610253 [hep-ph].

[370] S. Davidson and H. Logan. "Dirac neutrinos from a second Higgs doublet". *Phys.Rev.* D80 (2009), p. 095008. DOI: 10.1103/PhysRevD.80.095008. arXiv: 0906.3335 [hep-ph].

[371] V. Khachatryan et al. "Search for neutral MSSM Higgs bosons decaying to a pair of tau leptons in pp collisions". *JHEP* 1410 (2014), p. 160. DOI: 10.1007/JHEP10(2014)160. arXiv: 1408.3316 [hep-ex].

[372] J. Gunion and H. Haber. "The CP conserving two Higgs doublet model: The Approach to the decoupling limit". *Phys.Rev.* D67 (2003), p. 075019. DOI: 10.1103/PhysRevD.67.075019. arXiv: hep-ph/0207010 [hep-ph].

[373] N. Deshpande and E. Ma. "Pattern of Symmetry Breaking with Two Higgs Doublets". *Phys.Rev.* D18 (1978), p. 2574. DOI: 10.1103/PhysRevD.18.2574.

[374] K. Klimenko. "On Necessary and Sufficient Conditions for Some Higgs Potentials to Be Bounded From Below". *Theor.Math.Phys.* 62 (1985), pp. 58–65. DOI: 10.1007/BF01034825.

[375] M. Maniatis et al. "Stability and symmetry breaking in the general two-Higgs-doublet model". *Eur.Phys.J.* C48 (2006), pp. 805–823. DOI: 10.1140/epjc/s10052-006-0016-6. arXiv: hep-ph/0605184 [hep-ph].

[376] A. Barroso et al. "Metastability bounds on the two Higgs doublet model". *JHEP* 1306 (2013), p. 045. DOI: 10.1007/JHEP06(2013)045. arXiv: 1303.5098 [hep-ph].

[377] S. Kanemura, T. Kubota, and E. Takasugi. "Lee-Quigg-Thacker bounds for Higgs boson masses in a two doublet model". *Phys.Lett.* B313 (1993), pp. 155–160. DOI: 10.1016/0370-2693(93)91205-2. arXiv: hep-ph/9303263 [hep-ph].

[378] A. Akeroyd, A. Arhrib, and E.-M. Naimi. “Note on tree level unitarity in the general two Higgs doublet model”. *Phys.Lett.* B490 (2000), pp. 119–124. DOI: `10.1016/S0370-2693(00)00962-X`. arXiv: `hep-ph/0006035 [hep-ph]`.

[379] I. Ginzburg and I. Ivanov. “Tree-level unitarity constraints in the most general 2HDM”. *Phys.Rev.* D72 (2005), p. 115010. DOI: `10.1103/PhysRevD.72.115010`. arXiv: `hep-ph/0508020 [hep-ph]`.

[380] U. Nierste and K. Riesselmann. “Higgs sector renormalization group in the MS and OMS scheme: The Breakdown of perturbation theory for a heavy Higgs”. *Phys.Rev.* D53 (1996), pp. 6638–6652. DOI: `10.1103/PhysRevD.53.6638`. arXiv: `hep-ph/9511407 [hep-ph]`.

[381] N. Chakrabarty, U. Dey, and B. Mukhopadhyaya. “High-scale validity of a two-Higgs doublet scenario: a study including LHC data”. *JHEP* 1412 (2014), p. 166. DOI: `10.1007/JHEP12(2014)166`. arXiv: `1407.2145 [hep-ph]`.

[382] D. Das and I. Saha. “Search for a stable alignment limit in two-Higgs-doublet models”. *Phys.Rev.* D91.9 (2015), p. 095024. DOI: `10.1103/PhysRevD.91.095024`. arXiv: `1503.02135 [hep-ph]`.

[383] D. Chowdhury and O. Eberhardt. “Global fits of the two-loop renormalized Two-Higgs-Doublet model with soft Z_2 breaking” (2015). arXiv: `1503.08216 [hep-ph]`.

[384] J. Bijnens, J. Lu, and J. Rathsman. “Constraining General Two Higgs Doublet Models by the Evolution of Yukawa Couplings”. *JHEP* 1205 (2012), p. 118. DOI: `10.1007/JHEP05(2012)118`. arXiv: `1111.5760 [hep-ph]`.

[385] C.-Y. Chen, S. Dawson, and M. Sher. “Heavy Higgs Searches and Constraints on Two Higgs Doublet Models”. *Phys.Rev.* D88 (2013), p. 015018. DOI: `10.1103/PhysRevD.88.015018`, `10.1103/PhysRevD.88.039901`. arXiv: `1305.1624 [hep-ph]`.

[386] O. Eberhardt, U. Nierste, and M. Wiebusch. “Status of the two-Higgs-doublet model of type II”. *JHEP* 1307 (2013), p. 118. DOI: `10.1007/JHEP07(2013)118`. arXiv: `1305.1649 [hep-ph]`.

[387] N. Craig, J. Galloway, and S. Thomas. “Searching for Signs of the Second Higgs Doublet” (2013). arXiv: `1305.2424 [hep-ph]`.

[388] S. Chang et al. “Two Higgs doublet models for the LHC Higgs boson data at $\sqrt{s} = 7$ and 8 TeV”. *JHEP* 1409 (2014), p. 101. DOI: `10.1007/JHEP09(2014)101`. arXiv: `1310.3374 [hep-ph]`.

[389] B. Dumont et al. “Constraints on and future prospects for Two-Higgs-Doublet Models in light of the LHC Higgs signal”. *Phys.Rev.* D90 (2014), p. 035021. DOI: 10.1103/PhysRevD.90.035021. arXiv: 1405.3584 [hep-ph].

[390] Y. Amhis et al. “Averages of b-hadron, c-hadron, and τ-lepton properties as of summer 2014” (2014). arXiv: 1412.7515 [hep-ex].

[391] M. Misiak et al. “Updated NNLO QCD predictions for the weak radiative B-meson decays” (2015). arXiv: 1503.01789 [hep-ph].

[392] T. Junk et al. “Search for charged Higgs bosons: Preliminary combined results using LEP data collected at energies up to 209-GeV” (2001). arXiv: hep-ex/0107031 [hep-ex].

[393] G. Aad et al. “Search for neutral Higgs bosons of the minimal supersymmetric standard model in pp collisions at $\sqrt{s}$ = 8 TeV with the ATLAS detector”. *JHEP* 1411 (2014), p. 056. DOI: 10.1007/JHEP11(2014)056. arXiv: 1409.6064 [hep-ex].

[394] G. Aad et al. “Search for charged Higgs bosons decaying via $H^{\pm} \to \tau^{\pm}\nu$ in fully hadronic final states using pp collision data at $\sqrt{s} = 8$ TeV with the ATLAS detector”. *JHEP* 1503 (2015), p. 088. DOI: 10.1007/JHEP03(2015)088. arXiv: 1412.6663 [hep-ex].

[395] C. Collaboration. *Search for charged Higgs bosons with the $H^{+} \to \tau\nu$ decay channel in the fully hadronic final state at $\sqrt{s} = 8$ TeV*. Tech. rep. CMS-PAS-HIG-14-020. 2014.

[396] T. Toma and A. Vicente. “Lepton Flavor Violation in the Scotogenic Model”. *JHEP* 1401 (2014), p. 160. DOI: 10.1007/JHEP01(2014)160. arXiv: 1312.2840.

[397] B. Grzadkowski, M. Lindner, and S. Theisen. “Nonlinear Evolution of Yukawa Couplings in the Double Higgs and Supersymmetric Extensions of the Standard Model”. *Phys.Lett.* B198 (1987), p. 64. DOI: 10.1016/0370-2693(87)90160-2.

[398] A. Merle and M. Platscher. “Parity Problem of the Scotogenic Neutrino Model” (2015). arXiv: 1502.03098 [hep-ph].

[399] S. Davidson, E. Nardi, and Y. Nir. “Leptogenesis”. *Phys.Rept.* 466 (2008), pp. 105–177. DOI: 10.1016/j.physrep.2008.06.002. arXiv: 0802.2962 [hep-ph].

[400] N. Haba and O. Seto. “Low scale thermal leptogenesis in neutrinophilic Higgs doublet models”. *Prog.Theor.Phys.* 125 (2011), pp. 1155–1169. DOI: 10.1143/PTP.125.1155. arXiv: 1102.2889 [hep-ph].

[401] E. Ma. "Common origin of neutrino mass, dark matter, and baryogenesis". *Mod.Phys.Lett.* A21 (2006), pp. 1777–1782. DOI: 10.1142/S0217732306021141. arXiv: hep-ph/0605180 [hep-ph].

[402] T. Hambye et al. "Scalar Multiplet Dark Matter". *JHEP* 0907 (2009), p. 090. DOI: 10.1007/JHEP05(2010)066, 10.1088/1126-6708/2009/07/090. arXiv: 0903.4010 [hep-ph].

[403] D. Suematsu. "Thermal Leptogenesis in a TeV Scale Model for Neutrino Masses". *Eur.Phys.J.* C72 (2012), p. 1951. DOI: 10.1140/epjc/s10052-012-1951-z. arXiv: 1103.0857 [hep-ph].

[404] S. Kashiwase and D. Suematsu. "Baryon number asymmetry and dark matter in the neutrino mass model with an inert doublet". *Phys.Rev.* D86 (2012), p. 053001. DOI: 10.1103/PhysRevD.86.053001. arXiv: 1207.2594 [hep-ph].

[405] J. Racker. "Mass bounds for baryogenesis from particle decays and the inert doublet model". *JCAP* 1403 (2014), p. 025. DOI: 10.1088/1475-7516/2014/03/025. arXiv: 1308.1840 [hep-ph].

[406] A. Abada et al. "Flavor issues in leptogenesis". *JCAP* 0604 (2006), p. 004. DOI: 10.1088/1475-7516/2006/04/004. arXiv: hep-ph/0601083 [hep-ph].

[407] E. Nardi et al. "The Importance of flavor in leptogenesis". *JHEP* 01 (2006), p. 164. DOI: 10.1088/1126-6708/2006/01/164. arXiv: hep-ph/0601084 [hep-ph].

[408] A. Abada et al. "Flavour Matters in Leptogenesis". *JHEP* 09 (2006), p. 010. DOI: 10.1088/1126-6708/2006/09/010. arXiv: hep-ph/0605281 [hep-ph].

[409] P. S. Bhupal Dev et al. "Flavour Covariant Transport Equations: an Application to Resonant Leptogenesis". *Nucl. Phys.* B886 (2014), pp. 569–664. DOI: 10.1016/j.nuclphysb.2014.06.020. arXiv: 1404.1003 [hep-ph].

[410] S. Bertolini et al. "Massive neutrinos and invisible axion minimally connected". *Phys. Rev.* D91.5 (2015), p. 055014. DOI: 10.1103/PhysRevD.91.055014. arXiv: 1412.7105 [hep-ph].

[411] A. G. Dias et al. "The Quest for an Intermediate-Scale Accidental Axion and Further ALPs". *JHEP* 06 (2014), p. 037. DOI: 10.1007/JHEP06(2014)037. arXiv: 1403.5760 [hep-ph].

[412] A. G. Dias. "Neutrino Mass Through Concomitant Breakdown of the U(1) Chiral and Scale Symmetries". *Phys. Rev.* D73 (2006), p. 096002. DOI: 10.1103/PhysRevD.73.096002. arXiv: hep-ph/0604219 [hep-ph].

[413] P. Langacker, R. D. Peccei, and T. Yanagida. "Invisible Axions and Light Neutrinos: Are They Connected?" *Mod. Phys. Lett.* A1 (1986), p. 541. DOI: 10.1142/S0217732386000683.

[414] J. R. Ellis and M. K. Gaillard. "Strong and Weak CP Violation". *Nucl. Phys.* B150 (1979), p. 141. DOI: 10.1016/0550-3213(79)90297-9.

[415] H. Georgi and L. Randall. "Flavor Conserving CP Violation in Invisible Axion Models". *Nucl. Phys.* B276 (1986), p. 241. DOI: 10.1016/0550-3213(86)90022-2.

[416] J. Kim and G. Carosi. "Axions and the Strong CP Problem". *Rev.Mod.Phys.* 82 (2010), pp. 557–602. DOI: 10.1103/RevModPhys.82.557. arXiv: 0807.3125 [hep-ph].

[417] G. Raffelt. "Axion Constraints From White Dwarf Cooling Times". *Phys.Lett.* B166 (1986), p. 402. DOI: 10.1016/0370-2693(86)91588-1.

[418] G. Raffelt and A. Weiss. "Red giant bound on the axion - electron coupling revisited". *Phys.Rev.* D51 (1995), pp. 1495–1498. DOI: 10.1103/PhysRevD.51.1495. arXiv: hep-ph/9410205 [hep-ph].

[419] J. Isern et al. "Axions and the cooling of white dwarf stars". *Astrophys.J.* 682 (2008), p. L109. DOI: 10.1086/591042. arXiv: 0806.2807 [astro-ph].

[420] J. Preskill, M. Wise, and F. Wilczek. "Cosmology of the Invisible Axion". *Phys.Lett.* B120 (1983), pp. 127–132. DOI: 10.1016/0370-2693(83)90637-8.

[421] L. Abbott and P. Sikivie. "A Cosmological Bound on the Invisible Axion". *Phys.Lett.* B120 (1983), pp. 133–136. DOI: 10.1016/0370-2693(83)90638-X.

[422] M. Dine and W. Fischler. "The Not So Harmless Axion". *Phys.Lett.* B120 (1983), pp. 137–141. DOI: 10.1016/0370-2693(83)90639-1.

[423] P. Sikivie. "Axion Cosmology". *Lect.Notes Phys.* 741 (2008), pp. 19–50. DOI: 10.1007/978-3-540-73518-2_2. arXiv: astro-ph/0610440 [astro-ph].

[424] R. Peccei. "The Strong CP problem and axions". *Lect.Notes Phys.* 741 (2008), pp. 3–17. DOI: 10.1007/978-3-540-73518-2_1. arXiv: hep-ph/0607268 [hep-ph].

[425] S.-Y. Pi. "Inflation Without Tears". *Phys.Rev.Lett.* 52 (1984), pp. 1725–1728. DOI: 10.1103/PhysRevLett.52.1725.

[426] P. Sikivie. "Experimental Tests of the Invisible Axion". *Phys.Rev.Lett.* 51 (1983), pp. 1415–1417. DOI: 10.1103/PhysRevLett.51.1415.

[427] *Center for Axion and Precision Physics Research*. https://capp.ibs.re.kr/html/capp_en/. Accessed: 2015-04-14.

[428] M. Boylan-Kolchin, J. S. Bullock, and M. Kaplinghat. "Too big to fail? The puzzling darkness of massive Milky Way subhaloes". *Mon. Not. Roy. Astron. Soc.* 415 (2011), p. L40. arXiv: `1103.0007 [astro-ph.CO]`.

[429] B. Moore. "Evidence against dissipationless dark matter from observations of galaxy haloes". *Nature* 370 (1994), p. 629. DOI: `10.1038/370629a0`.

[430] D. N. Spergel and P. J. Steinhardt. "Observational evidence for selfinteracting cold dark matter". *Phys. Rev. Lett.* 84 (2000), pp. 3760–3763. DOI: `10.1103/PhysRevLett.84.3760`. arXiv: `astro-ph/9909386 [astro-ph]`.

[431] R. Foot. "Mirror matter-type dark matter". *Int. J. Mod. Phys.* D13 (2004), pp. 2161–2192. DOI: `10.1142/S0218271804006449`. arXiv: `astro-ph/0407623 [astro-ph]`.

[432] R. Foot. "Mirror dark matter: Cosmology, galaxy structure and direct detection". *Int. J. Mod. Phys.* A29 (2014), p. 1430013. DOI: `10.1142/S0217751X14300130`. arXiv: `1401.3965 [astro-ph.CO]`.

[433] H. Goldberg and L. J. Hall. "A New Candidate for Dark Matter". *Phys. Lett.* B174 (1986), p. 151. DOI: `10.1016/0370-2693(86)90731-8`.

[434] A. Ibarra, A. Ringwald, and C. Weniger. "Hidden gauginos of an unbroken U(1): Cosmological constraints and phenomenological prospects". *JCAP* 0901 (2009), p. 003. DOI: `10.1088/1475-7516/2009/01/003`. arXiv: `0809.3196 [hep-ph]`.

[435] L. Ackerman et al. "Dark Matter and Dark Radiation". *Phys. Rev.* D79 (2009), p. 023519. DOI: `10.1103/PhysRevD.79.023519, 10.1142/9789814293792_0021`. arXiv: `0810.5126 [hep-ph]`.

[436] N. Arkani-Hamed et al. "A Theory of Dark Matter". *Phys. Rev.* D79 (2009), p. 015014. DOI: `10.1103/PhysRevD.79.015014`. arXiv: `0810.0713 [hep-ph]`.

[437] J. L. Feng et al. "Hidden Charged Dark Matter". *JCAP* 0907 (2009), p. 004. DOI: `10.1088/1475-7516/2009/07/004`. arXiv: `0905.3039 [hep-ph]`.

[438] D. E. Kaplan et al. "Atomic Dark Matter". *JCAP* 1005 (2010), p. 021. DOI: `10.1088/1475-7516/2010/05/021`. arXiv: `0909.0753 [hep-ph]`.

[439] S. Andreas, M. D. Goodsell, and A. Ringwald. "Dark matter and dark forces from a supersymmetric hidden sector". *Phys. Rev.* D87.2 (2013), p. 025007. DOI: `10.1103/PhysRevD.87.025007`. arXiv: `1109.2869 [hep-ph]`.

[440] J. M. Cline, Z. Liu, and W. Xue. "Millicharged Atomic Dark Matter". *Phys. Rev.* D85 (2012), p. 101302. DOI: 10.1103/PhysRevD.85.101302. arXiv: 1201.4858 [hep-ph].

[441] J.-W. Cui et al. "Spontaneous Mirror Parity Violation, Common Origin of Matter and Dark Matter, and the LHC Signatures". *Phys. Rev.* D85 (2012), p. 096003. DOI: 10.1103/PhysRevD.85.096003. arXiv: 1110.6893 [hep-ph].

[442] J. Fan et al. "Double-Disk Dark Matter". *Phys. Dark Univ.* 2 (2013), pp. 139–156. DOI: 10.1016/j.dark.2013.07.001. arXiv: 1303.1521 [astro-ph.CO].

[443] K. Petraki, L. Pearce, and A. Kusenko. "Self-interacting asymmetric dark matter coupled to a light massive dark photon". *JCAP* 1407 (2014), p. 039. DOI: 10.1088/1475-7516/2014/07/039. arXiv: 1403.1077 [hep-ph].

[444] R. Foot and S. Vagnozzi. "Dissipative hidden sector dark matter". *Phys. Rev.* D91 (2015), p. 023512. DOI: 10.1103/PhysRevD.91.023512. arXiv: 1409.7174 [hep-ph].

[445] R. Foot. "Can dark matter - electron scattering explain the DAMA annual modulation signal?" *Phys. Rev.* D90.12 (2014), p. 121302. DOI: 10.1103/PhysRevD.90.121302. arXiv: 1407.4213 [hep-ph].

[446] R. Bernabei et al. "Dark matter search". *Riv. Nuovo Cim.* 26N1 (2003), pp. 1–73. arXiv: astro-ph/0307403 [astro-ph].

[447] R. Bernabei et al. "Search for WIMP annual modulation signature: Results from DAMA / NaI-3 and DAMA / NaI-4 and the global combined analysis". *Phys. Lett.* B480 (2000), pp. 23–31. DOI: 10.1016/S0370-2693(00)00405-6.

[448] R. Bernabei et al. "New results from DAMA/LIBRA". *Eur. Phys. J.* C67 (2010), pp. 39–49. DOI: 10.1140/epjc/s10052-010-1303-9. arXiv: 1002.1028 [astro-ph.GA].

[449] J. R. Spreiter, A. L. Summers, and A. W. Rizzi. "Solar wind flow past non-magnetic planets - Venus and Mars". *Planetary and Space Science* 18 (Sept. 1970), pp. 1281–1299. DOI: 10.1016/0032-0633(70)90139-X.

[450] J. G. Luhmann, S. A. Ledvina, and C. T. Russell. "Induced magnetospheres". *Advances in Space Research* 33 (Jan. 2004), pp. 1905–1912. DOI: 10.1016/j.asr.2003.03.031.

[451] R. Foot and X.-G. He. "Comment on Z Z-prime mixing in extended gauge theories". *Phys.Lett.* B267 (1991), pp. 509–512. DOI: 10.1016/0370-2693(91)90901-2.

[452] R. Foot. "Galactic structure explained with dissipative mirror dark matter". *Phys. Rev.* D88.2 (2013), p. 023520. DOI: 10.1103/PhysRevD.88.023520. arXiv: 1304.4717 [astro-ph.CO].

[453] R. Foot and R. R. Volkas. "Spheroidal galactic halos and mirror dark matter". *Phys. Rev.* D70 (2004), p. 123508. DOI: 10.1103/PhysRevD.70.123508. arXiv: astro-ph/0407522 [astro-ph].

[454] R. Foot. "Tully-Fisher relation, galactic rotation curves and dissipative mirror dark matter". *JCAP* 1412.12 (2014), p. 047. DOI: 10.1088/1475-7516/2014/12/047. arXiv: 1307.1755 [astro-ph.GA].

[455] R. Foot. "Dissipative dark matter explains rotation curves". *Phys. Rev.* D91.12 (2015), p. 123543. DOI: 10.1103/PhysRevD.91.123543. arXiv: 1502.07817 [astro-ph.GA].

[456] Z. Berezhiani, D. Comelli, and F. L. Villante. "The Early mirror universe: Inflation, baryogenesis, nucleosynthesis and dark matter". *Phys. Lett.* B503 (2001), pp. 362–375. DOI: 10.1016/S0370-2693(01)00217-9. arXiv: hep-ph/0008105 [hep-ph].

[457] A. Yu. Ignatiev and R. R. Volkas. "Mirror dark matter and large scale structure". *Phys. Rev.* D68 (2003), p. 023518. DOI: 10.1103/PhysRevD.68.023518. arXiv: hep-ph/0304260 [hep-ph].

[458] Z. Berezhiani et al. "Structure formation with mirror dark matter: CMB and LSS". *Int. J. Mod. Phys.* D14 (2005), pp. 107–120. DOI: 10.1142/S0218271805005165. arXiv: astro-ph/0312605 [astro-ph].

[459] R. Foot. "Mirror dark matter cosmology - predictions for $N_{eff}[CMB]$ and $N_{eff}[BBN]$". *Phys. Lett.* B711 (2012), pp. 238–243. DOI: 10.1016/j.physletb.2012.04.023. arXiv: 1111.6366 [astro-ph.CO].

[460] R. Foot. "Implications of mirror dark matter kinetic mixing for CMB anisotropies". *Phys. Lett.* B718 (2013), pp. 745–751. DOI: 10.1016/j.physletb.2012.12.001. arXiv: 1208.6022 [astro-ph.CO].

[461] P. Ciarcelluti and Q. Wallemacq. "Is dark matter made of mirror matter? Evidence from cosmological data". *Phys. Lett.* B729 (2014), pp. 62–66. DOI: 10.1016/j.physletb.2013.12.057. arXiv: 1211.5354 [astro-ph.CO].

[462] K. Petraki, M. Trodden, and R. R. Volkas. "Visible and dark matter from a first-order phase transition in a baryon-symmetric universe". *JCAP* 1202 (2012), p. 044. DOI: 10.1088/1475-7516/2012/02/044. arXiv: 1111.4786 [hep-ph].

[463] B. von Harling, K. Petraki, and R. R. Volkas. "Affleck-Dine dynamics and the dark sector of pangenesis". *JCAP* 1205 (2012), p. 021. DOI: 10.1088/1475-7516/2012/05/021. arXiv: 1201.2200 [hep-ph].

[464] F.-Y. Cyr-Racine and K. Sigurdson. "Cosmology of atomic dark matter". *Phys. Rev.* D87.10 (2013), p. 103515. DOI: 10.1103/PhysRevD.87.103515. arXiv: 1209.5752 [astro-ph.CO].

[465] F.-Y. Cyr-Racine et al. "Constraints on Large-Scale Dark Acoustic Oscillations from Cosmology". *Phys. Rev.* D89.6 (2014), p. 063517. DOI: 10.1103/PhysRevD.89.063517. arXiv: 1310.3278 [astro-ph.CO].

[466] H. Vogel and J. Redondo. "Dark Radiation constraints on minicharged particles in models with a hidden photon". *JCAP* 1402 (2014), p. 029. DOI: 10.1088/1475-7516/2014/02/029. arXiv: 1311.2600 [hep-ph].

[467] D. Clowe et al. "A direct empirical proof of the existence of dark matter". *Astrophys. J.* 648 (2006), pp. L109–L113. DOI: 10.1086/508162. arXiv: astro-ph/0608407 [astro-ph].

[468] M. Heikinheimo et al. "Dark matter self-interactions via collisionless shocks in cluster mergers". *Phys. Lett.* B749 (2015), pp. 236–241. DOI: 10.1016/j.physletb.2015.08.012. arXiv: 1504.04371 [hep-ph].

[469] Z. K. Silagadze. "Mirror dark matter discovered?" *ICFAI U. J. Phys.* 2 (2009), pp. 143–154. arXiv: 0808.2595 [astro-ph].

[470] R. Foot. "Diurnal modulation due to self-interacting mirror and hidden sector dark matter". *JCAP* 1204 (2012), p. 014. DOI: 10.1088/1475-7516/2012/04/014. arXiv: 1110.2908 [hep-ph].

[471] R. Foot and S. Vagnozzi. "Diurnal modulation signal from dissipative hidden sector dark matter". *Phys. Lett.* B748 (2015), pp. 61–66. DOI: 10.1016/j.physletb.2015.06.063. arXiv: 1412.0762 [hep-ph].

[472] A. M. Dziewonski and D. L. Anderson. "Preliminary reference earth model". *Phys. Earth Planet. Interiors* 25 (1981), pp. 297–356. DOI: 10.1016/0031-9201(81)90046-7.

[473] W. Cui and L. Li. "2D MHD Simulation of the Lunar Wake". *Chinese Journal of Space Science* 28.3, 189 (2008), p. 189. DOI: 10.11728/cjss2008.03.189.

[474] L. Xie et al. "Three-dimensional MHD simulation of the lunar wake". English. *Science China Earth Sciences* 56.2 (2013), pp. 330–338. ISSN: 1674-7313. DOI: 10.1007/s11430-012-4383-6.

[475] T. Tanaka. "Configurations of the solar wind flow and magnetic field around the planets with no magnetic field: Calculation by a new MHD simulation scheme". *J. Geophys. Res.* 98 (Oct. 1993), pp. 17251–17262. DOI: 10.1029/93JA01516.

[476] S. Cable and R. S. Steinolfson. "Three-dimensional MHD simulations of the interaction between Venus and the solar wind". *J. Geophys. Res.* 100 (Nov. 1995), pp. 21645–21658. DOI: 10.1029/95JA02174.

[477] D. L. De Zeeuw et al. "A new axisymmetric MHD model of the interaction of the solar wind with Venus". *J. Geophys. Res.* 101 (1996), pp. 4547–4556. DOI: 10.1029/95JE03363.

[478] E. Kallio, J. G. Luhmann, and J. G. Lyon. "Magnetic field near Venus - A comparison between Pioneer Venus Orbiter magnetic field observations and an MHD simulation". *J. Geophys. Res.* 103 (Mar. 1998), p. 4723. DOI: 10.1029/97JA02862.

[479] A. Mignone et al. "PLUTO: A Numerical Code for Computational Astrophysics". *Astrophys. J. Suppl.* 170 (2007), p. 228. DOI: 10.1086/513316. arXiv: astro-ph/0701854 [ASTRO-PH].

[480] M. Adams et al. *Chombo Software Package for AMR Applications: Design Document*. Tech. rep. LBNL-6616E. Lawrence Berkeley National Laboratory, 2014.

[481] M. Holmström et al. "The interaction between the Moon and the solar wind". *Earth, Planets, and Space* 64 (Feb. 2012), pp. 237–245. DOI: 10.5047/eps.2011.06.040. arXiv: 1104.1440 [physics.space-ph].

[482] A. K. Drukier, K. Freese, and D. N. Spergel. "Detecting Cold Dark Matter Candidates". *Phys. Rev.* D33 (1986), pp. 3495–3508. DOI: 10.1103/PhysRevD.33.3495.

[483] K. Freese, J. A. Frieman, and A. Gould. "Signal Modulation in Cold Dark Matter Detection". *Phys. Rev.* D37 (1988), pp. 3388–3405. DOI: 10.1103/PhysRevD.37.3388.

[484] X. Cao et al. "PandaX: A Liquid Xenon Dark Matter Experiment at CJPL". *Sci. China Phys. Mech. Astron.* 57 (2014), pp. 1476–1494. DOI: 10.1007/s11433-014-5521-2. arXiv: 1405.2882 [physics.ins-det].

[485] E. Shields, J. Xu, and F. Calaprice. "SABRE: A New NaI(T1) Dark Matter Direct Detection Experiment". *Phys. Procedia* 61 (2015), pp. 169–178. DOI: 10.1016/j.phpro.2014.12.028.

[486] J. I. Collar and F. T. Avignone. "Diurnal modulation effects in cold dark matter experiments". *Phys. Lett.* B275 (1992), pp. 181–185. DOI: 10.1016/0370-2693(92)90873-3.

[487] J. I. Collar and F. T. Avignone III. "The Effect of elastic scattering in the Earth on cold dark matter experiments". *Phys. Rev.* D47 (1993), pp. 5238–5246. DOI: 10.1103/PhysRevD.47.5238.

[488] C. Kouvaris and I. M. Shoemaker. "Daily modulation as a smoking gun of dark matter with significant stopping rate". *Phys. Rev.* D90 (2014), p. 095011. DOI: 10.1103/PhysRevD.90.095011. arXiv: 1405.1729 [hep-ph].

[489] R. Foot. "A comprehensive analysis of the dark matter direct detection experiments in the mirror dark matter framework". *Phys. Rev.* D82 (2010), p. 095001. DOI: 10.1103/PhysRevD.82.095001. arXiv: 1008.0685 [hep-ph].

[490] R. Foot. "Mirror and hidden sector dark matter in the light of new CoGeNT data". *Phys. Lett.* B703 (2011), pp. 7–13. DOI: 10.1016/j.physletb.2011.07.044. arXiv: 1106.2688 [hep-ph].

[491] R. Bernabei et al. "A few final comments to arXiv:1210.7548[hep-ph]" (2012). arXiv: 1211.6346 [hep-ph].

[492] E. Aprile et al. "Dark Matter Results from 225 Live Days of XENON100 Data". *Phys. Rev. Lett.* 109 (2012), p. 181301. DOI: 10.1103/PhysRevLett.109.181301. arXiv: 1207.5988 [astro-ph.CO].

[493] D. S. Akerib et al. "First results from the LUX dark matter experiment at the Sanford Underground Research Facility". *Phys. Rev. Lett.* 112 (2014), p. 091303. DOI: 10.1103/PhysRevLett.112.091303. arXiv: 1310.8214 [astro-ph.CO].

[494] G. Angloher et al. "Results on low mass WIMPs using an upgraded CRESST-II detector". *Eur. Phys. J.* C74.12 (2014), p. 3184. DOI: 10.1140/epjc/s10052-014-3184-9. arXiv: 1407.3146 [astro-ph.CO].

[495] Z. Ahmed et al. "Dark Matter Search Results from the CDMS II Experiment". *Science* 327 (2010), pp. 1619–1621. DOI: 10.1126/science.1186112. arXiv: 0912.3592 [astro-ph.CO].

[496] C. E. Aalseth et al. "Search for An Annual Modulation in Three Years of CoGeNT Dark Matter Detector Data" (2014). arXiv: 1401.3295 [astro-ph.CO].

[497] E. Aprile et al. "Exclusion of Leptophilic Dark Matter Models using XENON100 Electronic Recoil Data". *Science* 349.6250 (2015), pp. 851–854. DOI: 10.1126/science.aab2069. arXiv: 1507.07747 [astro-ph.CO].

[498] R. Bernabei et al. "Model independent result on possible diurnal effect in DAMA/LIBRA-phase1". *Eur. Phys. J.* C74.3 (2014), p. 2827. DOI: 10.1140/epjc/s10052-014-2827-1. arXiv: 1403.4733 [astro-ph.GA].

[499] W. Buchmuller and M. Plumacher. "CP asymmetry in Majorana neutrino decays". *Phys.Lett.* B431 (1998), pp. 354–362. DOI: 10.1016/S0370-2693(97)01548-7. arXiv: hep-ph/9710460 [hep-ph].